

Sheffield Hallam University

Effects of cold metal transfer welding on properties of ferritic stainless steel

MAGOWAN, Stephen

Available from the Sheffield Hallam University Research Archive (SHURA) at:

<http://shura.shu.ac.uk/17304/>

A Sheffield Hallam University thesis

This thesis is protected by copyright which belongs to the author.

The content must not be changed in any way or sold commercially in any format or medium without the formal permission of the author.

When referring to this work, full bibliographic details including the author, title, awarding institution and date of the thesis must be given.

Please visit <http://shura.shu.ac.uk/17304/> and <http://shura.shu.ac.uk/information.html> for further details about copyright and re-use permissions.

Effects of Cold Metal Transfer Welding on Properties of Ferritic Stainless Steel

Stephen Magowan

A thesis submitted in partial fulfilment of the requirements of
Sheffield Hallam University
for the degree of Doctor of Philosophy

January 2017

Collaborating Organisations
Outokumpu Research Foundation

Abstract

Stainless steels are a classification of materials that have been available for over 100 years and over that time manufacturers have created variations on chemical composition and manufacturing route, to create materials that meet specific criteria set by the consumer. One type of stainless steel, ferritic, is restricted in applications as a result of a reduction in properties, namely toughness, when it is welded as a result of grain coarsening in the heat affected zone. Welding equipment manufacturers are constantly incorporating new technologies and capabilities into welding equipment, to make welding easier and create better welds, which then gives that manufacturer a competitive advantage. Cold Metal Transfer (CMT) welding is one such innovation and is claimed by the manufacturer to be a lower heat input process. This research project examines the effects of this lower heat welding process, on the joining of ferritic stainless steels to determine if CMT can reduce the detrimental effects, seen in this material, through welding.

The research examines the mechanical and metallurgical effects of using the Cold Metal Transfer (CMT) welding process to weld various grades of ferritic stainless steel including, EN1.4016, EN1.4509, EN1.4521 and EN1.4003 and compares them to welds created using a standard Gas Metal Arc Welding (GMAW) technique, with comparisons made using tensile testing, hardness testing, impact testing, fatigue testing and microstructural characterisation.

Experimental results show that grades such as EN1.4016 and EN1.4003 are more sensitive to the welding process due to a phase change to martensite present within the heat affected zone. Work has been conducted to determine the temperature at which ferrite transforms to austenite, prior to transformation to martensite under non equilibrium cooling. Some of the findings from this work included;

Fatigue testing and microstructural characterisation has shown a benefit in properties for using CMT over the conventional GMAW process for the EN1.4003 material.

A relationship has also been proposed which examines the effect of the percentage of fusion zone defects on the fatigue life of the welded joints.

Overall it was found that there was variation in the voltage and current by 1.9 Volts and 15 Amps respectively through a 400mm weld.

The ALC settings from -30% to +30% affected the net heat input by 6J/mm

NDT techniques utilised in the study were ineffective at detecting the lack of side wall fusion evident in some of the welds.

Acknowledgements

The author would like to express sincere gratitude to the people, that without their help, the work would have never been completed. To my supervisor, Professor Alan Smith, for the never ending support and guidance throughout, thanks also to David Dulieu and Professor Staffan Hertzman for their support through this project and the Outokumpu Research Foundation, for sponsoring the project.

Thanks also must be given to Seppo Lantto and Hannu-Pekka Heikkinen of Outokumpu Tornio, for the manufacture of MAG welds, advice and the supply of material. At Sheffield Hallam University, thanks to Jamie Boulding for support provided within the Materials Characterisation Laboratory, to Tim O'Hara and Phil Stevenson for all the support with the Fatigue testing, Michael Wilson and Samuel Naylor for conducting some of the heat treatments, Russ Mather and James Harcus for the support with the Radiography, Jeremy Bladen for support with the drawings, Vinay Patel, Simone Robinson, Steve McCluskey, Josh Chetham, Danny Deugo and Liam Cuthbert for undertaking some of the testing.

Thanks to Darren Helley, who set me on the path that led to this and for the entertainment along the way, to family and other friends who kept me sane throughout, in particular Dad, Mum, Michelle, Brandon, Mike, Dave, Bob, Andy, Dan, Phil, Dave S, Andy R, Colin and finally, but certainly not least, the first welder in the family, my Nan, Mabel Milton.

Table of Contents	Page No.
1 Introduction	1
2 Literature Review	4
2.1 Stainless Steel	4
2.1.1 Definition of Stainless Steel	4
2.1.2 History of Stainless Steel	4
2.1.3 Manufacturing Methods of Stainless Steel	7
2.1.4 Types of Stainless Steel	9
2.1.5 Alloying Additions Used in Stainless Steels	16
2.2 Definition of Welding & Brief History	18
2.2.1 Fusion Welding Processes	19
2.3 Welding Stainless Steel	49
2.3.1 Grain Growth	50
2.3.2 Sensitization	51
2.3.3 Formation of Secondary Phases	52
2.3.4 Solidification Cracking	57
2.3.5 475°C Embrittlement	59
2.3.6 Sigma Phase Embrittlement	60
2.3.7 High Temperature Embrittlement	62
2.3.8 Liquation	63
2.3.9 Impurity Elements	63
2.3.10 Liquid Metal Embrittlement	64
2.3.11 Stainless steel summary	66
2.4 Fatigue	66
2.4.1 Fatigue Testing	67
2.4.2 Different types of fatigue testing	69
2.4.3 Fatigue Failure Mechanisms	72
2.4.4 Key factors affecting fatigue performance of welds	78
2.4.5 Models for fatigue life prediction	82
2.5 Summary of the Literature	83
3 Experimental Procedure	84
3.1 Materials Used in the Research	84
3.1.1 Parent Materials	84

3.1.2	Welding Filler Materials	85
3.1.3	Shielding Gas Used in the Project	86
3.2	Comparison Trial between CMT & MAG Welds in Different Grades and Thicknesses.....	86
3.3	CMT Welding Trials to Examine the Effect of Variation of Welding Gap & Speed to Reduce Heat Input	87
3.4	Trial to Determine the Consistency of Welds Produce Using CMT Process	88
3.5	EN1.4003 CMT/MAG Welding Comparison Trial Comparing Microstructure and Mechanical Properties.....	91
3.6	HAZ Thermal Cycle Simulation Trials.....	92
3.7	Process for the Creation of all CMT Welds & MAG Welds created at Sheffield Hallam University using EN1.4003 Grade Stainless Steel Parent Material in 3.8 & 5.8mm Thicknesses	94
3.7.1	Description of the Welding Test Coupon.....	94
3.7.2	Equipment Used to Create the Welds and Monitor the Welding Parameters.....	95
3.7.3	Heat Input	100
3.8	Non Destructive Examination.....	101
3.9	Microstructural Evaluation of all Welded Samples.....	102
3.9.1	Sectioning of As-Welded Samples	102
3.9.2	Hot Mounting of Welded Cross Sections.....	102
3.9.3	Grinding/Polishing of Welded Cross Sections.....	103
3.9.4	Etching of the As-Polished Welded Cross Sections.....	104
3.9.5	Optical Examination of Welded Cross Sections	106
3.9.6	Infinite Focus Microscope Examination of Weld Profiles on Untested Fatigue Samples	108
3.10	Mechanical Evaluation of Welds	108
3.10.1	Hardness Testing	108
3.10.2	Tensile Testing of Welded Samples	109
3.10.3	Impact Testing of Welded and Heat Treated Samples	110
3.10.4	Fatigue Testing of As-Welded Samples.....	112
3.10.5	Staircase Fatigue Testing Procedure and Equations.....	114
3.11	Compositional Analysis of Parent Materials Used in the Study.....	116
3.11.1	Optical Emission Spectrometry	116
4	Experimental Results	117

4.1	Materials Characterisation of the Parent Materials Used in the Study	117
4.1.1	EN 1.4003 Grade Stainless Steel	117
	EN 1.4016 Grade Stainless Steel	118
4.1.2	EN 1.4509 Grade Stainless Steel	119
4.1.3	EN 1.4521 Grade Stainless Steel	119
4.2	Initial Comparison of Requisite Heat Input for MAG and CMT Welds on EN1.4016, EN1.4509 & EN1.4521 Ferritic Stainless Steel Parent Materials.	120
4.3	The Effect of Heat Input on Weld/HAZ Shape & Size, Penetration Levels and HAZ Grain Size, using CMT	124
4.4	Trial to Examine the Effects of Variation in the Welding Gap, Torch Traverse Speed and Torch Angle using 2mm Thickness EN1.4016 and EN1.4509 Parent Materials.....	129
4.5	Trial to Determine the Consistency of the Welding Parameters and Subsequent Welds with the CMT Welding Process	132
4.5.1	Power Setting	136
4.5.2	Traverse Speed.....	140
4.5.3	Torch Angle	141
4.5.4	Arc Length Correction	143
4.5.5	Pulse Correction	146
4.6	Comparison of CMT Welded and MAG Welded EN 1.4003 Parent Material in 3.8mm & 5.8mm Thicknesses	149
4.7	CMT/MAG 1.4003 Comparison Trial	149
4.7.1	Non Destructive Examination and Destructive Validification.....	150
4.7.2	Comparison of Microstructural Analysis of CMT & MAG Welds in 3.8mm Thick EN1.4003 Parent Material.....	154
4.7.3	Tensile Data of CMT and MAG Welded Joints	157
4.7.4	Impact Results of CMT and MAG Welded Joints	161
4.7.5	Fatigue Results	163
4.7.6	Bulk Effect of Fusion Defects on Fatigue Properties.....	167
4.7.7	Comparison of Weld Angle with Fatigue Results.....	171
4.8	Heat Treatment Trial To Identify Key Temperatures At Which Microstructural Changes Occur And The Effect of Time On These Changes.	186
4.8.1	Effect of Thermal Cycles on the Mechanical Properties and Grain Size of the EN1.4003 Grade Stainless Steel.....	205
5	Discussion	209

5.1	Microstructural Materials Characterisation	209
5.2	Initial Comparison of Required Heat Input for MAG and CMT On EN1.4016, EN1.4509 & EN1.4521 Ferritic Stainless Steel Parent Materials.....	209
5.3	Effect on Microstructure and Weld Dimensions of Heat Input Using Pulsed Arc with CMT on EN1.4016 2mm Thick Parent	211
5.4	Trial to Examine the Effects of Variation in the Welding Gap, Torch Traverse Speed and Torch Angle on the Heat Input Required to Give a Fully Penetrating Weld using 2mm Thickness EN1.4016 and EN1.4509 Parent Materials.	213
5.5	Trial to Determine the Consistency of the Welding Parameters and Subsequent Welds with the CMT Welding Process	215
5.5.1	CMT Power Setting.....	216
5.5.2	Arc Length Correction	218
5.5.3	Pulse Correction	219
5.5.4	Traverse Speed.....	221
5.5.5	Torch Angle	221
5.5.6	ALX Data	222
5.6	Comparison of Microstructure and Mechanical Properties for CMT Welded and MAG Welded EN 1.4003 Parent Material in 3.8mm & 5.8mm Thicknesses	224
5.6.1	Non Destructive Examination - Radiography.....	226
5.6.2	Microstructural Comparison for Welds Created Using the CMT Welding Process and MAG Welding Process Using 3.8mm Thick EN1.4003	227
5.6.3	Comparison of Tensile Data for Welds Created Using the CMT Welding Process and MAG Welding Process Using 3.8mm & 5.8mm Thick EN1.4003	229
5.6.4	Impact Results From 3.8mm & 5.8mm Thick EN1.4003 MAG/CMT Comparison.....	233
5.6.5	Fatigue Results From 3.8mm Thick EN1.4003 MAG/CMT Comparison..	234
5.6.6	Effect of Weld Defects on the Fatigue Properties of 3.8mm Thick EN1.4003 Parent Material	235
5.6.7	Effect on Fatigue Properties of the Parent Metal to Reinforcement Weld Angle	237
5.7	Heat Treatment Trial To Identify Key Temperatures At Which Microstructural Changes Occur And The Effect of Time On These Changes.	237
6	Conclusions	241
6.1	Research on thin grades (<2mm) of ferritic stainless steel welded using CMT & MAG techniques	241

6.2	Grade EN1.4003 3.8mm and 5.8mm thick material welded using CMT and MAG techniques	242
7	Further Work	244
8	Works Cited.....	245
9	List of Equipment.....	257

List of Figures

Figure 1.	Fusion weld, showing heat affected zone either side of the weld (Magowan & Smith, 2010). Arrowed is the detrimental grain coarsening within the HAZ.	2
Figure 2.	Manufacturing route of stainless steel as utilised at Kawasaki Steel (Ono & Kaito, 1986).	8
Figure 3.	Schaeffler diagram with stainless steel grades indicated (Outokumpu, 2010).	11
Figure 4.	Showing the difference in power densities for various fusion welding processes (Lancaster, 1984).....	20
Figure 5.	Schematic of resistance spot welding (Westgate, 2009).....	21
Figure 6.	Image showing a resistance spot weld (RSW) (Westgate, 2009).	22
Figure 7.	Schematic of resistance seam welding (Pires, Louriero, & Bolmsjo, 2006)....	23
Figure 8.	Showing resistance seam welding (Westgate, 2009).	23
Figure 9.	Diagram of the manual metal arc welding process (Wermac, 2016)	26
Figure 10.	Diagram showing the submerged arc welding process (The Welding Institute Limited, 1995)	27
Figure 11.	Diagram of the gas tungsten arc welding process (Mechanical Engineering, 2016)	28
Figure 12.	Diagram showing transfer modes according to arc current (I) and voltage (V) (Iordachescu & Quintino, 2008).....	31
Figure 13.	Showing globular transfer (Lucas, Iordachescu, & Ponomarev, 2005).....	32
Figure 14.	Showing short circuit cycle with effect on current and voltage (ESAB).....	33
Figure 15.	Showing short circuit transfer (Lucas, Iordachescu, & Ponomarev, 2005)....	33
Figure 16.	Showing spray transfer (Lucas, Iordachescu, & Ponomarev, 2005).	34
Figure 17.	Pulsed spray transfer graph of current (I) against time (t) for two pulsing cycles and images depicting the events for one pulsing cycle (Hackl).	35
Figure 18.	Showing pulsed transfer (Lucas, Iordachescu, & Ponomarev, 2005).	36
Figure 19.	MIG/MAG process diagram (The Welding Institute, 2010).	36
Figure 20.	Images showing dip arc transfer (Izutani, Shimizu, Suzuki, & Koshiishi, 2007) where the first image (far left) shows the arc and the consumable electrode with a spherical molten mass as the end moving toward the work piece as the wire is fed. The second image (centre) shows the consumable electrode in contact with the weld pool, provided the short circuit phase. The third image (far right) shows the transfer of	

the molten portion of the consumable electrode, which eliminates the contact with it and so the arc is re-established.	37
Figure 21. Schematic diagram of the CMT process showing wire motion, arrowed (Fronius International GmbH, 2007).	38
Figure 22. High speed images showing CMT cycle (Fronius International GmbH, 2004). Corresponding to the schematic in Figure 22 above.	38
Figure 23. Graphs showing voltage (V)(top) and current (I) (bottom) against time for the CMT process (Rosado, Almeida, Pires, Miranda, & Quintino, 2008).	39
Figure 24. Showing effect on transfer mode of carbon dioxide addition to argon shielding gas (Zielinska, et al., 2009).	46
Figure 25. Image showing grain growth in GMA welded ferritic stainless steel (Magowan & Smith, 2010).	50
Figure 26. Iron-Chromium equilibrium diagram (Computational Thermodynamics Inc., 2011).	53
Figure 27. Part of Iron - Chromium equilibrium diagram showing effects of carbon and nitrogen on the shape and size of the gamma loop (Deddoes, Parr, & Hanson, 1999).	53
Figure 28. Time Temperature Transformation diagram for delta ferrite to austenite in the high temperature HAZ (Warmelo, Nolan, & Norrish, 2007).	56
Figure 29. Diagram showing mechanics of shrinkage cracking (University of Ljubljana, 2000)	57
Figure 30. Suutala diagram for predicting susceptibility to shrinkage cracking from weld metal composition (Kujanpaa, Suutala, Takalo, & Moision, 1979).	58
Figure 31. Use of modified versions of Murakami's reagent to colour delta ferrite and sigma phase in stainless steel welds. (a) Delta ferrite coloured blue and brown in an austenitic matrix in type 312 stainless steel weld metal (as-welded) using modified Murakami's reagent (30 g sodium hydroxide, 30 g potassium ferricyanide, 100 mL water, at 100 °C, or 212 °F, for 10 s). The arrow points to a slag inclusion in the weld nugget. (b) Sigma phase formed in a type 312 stainless steel weld (from the delta ferrite phase) by aging at 816 °C (1500 °F) for 160 h. Sigma was coloured green and orange by etching with Murakami's reagent (10 g sodium hydroxide, 10 g potassium ferricyanide, 100 mL water) for 60 s at 80 °C (175 °F). The magnification bars are 20 µm in length (Vandervoort, Colour Metallography - Film Formation and Interference Techniques, 2004).	61
Figure 32. Image showing Sigma phase (Vandervoort, Examination of Microstructures, 2003).	62
Figure 33. Image showing liquid copper which has penetrated down the grain boundaries of an AISI 304 austenitic stainless steel (Magowan S. , 2006).	65
Figure 34. Showing different fatigue cycles. (NDT Resource Centre, 2016)	68
Figure 35. Presentation of data from low cycle fatigue testing (KTH, 2003)	70
Figure 36. Showing S-N curve typical reporting of high cycle fatigue data (eFUNDA, 2016).	70
Figure 37. Showing three stages of crack growth rate (Engineers Edge, 2016).	72
Figure 38. Figure showing persistent slip bands. (NDT Resource Centre, 2016)	74

Figure 39. Showing fatigue crack propagation (Key to Metals AG, 2005)	75
Figure 40. SEM image showing fatigue striations (ASM International, 2008).	75
Figure 41. Showing relationship between parent/weld interface angle and fatigue strength (Harris & Syers, 1979).	79
Figure 42. Graph showing relationship between penetration root angle and fatigue life for similar thickness CMT welds (Ashcroft, 2008).	80
Figure 43. 9—S—N curves of the investigated specimens with different maximum pore volumes (PV) for A1Si7Mg0.3 (Tijani, Heinreitz, Stets, & Voigt, 2013).....	81
Figure 44. Fatigue test results for defect-free and defective 6mm high strength steel parent specimen (Ottersbock, Leitner, Stoschka, & Maurer, 2016).....	81
Figure 45. Sectioning of weld plan, sections taken at 10mm, 40mm, 70mm, 110mm, 140mm and 170mm. Green arrow shows welding direction (Boulding, The Effects of Parameters and Consistency of Cold Metal Transfer Welded Ferritic Stainless Steel Joints, 2012).	90
Figure 46. Schematic of parent plate size and setup for all CMT & MAG welded samples the plate length was either 400mm as indicated above, or 200mm.....	95
Figure 47. Showing the CMT welding equipment at Sheffield Hallam University.	96
Figure 48. Image showing tractor and track used to traverse the welding torch.	97
Figure 49. Image showing ABB robotic arm used in some of the CMT and MAG welding trials.....	98
Figure 50. Welding set up showing ALX weld monitoring equipment (Boulding, The Effects of Parameters and Consistency of Cold Metal Transfer Welded Ferritic Stainless Steel Joints, 2012).	99
Figure 51. Showing clamping arrangement for holding the parent material in place whilst welding.	100
Figure 52. Images showing fresh glyceresia (left) and glyceresia following approximately 1 hours use (right) where it requires disposal.....	105
Figure 53. Schematic of weld cross section showing measurements made on optical examination	106
Figure 54. Image showing calibration of measurement capability of DM2500 optical measuring system.	107
Figure 55. Leica DM2500 optical microscope, connected to Buehler Omnimet 9.0 image analysis software.....	107
Figure 56. Schematic of hardness testing survey positions.	109
Figure 57. Instron Dynatup 9250 impact test machine.	110
Figure 58. Showing the sampling of impact (left), microstructural (middle) and tensile specimens (right) from the welded sheet.....	111
Figure 59. ESH Fatigue testing machine.....	112
Figure 60. Showing the sampling of fatigue specimens from the as-welded sheet.	113
Figure 61. Etched microstructure of 3.8mm thick EN1.4003 used in the study showing an equiaxed fully ferritic structure (Etched in Glyceresia).	117
Figure 62. Etched microstructure of 5.8mm thick EN1.4003 used in the study showing an equiaxed fully ferritic structure (Etched in Glyceresia).	118

Figure 63. Etched microstructure of the EN1.4016 material used in the study showing an equiaxed fully ferritic structure (Etched in Glyceregia).	118
Figure 64. Etched microstructure of the EN 1.4509 material used in the study showing an equiaxed fully ferritic structure (Etched in Glyceregia).	119
Figure 65. Etched microstructure of the EN 1.4521 material used in the study showing an equiaxed fully ferritic structure with carbides arrowed (Etched in Glyceregia).	119
Figure 66. Graph comparing calculated heat input, weld bead and heat affected zone width of MAG and CMT welded joints.	121
Figure 67. Image taken within the HAZ of the CMT welded EN1.4016 material, showing martensite (red arrow) at the grain boundaries.	121
Figure 68. Comparison of the 1.4016 MAG weld/HAZ middle hardness profiles.	122
Figure 69. Comparison of the 1.4016 CMT weld/HAZ middle micro hardness profiles.	123
Figure 70. Showing effect of heat input on HAZ width for pure CMT and CMT with Pulsed arc welded samples, EN1.4016 parent material.	126
Figure 71. Showing effect of heat input on grain size for pure CMT and CMT with pulsed arc welded samples, EN1.4016 parent material.	126
Figure 72. Line scan of interface between AISI 430 parent metal and AISI 308L weld metal.	127
Figure 73. Elemental Map of parent metal and weld metal interface for AISI 430 parent material and 308LSi filler.	128
Figure 74. Graph showing forehand (15°) welds produced using 1.4016 material at 1mm, 1.15mm and 1.25mm joint gaps and 762, 1016 & 1270 mm/min welding speeds, categorised according to whether weld penetration was achieved.	129
Figure 75. Graph showing forehand (15°) welds produced using 1.4509 material at 1mm, 1.15mm and 1.25mm joint gaps and 762, 1016 & 1270 mm/min welding speeds, categorised according to whether weld penetration was achieved.	130
Figure 76. Graph showing the effect of torch angle on achieving penetration of welds produced using grade 1.4016 parent material, using a 1mm joint gap, at different welding speeds.	130
Figure 77. Graph showing the effect of torch angle on achieving penetration of welds produced using grade 1.4509 parent material, using a 1mm joint gap, at different welding speeds.	131
Figure 78. Image showing the effect of heat input on weld and HAZ dimensions. The left hand weld cross section of 2mm thick, CMT+P welded, 1.4016 material with heat input of 0.113 kJ/mm and the right is the same material and welded using the same process but with a net heat input of 0.060 kJ/mm.	131
Figure 79. Example 1, showing a fully penetrated weld (Boulding, The Effects of Parameters and Consistency of Cold Metal Transfer Welded Ferritic Stainless Steel Joints, 2012).	135
Figure 80. Example 2, showing an incomplete penetrated weld (Boulding, The Effects of Parameters and Consistency of Cold Metal Transfer Welded Ferritic Stainless Steel Joints, 2012).	135

Figure 81. Example 3, showing misaligned parent/penetration to one side (Boulding, The Effects of Parameters and Consistency of Cold Metal Transfer Welded Ferritic Stainless Steel Joints, 2012).	135
Figure 82. Graph showing the width of the HAZ for each of the CMT welds conducted at 3.5m/min (average net heat input 72.2 J/mm) on EN1.4016 grade parent material.	137
Figure 83. Graph showing the width of the HAZ for each of the CMT welds conducted at 4.5m/min (average net heat input 88.5 J/mm) on EN1.4016 grade parent material.	137
Figure 84. Graph showing the width of the HAZ for each of the CMT welds conducted at 5.5m/min (average net heat input 109.3 J/mm) on EN1.4016 grade parent material.	138
Figure 85. Graph showing the current and voltage trace for the CMT weld conducted at 3.5m/min on EN1.4016 grade parent material.	138
Figure 86. Graph showing the current and voltage trace for the CMT weld conducted at 4.5m/min on EN1.4016 grade parent material.	139
Figure 87. Graph showing the current and voltage trace for the CMT weld conducted at 5.5m/min on EN1.4016 grade parent material.	139
Figure 88. Graph showing the width of the HAZ for each of the CMT welds conducted at a traverse speed of 0.762m/min (average net heat input 118.3 J/mm) on EN1.4016 grade parent material.	140
Figure 89. Graph showing the width of the HAZ for each of the CMT welds conducted at a traverse speed of 1.27m/min (average net heat input 69.6 J/mm) on EN1.4016 grade parent material.	141
Figure 90. Graph showing the width of the HAZ for each of the CMT welds created using a torch orientation +15° to the direction of traverse on EN1.4016 grade parent material.	142
Figure 91. Graph showing the width of the HAZ for each of the CMT welds created using a torch orientation -15° to the direction of traverse on EN1.4016 grade parent material.	142
Figure 92. Graph showing the width of the HAZ for each of the CMT welds conducted with an ALC value of -30 on EN1.4016 grade parent material.	143
Figure 93. Graph showing the width of the HAZ for each of the CMT welds conducted with an ALC value of +30 on EN1.4016 grade parent material.	144
Figure 94. Graph showing voltage and current trace for a CMT weld conducted with an ALC of -30 on EN1.4016 grade parent material.	145
Figure 95. Graph showing voltage and current trace for a CMT weld conducted with an ALC of +30 on EN1.4016 grade parent material.	145
Figure 96. Graph showing the width of the HAZ for each of the CMT welds conducted with a PC of -5 on EN1.4016 grade parent material.	146
Figure 97. Graph showing the width of the HAZ for each of the CMT welds conducted with a PC of +5 on EN1.4016 grade parent material.	147

Figure 98. Graph showing the current and voltage trace for a CMT weld conducted with a pulse correction of -5 on EN1.4016 grade parent material.....	147
Figure 99. Graph showing the current and voltage trace for a CMT weld conducted using a pulse correction of +5 on EN1.4016 grade parent material.....	148
Figure 100. CMT weld cross section of the 5.8mm thick EN1.4003 grade parent material	149
Figure 101. Lack of side wall fusion in CMT weld produced using the 5.8mm thick EN1.4003 grade material.	149
Figure 102. Showing radiograph for test weld that was sectioned to destructively examine, with identification of indications observed through examination of the radiograph and suggested possibility of defect type. Red arrows showing spatter, blue arrows showing gas porosity and yellow arrows showing indications of a lack of side wall fusion.	150
Figure 103. showing section 7 of the weld, the three pieces of spatter circled (Robinson, 2014)	151
Figure 104. Lack of side wall fusion in root of section 1a of CMT welded 5.8mm thick EN1.4003 (Robinson, 2014).....	152
Figure 105. Showing gas porosity in section 5a of CMT welded 5.8mm thick EN1.4003 (Robinson, 2014).	152
Figure 106. Gas porosity (left) lack of side wall fusion (right) in section 9a of CMT welded 5.8mm thick EN1.4003 (Robinson, 2014).....	153
Figure 107. Image showing weld (top right) and HAZ , which has two distinct regions, the first next to the weld (red arrow) has a martensitic structure and grain coarsening, the second region of the HAZ (orange arrow) has a martensitic structure but without any grain coarsening and then the blue arrow indicates unaffected parent material of 3.8mm thick EN1.4003 parent, CMT welded sample 25.10 (etched in glyceresia).	155
Figure 108. Image showing weld (top right) and grain coarsened with martensite HAZ (mid image) and martensite HAZ (bottom left) of 3.8mm thick EN1.4003 parent, CMT welded sample 25.10 (etched in glyceresia)	155
Figure 109. Image showing weld (top left) and HAZ , which has two distinct regions, the first next to the weld has a martensitic structure and grain coarsening (red arrow), the second region of the HAZ (orange arrow) has a martensitic structure but without any grain coarsening and then the blue arrow indicates unaffected parent material of 3.8mm thick EN1.4003 parent, MAG welded sample 30.7 (etched in glyceresia).....	156
Figure 110. Image showing weld (top left) and twin region HAZ (mid image & bottom right) of 3.8mm thick EN1.4003 parent, MAG welded sample 30.7 (etched in glyceresia).	156
Figure 111. Staircase Fatigue results for the CMT welded samples.	163
Figure 112. Graph to show fatigue load range for CMT welded 3.8mm thick EN1.4003 (red line indicates the pass criteria of 2 million cycles).	164
Figure 113. Staircase Fatigue results for the MAG welded samples.	165
Figure 114. Graph to show fatigue load range for MAG welded 3.8mm thick EN1.4003 (red line indicates the pass criteria of 2 million cycles).	166

Figure 115. Image showing a lack of side wall fusion (arrowed).....	167
Figure 116. Image showing a lack of root penetration (arrowed).....	167
Figure 117. Image showing weld porosity (arrowed).	167
Figure 118. SEM image showing a region with a lack of fusion and the areas where analysis.....	168
Figure 119. Graph of element analysis spectrum 3.....	168
Figure 120. Graph of element analysis spectrum 4.	168
Figure 121. Graph showing the effect of defect area of the fracture face against number of cycles to failure for CMT welded samples.	169
Figure 122. Graph showing the effect of defect area of the fracture face against the number of cycles to failure for each of the tested loads on CMT welded samples.	169
Figure 123. Graph showing the effect on gradient of the % defects within the fracture surface against the number of cycles survived for each load, therefore as the load is increased the gradient also increases on the EN1.4003 parent CMT welded samples.	170
Figure 124. Graph showing the effect on gradient of the % defects within the fracture surface against the number of cycles survived for each load, with the result for 46kN removed, therefore as the load is increased the gradient also increases on the EN1.4003 parent CMT welded samples.....	170
Figure 125. Showing plan of the weld cap of a MAG welded sample, red line showing location for one of profiles taken.	172
Figure 126. Profile trace for weld cap of MAG welded sample as seen in Figure 122.	173
Figure 127. Showing IFM 3D scan of the weld cap of a MAG welded sample.....	174
Figure 128. Showing plan of the weld root of a MAG welded sample, red line showing location for one of profiles taken.	175
Figure 129. Profile trace for weld root of MAG welded sample as seen in Figure 125.	176
Figure 130. Showing IFM 3D scan of the weld root of a MAG welded sample.	177
Figure 131. Graph showing weld root angle against the number of cycles before failure for the CMT welded samples fatigue tested at 46 kN.....	178
Figure 132. Graph showing weld root angle against the number of cycles before failure for the CMT welded samples fatigue tested at 45.5 kN.....	179
Figure 133. Graph showing weld root angle against the number of cycles before failure for the CMT welded samples fatigue tested at 45 kN.....	179
Figure 134. Graph showing weld root angle against the number of cycles before failure for the CMT welded samples fatigue tested at 44.5 kN.....	180
Figure 135. Graph showing weld root angle against the number of cycles before failure for the CMT welded samples fatigue tested at 44 kN.....	180
Figure 136. Graph showing weld root angle against the number of cycles before failure for the CMT welded samples fatigue tested at 43.5 kN.....	181
Figure 137. Graph showing weld root angle against the number of cycles before failure for the CMT welded samples fatigue tested at 43 kN.....	181

Figure 138. Graph showing weld root angle against the number of cycles before failure for the CMT welded samples fatigue tested at 42.5 kN	182
Figure 139. Graph showing weld root angle against the number of cycles before failure for the CMT welded samples fatigue tested at 42 kN	182
Figure 140. Graph showing weld root angle against the number of cycles before failure for the CMT welded samples fatigue tested at 41.5 kN	183
Figure 141. Showing the root angle against number of cycles for the CMT welded samples.	183
Figure 142. Graph showing weld root angle against the number of cycles before failure for the MAG welded samples fatigue tested at 38.5kN	184
Figure 143. Graph showing weld root angle against the number of cycles before failure for the MAG welded samples fatigue tested at 35.5kN	184
Figure 144. Graph showing weld root angle against the number of cycles before failure for the MAG welded samples fatigue tested at 32.5kN	185
Figure 145. Graph showing weld root angle against the number of cycles before failure for the MAG welded samples fatigue tested at 29.5kN	185
Figure 146. Showing the root angle against number of cycles for the MAG welded samples.	186
Figure 147. Image showing fully ferritic microstructure of sample subjected to 700°C 20 min soak water quench as seen in the as received EN1.4003 material	187
Figure 148. Image Showing fully ferritic microstructure of sample subjected to 700°C 20 min soak water quench as seen in the as received EN1.4003 material.	187
Figure 149. Image showing ferritic (light areas) and martensitic (dark areas) microstructure of sample subjected to 800°C 20 min soak water quench similar to the microstructure in the region of the HAZ furthest from the fusion zone of welds on a EN1.4003 grade material.	188
Figure 150. Image showing ferritic and martensitic microstructure (250 HV ₁₀) of sample subjected to 800°C 20 min soak water quench similar to the microstructure in the region of the HAZ furthest from the fusion zone of welds on an EN1.4003 grade material.	188
Figure 151. Image showing martensitic microstructure of EN1.4003 sample subjected to 900°C 20 min soak water quench.	189
Figure 152. Image showing martensitic microstructure (277 HV ₁₀) of EN1.4003 sample subjected to 900°C 20 min soak water quench.	189
Figure 153. Image showing martensitic microstructure with some grain growth of EN1.4003 sample subjected to 1000°C 20 min soak water quench, this is similar to what would be seen in the region of the HAZ closest to the fusion zone.	190
Figure 154. Image showing martensitic microstructure with some grain growth of EN1.4003 sample subjected to 1000°C 20 min soak water quench, this is similar to what would be seen in the region of the HAZ closest to the fusion zone.	190
Figure 155. Image showing martensitic microstructure and grain growth of EN1.4003 sample subjected to 1100°C 20 min soak water quench, this is similar to what would be seen in the region of the HAZ closest to the fusion zone.	191

Figure 156. Image showing ferritic and martensitic microstructure and grain growth of EN1.4003 sample subjected to 1100°C 20 min soak water quench, this is similar to what would be seen in the region of the HAZ closest to the fusion zone.	191
Figure 157. Image showing ferritic microstructure of EN1.4003 sample subjected to 747°C 20 min soak water quench, as would be seen in the unaffected parent material.	192
Figure 158. Image showing ferritic microstructure of sample subjected to 747°C 20 min soak water quench, as would be seen in the unaffected parent material.	192
Figure 159. Image showing ferritic microstructure of an EN1.4003 sample subjected to 758°C 20 min soak water quench as would be seen in the unaffected parent material.	193
Figure 160. Image showing ferritic microstructure of an EN1.4003 sample subjected to 758°C 20 min soak water quench as would be seen in the unaffected parent material.	193
Figure 161. Image showing ferritic microstructure (light areas) with martensite (dark areas) at the grain boundaries of an EN1.4003 sample subjected to 769°C 20 min soak water quench, this would be typical of a microstructure seen in the HAZ at its furthest distance from the fusion zone.	194
Figure 162. Image showing ferritic microstructure with martensite at the grain boundaries of an EN1.4003 sample subjected to 769°C 20 min soak water quench, this would be typical of a microstructure seen in the HAZ at its furthest distance from the fusion zone.	194
Figure 163. Image showing ferritic (light areas) and martensitic (dark areas) microstructure of an EN1.4003 sample subjected to 779°C 20 min soak water quench.	195
Figure 164. Image showing ferritic (light areas) and martensitic (dark areas) microstructure of an EN1.4003 sample subjected to 779°C 20 min soak water quench.	195
Figure 165. Image showing ferritic (light areas) and martensitic (dark areas) microstructure of an EN1.4003 sample subjected to 790°C 20 min soak water quench.	196
Figure 166. Image showing ferritic (light areas) and martensitic (dark areas) microstructure of an EN1.4003 sample subjected to 790°C 20 min soak water quench.	196
Figure 167. Image showing martensitic microstructure of an EN1.4003 sample subjected to 800°C 2 hour soak water quench.	197
Figure 168. Image showing martensitic microstructure of an EN1.4003 sample subjected to 800°C 2 hour soak water quench.	197
Figure 169. Image showing ferritic (light areas) and martensitic (dark areas) microstructure of an EN1.4003 sample subjected to 770°C 2 hour soak water quench.	198

Figure 170. Image showing ferritic (light areas) and martensitic (dark areas) microstructure of an EN1.4003 sample subjected to 760°C 2 hour soak water quench.	198
Figure 171. Image showing ferritic (light areas) and martensitic (dark areas) microstructure of EN 1.4003 sample subjected to 750°C 2 hour soak water quench.	199
Figure 172. Image showing ferritic microstructure of an EN 1.4003 sample subjected to 740°C 2 hour soak water quench.	199
Figure 173. Image showing martensitic microstructure of an EN1.4003 sample subjected to 800°C 2 hour soak Furnace cool to determine the effect of time at temperature.	200
Figure 174. Image showing martensitic microstructure of an EN1.4003 sample subjected to 800°C 2 hour soak Furnace cool to determine the effect of time at temperature.	200
Figure 175. Image showing ferritic (light areas) and martensitic (dark areas) microstructure of an EN1.4003 sample subjected to 800°C 6 hour soak 30°C/hour cool rate.	201
Figure 176. Image showing ferritic (light areas) and martensitic (dark areas) microstructure of an EN1.4003 sample subjected to 800°C 6 hour soak 30°C/hour cool rate.	201
Figure 177. Image showing martensitic microstructure of an EN1.4003 sample subjected to 1000°C 6 hour soak 30°C/hour cool rate grain coarsening also evident.	202
Figure 178. Image showing martensitic microstructure of an EN1.4003 sample subjected to 1000°C 6 hour soak 30°C/hour cool rate, grain coarsening also evident.	202
Figure 179. Image showing martensitic microstructure of an EN1.4003 sample subjected to 900°C 6 hour soak 30°C/hour cool rate, grain coarsening also evident.	203
Figure 180. Image showing martensitic microstructure of an EN1.4003 sample subjected to 900°C 6 hour soak 30°C/hour cool rate, grain coarsening also evident.	203
Figure 181. Figure showing microstructures of samples subjected to a hold for a time at a temperature.	204
Figure 182. Graph showing effect of peak temperature on hardness (HV ₁₀).....	205
Figure 183. Graph showing effect of peak temperature on grain size.	206
Figure 184. Graph showing effect of grain size on material toughness.	206
Figure 185. Graph showing effect of different thermal cycles on impact properties.	207
Figure 186. Graph showing effect of various thermal cycles on hardness.....	207
Figure 187. Graph showing effect of various thermal cycles on grain size.	208
Figure 188. CMT weld cross section of the 5.8mm thick EN1.4003 grade parent material	224
Figure 189. . Image showing weld (top right) and HAZ , which has two distinct regions, the first next to the weld (red arrow) has a martensitic structure and grain coarsening, the second region of the HAZ (orange arrow) has a martensitic structure but without any grain coarsening and then the blue arrow indicates unaffected parent material of 3.8mm thick EN1.4003 parent, CMT welded sample 25.10 (etched in glyceresia).	227

Figure 190. . Image showing weld (top left) and HAZ , which has two distinct regions, the first next to the weld has a martensitic structure and grain coarsening (red arrow), the second region of the HAZ (orange arrow) has a martensitic structure but without any grain coarsening and then the blue arrow indicates unaffected parent material of 3.8mm thick EN1.4003 parent, MAG welded sample 30.7 (etched in glycergia).....228

List of Tables

Table 1. Table showing stainless steel grades and chemical compositions (Outokumpu, 2010).	10
Table 2. Classification of droplet transfer modes and typical process mode utilised (Izutani, Shimizu, Suzuki, & Koshiishi, 2007).....	30
Table 3. Showing the properties of various shielding gases (Praxair, 2005).	43
Table 4. Materials and thicknesses used in the research.	84
Table 5. Mechanical properties of ferritic stainless steels at room temperature (Outokumpu, 2011).....	85
Table 6. Chemical analysis data of the parent materials used within the project.	85
Table 7. Composition of AISI 308L-Si filler material (Avesta Welding, 2006).....	85
Table 8. Table showing variation of each of the ten settings used in the CMT consistency trial (Boulding, The Effects of Parameters and Consistency of Cold Metal Transfer Welded Ferritic Stainless Steel Joints, 2012).....	89
Table 9. Welding parameters used in the EN1.4003 CMT/MAG comparison trial.	92
Table 10. Showing heat treatment temperature, durations and method of cooling for samples of 5.8mm thick EN1.4003 (where WQ = Water Quenched).	93
Table 11. Showing chemical composition to make 120ml of glycergia.	104
Table 12. Table showing parameters for scans performed on the IFM.....	108
Table 13. Table used to collect the staircase fatigue testing data also provides information necessary for calculations to determine mean fatigue load.	114
Table 14. Showing some of the welding parameters and calculated heat inputs.....	120
Table 15 Summary of weld/HAZ dimensions for pure CMT welded samples with increasing net heat input.	124
Table 16. Summary of weld/HAZ dimensions for CMT with pulsed arc welded samples with increasing net heat input.	125
Table 17. Table showing actual readings and calculated heat inputs for each weld produced on the trial.	133
Table 18. Showing assessments of the extent of penetration of the filler metal for each sample examined (Boulding, The Effects of Parameters and Consistency of Cold Metal Transfer Welded Ferritic Stainless Steel Joints, 2012). For colour coding PTO.	134
Table 19. Showing key to assessments made on penetration (Boulding, The Effects of Parameters and Consistency of Cold Metal Transfer Welded Ferritic Stainless Steel Joints, 2012).	135

Table 20. Table showing defects observed through microstructural examination of EN1.4003 5.8mm thick CMT welded plate. The sample identification numbers in the left hand column are based on those presented in Figure 99.....	151
Table 21. Showing average measured values for the HAZ in the coarse region and the entire HAZ width and the grain size taken in the coarse region of the HAZ of 3.8mm thick EN1.4003 grade parent material.....	154
Table 22. CMT 3.8mm EN1.4003 Tensile results.....	157
Table 23. MAG 3.8mm EN1.4003 Tensile results. (* sample M28.9 not included in calculations as failed next to spatter).	158
Table 24. Statistical T.Test P values comparing the data for the 3.8mm thick CMT and MAG welded tensile data.....	158
Table 25. CMT 5.8mm EN1.4003 Tensile results.....	159
Table 26. MAG 5.8mm EN1.4003 Tensile results.....	160
Table 27. Statistical T.Test P values comparing the data for the 5.8mm thick CMT and MAG welded tensile data.....	160
Table 28. Impact test results for CMT welded 3.8mm thick EN1.4003.	161
Table 29. Impact test results for MAG welded 3.8mm thick EN1.4003.....	161
Table 30. Statistical T.Test P values comparing the data for the 3.8mm thick CMT and MAG welded impact data.	161
Table 31. Impact test results for CMT welded 5.8mm thick EN1.4003.	162
Table 32. Impact test results for MAG welded 5.8mm thick EN1.4003.....	162
Table 33. Statistical T.Test P values comparing the data for the 5.8mm thick CMT and MAG welded impact data.	162

List of Equations

Equation 1. Equation showing amount of niobium required to stabilise a stainless steel.	18
Equation 2. Equation to calculate arc energy.	47
Equation 3. Equation to calculate weld heat input.....	47
Equation 4. Equation to determine the ferrite factor (Zheng, Ye, Jiang, Wang, Liu, & Wang, 2010)	56
Equation 5. Equation to determine the chromium equivalent.....	58
Equation 6. Equation to determine the nickel equivalent.....	58
Equation 7. Equation to determine the maximum fatigue stress.	68
Equation 8. Equation to determine the minimum fatigue stress.	68
Equation 9. Equation to determine the mean fatigue stress.....	68
Equation 10. Equation to determine the fatigue stress range.	68
Equation 11. Equation to determine the fatigue stress ratio	68
Equation 12. Paris equation to model crack growth.	73
Equation 13. Ashcrofts model for fatigue life prediction against root angle.	82
Equation 14. Equation to calculate mean fatigue load.....	115

Equation 15. Equation to calculate convergence factor	115
Equation 16. Equation to calculate standard deviation.....	115
Equation 17. Equation to calculate standard error for mean fatigue load.....	115

List of Acronyms

ALC	Arc Length Correction
BCC	Body Centred Cubic
BCT	Body Centred Tetragonal
CCT	Continuous Cooling Transformation
CMT	Cold Metal Transfer
CMT+P	Cold Metal Transfer with Pulsed Arc
FCC	Face Centred Cubic
GMAW	Gas Metal Arc Welding
GTAW	Gas Tungsten Arc Welding
HAZ	Heat Affected Zone
HTHAZ	High Temperature Heat Affected Zone
MIG	Metal Inert Gas
MAG	Metal Active Gas
PC	Pulse Correction
TTT	Time Temperature Transformation
XRF	X-Ray Fluorescence

1 Introduction

Welding is a widely used and effective method of joining different components together. There is however no single welding process that will obtain the optimum weld in every situation. Factors such as process applicability, cost, time, access to the area to be joined, deposition rate and the service environment of the joint will be paramount in selecting the most appropriate joining method, such as welds produced on an aftermarket sports exhaust tailpipe, where Gas Tungsten Arc Welding (GTAW) is used for the aesthetical appearance or where Resistance Spot Welding (RSW) is not used due to the requirement of overlap of the parent materials, which creates the crevices for corrosion to initiate and accelerate.

As fusion welds tend to require a heat source (the exception being friction stir welding), there is also an effect on the parent materials as a result of this heat, which produces what is commonly known as the Heat Affected Zone (HAZ). The heat affected zone can contain a whole host of differences to that of the base material. They can, for example, contain a totally different phase in the microstructure, they could contain portions of a different microstructure, the formation of carbides or other phases are common within the heat affected zone, there can also be grain coarsening within this region. All of these aspects have the potential to effect the material properties in this area, this effect may be an increase or decrease in strength, toughness, ductility, hardness or corrosion resistance, sometimes this may be beneficial, other times detrimental to the component or structure.

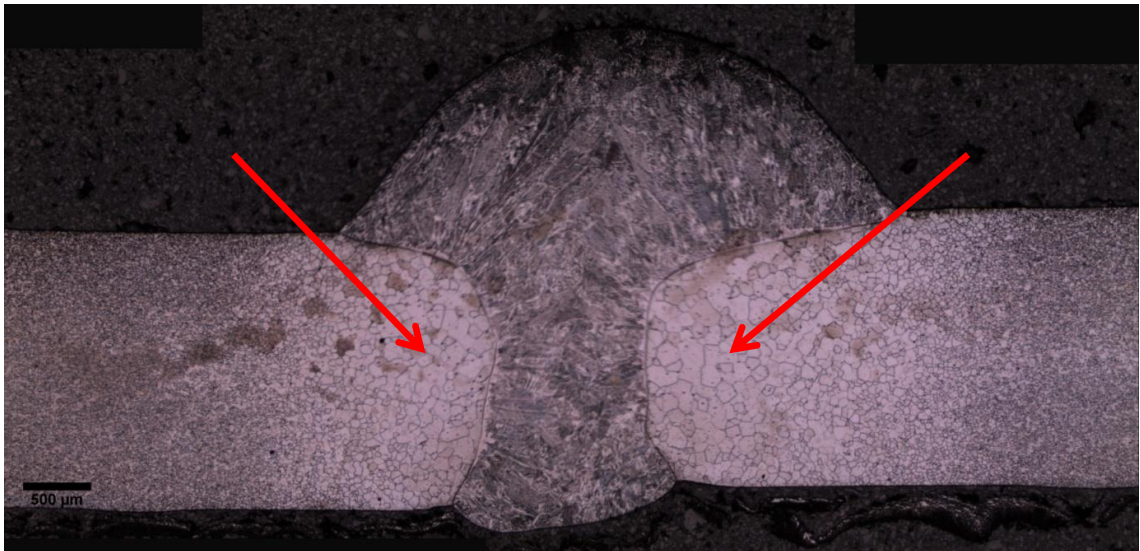


Figure 1. Fusion weld, showing heat affected zone either side of the weld (Magowan & Smith, 2010). Arrowed is the detrimental grain coarsening within the HAZ.

One such material type investigated within this research is a group of stainless steel grades known as 'Ferritics', so named after the ferritic microstructure of the grades that fall into this category. One of the main issues with the welding of ferritic stainless steel is a grain coarsening effect within the heat affected zone as seen in Figure 1. The problem with this is the detrimental effect it has on the material properties as described later in this report. Owing to this, ferritic stainless steel does not get used in some applications and a more expensive material, such as an austenitic stainless steel is selected instead. Therefore there is a need to reduce or eliminate the detrimental effect associated with welding ferritic stainless steels which could allow the incorporation of these materials into components or structures and therefore potentially reduce the cost or increase the corrosion resistance of the fabricated part.

Cold Metal Transfer (CMT) is a process developed by an Austrian company (Fronius), through a need for a low heat, welding process for the joining of aluminium. This research will attempt to exploit the benefits of the reduced heat input from the CMT

welding process to joining ferritic stainless steels, where this has the detrimental effects associated with the thermal cycle of the fusion.

Therefore this research aims to assess the capability of the CMT process when welding ferritic stainless steel parent materials and comparing with conventional Gas Metal Arc Welding (GMAW), this is to be qualified through assessment of mechanical properties and microstructural evaluations. The use of this process for the joining of ferritic stainless steel is limited and therefore this research will expand the body of knowledge in this area of welding and if CMT offers significant advantages over the conventional welding process, could mean that ferritic stainless steels could replace the use of austenitic stainless steels in some applications.

2 Literature Review

2.1 Stainless Steel

2.1.1 Definition of Stainless Steel

Stainless steels are a group of materials which, using iron as the primary element, may also include other significant additions such as chromium, nickel, and carbon depending on the particular type of stainless steel intended. To be considered stainless, the material must contain at least 10.5% chromium (Lippold & Kotecki, 2005) as this permits the formation of a chromium rich oxide layer on the surface of the material, thereby providing protection from atmospheric conditions. It must be noted that some alloys containing equal or greater amounts of the prescribed chromium content will still in fact corrode. The reason for this is that chromium has a strong affinity for carbon and so has a tendency to form carbides, thus, reducing free chromium from the matrix and thereby limiting the chromium content available to form the passive oxide layer.

2.1.2 History of Stainless Steel

Making additions of chromium to steel and noting the benefits with regards to corrosion performance has been documented from as early as 1821 during experiments conducted by Pierre Berthier (Cobb, 2010). This first instance recorded gave the development of a 1.5% Cr alloy that was suggested could be suitable for use in the cutlery industry. However the high carbon content reduced the alloys formability, so it was not adopted. This work was conducted as a result of reading about trials using additions of chromium to steel to create metallic mirrors that didn't

tarnish (Stodart & Faraday, 1822). In June 1872, J.E.T. Woods and J. Clark obtained British Provisional Patent 1932, for a weather resistant iron alloy that contained 30-35% chromium and 2% tungsten, the first patent for what would now be considered a stainless steel.

In 1892 high chromium steels were under investigation by Robert A. Hadfield in Sheffield, England. Using relatively high carbon contents (up to 2%) and chromium contents up to 16.74%, the materials were rejected as it displayed a reduction in corrosion performance under the conditions of the test. This was due to the accelerated corrosion test using a solution of 50% sulphuric acid, utilised by scientists of the day, under the common belief, that the media used was representative of corrosion in general.

In 1912 Harry Brearley visited a small arms factory to look at issues with gun barrels, his recommendations were to develop a low carbon, high chromium steel. On the 20th August 1913 (Cobb, 2010) Brearley produced a cast which contained 0.24% carbon and 12.8% chromium and when trying to etch the alloy, to permit microstructural analysis he found that this alloy did not etch or etched very slowly (Brearley, 1991) and is therefore credited with the invention of ferritic stainless steel (British Stainless Steel Association).

Around the same time that Brearley was experimenting with chromium contents in steel above that required to give the self healing layer, it is reported that others were also investigating these materials. The Americans claim that Elwood Haynes, was the first person to discover stainless steel and that it was only as a result of Brearley not being able to get the patent for the process in England and that he was successful in getting it in the U.S. that meant he was credited with the discovery (Marble, 1921).

The French scientist Leon Guillet was examining materials with compositions that would now be considered as martensitic grades, whilst another Frenchman, Albert Portevin was looking at steels with compositions similar to those now classed as EN 1.4016 ferritic stainless steel, whilst in 1908 the Krupp Iron Works in Germany had produced a chromium nickel steel for the hull of a yacht, the actual composition of the steel is not known, however two employees of the Krupp Iron Works, Eduard Maurer and Benno Strauss were at the same time as Brearley working on austenitic stainless steels (British Stainless Steel Association). So although there was a significant amount of research into these materials, globally, it was Brearley who has been recorded as the inventor.

2.1.3 Manufacturing Methods of Stainless Steel

The manufacturing procedure for stainless steel varies according to the product being produced and the intended application. The manufacturing route seen in Figure 2, used by Kawasaki, gives a general indication of the processes involved, with the use of the Electric Arc Furnace (EAF) being the start of the journey, melting the raw material (and potentially recycled materials) and then the molten material is transferred to the Argon Oxygen Decarburisation (AOD) plant, where two gases (argon and oxygen) are blown through the molten material to reduce the amount of carbon in the steel. The inert gas is used to lower the partial pressure of carbon monoxide allowing higher chromium contents to be in equilibrium with lower carbon contents, the oxygen is there to combine with the carbon to form carbon monoxide which can then be expelled (Choulet, 1997). At this point alloying additions may be made or they may be made just prior to continuous casting if that is the following route. If it is, then the molten material is poured into the casting machine where it is cast into the desired size, cooled and then cut to length. Some grinding may be conducted to remove surface defects prior to hot rolling. On hot rolling the material is heated to temperatures around 1250°C and then rolled, initially on a roughing mill where large reductions in the thickness can be made. The steel is then passed through another furnace to keep the temperature above the recrystallisation temperature of the steel and then rolled again to reduce the thickness further. It is then cooled and coiled (ArcelorMittal).

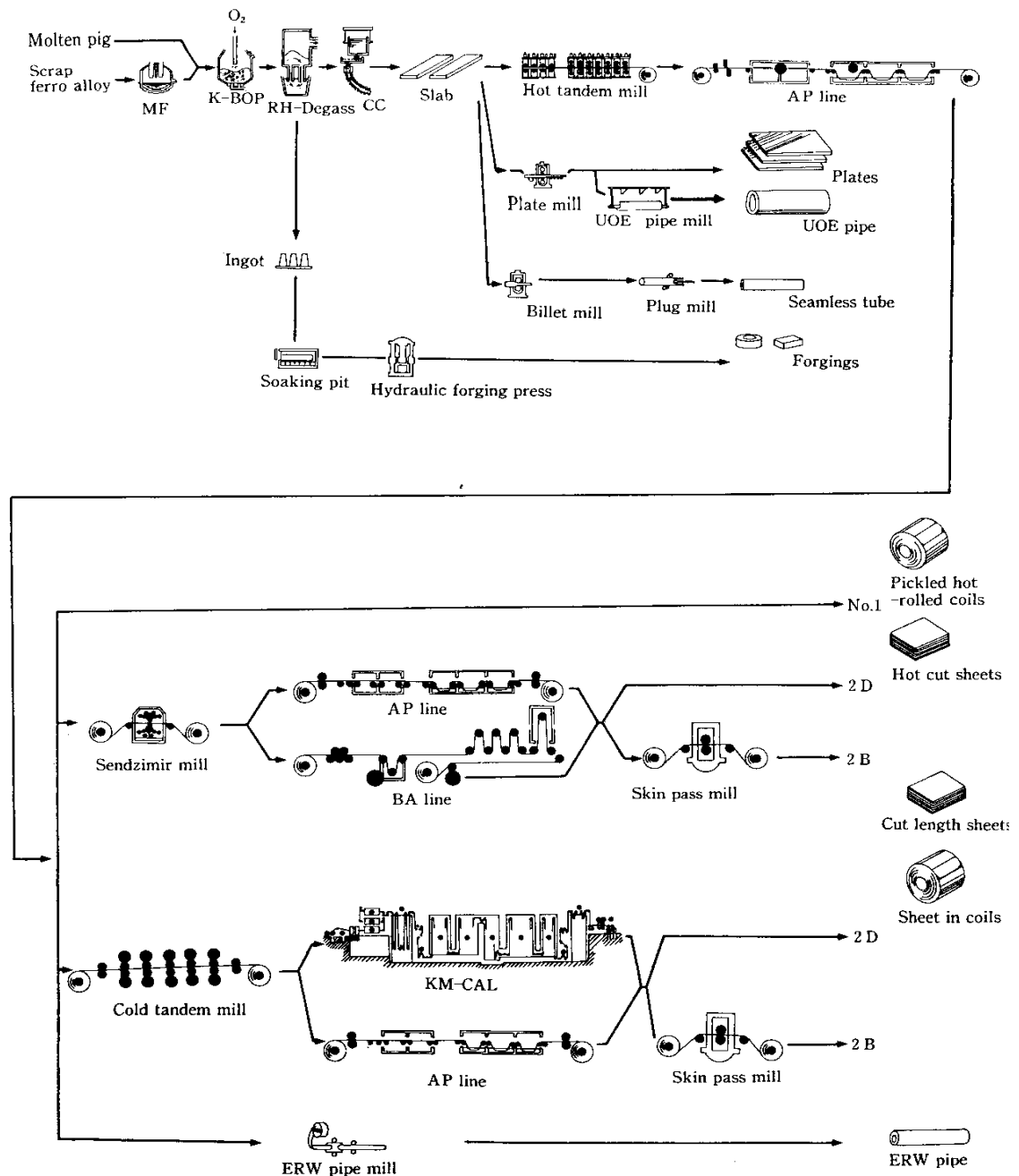


Figure 2. Manufacturing route of stainless steel as utilised at Kawasaki Steel (Ono & Kaito, 1986).

The stainless steel can now be annealed to soften the material and then shot blast to remove some of the oxide scale and then the steel is pickled to remove the remainder of the scale. To achieve an enhanced surface finish the steel would require further processing and that may include cold rolling followed possibly by a anneal and acid pickle (ArcelorMittal).

2.1.4 Types of Stainless Steel

Stainless steels are grouped according to the microstructure of the material, which gives the following three different classifications:

- Ferritic
- Austentic
- Martensitic

However there are two other categories of stainless:

- Duplex
- Precipitation Hardenable

There are a multitude of grades in various conditions associated with each type, detailed information about which can be found in the following sections, and in

Table 1.

Stainless Classification	Outokumpu steel name	Designation		Composition (%)					
		EN	ASTM	C	N	Cr	Ni	Mo	Others
Ferritic	4512	1.4512	409	0.02	-	11.5	0.2	-	Ti
	4003	1.4003	S40977	0.02	-	11.5	0.5	-	-
	4000	1.4	4105	0.03	-	12.5	-	-	-
	4016	1.4016	430	0.04	-	16.5	-	-	-
	4509	1.4509	S43932	0.02	-	18	-	-	Nb,Ti
	4521	1.4521	444	0.02	-	18	-	2.1	Ti
Martensitic	4006	1.4006	410	0.12	0.04	12	-	-	-
	4006	1.4006	416	0.1	0.04	13	-	-	S
	4021	1.4021	420	0.2	-	13	-	-	-
	4028	1.4028	420	0.3	-	12.5	-	-	-
	4313	1.4313	S41500	0.03	0.04	12.5	4.1	0.6	-
	4548	1.4548	-	0.05	0.07	15.5	4.2	-	Mn
Duplex	LDX2101	1.4162	S32101	0.03	0.22	21.5	1.5	0.3	5Mn
	2304	1.4362	S32304	0.02	0.1	23	4.8	0.3	-
	LDX2404	1.4662	S92441	0.02	0.27	24	3.6	1.6	3Mn
	2206	1.4462	S32205	0.02	0.17	22	5.7	3.1	-
	4501	1.4501	S32760	0.02	0.27	25.4	6.9	3.8	W, Cu
	2507	1.4410	S32750	0.02	0.27	25	7	4	-
Austenitic	4310	1.4310	301	0.1	-	17	7	-	-
	4372	1.4372	201	0.05	0.2	17	4	-	7Mn
	4301	1.4301	304	0.04	-	18.1	8.1	-	-
	4307	1.4307	304L	0.02	-	18.1	8.1	-	-
	4541	1.4541	321	0.04	-	17.3	9.1	-	Ti
	4305	1.4305	303	0.06	-	17.3	8.2	-	S
	4306	1.4306	304L	0.02	-	18.2	10.1	-	-
	4401	1.4401	306	0.04	-	17.2	10.1	2.1	-
	4404	1.4404	306L	0.02	-	17.2	10.1	2.1	-
	4406	1.4406	316LN	0.02	0.14	17.2	10.3	2.1	-
	4429	1.4429	S31653	0.02	0.14	17.3	12.5	2.6	-

Table 1. Table showing stainless steel grades and chemical compositions (Outokumpu, 2010).

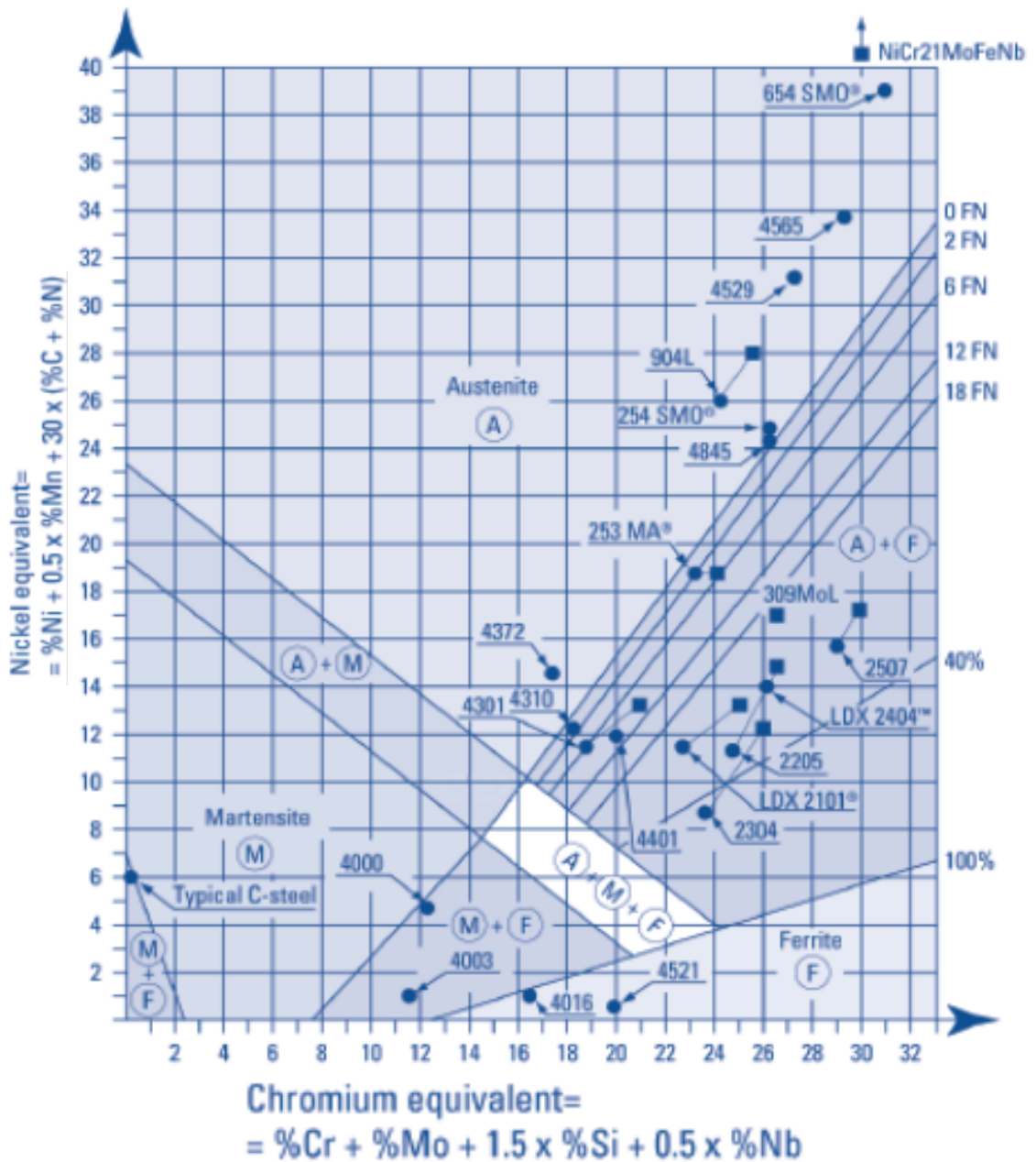


Figure 3. Schaeffler diagram with stainless steel grades indicated (Outokumpu, 2010).

2.1.4.1 Ferritic Stainless Steel

Ferritic stainless steels are a range of stainless steels that contain low levels of carbon and chromium contents from 10.5% to upto 40% (Cortie, 1993) for the super ferritics.

The American Iron and Steel Institute (AISI) designates the ferritic steels as a part of the 400 series of stainless steels (other steels in the 400 series include the martensitic types). With the more commonly used grades such as AISI 409 with a low chromium

content, AISI 430 with a medium chromium content and AISI 446 with a high chromium content as seen in Table 1.

The ferritic stainless steels generally have a Body Centred Cubic (BCC) crystal structure with a ferritic microstructure from room temperature to the melting point of the material. As this structure only holds small amounts of carbon in solution, carbon is generally present in the form of chromium carbide precipitates (Demo, 1982).

The exception to this is when the gamma loop, as seen on the iron – chromium equilibrium diagram in Figure 26 (page 53), extends into the region of the particular ferritic alloy in question. Upon cooling from melting point, this will cause a transformation from ferrite to austenite and if the cooling rate is slow enough, back to ferrite. If it isn't slow enough the transformation will create martensite. This is because austenite is able to hold considerably more carbon in solution than ferrite and so upon a fast cool the carbon has insufficient time to come out of solution and martensite forms. Therefore, in general, unless the gamma loop impinges on the alloy, it is not possible to harden a ferritic stainless steel through heating and rapidly cooling. The strengthening mechanisms which can occur in ferritic stainless steels, through heat treatment are generally not desirable due to the significant reduction in the ductility and toughness (Demo, 1982).

Ferritic stainless steels are generally used in environments that are subjected to fresh water and in temperatures upto 650°C. There are however some grades that are used within catalytic convertors operating at higher temperatures than 650°C and some of the higher chromium content ferritics are used within the marine industry (Lula, 1989).

2.1.4.2 Austenitic Stainless Steel

Generally the austenitic class of stainless steels are within the 300 series of the AISI designations. The grades contain significant proportions of austenite phase, stabilising elements, predominantly nickel and carbon, but also manganese and nitrogen, amongst others, which allow austenite to be present at room temperature. Like the ferritic grades, this type of stainless steel cannot be hardened via heat treatment, regardless of the cooling rate (Lula, 1989).

The austenitic stainless steels have a Face Centre Cubic (FCC) crystal structure (Ashby & Jones, 2001) and are therefore less susceptible to a reduction in toughness at low temperatures than the ferritic stainless steels. They are also nonmagnetic when fully austenitic, which makes them better suited to environments where magnetic materials could be detrimental to the component or structure, such as a mine sweeper or a scanning electron microscope (Ashby & Jones, 2001).

The environments where the materials are commonly employed include service conditions subjected to atmospheric corrosion, marine environment, low temperatures and high temperatures above 650°C (Lula, 1989).

2.1.4.3 Martensitic Stainless Steel

The martensitic grades of stainless steel, as can be seen in Table 1, are categorised within the AISI 400 series, with the common grades being the AISI 410, 420 and 440. The chromium content is generally in the range of 12-17%, with an associated high carbon content of approximately 0.1 to 0.5%, they contain relatively few other additions, occasionally silicon for an increased resistance to scale and nickel

to maintain the hardenability in some of the higher chromium grades (Colombier & Hochmann, 1967) The crystal structure of the martensitic stainless steel is Body Centred Tetragonal (BCT) and is the product of a diffusionless shear transformation. During the transformation to BCT there is insufficient time for carbon to move to preferred sites within the crystal lattice and so becomes trapped and subsequently distorts the crystal lattice. This distortion of the lattice prevents the occurrence of slip which is manifested by increases in the hardness and yield strength, but with associated low ductility (Higgins, 2001).

Unlike both the austenitic and ferritic grades of stainless steel, the martensitic grades rely on heat treatment to attain the desired properties of the material, but careful control of the furnace atmosphere must be made during these heat treatments as martensitic stainless steels can be very susceptible to surface decarburisation (ASM Handbook Committee, 1988).

The martensitic grades are used where the materials require high strength at room temperature or maintain strength at high temperature (Lula, 1989).

2.1.4.4 Duplex Stainless Steel

Duplex stainless steels contain a combination of microstructures, they have ferrite and austenite in varying quantities (Colombier & Hochmann, 1967) and therefore a mixture of the body centred cubic and face centred cubic crystal structures within the separate phases. This class of materials can offer a compromise between the properties of the austenitic and ferritic stainless steels, therefore utilising the benefits of both whilst still

subject to the problems of either. They are also able to exhibit super plasticity, where tensile stress is spread out as opposed to localised (Beddoes & Parr, 1999).

Duplex stainless steels exhibit corrosion resistance to both, localised and uniform corrosion, with a good resistance to stress corrosion cracking (Outokumpu, 2012).

2.1.4.5 Precipitation Hardenable Stainless Steel

Precipitation hardenable stainless steels can have a matrix of any of the three phases identified above (ferrite, austenite or martensite). However, generally they have a matrix of either austenite or martensite, where they are utilised in applications such as jet engine frames, turbine blades and surgical blades for the austenitic variants and gears, shafts and valves for those grades whose microstructure is that of martensite (Lippold & Kotecki, 2005).

This category of stainless steel can achieve very high tensile strengths above 1520 N/mm² and is able to do this through the addition of elements which are taken into solution and then encouraged to form very small precipitates within the structure that act as barriers to dislocation movement (Chakrabarty, 1987). These materials are used in situations where strength is required at temperature (Lula, 1989). Elements commonly used to produce the precipitates include aluminium, molybdenum or copper (Beddoes & Parr, 1999).

2.1.5 Alloying Additions Used in Stainless Steels

The various grades of stainless steel include the use of a number of purposefully added elements which benefit the steel in different ways. Details of the main elements used in stainless steels are as follows.

2.1.5.1 Carbon (C)

A crucial component in stainless steel, but generally maintained at levels below 0.1% and when welding stainless steel carbon levels significantly below this are preferred. It provides the steel with strength and is an important addition in the martensitic grades. Carbon is a very strong austenite stabiliser but uncontrolled it can combine with other elements and reduce the corrosion resistance of the steel (Cunat, 2004).

2.1.5.2 Chromium (Cr)

As previously stated the addition of chromium to the steel at levels above 10.5% is what provides the self healing protective oxide layer that imparts the improved corrosion performance of the material. It is a ferrite stabiliser and readily combines with carbon and nitrogen to form various forms of carbides, nitrides and carbo-nitrides (Streicher, 1977). It is also a key element in the embrittling phases which hinder stainless steel, such as sigma phase which is a combination of chromium and iron, but it is also present within the Chi and Laves phases (Sigma phase considered later in section 2.3.6).

2.1.5.3 Nickel (Ni)

The primary function for the addition of nickel is generally to stabilise the austenitic phase. Unlike chromium it does not readily combine with other elements such as carbon or nitrogen. At levels in the range of 8-10% nickel there is a marked reduction in the ability of the stainless steel to resist stress corrosion cracking however

increasing or decreasing from this range yields a greater resistance to this detrimental corrosion mechanism (The Specialty Steel Industry of North America, 2016). Nickel also suppresses the gamma loop seen on the left hand side of the Fe-Cr equilibrium diagram (Figure 26).

2.1.5.4 Manganese (Mn)

Manganese is added to stainless steels in various quantities, and in general is regarded as an austenite stabiliser, with its potency dependant on the nickel content. The main purpose for the addition of manganese is to combine with sulphur and thus prevent the formation of a low melting point iron sulphide that, in extreme cases, can cause a material to fall apart when the melting point of this iron sulphide is passed, this phenomena is commonly referred to as hot shortness (AMG Vanadium Inc., 2009).

2.1.5.5 Silicon (Si)

Silicon can provide the steel with a number of benefits including an increase in the fluidity of the melt, which can increase the complexity of casting which may be produced. It is primarily added as a deoxidiser within the melting process but can also add advantages in terms of oxidation resistance of the resultant alloy, at high temperature. Low levels of silicon have little effect on stabilising either ferrite or austenite, however higher levels are reported to stabilise ferrite. It can combine with iron to form iron silicides which can be detrimental to the mechanical properties of the steel (Lippold & Kotecki, 2005).

2.1.5.6 Molybdenum (Mo)

Molybdenum is a ferrite stabilising element and is added, normally in quantities of 2-4%, sometimes upto 8% (Cunat, 2004) to increase corrosion resistance of the stainless steel. It can also increase the hot strength of the steel, however this can provide

problems when hot working the material. Molybdenum is also added to some of the precipitation hardenable series of stainless steels to promote the precipitation reaction (Mathers, Precipitation hardening stainless steel : Job knowledge 102, 2016)

2.1.5.7 Titanium (Ti)

In a role similar to niobium, titanium is added to combine with the nitrogen and carbon within the stainless steel. The stoichiometric quantity of titanium required to combine with the available nitrogen and carbon can be calculated however as titanium also has an affinity for sulphur additional titanium must be added (Galenko & Zhuravlev, 1995).

2.1.5.8 Niobium (Nb)

The addition of niobium is used to stabilise the carbon and prevent it from combining with the chromium and therefore reducing the amount of chromium to produce the passive layer. The amount of niobium necessary to stabilise the stainless steel can be calculated from the following equation;

Equation 1. Equation showing amount of niobium required to stabilise a stainless steel.
 $\%Nb \leq 0.2 + 5 (\%C + \%N)$ (Cunat, 2004)

It is also reported that in ferritic stainless steels the addition of niobium is an effective method to increase the high temperature fatigue properties of the material (Stainless Steel for Design Engineers, 2014).

2.2 Definition of Welding & Brief History

Welding can be described as the fusion of two or more pieces of either the same or different materials. When designing a component the designer must account for the processing method to ensure the component will endure the entirety of its design life,

in the expected service environment. Welding has increasingly become a prominent fabrication method since its inception and allows the manufacture of parts of a component at separate sites and facilitates the combination of these parts at its intended location, an example of this could be oil pipelines (Easterling, 1992) or automotive exhaust systems.

Although forge welding, as practiced by blacksmiths had been in existence for thousands of years, welding, as it is commonly recognised, has its roots when Sir Humphry Davy demonstrated the creation of an electrical arc between two carbon electrodes, using a battery in 1800 (Cary, The History of Welding, 1998). This paved the way for the development of electrical welding processes, with the first patent for an electrical welding technique being applied for in 1864 (Kjellberg, 2004). Gas welding was developed and in use before the turn of the 20th century, with the discovery of acetylene by Edmund Davy in 1836 it wasn't until about 1900 when acetylene was used for the purposes of cutting and welding (Hobart Institute of Welding Technology, 1998)

2.2.1 Fusion Welding Processes

There are a number of fusion joining processes with variations within each of these processes, such as with Gas Metal Arc Welding (GMAW), there are a high number of variants including Cold Metal Transfer (CMT) welding. The differences are broad using completely different technologies to achieve the joint. Resistance welding, for example, uses the resistance of the material to be joined, to the flow of electricity to create sufficient heat to permit local melting of the materials. Then there are the processes that use an arc to create very high local temperatures, allowing melting and subsequent fusion. More specialised high energy processes such as laser beam and

electron beam welding can produce welds of extremely high depth to width ratios (American Welding Society, 1991). Figure 4 shows the relative differences in some of the processes according to the power density.

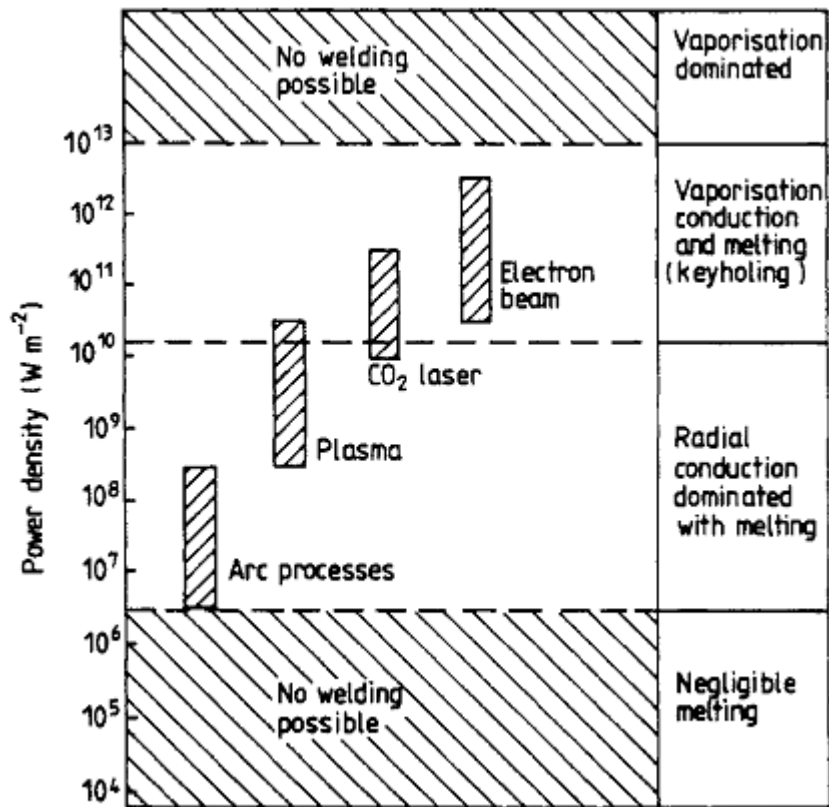


Figure 4. Showing the difference in power densities for various fusion welding processes (Lancaster, 1984).

2.2.1.1 Resistance Welding Processes

Resistance welding processes are a group of welding techniques that utilises the materials to be joined, electrical resistance, to produce a heat source which causes local melting and therefore coalescence of the faying surfaces and with the application of an externally supplied pressure a joint is created (Cary & Helzer, Modern Welding Technology, 2005)

2.2.1.1.1 Spot Welding

The average automobile contains somewhere in the region of 3000-4000 spot welds (Bayraktar, Kaplan, & Grumbach, 2004). Spot welding is a resistance welding process that utilises resistance heating and pressure to produce a weld (Cary & Helzer, Modern Welding Technology, 2005), this process can be observed in Figure 5, with an image of a cross section of the resultant weld as seen in Figure 6.

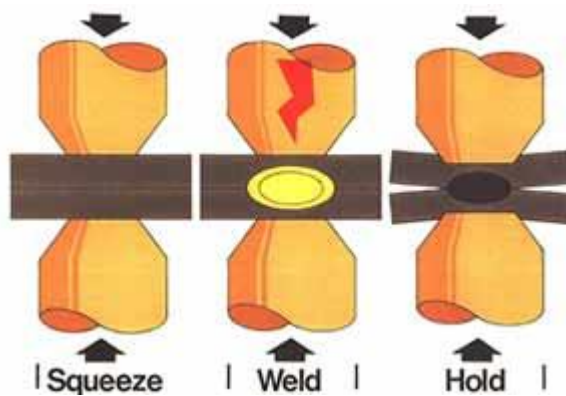


Figure 5. Schematic of resistance spot welding (Westgate, 2009).

To conduct a spot weld there is a minimum requirement of the following equipment;

- A welding transformer
- A suitable method to produce pressure on the joint
- A controller
- An electrode to allow the current to be transferred from the power supply to the work piece (Cary & Helzer, Modern Welding Technology, 2005).

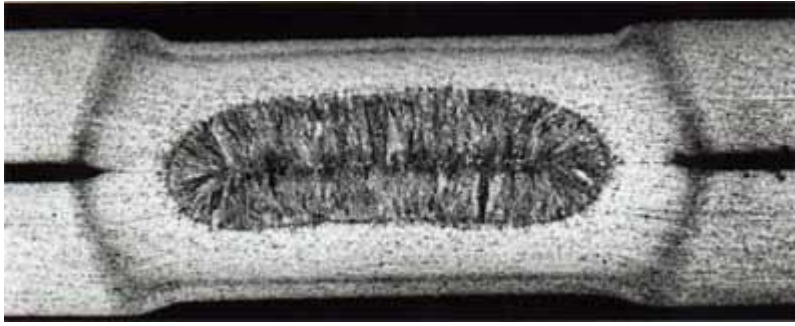


Figure 6. Image showing a resistance spot weld (RSW) (Westgate, 2009).

Resistance spot welding has significant advantages which justify its use in, for example the automotive industry as it is easily automated and is a very fast joining process, which provides low cost, predominantly autogeneous joints (Rajput, 2007). The process has some disadvantages however, such as;

- Equipment repair/ maintenance is difficult.
- Process can only produce lap joints which requires access to both sides of joint and adds to cost and weight of component.
- Equipment costs compared to arc welding equipment, are relatively high.
- Strength (fatigue and tensile) is relatively low in comparison to joints produced using other processes (American Welding Society, 1991).

2.2.1.1.2 Seam Welding

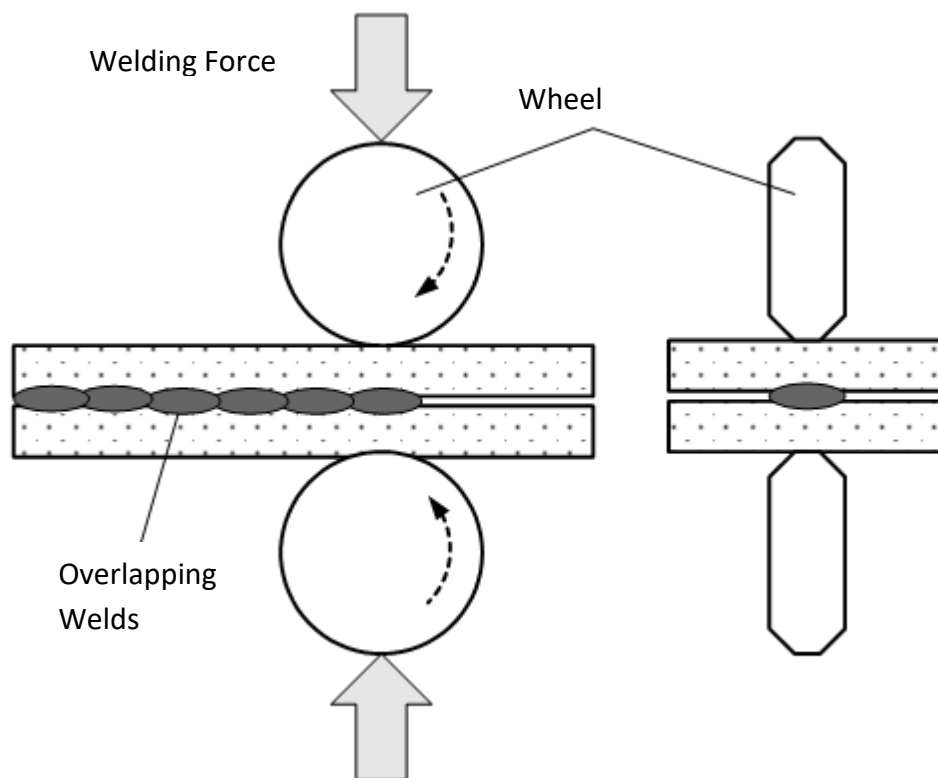


Figure 7. Schematic of resistance seam welding (Pires, Louriero, & Bolmsjo, 2006).



Figure 8. Showing resistance seam welding (Westgate, 2009).

Seam welding as seen schematically in Figure 7 and in practice in Figure 8, is a resistance joining process that produces a gas tight continuous weld (EWI, 2016) and

essentially is produced by continuously producing spot welds that are spaced so that they enable overlap. The wheels which act as the electrodes are driven and they also exert a force on the materials to be joined.

2.2.1.2 High Power Density Welding Processes

These processes use a focused high energy beam to provide the heat for melting of the parent/filler materials.

2.2.1.2.1 Electron Beam Welding (EBW)

Electron Beam Welding (EBW) uses electrons to generate heat in a component. A basic explanation of the process consists of a technology that enables the release of electrons from a source, which are then accelerated away from the source (same basis for a simple cathode ray tube, X-ray generation tube or electron microscope column). The electrons are then focussed using an electromagnetic lens onto the joint location. Interaction with the generated electrons and molecules/atoms between the electron generation source and the work piece are limited via the use of a high vacuum. The electrons penetrate into the intended joint location and give up their kinetic energy as heat.

The technique can produce welds with high depth to width ratios and operate at speeds up to 12000mm/min. The low energy input results in minimised distortion and shrinkage and it is reported that the technique can produce welds with zero contamination (GKN Aerospace, 2016).

2.2.1.2.2 Laser Beam Welding (LBW)

The Laser Beam Welding (LBW) process uses a focussed beam of light to vaporise the metal at the point of focus. This, like EBW can give high depth the width ratios, for

LBW ratios of 8:1 are possible (for EBW ratios of 30:1 are achievable) with power densities in the range of $10^{10} - 10^{12} \text{ Wm}^{-2}$ (Kaul, Ganesh, Tripathi, Nandedkar, & Nath, 2003).

Laser beam welding can be used to produce autogeneous welds and unlike EBW does not need to be conducted under a vacuum and does not create X-rays as a by-product as EBW does. It is a process that is easily automated and has the ability to join a wide range of materials (American Welding Society, 1991).

2.2.1.3 Arc Welding Processes

Arc welding processes are so characterised due to the fact that they utilise an electric arc as a means of introducing thermal energy into the process. This encompasses a wide range of welding techniques currently employed in fabrication applications.

2.2.1.3.1 Manual Metal Arc Welding (MMA)

Sometimes known as shielded metal arc welding, this is one of the early arc welding processes. A simple set up for the technique can be seen in Figure 9, which consists of a power source, which transfers power to the electrode holder via a lead. The electrode holder allows attachment of the consumable electrode. It must also be able to transfer the power from the welding lead to the electrode and be designed in a way that allows the operator to manipulate it effectively to carry out the weld. The electrodes consist of a wire coated in a mixture of different materials (predominantly non metal) which disassociate under the arc, stabilising it and provide a gas shield around it, finally it forms a protective slag on the weld pool, which prevents interaction with gases in the surrounding environment.

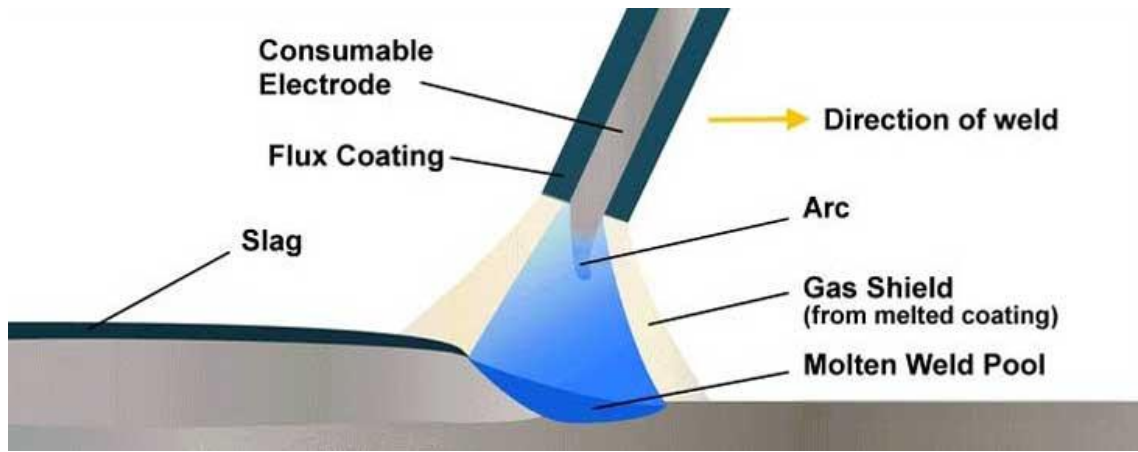


Figure 9. Diagram of the manual metal arc welding process (Wermac, 2016)

This process is versatile and the power source does not have to be directly adjacent to the welder, the power lead and torch are not cumbersome, which allows good flexibility and manipulation of the electrode. Some considerations with this process are the costs of which the majority come from labour. The material costs are also relatively high as only approximately 60% of the weight of purchased electrodes is deposited as weld filler. In part this is due to the flux coating which doesn't form a permanent part of the weld, but also the welder is unable to utilise the entire length of the electrode. The reason for this is that the electrode is getting shorter as the weld is being undertaken to the point where the electrode and the heat associated with it gets closer to the electrode holder and operator. To prevent damage to either, the weld is stopped prior to the end of the electrode. One of the other limitations of the technique is the stop/start nature of the process due to the reason mentioned above. The slag that forms on the surface of the weld needs removing before the weld can be re-started. This in turn increases the time and therefore the labour costs associated with this process. Ineffective removal of the slag may result in slag inclusions (Bax, Short, & Bayliss, 1988) within the weld which could present problems with the mechanical properties of the joint.

2.2.1.3.2 Submerged Arc Welding (SAW)

Submerged arc welding is an arc welding process that is conducted beneath a granular flux, due to this there is not the same fume generation and ultraviolet radiation associated with some of the other arc welding processes. The process, of which a schematic can be seen in Figure 10, consists of an automated wire feed system which feeds the wire into the granulated flux to the work piece, surrounding the arc the granulated flux melts, protecting the resultant weld.

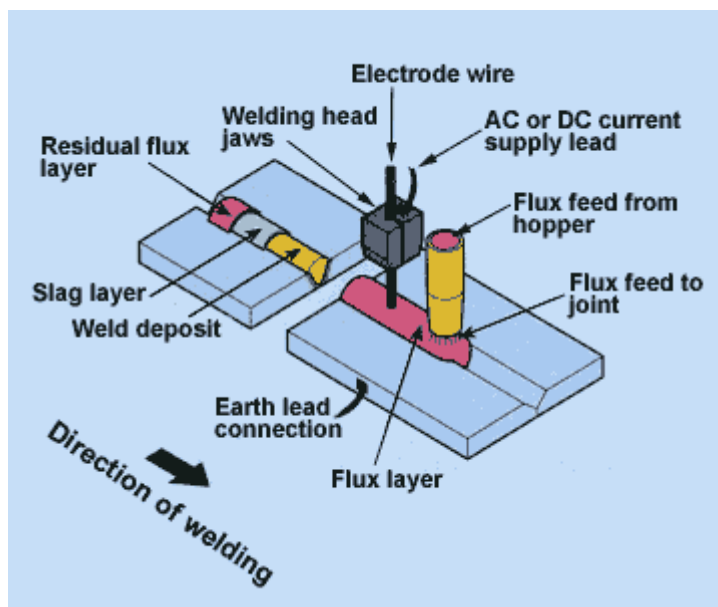


Figure 10. Diagram showing the submerged arc welding process (The Welding Institute Limited, 1995)

Submerged arc welding is generally conducted as a fully automated process and is able to produce welds in the flat and horizontal positions only. It can traverse at high speeds, up to 5040mm/min (American Welding Society, 1991). Also, this process produces high deposition rates.

2.2.1.3.3 Gas Tungsten Arc Welding (GTAW)

Gas tungsten arc welding, more commonly referred to as TIG (Tungsten Inert Gas), as it is generally conducted using an inert shielding gas. In the UK the gas primarily used for the technique is argon, however helium can also be used, which provides an enhanced surface cleaning action. Combinations of the two gases are sometimes utilised.

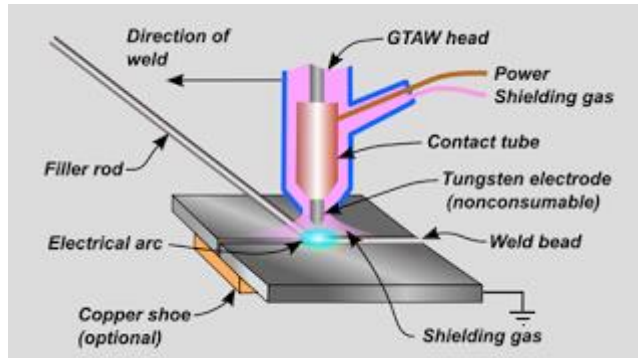


Figure 11. Diagram of the gas tungsten arc welding process (Mechanical Engineering, 2016)

The process seen in Figure 11, consists of a power source, this can be D.C. or A.C. depending on material to be welded and a hose which contains the power lead and gas piping to the torch. The torch itself contains the termination of the gas pipe which then goes through a diffuser to evenly distribute the protective shielding gas around the electrode and resultant arc. The torch also contains the electrode which is electrically coupled to the power lead. The non-consumable electrodes are predominantly tungsten with the addition of other materials such as thorium or zirconium. These additions improve electron emission and arc stability.

When using A.C. with an argon shielding gas, one half of the cycle provides a cleaning action, removing tenacious oxide layers as found on aluminium and magnesium. The other half of the cycle gives the heating action which melts the material and therefore allows the potential for fusion to occur. Therefore A.C. TIG is generally used for the

welding of aluminium and magnesium and their alloys (American Welding Society, 1991).

With D.C. either half of the cycle can be used, however D.C. electrode negative is generally used for other materials such as stainless steel (Miller, 2013).

GTAW lends itself readily to automation although it is skilfully employed as a manual process and is one of the few arc welding processes that can be used to produce autogeneous welds. If a filler is required it can be fed in to the joint manually or automated feeding mechanisms can be employed.

2.2.1.3.4 Gas Metal Arc Welding (GMAW)

Gas metal arc welding is a term that encompasses a number of different welding techniques that all use an electric arc as the heat source. They also utilise an automatically fed consumable metal electrode and externally supplied shielding gas.

The process was basically demonstrated in the 1920's, but it was not applied in the commercial environment until 1948, where it was used with an inert shielding gas (argon) for use in welding aluminium and so was, and still is, more commonly referred to by the name of MIG (Metal Inert Gas) welding (Armao, Byall, Kotecki, & Miller, 2014).

2.2.1.3.4.1 *Transfer Modes*

There are number of different transfer modes in GMAW, where the type of transfer can be dictated by a number of different variables, such as current, shielding gas and electrode (BOC, 2007). The different transfer modes and their various permutations can be seen in Table 2.

Droplet transfer mode	Typical welding process
1. Free flight transfer	
1.1 Globular transfer	
1.1.1 Drop transfer	Low-current GMA
1.1.2 Repelled transfer	CO ₂ -shielded GMA
1.2 Spray transfer	
1.2.1 Projected transfer	Intermediate-current GMA
1.2.2 Streaming transfer	Medium-current GMA
1.2.3 Rotating transfer	High-current GMA
1.3 Explosive transfer	SMA (Covered electrode)
2. Bridging transfer	
2.1 Short-circuiting transfer	Short-arc
2.2 Continuous bridging transfer	Welding with filler wire addition
3. Slag-protected transfer	
3.1 Flux-wall guided transfer	Submerged arc
3.2 Other modes	SMA, Cored wire, Electroslag

Table 2. Classification of droplet transfer modes and typical process mode utilised (Izutani, Shimizu, Suzuki, & Koshiishi, 2007).

The main transfer modes relevant to this study are the two free flight transfer modes, globular and spray transfer and the bridging transfer mode, short circuit transfer.

These can be seen graphically in Figure 12 and the visual appearance can be seen in Figure 13 to Figure 18. The pulsed arc utilises spray transfer through controlled pulsing of the current, which allows this transfer mode to be used in a greater range of applications (TWI, 2016).

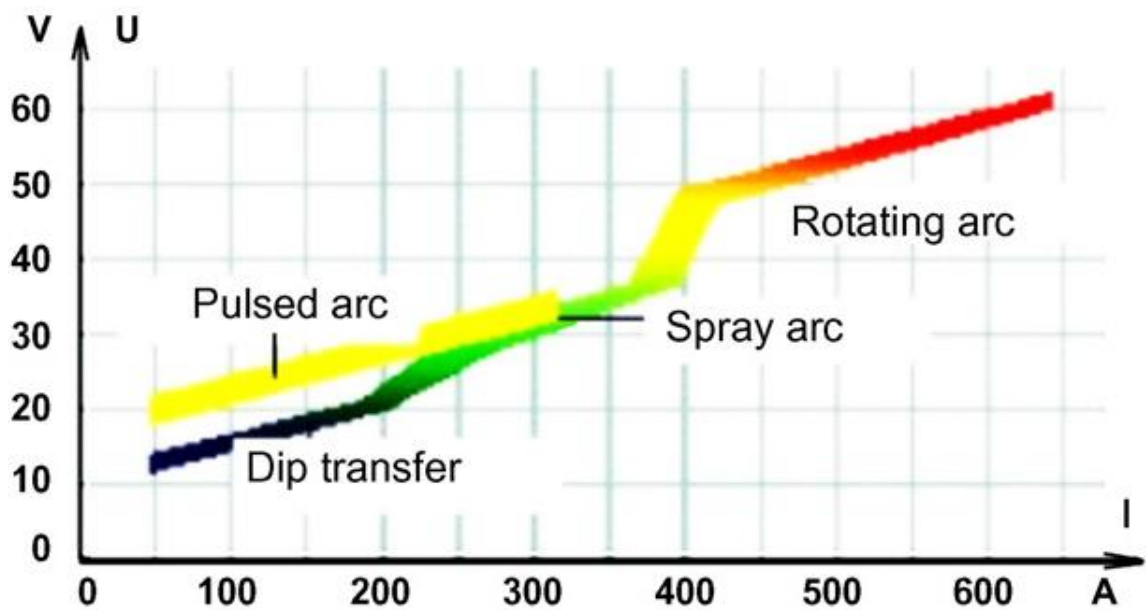


Figure 12. Diagram showing transfer modes according to arc current (I) and voltage (V) (Iordachescu & Quintino, 2008).

2.2.1.3.4.1.1 Globular Transfer

Globular transfer is characterised by the molten droplet which forms on the tip of the electrode and has a diameter greater than that of the electrode (Izutani, Shimizu, Suzuki, & Koshiishi, 2007). The formation of this size of droplet is through a combination of forces acting together, specifically the surface tension of the molten drop and the repelling force of the arc. These forces counter the detaching force induced by the electromagnetic pinch effect and gravitational forces (Izutani, Shimizu, Suzuki, & Koshiishi, 2007) (Iordachescu & Quintino, 2008). Transfer is thought to be through two modes, the first is drop transfer where the gravitational forces exceed the forces exerted by the arc and surface tension and so the droplet detaches and falls through gravity to the work piece (Lucas, Iordachescu, & Ponomarev, 2005) (Izutani, Shimizu, Suzuki, & Koshiishi, 2007) (Iordachescu & Quintino, 2008). The second transfer mode is termed repelled and occurs at higher currents and predominantly when using a carbon dioxide shielding gas (Iordachescu & Quintino, 2008). When

using this gas, the arc is constricted and so concentrates at the lower portion of the droplet, which in turn concentrates forces applied by the arc in this region. This results in the droplet being repelled from the work piece (Izutani, Shimizu, Suzuki, & Koshiishi, 2007). The droplet may detach and transfer to the work piece with no detrimental effect, as seen in Figure 13. However, it is considered more likely that the droplet will short circuit the arc and violently disperse, causing significant spatter, which has restricted the use of carbon dioxide in a large number of applications (Linde AG, 2016).



Figure 13. Showing globular transfer (Lucas, Iordachescu, & Ponomarev, 2005).

2.2.1.3.4.1.2 Short Circuit Transfer

Short circuit or dip transfer occurs at low currents and can be characterised by the molten material which forms at the tip of the electrode, coming into contact with the molten weld pool (The Welding Institute, 2010). At the point of contact with the weld pool a short circuit is established, the arc is extinguished with a corresponding rise in the current. The bridge between the weld pool and electrode is simultaneously attracted to both through surface tension. Therefore, the portion in the middle which thins, has an increased current density and so creates the magnetic pinch which becomes sufficient to fracture the molten bridge and so the arc is re established (Izutani, Shimizu, Suzuki, & Koshiishi, 2007). If the rate of current increase is too high, then violent separation of the molten bridge will occur which will result in excessive

spatter (Smith, 2014). This cycle can be seen in Figure 14 and images of the short circuit transfer seen in Figure 15.

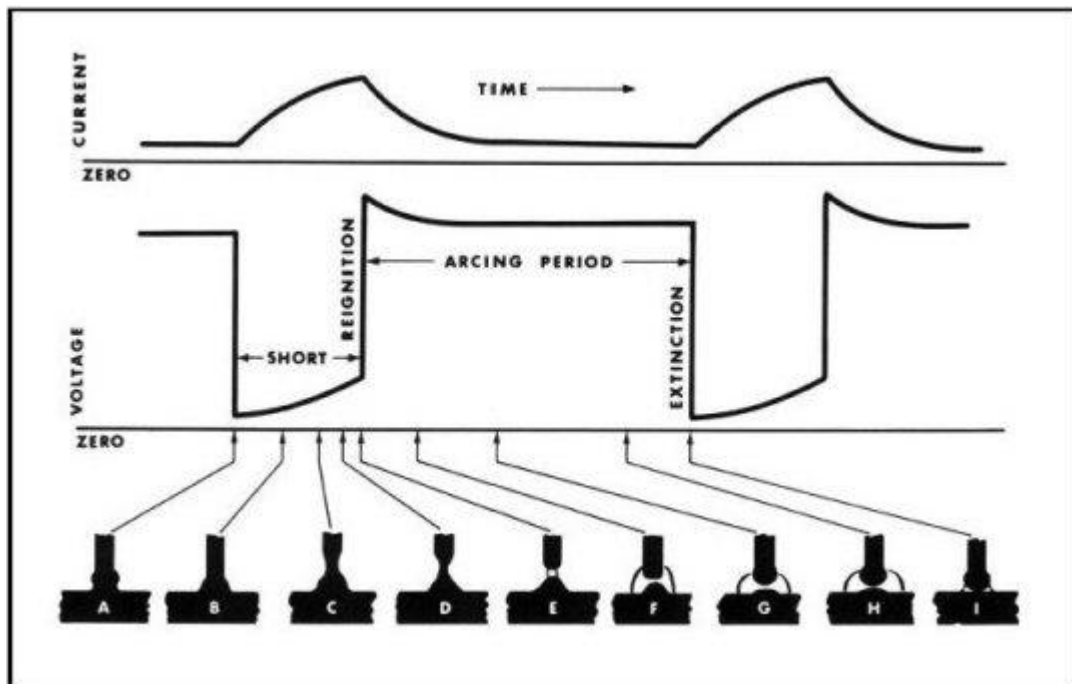


Figure 14. Showing short circuit cycle with effect on current and voltage (ESAB)

The process cycle occurs in the range of 20 to over 200 times per second. The shielding gas used can have significant influence over the surface tension and short circuit duration as well as the characteristics of the arc and levels of penetration (WWS Group, 2005).

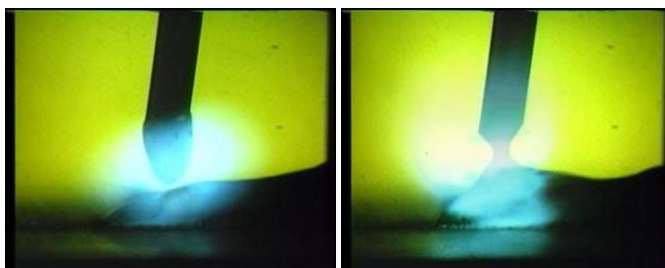


Figure 15. Showing short circuit transfer (Lucas, Iordachescu, & Ponomarev, 2005).

2.2.1.3.4.1.3 *Spray Transfer*

Spray transfer, as seen in Figure 16, can be characterised as being small droplets being transferred to the weld pool through the arc at rates of hundreds of droplets per second (Mathison, 2008). The operating current, for this type of transfer, must be above the transition current (influenced by liquid metal surface tension, electrode diameter, electrode composition and shielding gas) as indicated in Figure 12, otherwise globular transfer will occur with the droplet size significantly larger and transfer occurring at rates of a few per second (Lancaster, 1984). This transfer tends to be done using an argon rich shielding gas. This does not cause restriction of the arc column and therefore does not cause repulsion of the molten droplet, and so can result in a spatter free joint with narrow penetration (Izutani, Shimizu, Suzuki, & Koshiishi, 2007). As the droplets are accelerated to velocities which are greater than gravitational forces, this transfer mode can be used in any position (American Welding Society, 1991).

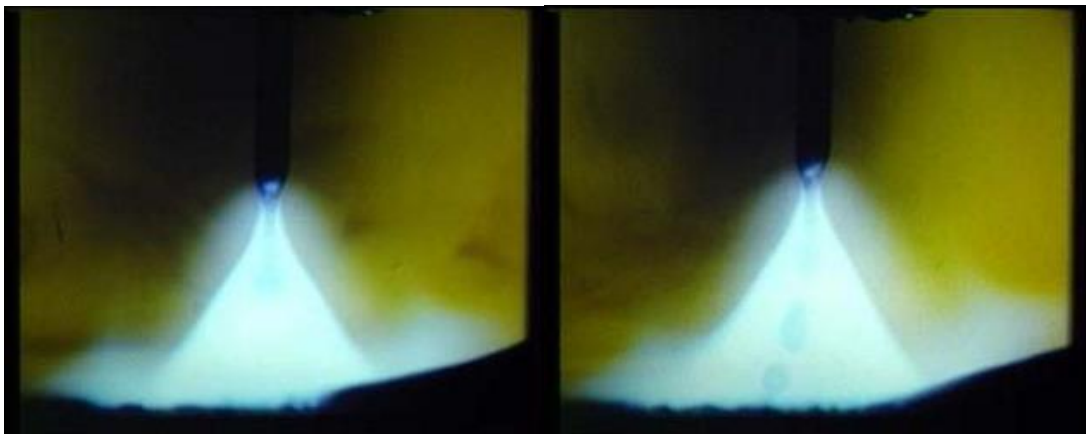


Figure 16. Showing spray transfer (Lucas, Iordachescu, & Ponomarev, 2005).

2.2.1.3.4.1.4 Pulsed Spray Transfer

One of the limitations to spray transfer is that although it can be used on most metal or alloys, owing to the high currents it is not suitable for thin sheets as it would cut through them instead of welding them (Rao, 1999). Pulsing the current as seen in Figure 17 overcomes this limitation as the average current is lower than that required for spray transfer, but at regular intervals a pulse of current above the transition current is applied which is in the spray transfer range. This causes a droplet or droplets to detach, as seen in Figure 18, and transfer to the work piece. The pulsing is controlled by the power supply. The use of pulsed spray transfer has also been reported to yield grain refinement in the heat affected zone and therefore enhance the mechanical properties of the material in this area. Also with an increased pulse frequency it has been observed that there is an associated increase in the weld depth to width ratio (Pal & Pal, 2011).

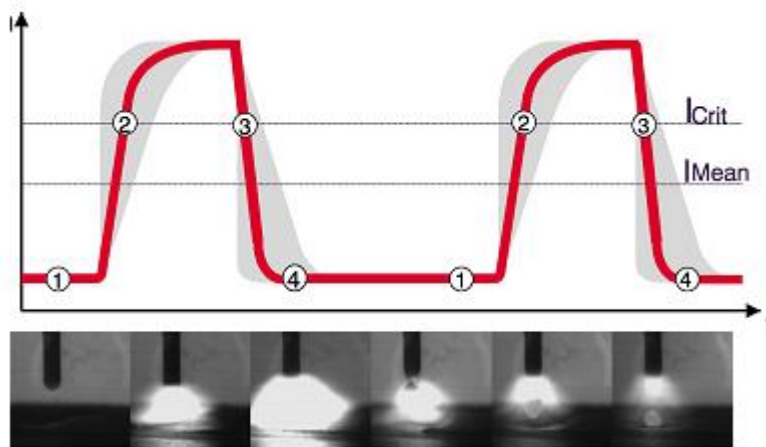


Figure 17. Pulsed spray transfer graph of current (I) against time (t) for two pulsing cycles and images depicting the events for one pulsing cycle (Hackl).



Figure 18. Showing pulsed transfer (Lucas, Iordachescu, & Ponomarev, 2005).

2.2.1.3.4.2 Metal Active Gas (MAG) Welding & Metal Inert Gas (MIG) Welding

The conventional Gas Metal Arc Welding (GMAW) processes, Metal Active Gas (MAG) and Metal Inert Gas (MIG) welding, as seen schematically in Figure 19, differ only in the shielding gas used, MIG has an inert shielding gas, such as argon and MAG welding contains an active gas component, within the shielding gas, such as carbon dioxide in argon. Both of these processes can operate in any of the droplet transfer modes and current power supplies allow the combination of GMAW short circuit with variable pulse spray transfer cycles, thereby combining the advantages of both (The Welding Institute, 2010).

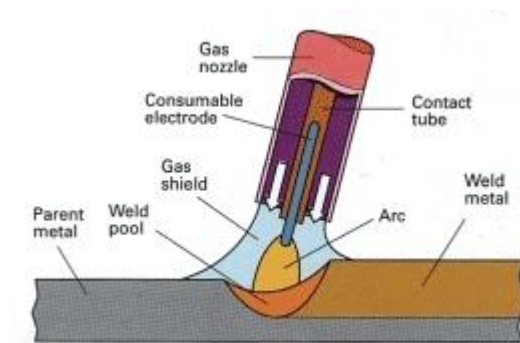


Figure 19. MIG/MAG process diagram (The Welding Institute, 2010).

2.2.1.3.4.3 Cold Metal Transfer (CMT)

Cold Metal Transfer (CMT) is a relatively new gas metal arc welding (GMAW) process developed by an Austrian company called Fronius.

Initial development into joining steel to aluminium in 1991 began the background work to the CMT process (Himmelbauer, 2004). The idea of retracting the wire as well as feeding, as opposed to just feeding, which is standard on traditional gas metal arc welding (GMAW) processes, was first utilised in a technology called spatter free ignition (SFI) also developed by Fronius in 1997 (Fronius International GmbH, 2004). Following research conducted by the company, to join thin sheet with limited filler material (Himmelbauer, 2004), by 2002 the CMT process was a proven technology. By 2004 the equipment entered the commercial marketplace (Fonius International GmbH, 2005).

Cold metal transfer welding is based around the dip transfer process (short circuit transfer) where the filler material is transferred to the weld pool through the consumable electrode coming into contact with it. Images showing dip transfer can be seen in Figure 15 and Figure 20 (with time frame between images).



Figure 20. Images showing dip arc transfer (Izutani, Shimizu, Suzuki, & Koshiishi, 2007) where the first image (far left) shows the arc and the consumable electrode with a spherical molten mass as the end moving toward the work piece as the wire is fed. The second image (centre) shows the consumable electrode in contact with the weld pool, provided the short circuit phase. The third image (far right) shows the transfer of the molten portion of the consumable electrode, which eliminates the contact with it and so the arc is re-established.

One of the main benefits of CMT is a reduced overall heat input into the joint, which is where the term “cold” in the process title originates. The process is an arc welding process and so it is only ‘cold’ in respect to the more conventional arc welding processes.

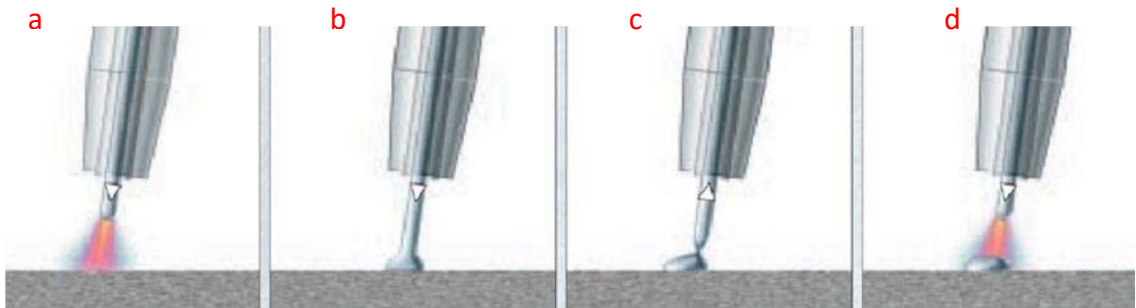


Figure 21. Schematic diagram of the CMT process showing wire motion, arrowed (Fronius International GmbH, 2007).

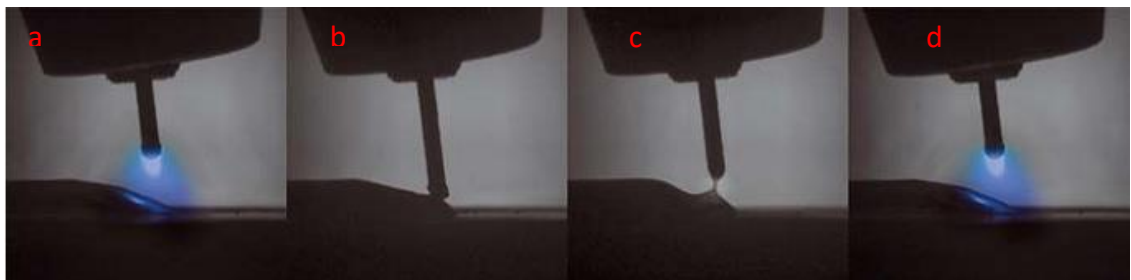


Figure 22. High speed images showing CMT cycle (Fronius International GmbH, 2004). Corresponding to the schematic in Figure 21 above.

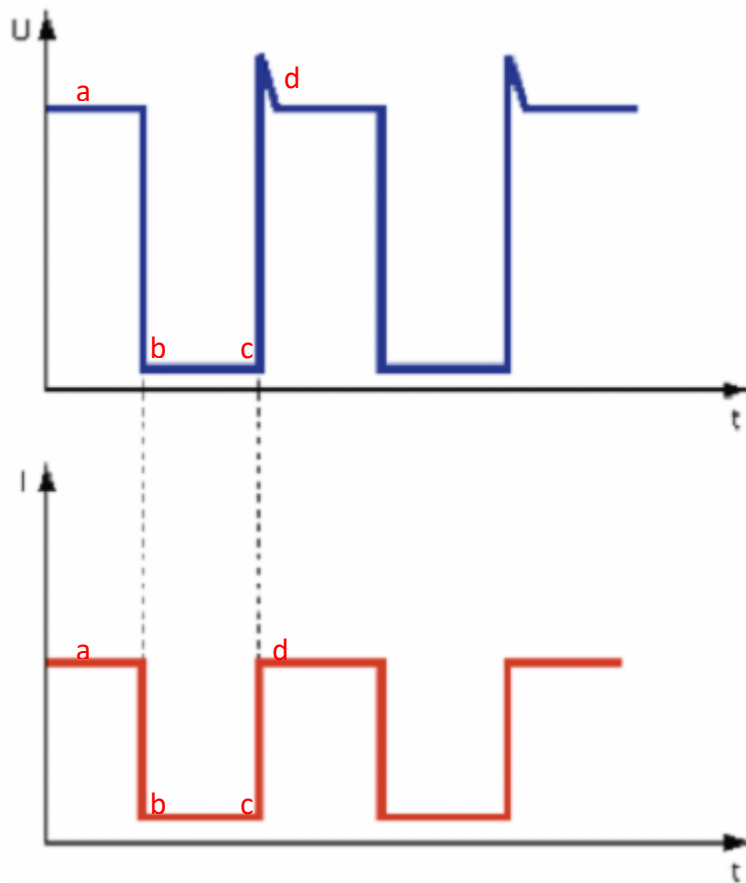


Figure 23. Graphs showing voltage (V)(top) and current (I) (bottom) against time for the CMT process (Rosado, Almeida, Pires, Miranda, & Quintino, 2008).

A description of the process is as follows; with the current relatively high, an arc is established and a molten drop of metal is formed on the end of the electrode. The wire is fed towards the intended joint, as in a standard MIG/MAG cycle, this is represented in 'a' of Figure 21, Figure 22 & Figure 23. As soon as the electrode contacts the molten weld pool, a short circuit is created, this is detected by the control software and the control system automatically reduces the current as seen as 'b' in the previously mentioned figures, as can be seen in Figure 14 for the standard GMAW process as the short circuit phase initiates the current rises which gives the GMAW a higher heat input. The system then reverses the electrode motion and allows the surface tension of the molten weld pool to remove the molten drop on the end of the

electrode. This gives the process a spatter free transfer and can be seen in 'c' on the above figures. Finally the electrode is sufficiently retracted to allow detachment of the molten droplet from the end of the electrode. The short circuit is then broken, the control software detects this and so rapidly increases the current and reverses the wire motion so that the arc is re-established and the electrode is driven towards the work piece as seen in 'd' in Figure 21 to Figure 23. This oscillation of the wire can happen at up to 70 times per second (Himmelbauer, 2004).

One of the variables of the CMT process is the ability to vary the short circuiting duration of the welding cycle as in b to c in Figure 23. The variation of this parameter can have an effect on the heat input of the process. By increasing the short circuiting duration there will be a reduction in the frequency of filler deposition, but this has been found to have very little effect on the amount of materials deposited (Pickin, Williams, & Lunt, 2011). Pickin et al (2011) also found that variation of the Arc Length Correction (ALC), the parameter which alters the short circuit duration, from +10% to -30% alters the duration of the short circuiting phase of the cycle from approximately 5ms to approximately 10ms, the portion of Figure 23 between 'b' and 'c'. There was not any reported effect from the variation in short circuit phase.

It was found by Feng et al (2009) in their study on joining aluminium, that when using CMT welding it required less current for the same amount of weld deposited in comparison to the conventional pulsed MIG process. Therefore this can allow the use of faster welding speeds and a reduced power cost when producing welds using CMT welding, it was also found in the same study that by using CMT on 1mm thick pure aluminium parent material, the use of CMT reduced the amount of deformation of the sheets due to welding (Feng, Zhang, & He, 2009). Research conducted by Elrefaey

(2015) also found advantages with welding aluminium materials using CMT over using conventional MIG or TIG techniques and identified them as comparable to welds created using the friction stir welding process and laser beam welding technique. On research conducted examining the use of CMT for welding aluminium to steel, CMT welds were created with and without a pulsed arc, with tensile samples created and tested for each (Madhavan, Kamaraj, & Vijayaraghavan, 2016). Although the welding of these materials creates an intermetallic compound that normally weakens the joint, it was reported in this study that although this intermetallic compound was present in small amounts, the tensile tests all failed in the heat affected zone region on the aluminium, with the addition of a pulsed current to the CMT cycle increasing the joint strength and hardness (Madhavan, Kamaraj, & Vijayaraghavan, 2016). This was not the same found for a study examining the joining of an aluminium alloy (1060) and a magnesium alloy (AZ31), where under tensile testing failures were seen in the fusion zone along a brittle intermetallic layer that had formed during the welding (Wang, Feng, & Wang, 2008).

Work conducted look at joining Inconel 718 found the welds to be aesthetically similar to those conducted using the conventional MIG technique, but with the lower heat input of the CMT process provided a reduced HAZ size and reduced residual stress levels, in comparison to the traditional MIG welding technique employed (Benoit, Jobez, Paillard, Klosek, & Baudin, 2011), therefore for a material more comparable to those under examination in this study, there appear to be advantages of CMT over the conventional GMA welding techniques.

2.2.1.3.4.4 Cold Metal Transfer Advanced

Welding processes are constantly being developed and the CMT process is no different. The CMT advanced process providing the ability to reverse the poles from positive to negative or vice versa during welding. This is reported to allow higher deposition rates (up to 60%) and an enhanced gap bridgability as well as providing an ability to reduce the heat input into the weld (Fronius International GmbH, 2009). This then permits the welding of thin materials (0.3mm) and bridging welding gaps as wide as 2mm across 2mm thick aluminium based parent materials using an aluminium silicon alloy filler material (Fronius UK, 2015).

2.2.1.3.5 Gas Shielding

The use of a shielding gas is primarily to exclude the atmosphere or more precisely, particular elements in the atmosphere (predominantly oxygen and nitrogen) from the molten material produced during the process. Without this shield the formation of porosity, oxides and nitrides may take place, causing detrimental effects to joint integrity. Shielding gases may be inert or active. The active gases contain proportions (eg 2%) of an active component (such as carbon dioxide or oxygen) in an inert gas, although the use of 100% carbon dioxide as a shielding gas is commonly used in the welding of steel. Different gases impart different properties (for details of the properties of some of the common shielding gases refer to Table 3) on the processes involved in the welding cycle. The development of new shielding gas mixtures has been with the aim of creating a more stable arc, to reduce fume emissions and/or to provide an enhanced molten metal transfer. All of which may have a positive effect on production, consistency and quality (Pires, Quintino, & Miranda, 2007). Subsequent

paragraphs will explain the main gases / gas mixtures with the effects on the welding process / weld.

	Argon	Carbon Dioxide	Helium	Hydrogen	Nitrogen	Oxygen
Chemical Symbol	Ar	CO ₂	He	H ₂	N ₂	O ₂
Specific Gravity (Air=1)	1.38	1.53	0.1368	0.0695	0.967	1.105
Density at 0°C, 1 atmosphere (kg/m ³)	1.78	1.98	0.18	0.090	1.25	1.43
Ionization Potential (eV)	15.7	14.4	24.5	13.5	14.5	13.2
Thermal Conductivity (W/m*K)	16.77	14.92	148.46	168.26	24.11	24.32
Cubic m/kg	0.604	0.545	6.037	11.986	0.862	0.754

Table 3. Showing the properties of various shielding gases (Praxair, 2005).

2.2.1.3.5.1 Argon

Argon is an inert gas which is approximately 1.4 times denser than air, as can be seen in Table 3, which makes it extremely good at shielding welds in the down hand position and is extensively used in pure form to join non ferrous materials such as aluminium, titanium and copper. In the UK it is the predominant shielding gas for GTA welding of these materials (BOC UK, 2010). The low ionization potential of argon, creates a stable, constricted, high density arc which results in a narrow penetration profile (Praxair, 1995).

2.2.1.3.5.2 Helium

Helium, another inert gas has a density of 0.169kg/m^3 (AIR LIQUIDE, 2009) against air which has a density of 1.202kg/m^3 (AIR LIQUIDE, 2009) at 15°C making it lot lighter than argon and therefore higher flow rates are required to afford the same levels of shielding. Welding with helium creates a hotter weld and due to the high thermal conductivity results in a broad weld profile with reduced penetration when used on stainless steel joints (Armao, Byall, Kotecki, & Miller, 2014).

2.2.1.3.5.3 Argon / Helium

It is common practice for shielding gases to be mixtures of two or more gases such as with a combination of 70% Ar and 30% He as recommended by Air Products (Air Products, 2017) for the joining of aluminium. The combination of argon and helium is used to combine the advantages of each for example when joining aluminium, magnesium or their alloys, argon improves arc stability and the cleaning action provided by the arc and helium is said to improve wetting and weld metal coalescence (ESAB, 2002). For welding stainless steel the addition of helium to argon, enhances the

fluidity of the weld pool, which increases the penetration. It also permits the use of faster welding speeds (Linde AG, 2012).

2.2.1.3.5.4 Argon / Oxygen

The addition of small quantities, such as 2% of oxygen to the argon based shielding gas creates a more stable arc. It also increases the speed at which molten droplets are transferred to the weld pool, reducing the amount of current required for spray transition and lengthens the duration for which the weld pool is molten and therefore effects weld penetration as a result (Praxair, 1995). However for stainless steel welds due to the oxidising effect, the weld bead will appear grey.

2.2.1.3.5.5 Argon / Carbon Dioxide

The use of pure argon tends to create an erratic arc and also a greater likelihood for undercut. The addition of small amounts of other elements reduces this effect. Carbon dioxide can be added in quantities of 3 to 25% to argon and produces a noticeable difference in the arc characteristics, and eliminates the problem of undercut afforded by pure argon. The addition of carbon dioxide also increases the “wettability” of the weld bead (Filho, Ferraresi, & Scotti, 2010), giving a greater amount of penetration than just argon alone. The use of argon/carbon dioxide mixes tends to be used for applications where the desired transfer mode is short circuit transfer. However, it is also suited for operating in spray and pulsed transfer modes (American Welding Society, 1991). It was reported by Zielinska et al (2009) that the addition of carbon dioxide to the argon shielding gas promotes a globular transfer mode, which can be seen in Figure 24, where the addition of 15% CO₂ to the argon shielding gas changes the transfer mode from spray to globular. This was found not to

be as stable as the spray arc transfer mode at the same currents without the addition of the carbon dioxide.

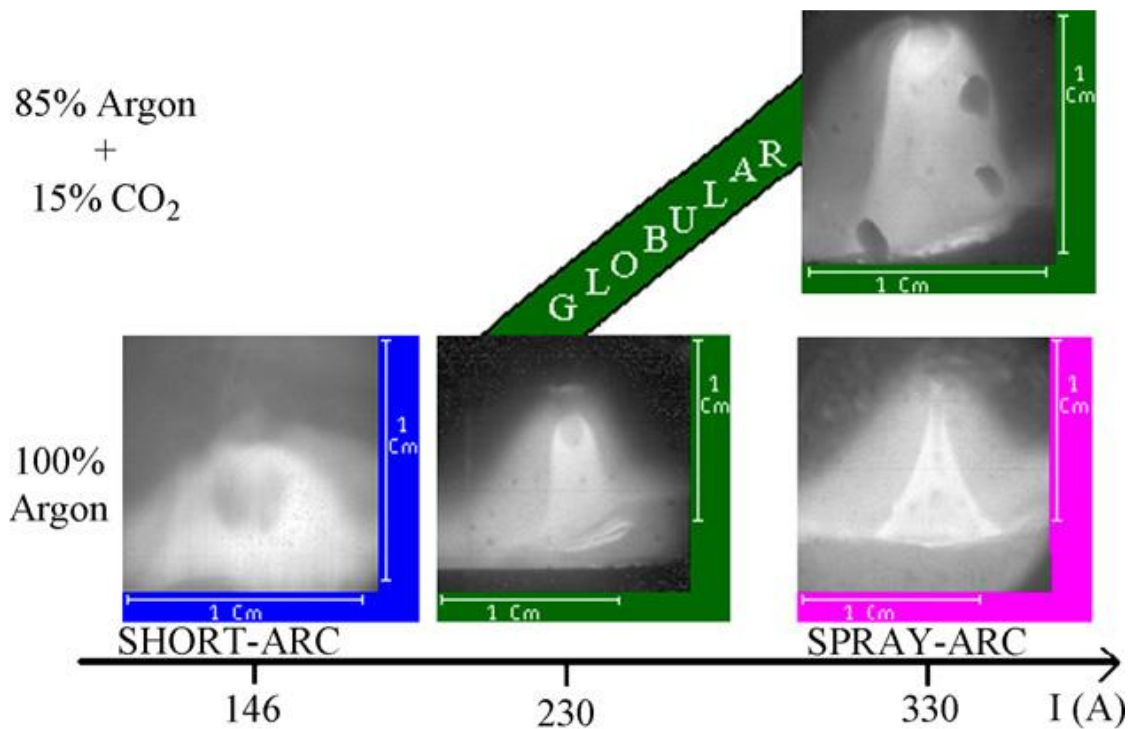


Figure 24. Showing effect on transfer mode of carbon dioxide addition to argon shielding gas (Zielinska, et al., 2009).

2.2.1.3.5.6 Carbon Dioxide

The use of carbon dioxide as a shielding gas has been widely applied in combination with gas metal arc welding processes. Carbon dioxide is the only active gas that can be used without combination to an inert gas. The use of the gas for shielding in welding applications tends to be in the joining of carbon and low alloy steels and provides the ability to weld at higher speeds, enhanced penetration and with reduction in cost to the shielding afforded by argon.

2.2.1.3.6 Arc Efficiency and Heat Input

One of the measures of a welding process is the heat input, that being the amount of heat that is being used to produce the weld. The calculation for heat input begins with calculating the arc energy using Equation 2;

Equation 2. Equation to calculate arc energy.

$$\text{Arc Energy (J/mm)} = \frac{VI}{v}$$

Where;

V = Voltage used (V)

I = Current used (A)

v = Traverse speed of welding torch (mm/s)

With a calculation of arc energy, the heat input maybe calculated using Equation 3;

Equation 3. Equation to calculate weld heat input.

Heat Input (J/mm) = η AE (British Standards Institution, 1998)

Where;

η = Process efficiency (0.8 for GMAW) (British Standards Institution, 1998)

AE = Arc Energy (J/mm)

The arc energy is simply the energy put into the welding process, per unit length of weld. However not all of the energy from the arc is transferred to the work piece, as some is lost from the sides of the arc, making the process less than 100% efficient.

Therefore the amount of losses which occurs during the process must be quantified so that adjustments can be made to give an accurate value of the heat input. The value

as specified by British Standards for the GMAW processes is 0.8 (British Standards Institution, 1998).

Work conducted by DuPont and Marder (1995) found that the arc efficiency for the gas metal arc welding process varied and with measured values of 0.84 they had a tolerance of ± 0.04 . Therefore potentially the process efficiency could be higher by 10%, with a process efficiency of 0.88 rather than the 0.8 stated within the British Standard.

Work has also been undertaken to assess the process efficiency of a number of the variant gas metal arc welding processes including the cold metal transfer process. The conclusions were that the process efficiency of CMT was 0.85 and that it was not too dissimilar to the standard GMAW process tested. (Pepe, Egerland, Colegrove, Yapp, Leonhartsberger, & Scotti, 2011) This then means that calculated heat inputs based on the process efficiency values given in the British Standard will appear lower than they actually are. It was also found that welding in a groove, such as with vee butt joint preparation for example, increased the process efficiency to around 0.9, this is thought to be due to less radiant heat being lost from the arc as it would have been absorbed by the walls of the material. This then may mean that when welding thicker sections with a wider gap, there is an increase in the process efficiency and therefore when calculating the heat input with either the value stated in the British Standard or one from recent research, may still yield inaccuracies in the values obtained.

2.3 Welding Stainless Steel

The integration of different materials into one component allows the part to take on the advantages of certain materials, whilst reducing or eliminating the effects of the disadvantages. Stainless steels can offer a vast array of properties to a component or structure, such as enhanced corrosion resistance, enhanced mechanical properties, wear resistance and aesthetical appearance. The cost of stainless steel may make it economically unviable to produce the entire component or structure from the material and this creates the need to find suitable technologies to allow the integration of this classification of materials into components and structures.

Various welding techniques have filled this requirement well and have allowed the combination of stainless steel with a whole host of different materials. Greater control of the welding process has allowed a greater consistency of weld. In particular advances in the electronic systems within welding equipment has allowed automated manipulation of certain parameters through the welding cycle and the instigation of welding robots have permitted greater consistency in the torch traverse speeds and distance to work piece. Investigations into the as welded metallurgical properties of the materials have permitted identification of problems associated with welding different materials. The following information highlights the main problems that may be encountered whilst welding stainless steels, the effects of which may be a reduction in corrosion resistance, alteration of mechanical properties or simply affecting the aesthetics of the part.

2.3.1 Grain Growth

One of the main problems associated with the welding of ferritic stainless steels is the issue around grain growth in the heat affected zone as can be seen arrowed in Figure 25. This grain growth reduces the toughness in this area and therefore in certain service environments could lead to failure in situations where an unwelded material would not fail.

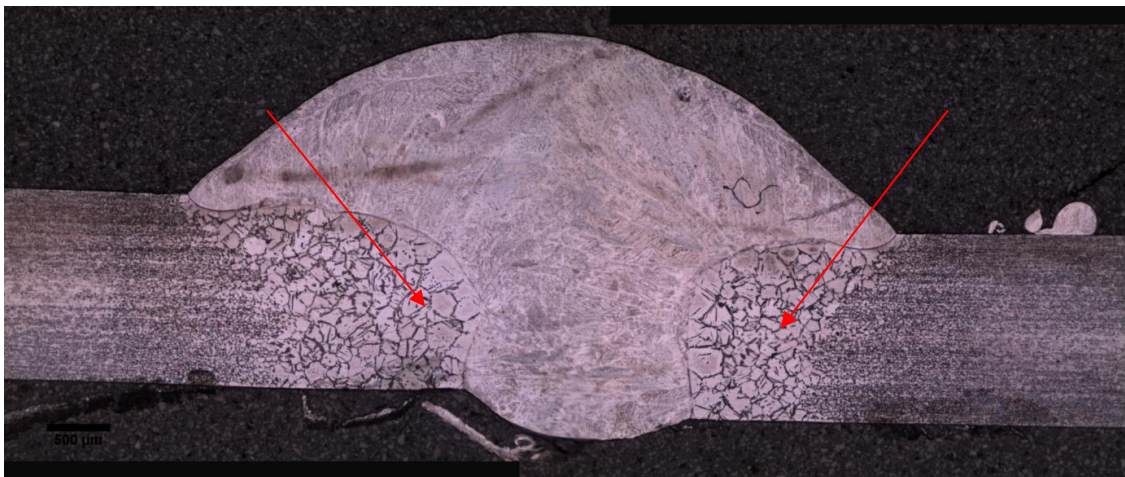


Figure 25. Image showing grain growth in GMA welded ferritic stainless steel (Magowan & Smith, 2010).

Grain growth during the welding of ferritic stainless steel arises as the parent material adjacent the weld is heated up to temperatures above 955°C . Heating above this temperature allows the ferritic grains to grow (Lakshminarayanan, Shanmugam, & Balasubramanian, 2009). The longer they are held in this region and the higher the temperature held in this region, the larger they can grow. There are certain actions that may be taken to minimise this growth such as the inclusion of carbide and nitride stabilising elements, (boron, aluminium, vanadium and zirconium) which essentially pin grain boundaries and hence minimise the ability of the grains to grow (Lakshminarayanan, Shanmugam, & Balasubramanian, 2009). There is also the effect in ferritic stainless steels of allowing some transformation to austenite at elevated

temperatures as this also reduces grain growth. However, without controlled cooling this can lead to other problems as discussed in 2.3.3.

2.3.2 Sensitization

Sensitization occurs in both austenitic and ferritic stainless steels and dramatically reduces the corrosion resistance of the material in aggressive environments. The problem arises during the welding cycle as temperatures in excess of 900°C provides sufficient energy to allow carbon to migrate through the grain to the grain boundary and form carbides. These carbides are predominantly with the chromium in the form of $M_{23}C_6$ or M_7C_3 (Amunda & Mridha, 2011). This leaves the area adjacent to the grain boundary denuded of free chromium, the element which gives stainless its protective, self healing, chromium oxide layer. Therefore this prevents the protective layer forming at this grain boundary and so leaves an area that is unable to resist attack from a corrosive media.

The techniques employed to reduce or eliminate the detrimental effects of sensitization include controlling the interstitial elements in the material, predominantly carbon and nitrogen. It is these elements which combine with the chromium and therefore reduce the levels of this element necessary for passivation. The addition of stabilising elements has been successfully used, with additions of elements such as titanium, vanadium, niobium, tantalum, yttrium and zirconium, being added to the material during manufacture of the steel. These elements then form stable carbides or nitrides and essentially reduce the amount of carbon within the material that is free to form carbides with the chromium (Amunda & Mridha, 2011).

Another method is via controlling the heat input and cooling rate of the welding process. It has been found that low heat inputs yield fast cooling rates during the early part of the thermal cycle which produces fully ferritic structures. This however gives a structure super saturated with carbon and therefore results in the formation of carbides and nitrides at the grain boundaries. As the cooling rates are high, it also prevents any reverse diffusion of the chromium back to any depleted regions. It has been claimed that higher heat inputs are critical in managing sensitization in ferritic stainless steels as it provides a slower cooling rate which allows the chromium to redistribute to areas of lower concentrations and essentially desensitize itself (Amunda & Mridha, 2011).

2.3.3 Formation of Secondary Phases

The thermal cycle induced within the parent material during welding raises the temperature to its melting point immediately adjacent to the weld and the temperature gradually diminishes with distance, the further away from the edge of the fusion zone. The speed of cooling is relatively fast, which, in some instances, prevents certain microstructural phases forming. One such instance of this is with certain grades of ferritic stainless steel. The microstructure that is not completely ferritic from room temperature to melting temperature, and there is the appearance of what is commonly referred to as the gamma loop. An example of an iron-chromium equilibrium diagram can be seen in Figure 26 with the loop apparent on the left hand side extending from the y-axis between 912 & 1394°C.

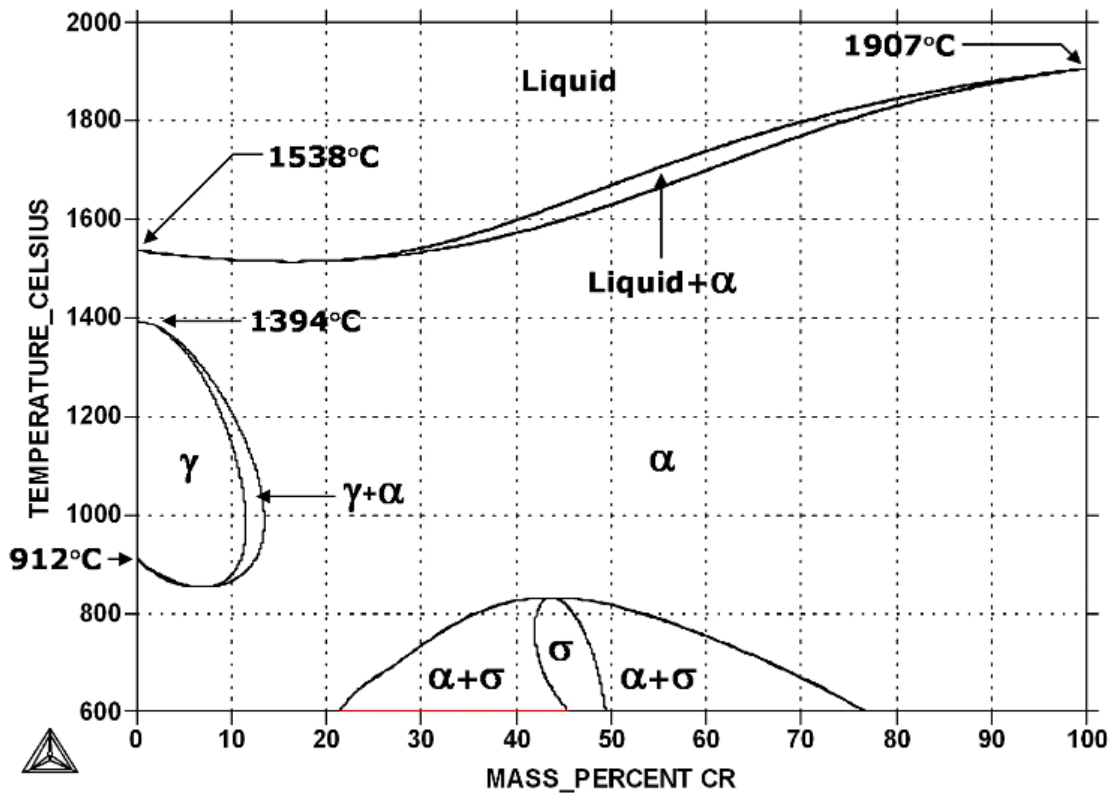


Figure 26. Iron-Chromium equilibrium diagram (Computational Thermodynamics Inc., 2011).

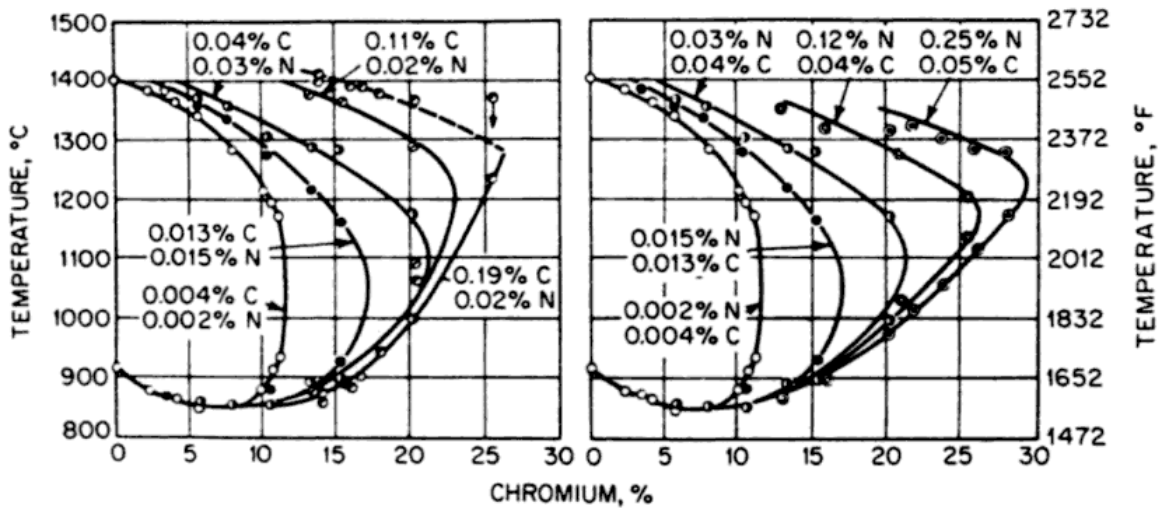


Figure 27. Part of Iron - Chromium equilibrium diagram showing effects of carbon and nitrogen on the shape and size of the gamma loop (Deddoes, Parr, & Hanson, 1999).

One of the difficulties of using equilibrium diagrams such as that seen in Figure 26, is that they are binary diagrams. They only display the relationship between the variation of the two elements shown within the diagram and make no consideration for the variation of additional elements present within the material. For stainless steels the manipulation of the composition is extremely important for example increasing the carbon content of martensitic stainless steels permits the transformation strengthening crucial for these materials. Using the same element for another example, an increased quantity of carbon within a ferritic stainless steel significantly increases the extent by which the gamma loop extends across the equilibrium diagram. This effect can be observed in Figure 27, where the effects of carbon and nitrogen are shown on the size and shape of the gamma loop. With low levels of interstitials the loop does not extend beyond twelve percent chromium. However, when relatively small increases are made with carbon and nitrogen, the loop extends to alloys containing nearly thirty percent chromium. The significance of this is that the gamma loop is a region where the ferritic material transforms to austenite. This has the associated crystal structure change from body centred cubic to face centred cubic and a volume contraction as a result. This is sometimes used by material engineers to the advantage of the material during welding as it restricts grain growth, however, it can hinder the properties of the material. Austenite, the structure formed within the gamma loop, has a strong affinity for carbon and is able to hold significantly more carbon in solution than can be accommodated in ferrite. For a 17% chromium ferritic stainless steel, it is reported that 0.15 wt% of carbon is soluble in ferrite at 1400°C, which rapidly reduces to 0.03 wt% on cooling down to 1000°C. In contrast the solubility of carbon in austenite of a 17% chromium stainless steel at 1200°C is 0.32 wt% (Lippold & Kotecki, 2005). The cooling part of the welding cycle, without

externally applied retardation, can be extremely fast and therefore non equilibrium. As a result of this, for a ferritic stainless steel that has a proportion of austenite within the microstructure, the austenite does not have sufficient time for the diffusion required to allow the transform to ferrite and carbide as predicted on the equilibrium diagram. Therefore other diagrams are used to predict microstructures formed under non equilibrium cooling conditions such as Time Temperature Transformation (TTT) diagrams. One such example of this is proposed by Warmelo et al (2007) and can be seen in Figure 28. Although the proposers identified it as a Continuous Cooling Transformation (CCT) diagram, it is in fact a TTT diagram as the x-axis is time base and not cooling rate. From the diagram (Figure 28) proposed by Warmelo et al (2007), it looks to be possible to miss the transformation to austenite and therefore subsequently unable to transform to martensite, if the cool was quick enough (1-2 seconds to 1050°C), this is described but with no validation of the mechanism for how this process occurs. This would indicate that within a HAZ, there could be regions close to the fusion zone that have experienced temperatures in excess of 1200°C that cool quick enough to maintain a ferritic structure, this would be clearly identifiable within a HAZ.

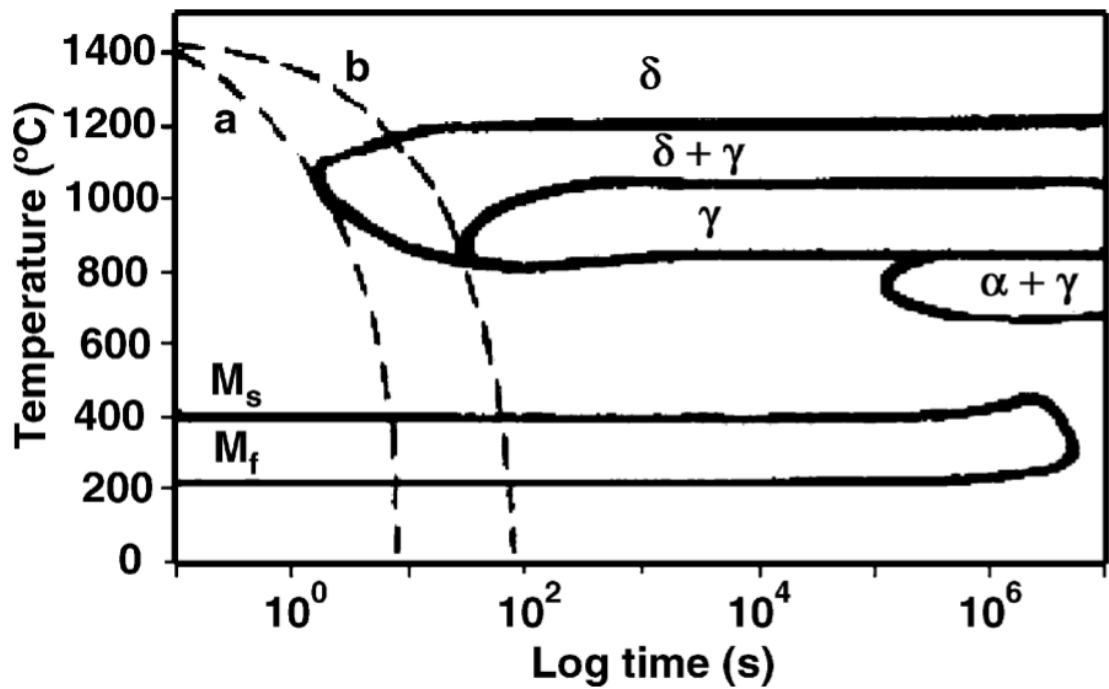


Figure 28. Time Temperature Transformation diagram for delta ferrite to austenite in the high temperature HAZ (Warmelo, Nolan, & Norrish, 2007).

Therefore the carbon gets trapped in solution and forms the phase martensite, which has a body centred tetragonal structure which can have a detrimental impact on mechanical properties and can result in premature failure by hydrogen induced cracking (Lippold & Kotecki, 2005). Work undertaken by Zheng et al (2010) identified that the correct balance between ferrite forming and austenite forming elements was important to prevent martensite formation in low carbon, 12% chromium stainless steels. They found that identification of the ferrite factor was important;

Equation 4. Equation to determine the ferrite factor (Zheng, Ye, Jiang, Wang, Liu, & Wang, 2010)

$$\text{Ferrite Factor (FF)} = \text{Cr} + 6\text{Si} + 8\text{Ti} + 4\text{Mo} + 2\text{Al} + 4\text{Nb} - 2\text{Mn} - 4\text{Ni} - 40(\text{C} + \text{N})$$

The research identified that when the FF is above 9.0, there would be little martensite within the high temperature heat affected zone, but as the FF decreases the amount of martensite increases, with 90% martensite content when the FF is reduced to 7.62.

2.3.4 Solidification Cracking

Solidification cracking is caused through the inability of the weld material to withstand the forces acting upon it as it solidifies (TWI Ltd, 2009). In the case of stainless steels this failure mode tends to be more of a problem for austenitics rather than ferritics and furthermore the inclusion of ferrite within the austenitic matrix reduces the susceptibility to this type of cracking.

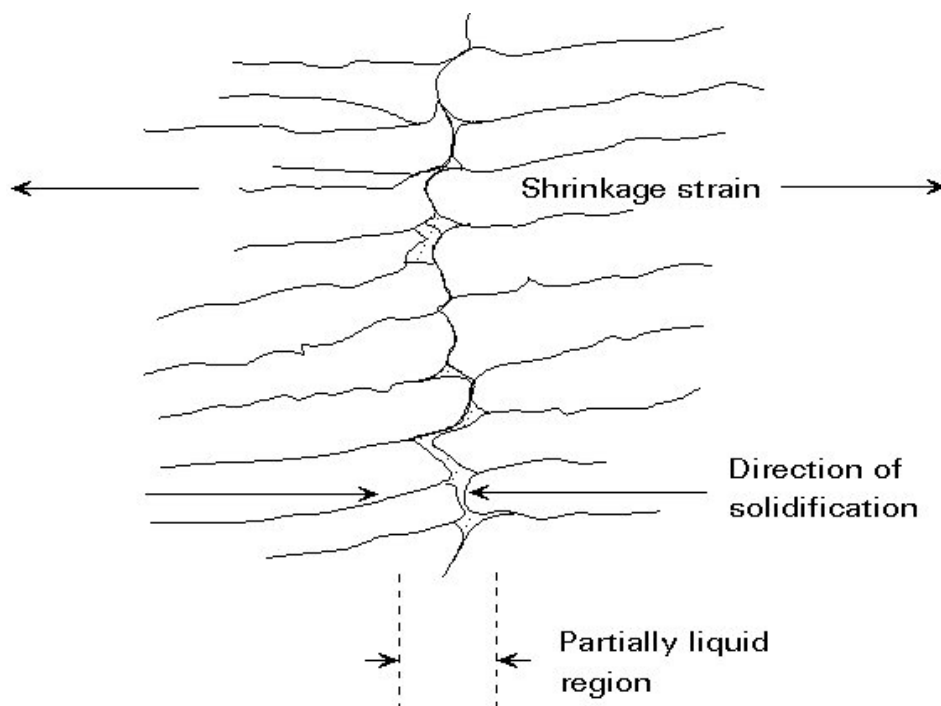
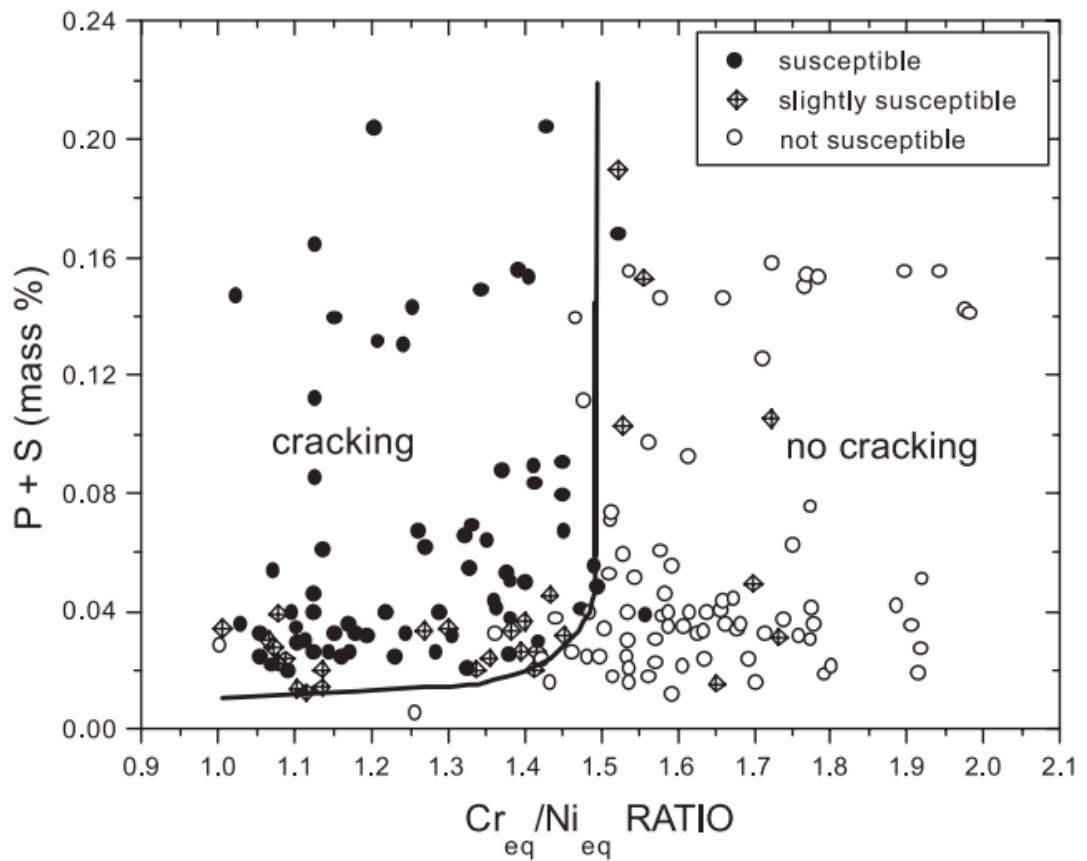


Figure 29. Diagram showing mechanics of shrinkage cracking (University of Ljubljana, 2000)

The mechanics of this type of cracking stems from a solidification front where the strains imposed on the final portion of metal to solidify are sufficient to pull the material apart. Contributing factors to this type of problem are thought to include weld bead size and shape, degree of restraint on the joint, physical properties of the materials, such as shrinkage rates and compositional contents, in particular impurities such as phosphorous and sulphur (TWI Ltd, 2009), (Shankar, Gill, Mannan, & Sundaresan, 2003).

Research conducted by Kujanpaa et al (1979) investigated the potential of shrinkage cracking based on the composition of the weld material and produced a predictive diagram often referred to as the Suutala diagram. The Suutala diagram as seen in Figure 30 shows that the risk of cracking is reduced with low levels of sulphur and phosphorus and also as the Cr_{eq} / Ni_{eq} ratio is increased above a particular level (approximately 1.5). This is representative of the shift in the solidification behaviour from primary austenite, to primary ferrite and so the susceptibility to the cracking type shows a dramatic decrease even at high impurity levels.



Equation 5. Equation to determine the chromium equivalent.
 $Cr_{eq} = Cr + 1.37Mo + 1.5Si + 2Nb + 3Ti$

Equation 6. Equation to determine the nickel equivalent.
 $Ni_{eq} = Ni + 0.31Mn + 22C + 14.2N + Cu$

Figure 30. Suutala diagram for predicting susceptibility to shrinkage cracking from weld metal composition (Kujanpaa, Suutala, Takalo, & Moisio, 1979).

2.3.5 475°C Embrittlement

Iron Chromium alloys containing 15 – 70wt% Cr can be affected by this type of embrittlement phenomena. To become embrittled through this mechanism the material must be held at a temperature in the range of 400°C to 550°C. Theories as to how this embrittlement occurs are not agreed by all, however the predominant theory is that it is due to the formation of a coherent precipitate. Materials within the prescribed compositional range that were held at temperatures below 550°C were found to form a chromium rich ferrite (alpha prime) and an iron rich ferrite (alpha) (Williams & Paxton, 1982). The time held at the aging temperature before the material becomes embrittled was found to vary according the composition of the material, in particular the chromium content. Higher chromium stainless steels become embrittled within a shorter period, although at a higher temperature, than the lower chromium containing stainless steels. For low to medium chromium stainless steels, the material needs to have been held at temperature in excess of 100 hours before the mechanism was detectable, although higher chromium steels exhibited a loss of ductility and toughness after shorter durations. The addition of carbide forming elements, such as molybdenum, niobium and titanium have been found to speed up the embrittlement. This may be as a result of the fact that they free up the amount of chromium available and so effectively raise the chromium content of the stainless steel that can combine with other elements (Lippold & Kotecki, 2005).

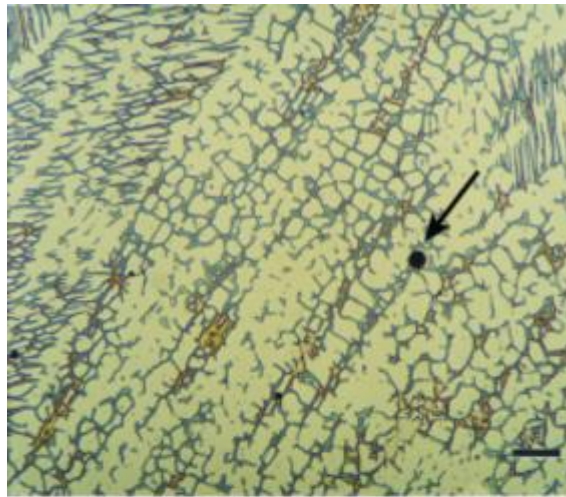
There are reports that the embrittlement effect, termed 475°C, brought about due to the formation of alpha prime results in an effect of the materials resistance to attack by corrosive media. This is thought to be as a result of the selective attack being directed at the iron rich ferritic phase, although this may be as a result of a reduction

in the free chromium content that is available to form the self healing passive oxide layer.

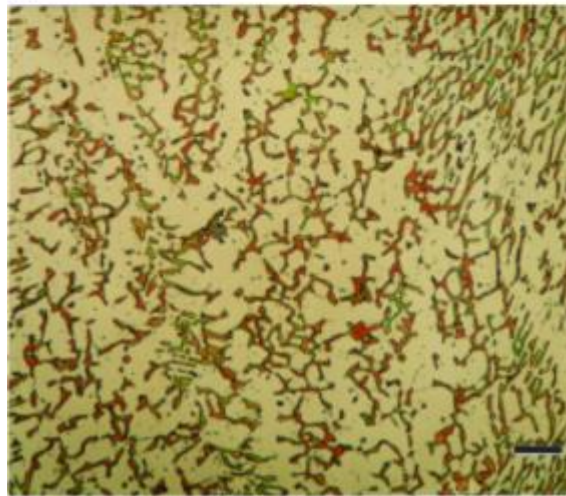
A remedy to the embrittlement is through heat treatment in the range of 550-600°C for a short period. Holding at these temperatures for excessive durations will encourage the onset of the detrimental sigma phase embrittlement, as discussed in section 2.3.6.

2.3.6 Sigma Phase Embrittlement

Sigma phase embrittlement affects iron – chromium alloys containing chromium contents in the range of 20 to 70wt% in environments held at temperatures within the range of 500 -800°C. As with the 475°C embrittlement, materials with higher chromium content's have an increased risk of this type of formation at lower times (typically a few hours). Steels with less than 20% chromium requires exposure in the critical temperature range for hundreds of hours before effects are observable. Examples of sigma phase can be seen in Figure 31 and Figure 32, etched using a modified Murikami's reagent (Vandervoort, Colour Metallography - Film Formation and Interference Techniques, 2004).



(a)



(b)

Figure 31. Use of modified versions of Murakami's reagent to colour delta ferrite and sigma phase in stainless steel welds. (a) Delta ferrite coloured blue and brown in an austenitic matrix in type 312 stainless steel weld metal (as-welded) using modified Murakami's reagent (30 g sodium hydroxide, 30 g potassium ferricyanide, 100 mL water, at 100 °C, or 212 °F, for 10 s). The arrow points to a slag inclusion in the weld nugget. (b) Sigma phase formed in a type 312 stainless steel weld (from the delta ferrite phase) by aging at 816 °C (1500 °F) for 160 h. Sigma was coloured green and orange by etching with Murakami's reagent (10 g sodium hydroxide, 10 g potassium ferricyanide, 100 mL water) for 60 s at 80 °C (175 °F). The magnification bars are 20 µm in length (Vandervoort, Colour Metallography - Film Formation and Interference Techniques, 2004).

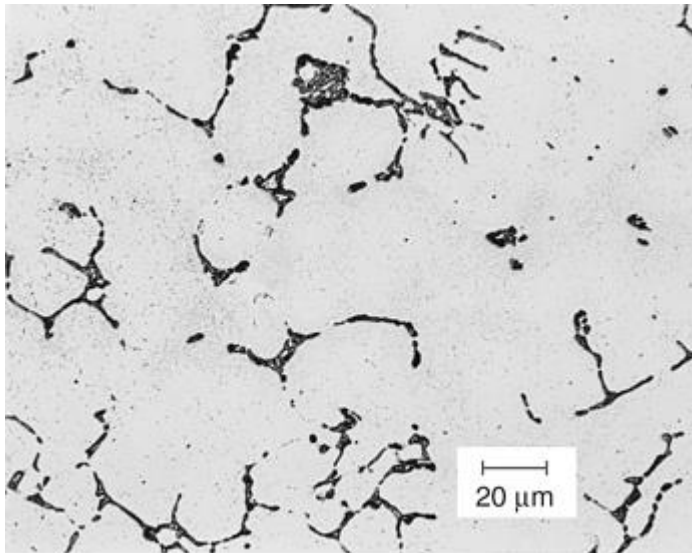


Figure 32. Image showing Sigma phase (Vandervoort, Examination of Microstructures, 2003).

2.3.7 High Temperature Embrittlement

Exposure to temperatures above approximately 0.7 of the steels melting temperature ($^{\circ}\text{K}$) results in an embrittlement phenomenon known as High Temperature Embrittlement (HTE). As the temperatures involved for the instigation of this form of embrittlement are so high, it is rarely experienced through service conditions. The temperatures involved are above those recommended, in particular, for ferritic stainless steels. The manifestation of this type of embrittlement is far more likely to come from the processing of the component/material. In particular it is likely induced through welding as a result of the temperatures involved in the thermal cycle.

The susceptibility to high temperature embrittlement is primarily governed by composition and grain size. The mechanics of embrittlement are through the formation of chromium rich carbides, nitrides or carbonitrides, where precipitates may form in the grains or on the grain boundaries. The location of these precipitates also has influence over the reduction in properties through this type of phenomenon. It

must be noted that stabilised grades do not form this type of embrittlement as easily as the non-stabilised grades.

2.3.8 Liquation

Liquation is an issue that presents more of a problem within the austenitic grades of stainless steel than ferritic. During welding liquation cracking can occur within the heat affected zone or in the weld itself. Within the heat affected zone this type of cracking is produced as a result of liquid films being produced at grain boundaries in partially melted regions. Mitigation from this form of cracking can be made by increasing the amount of ferrite that is formed in this region, reduction of the impurity levels in the stainless steel, reducing the grain size and reducing the heat input during the welding procedure. In welds, the resulting cracks are formed as a result of segregation and are more common in multipass welds due to the repeated thermal cycling. This allows the lower melting point materials that form on the grain boundaries, to melt and then form cracks upon solidification.

2.3.9 Impurity Elements

Certain elements have detrimental effects on stainless steel materials, the most prominent of these are phosphorous and sulphur.

2.3.9.1 Phosphorus

Phosphorus is an element that has been linked with a reduction in the corrosion resistance of a stainless steel and reported to have effect on increasing the likelihood of cracking during the welding process (DuPont, Microstructural Development and Solidification Cracking Susceptibility of a Stabilised Stainless Steel, 1999). In stainless steel it is recommended to have phosphorus levels less than 0.003% (Mathers, Welding of Austenitic Stainless Steel: Job Knowledge 103, 2016).

2.3.9.2 Sulphur

Sulphur is sometimes intentionally added to improve the machinability of the material, although it can result in a detrimental effect on the corrosion resistance of the material and may create problems when welding some of the grades (Lippold & Kotecki, 2005). As with phosphorus there is a recommendation to keep sulphur levels to less than 0.003%, however it has been reported that when sulphur levels get really low (<0.005%) the weld profile changes to a broader profile with less penetration, whereas when levels are above 0.010%, the weld is narrower with deeper penetration (Mathers, *Welding of Austenitic Stainless Steel: Job Knowledge 103*, 2016).

2.3.10 Liquid Metal Embrittlement

Liquid metal embrittlement or penetration is a phenomenon that occurs when stainless steel is in contact with a liquid metal such as zinc or copper (Bailey, 1994). The penetration occurs through the wetting of the molten material on the grain boundaries as can be observed in Figure 33. This results in the flowing of the media down the grain boundaries and essentially creating a crack, which weakens the material. Even if penetration does not completely pass through the material/component it could still dramatically affect the integrity of it under various loading conditions. The importance of this potentially damaging mechanism, whilst joining is that the integration of stainless steels into various components and structures may result in the contact of stainless with copper. For example if the joint is to be brazed using a copper braze material.

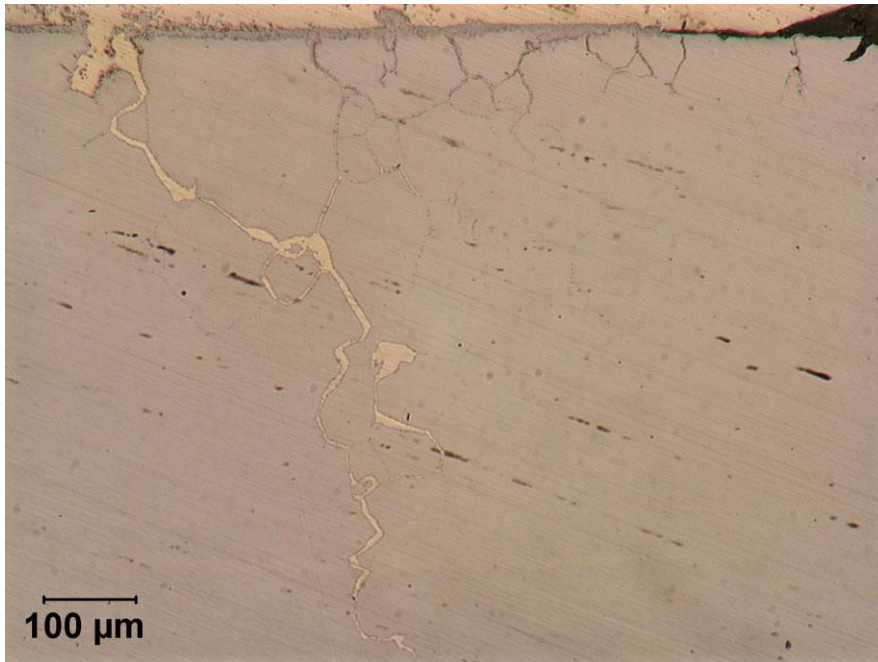


Figure 33. Image showing liquid copper which has penetrated down the grain boundaries of an AISI 304 austenitic stainless steel (Magowan S. , 2006).

The process is often exacerbated by the presence of a stress, be that in the form of an externally applied stress or residual stresses present within the material.

Determination of the presence of liquid metal penetration is made through microstructural observation where either destructively samples are taken, prepared and examined for the presence of the phenomena or the sample can be prepared in situ, normally to a high quality finish with optical examination and the use of replicas to determine any evidence of liquid metal penetration (The Welding Institute Ltd.).

Mechanically, the presence can be found through tensile testing, where in particular, a reduction in elongation , could be an indication of the liquid metal having penetrated the base metal (Burgin, 2008). Alternatively, tables exist which show classic material couplings which have resulted in liquid metal embrittlement. However, these are not definitive or exhaustive.

2.3.11 Stainless steel summary

The ferritic stainless steel grades are restricted in use due to the reduction in mechanical properties as a result of welding. Those particularly sensitive to welding are the non-stabilised grades such as the EN1.4016 and EN1.4003, which are susceptible to the formation of martensite as well as grain coarsening. Therefore due to the environments these materials may operate in it is imperative that the mechanical properties are well understood, including the tensile, hardness, impact and fatigue properties.

2.4 Fatigue

Fatigue is a failure mechanism resulting from some form of cyclic loading regime. This loading may not necessarily be in the traditional sense, of a load applied and then removed, but in the case of thermal fatigue could be as a result of cyclic stresses from the expansion and contraction as a structure undergoes multiple heating/cooling cycles. This could be as seen in the service environment for a typical engine block whilst in this same structure there will be con rods and cam/crankshafts, valves and pistons, all subject to more standard cyclic loading mechanisms; however these are all operating in contrasting environments, where temperature, corrosion products, abrasive particles will all influence the ability to succumb to a fatigue failure. An automotive suspension spring, although not subject to elevated temperatures will have a varied life being exposed to different corrosion products, the loading mechanism will be different for every spring depending on how the vehicle is loaded and the road surface and speed.

There are many failure mechanisms for materials and fatigue is a key one of these that accounts for a high proportion of failures. For some components this can be as high as 80% of failures accountable to a fatigue failure mechanism (Wirsching, 1983). The problem with fatigue as a failure mechanism is that there can be a whole host of factors that can influence a material or components susceptibility to fatigue failure. This can be from the material itself, to the alloying content, surface condition or geometry of a component as well as loading conditions, all of these can have a significant influence.

2.4.1 Fatigue Testing

The testing of a material or component which will operate under a fatigue regime, requires the load to be cycled. The loading sequence used for this can vary, Figure 34 shows some of the fatigue cycles that can be imposed. Figure 34 (a) gives an example of the tension/compression cycle, the material is initially in tension for the first portion of the cycle, increasing in stress until σ_{\max} is reached, then the stress is reduced over a period of time, whereby the sample is subjected to a compressive stress until reaching σ_{\min} where the compressive stress is removed, returning the stress state to zero and completing a full cycle. For the tension/tension loading (Figure 34(b)) the sample remains in tension for the entire cycle. Alternatively it could be compression/compression where the sample would be under compression for the complete cycle. The spectrum loading conditions (Figure 34c) are more attributed to a real component in a service environment, such as an automotive suspension spring.

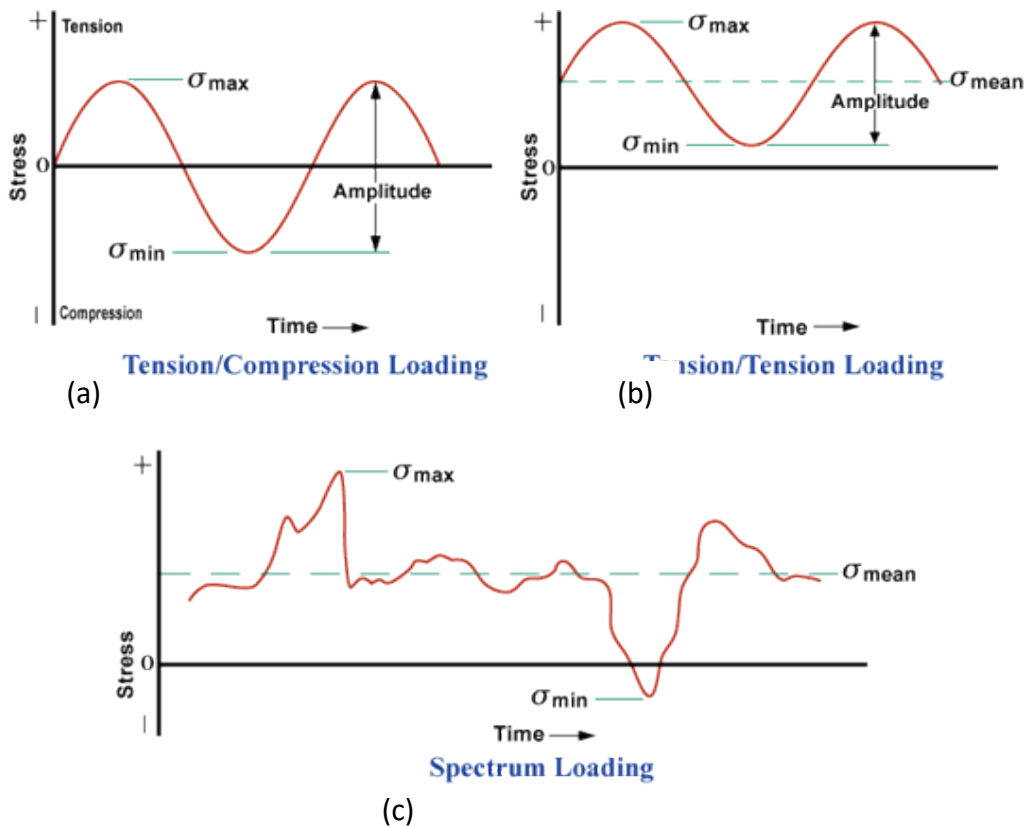


Figure 34. Showing different fatigue cycles. (NDT Resource Centre, 2016)

Mathematically a stress cycle is defined as $\sigma_m \pm \sigma_a$ (with tension stresses being positive and compressive stresses negative), therefore:

Equation 7. Equation to determine the maximum fatigue stress.

$$\sigma_{\max} = \sigma_m + \sigma_a$$

Equation 8. Equation to determine the minimum fatigue stress.

$$\sigma_{\min} = \sigma_m - \sigma_a$$

Equation 9. Equation to determine the mean fatigue stress.

$$\sigma_m = \frac{\sigma_{\max} + \sigma_{\min}}{2}$$

Equation 10. Equation to determine the fatigue stress range.

$$S = 2\sigma_a = \sigma_{\max} - \sigma_{\min}$$

Equation 11. Equation to determine the fatigue stress ratio

$$R = \sigma_{\min}/\sigma_{\max}$$

Where:

σ_m = Mean stress

σ_a = Alternating stress

σ_{\max} = Maximum stress

σ_{\min} = Minimum stress

S = Stress range

R = Stress ratio

(Pook, 2007)

2.4.2 Different types of fatigue testing

There are a number of different methods for fatigue testing a material or component but most fall under three categories; reversed direct stress, reversed plane bending and rotating bending (Frost, Marsh, & Pook, 1974). Although there are other types such as alternating torsion and combined stress (Fatigue Testing, 1986).

It has been found that the fatigue properties can vary across the aforementioned testing types with the fatigue limit varying by as much as 30% (Frost, Marsh, & Pook, 1974), therefore it is vitally important that the fatigue testing that is undertaken is in the form that closely resembles that which would be experienced under service conditions as this allows a better understanding of how the material or component would react in this environment and therefore permit a more accurate prediction of fatigue life and therefore a more effective design.

Further to this the type of fatigue test can be broken down into high cycle or low cycle fatigue testing. The generally accepted differentiation between the two, in terms of cycles would be anything below 10^4 cycles would be classed as low cycle and anything above 10^5 cycles classed as high cycle fatigue testing. As can be seen this is not a clear definition if the number of cycles should fall between 10^4 and 10^5 cycles then by this definition it could be either. In practice the differentiation is made as to whether the material is elastic or plastic under the dominant component of strain (Fatigue Testing, 1986) with low cycle fatigue testing inducing loads that are within the plastic region and high cycle, loads that are within the elastic region of the material.

Reporting of high and low cycle fatigue tests are generally conducted in different ways, with an example of the presentation of low cycle fatigue seen in Figure 35 whereby the data presented is the plastic strain range, as determined by the hysteresis loop

produced under testing against the number of cycles and high cycle fatigue seen in Figure 36, where it is a plot of stress against number of cycles.

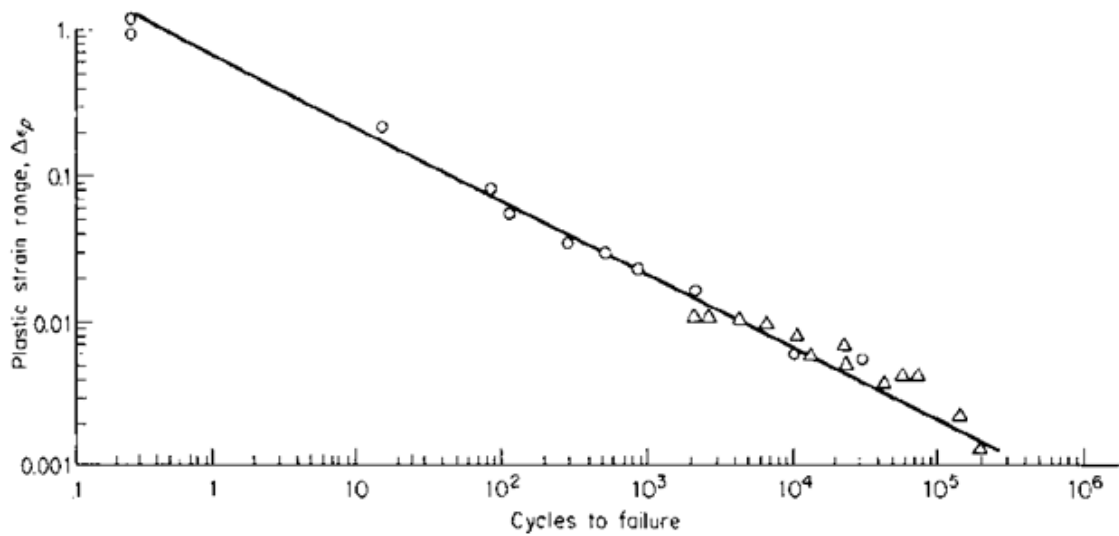


Figure 35. Presentation of data from low cycle fatigue testing (KTH, 2003)

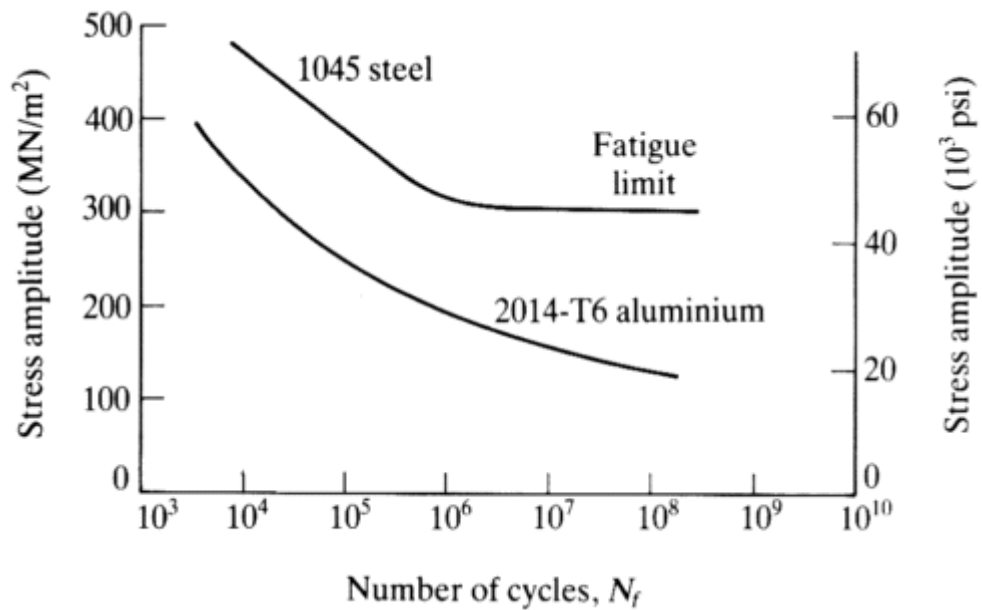


Figure 36. Showing S-N curve typical reporting of high cycle fatigue data (eFUNDA, 2016).

The determination of fatigue properties for a material can be extremely costly and time consuming and therefore methods have been developed to ascertain this information through the use of statistical theory. One such technique is the method

called Staircase Fatigue Testing, sometimes referred to as the up and down method (Grove & Campean, 2007).

The basis for staircase fatigue testing, is that statistically speaking the independent variable associated with a fatigue test is the stress at which it was tested, the discussions being that at the start of the test, the stress is known and the number of cycles to failure is unknown, but once the test is complete the life is known, leaving the stress as the variable. Realistically, the stress is not the independent variable, but rather the formation and growth of a crack. As it isn't possible to test samples under a fixed cycle to failure regime, which would allow determination of a mean strength and standard deviation, the staircase fatigue method and other probit methods have been created to allow such information to be determined (Frost, Marsh, & Pook, 1974).

Within the staircase fatigue testing process a sample is subjected to a particular stress level for a predetermined number of cycles. If the sample fails prior to the required life, then the next sample is tested at a stress level increment below. The particular increment relates to an expected level of the standard deviation (International Council on Combustion Engines, 2009). If the sample survives the pre-set life then the test is stopped, the sample removed and the next sample tested at an increment level above. This is continued for a number of samples, Grove and Campean (2007) suggest 12 to 20 samples, however the creators of this analysis suggested the sample size needed to be 40 to 50 (Dixon & Mood, 1948). Research conducted later determined that even with a sample size of 5 to 10 samples, the analysis is reliable (Brownlee, Hodges, & Rosenblatt, 1953). It is considered that the more samples tested the greater the reliability of the data, therefore a sample size of 25 is normally suggested (Frost, Marsh, & Pook, 1974).

2.4.3 Fatigue Failure Mechanisms

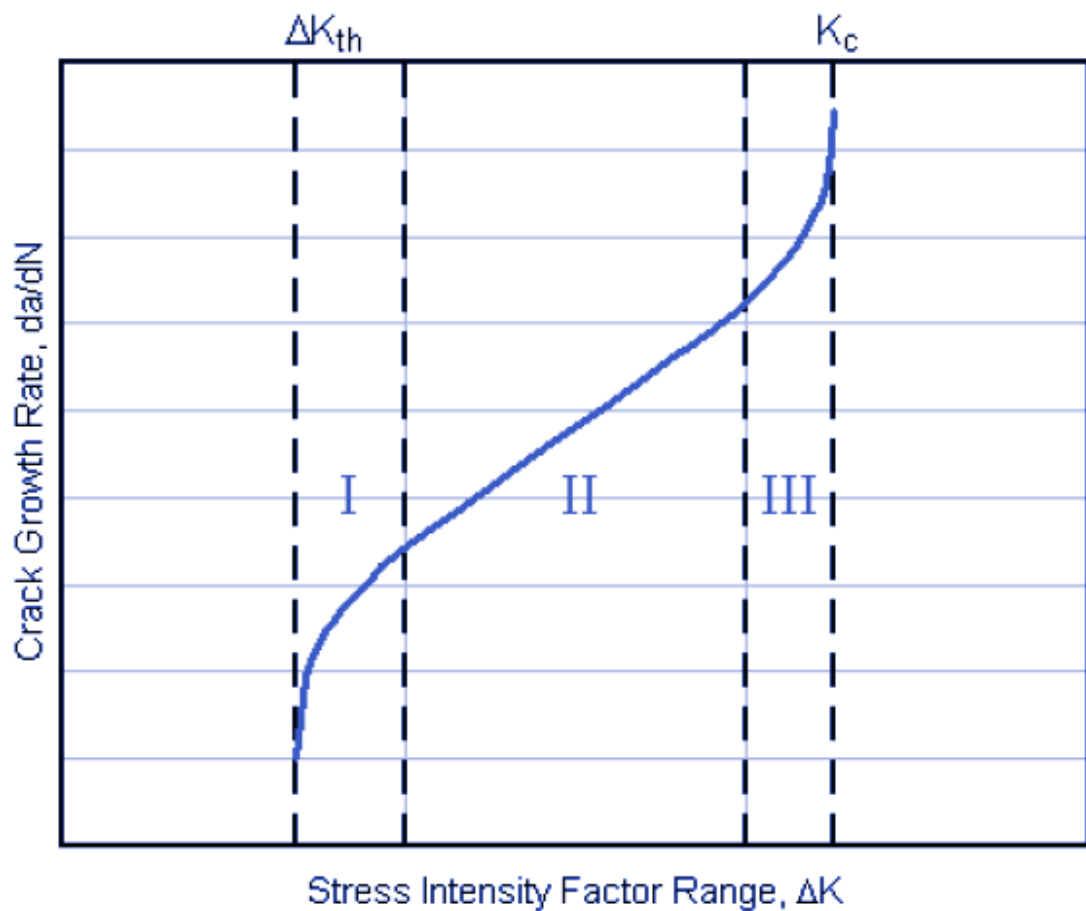


Figure 37. Showing three stages of crack growth rate (Engineers Edge, 2016).

When looking at fatigue failure it must be noted that the fatigue mechanism is not a linear process and can be broken into three distinct regions as shown in Figure 37. The portion of the graph to the left of ΔK_{th} is below the threshold of stress levels for a crack to grow under fatigue or the crack growth is so slow it is impossible to measure. Stage I gives a positive growth of a crack, however the actual determination of this point can be variable and sensitive to metallurgical variations (Pook, 2007). Stage II is the linear portion of the graph and the largest, which indicates stable crack growth. This portion of the graph can be modelled using the Paris equation (ASM International, 2008);

Equation 12. Paris equation to model crack growth.

$$\frac{da}{dn} = C(\Delta K)^m \text{ (inch/cycle)}$$

Where;

a = crack size (inches)

n = number of cycles

C = constant

m = constant

ΔK = stress intensity parameter range

Within the stage III portion of the graph the crack growth speeds up and eventually a tensile overload failure will occur.

Fatigue crack initiation, stems from plastic deformation of the grains, through the process of slip. This process can occur at lower loads than the yield stress of the material and results in the formation of microcracks within the grain. The process of slip occurs on favourably orientated planes at the maximum shear stress, which under uniaxial tension is 45°. It must be considered that slip takes place on a number of parallel planes resulting in extrusions and intrusions at the sample surface as shown in Figure 38. Eventually these stress concentrators create a crack to form which subsequently travels transgranular as the slip lines go through the grains (Pook, 2007). Eventually the stress field at the crack tip dominates and then the crack growth direction changes from 45° to perpendicular to the principle stress, this is the point when the crack changes from stage I to stage II as seen in Figure 37 and then the crack growth process changes to a continual blunting and sharpening as seen in Figure 39. This process then creates a distinguished surface with regular peaks and valleys as can

be seen in Figure 40, these are known as striations and can only be observed at high magnifications. It is considered that each striation is related to each fatigue cycle (ASM International, 2008), however it has been reported that this is not always the case and one striation may be as a result of a number of cycles, in the order of tens of thousands (Gross & Lampman, 1996).

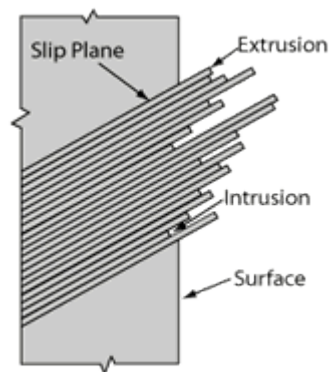


Figure 38. Figure showing persistent slip bands. (NDT Resource Centre, 2016)

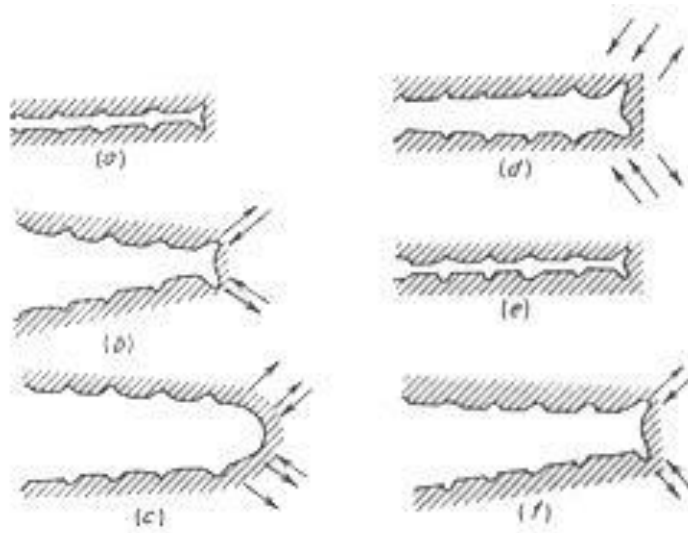


Figure 39. Showing fatigue crack propagation (Key to Metals AG, 2005)

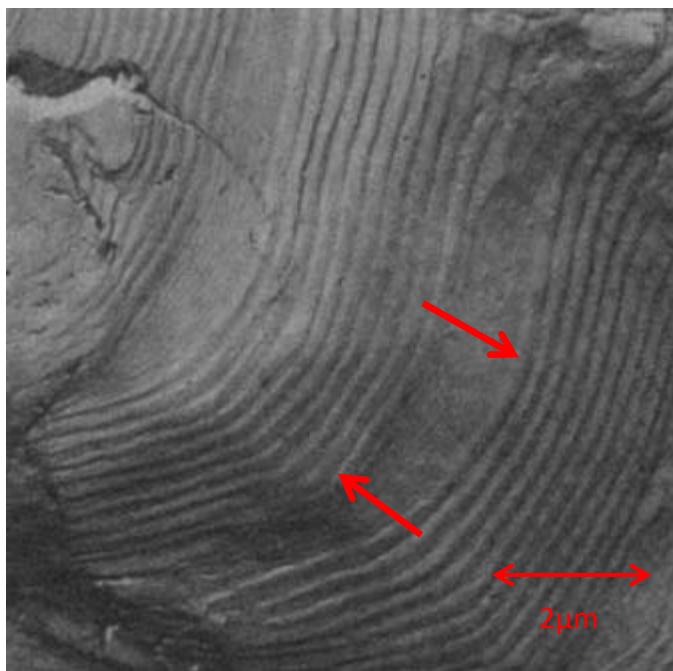


Figure 40. SEM image showing fatigue striations (ASM International, 2008).

2.4.3.1 The Effect of the Environment on Fatigue Life

The environment in which the fatigue is experienced can have significant impact on the properties of the material. The fatigue properties of a material under vacuum can be different to those in normal atmospheric conditions. The reason for this is reported to be that the growth rates of cracks is smaller under a vacuum, with reported levels for crack initiation being 1 to 2 orders of magnitude slower under vacuum than in air (Lukas, 1996). Therefore as reported by Frost et al (1974) preventing the atmosphere from reaching the specimen surface can increase fatigue properties. As well as gas interactions there is also the potential for chemical interaction thereby transforming the fatigue from a mechanical induced failure to one that also has some chemical assistance, this may be as simple as humidity levels in the atmosphere, where it has been shown on some aluminium alloys that the fatigue strength is lower when the humidity levels are higher (Frost, Marsh, & Pook, 1974). With the introduction of other environments such as an aqueous substance that may not corrode the material under a static condition, due to a protective layer that forms, for example in the case of stainless steel in an oxygen containing atmosphere, under fatigue conditions this layer may be broken allowing the corrosive media to react with the underlying material and therefore cause cracks to develop and propagate at lower stress levels than those operating within normal air environment without the additional chemical element (Frost, Marsh, & Pook, 1974).

Temperature has been found to have a significant effect on the fatigue properties, with testing conducted on a number of different materials at cryogenic temperatures and the results found a general improvement in retarding the crack growth in the near threshold region (McEvily, 1996). Research conducted on some titanium alloys found

that the fatigue properties were improved at elevated temperature (175°C) rather than at room temperature (25°C), and this was identified as being in part due to crack closure (Albertson, Stephens, & Bayha, 1997). Other research (Lim, Jeong, & Keum, 2003) identified that with a P92 Steel, up to a particular temperature there was no change in the fatigue properties however once a critical threshold temperature was exceeded then the fatigue performance of the material rapidly decreased.

2.4.3.2 Surface Condition

The surface condition of the material is paramount to fatigue initiation as it is considered that fatigue crack initiation in a metal is at the surface (Pook, 2007). Therefore the surface condition plays an important role in the fatigue life of a material. Firstly the surface profile is an important factor, as described in 2.4.3 the initial crack on a smooth surface initiates from the extrusions and intrusions as a result of dislocation motion, therefore by creating essentially coarser extrusions and intrusions through having a rougher surface can have a significant effect on the fatigue life of a material. In work conducted by Bayoumi and Abdellatif (1995) it was found that there was a significant decrease in the fatigue life when the surface finish was modified from 0.45µm R_a to a value of 1.8µm.

Stress at the surface also has an effect on the fatigue life of the material. Compressive stresses at the surface, induced by shot peening or a softened/hardened layer through a decarburisation process or carburisation process effects the ability for cracks to form at the surface layer (Pook, 2007). Research conducted by Mirzazadeh and Plumtree (2012) found that the effects associated with shot peening were varied, in certain instances tested, it had positive, neutral and negative effects on fatigue properties,

whereas the general consensus with processes such as shot peening is that it is beneficial in the enhancement of fatigue properties of a material (Battelle-Columbus, 1996) through the introduction of residual compressive stresses into the surface of the material.

2.4.4 Key factors affecting fatigue performance of welds

There is general agreement about the factors that affect the performance of a weld under fatigue conditions and the effect of each is something which comes under discussion, however these factors are:

- Applied stress amplitude
- Mean and residual stresses
- Material properties
- Geometrical stress concentrators
- Size and location of welding defects

(Lawrence, Dimitrakis, & Munse , 1996)

One of the factors that can affect the fatigue life of welds is the angle between the parent material and the weld reinforcement, Harris and Syers (1979) present data that demonstrates the effect of the angle between the two and how that affects the fatigue strength (see Figure 41). As can be seen a decrease in angle and therefore a greater stress concentrator, has a detrimental effect on the fatigue properties of the material. The two conditions shown, one for a machined surface and one which has a mill scale

on the surface have a parallel effect for this change in angle which demonstrates that although the surface finish has an effect of its own, the change in angle effects both in the same way and at similar rates. The study examined the effects on fatigue strength exceeding 2×10^6 cycles for the change in reinforcement angle and it was shown that for a machined plate, reducing the angle from 180° to 120° reduces the fatigue strength by approximately 67%, therefore a flatter weld bead enhances the fatigue properties of the material.

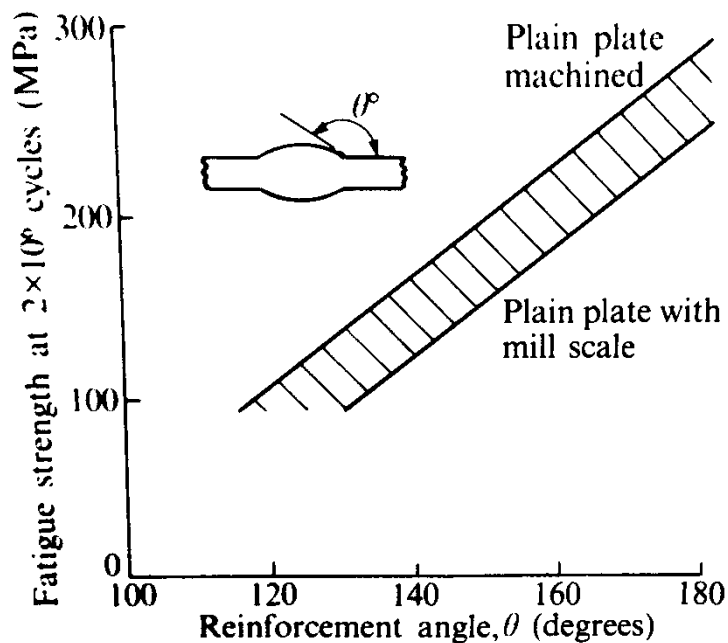


Figure 41. Showing relationship between parent/weld interface angle and fatigue strength (Harris & Syers, 1979).

Another component that has been identified as having a significant role in the fatigue life of a weld is the defects present within the weld. This is not just constrained to defects themselves but the size, shape and concentration of these defects as these traits can all play a significant part in the life of a component under cyclic loading conditions. Results from investigations looking at the effect of defect length and the

percentage of defects within butt welds shows a negative correlation on fatigue properties. For the defect length, the presence of the defect, reduces the endurance limit of the weld, this reduction is greater with a larger defect (Lieurade, 2008).

In work conducted by Ashcroft (2008), on Cold Metal Transfer welded joints, the same was found. In this work the angles were measured and subtracted from 180°, which is why in this work a seemingly opposite trend is seen in Figure 42. Therefore the increase in angle measured from the parent to the weld reinforcement (in this instance the root penetration) is shown to give a benefit in terms of the fatigue life of the component, with a change in 20° changing the number of cycles to failure from 50,000 to over 2,000,000 (test was stopped at 2 million cycles).

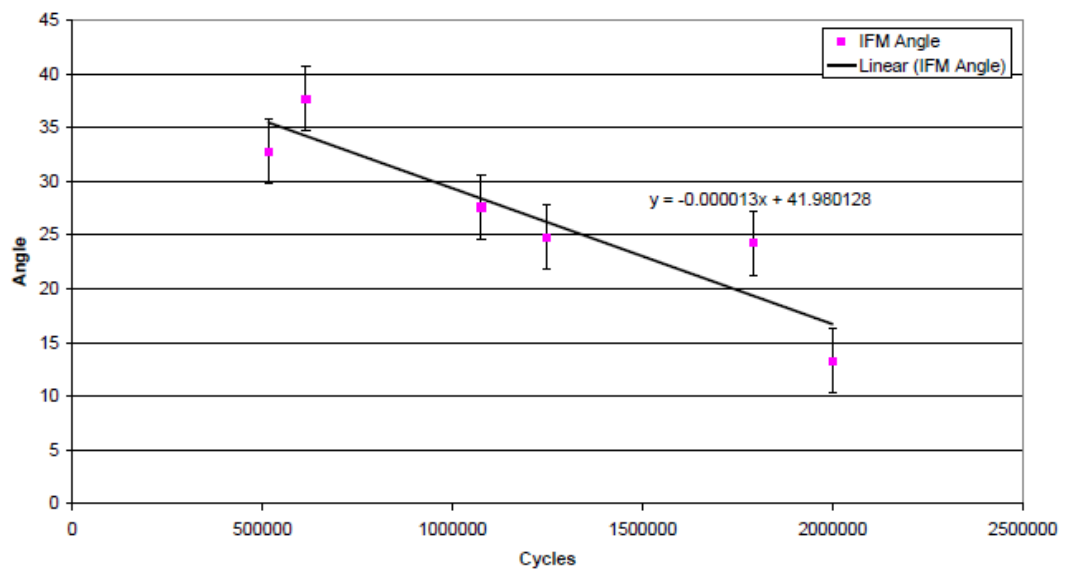


Figure 42. Graph showing relationship between penetration root angle and fatigue life for similar thickness CMT welds (Ashcroft, 2008).

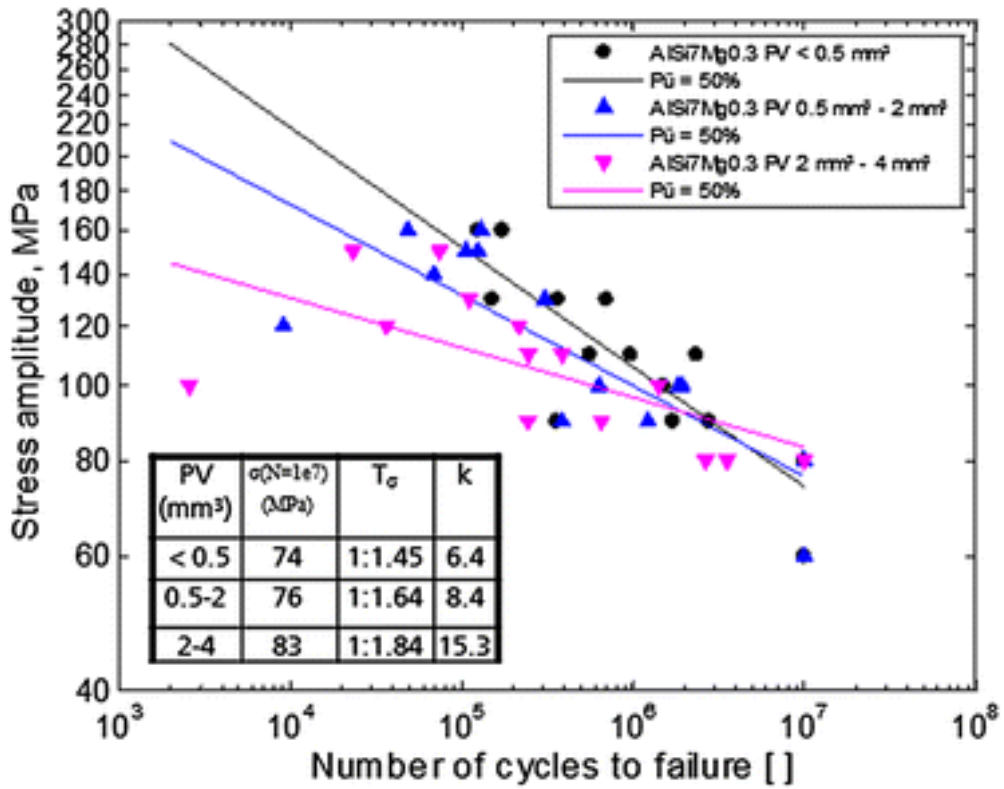


Figure 43. 9—S–N curves of the investigated specimens with different maximum pore volumes (PV) for A1Si7Mg0.3 (Tijani, Heinreitz, Stets, & Voigt, 2013)

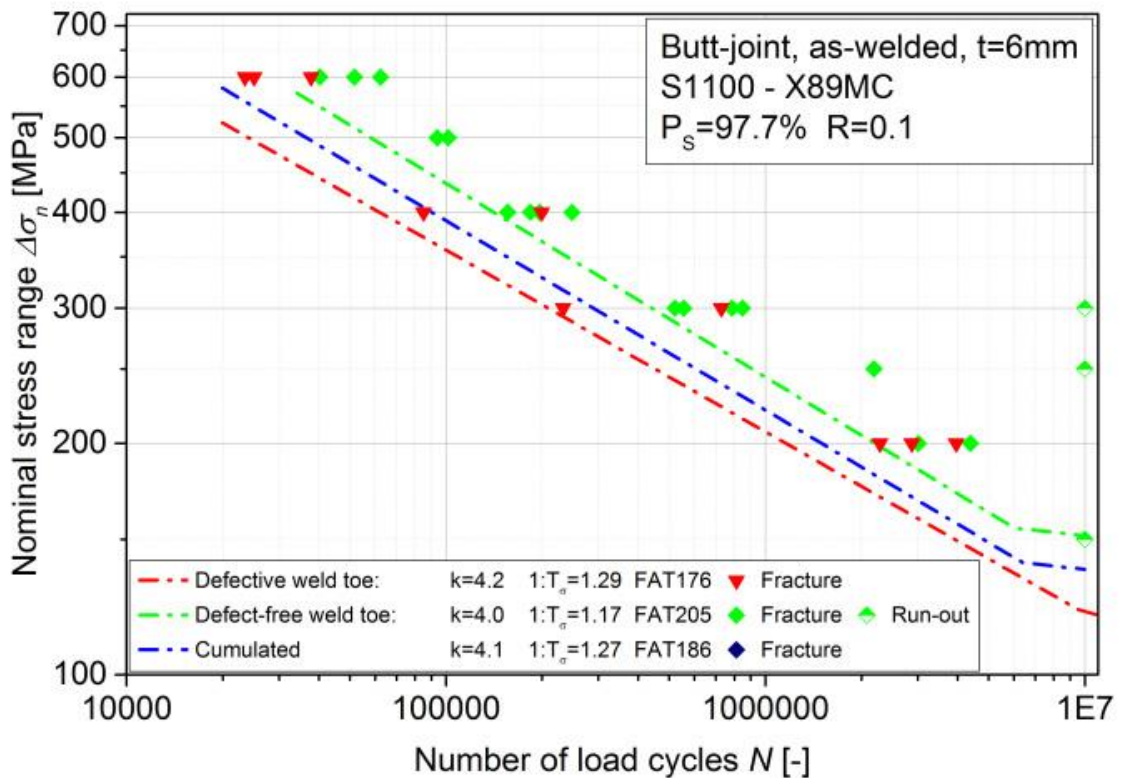


Figure 44. Fatigue test results for defect-free and defective 6mm high strength steel parent specimen (Ottersbock, Leitner, Stoschka, & Maurer, 2016)

In the study reported by Tijani et al (2013) there was an examination of the volume of defects within an aluminium alloy and the effect it had on the endurance limit. This work can be seen in Figure 43 where 3 different defect percentages were tested, pore volumes of <0.5, 0.5-2 and 2-4mm³. The results from this were that increasing the percentage of defects within the material had a negative impact on the subsequent fatigue properties. Other work (Ottersbock, Leitner, Stoschka, & Maurer, 2016) conducted on 6mm thick, high strength steel welds with and without defects also identified a reduction in the fatigue properties when defects were present, as seen in Figure 44.

2.4.5 Models for fatigue life prediction

In work conducted by Ashcroft (2008) looking at Cold Metal Transfer welded joints, the following model was proposed to predict the fatigue life of these joints based on a relationship between the weld root angle and the number of cycles to failure.

Equation 13. Ashcrofts model for fatigue life prediction against root angle.

$$\theta = -1.3 * 10^{-5} x + 41.98$$

Where,

θ = angle at root penetration (°)

x = fatigue life in cycles

2.5 Summary of the Literature

As have been discussed there are a number of different welding techniques that have advantages and disadvantages and a wide range of parameters within each of those processes that can have effect on the integrity of the final joint. One quantifiable measure of a weld is with the heat input, as this can have a considerable effect on the final joint in particular the HAZ. The arc efficiency factor has been questioned previously which ultimately may skew results if CMT is more efficient than MAG welding however the determination of this is outside the scope of this research.

The effects of porosity in the weld has been shown to reduce the fatigue life of a component and relationships have been drawn between weld root angles and fatigue endurance and these issues will be of interest in this research.

The use of ferritic stainless steels is limited due to the detrimental effects associated with welding, such as a reduced toughness owing to grain growth in the HAZ, phase transformations in the lower alloy content grades, reduction in corrosion resistance, therefore with a welding technique such as CMT that in principle induces less heat into the joint, should therefore minimise the detrimental effects associated with the heat. The following work investigates the welding of ferritic stainless steel using the CMT process and compares with the MAG welding process.

3 Experimental Procedure

The following section describes the, materials and equipment used and procedures followed for the research conducted.

3.1 Materials Used in the Research

A number of materials have been used for the purposes of this research. The parent materials used were all ferritic stainless steels as seen in Table 4. However other materials have also been used for the weld consumables and for the shielding gas, these are described below, and the chemical compositions for the materials can be seen in Table 6.

3.1.1 Parent Materials

A list of the parent materials and thicknesses used in this work can be seen in Table 4 and the mechanical properties for the grades in Table 5.

Material Grade	Thickness (mm)
1.4016	1.5
1.4016	2
1.4509	2
1.4521	1.5
1.4003	3.8
1.4003	5.8

Table 4. Materials and thicknesses used in the research.

Outokumpu typical values					EN, min. values, RT				ASTM, min. values, RT			
Outokumpu	R _{p0.2} MPa	R _{p1.0} MPa	R _m MPa	A %	No.	R _{p0.2} MPa	R _m MPa	A ₅ %	No.	R _{p0.2} MPa	R _m MPa	A _z %
4003	340	375	500	25	1.4003	320	450	20	S40977	280	450	18
4512	290	310	470	31	1.4512	220	380	25	S40910	170	380	20
4016	330	360	500	26	1.4016	280	450	20	S43000	205	450	22
4510	300	330	460	31	1.4510	240	420	23	S43035	205	415	22
4509	330	360	480	30	1.4509	250	430	18	S43932	205	415	22
4521	370	400	530	28	1.4521	320	420	20	S44400	275	415	20

Table 5. Mechanical properties of ferritic stainless steels at room temperature (Outokumpu, 2011).

Material	C (%)	Mn (%)	Si(%)	Cr(%)	Ni(%)	Nb(%)	Mo(%)
1.4016	0.018	0.315	0.248	17.216	0.232	0.046	0.098
1.4509	0.002	0.483	0.558	19.893	0.334	0.3	0.062
1.4521	0.013	0.512	0.457	19.526	0.29	0.28	1.087
1.4003	0.010	1.42	0.27	11.0	0.4	-	-

Table 6. Chemical analysis data of the parent materials used within the project.

3.1.2 Welding Filler Materials

The filler material recommended for the joining of ferritic stainless steel and therefore used in the research included:

1.0mm diameter AISI 308L-Si

1.2mm diameter AISI 308L-Si

Both of these wires are of the same chemical composition and this analysis can be seen in Table 7, the material is an austenitic stainless steel.

Element	C	Cr	Si	Ni	Mn
Composition (%)	0.02	20	0.85	10.5	1.8

Table 7. Composition of AISI 308L-Si filler material (Avesta Welding, 2006).

3.1.3 Shielding Gas Used in the Project

High purity shielding gas mixtures used in the work included:

1% Oxygen, 99% Argon

2% Oxygen, 98% Argon

2% Carbon Dioxide, 98% Argon

3.2 Comparison Trial between CMT & MAG Welds in Different Grades and Thicknesses

Pulsed Metal Active Gas (MAG) welds were produced at the Outokumpu research facility in Tornio, Finland. Parent material from the same batch as shown in Table 6, was sent to the ACES welding laboratory at Sheffield Hallam University to allow comparable welds to be produced using the Cold Metal Transfer (CMT) process, with and without pulsed arc.

Stainless steel grades used in the trials were 1.4016 (1.5mm thick), 1.4509 (2mm thick) and 1.4521 (1.5mm thick). The filler wire used in all cases was 1mm diameter, 308L.

The shielding gas used in the manufacture of the CMT welds for this part of the work, was argon with 2% oxygen and the joint gap was held constant at 0.5mm. All MAG welds were produced using a shielding gas of argon with 2% CO₂ and the joint gap set between 0.5 and 1mm.

3.3 CMT Welding Trials to Examine the Effect of Variation of Welding Gap & Speed to Reduce Heat Input

In Gas Metal Arc Welding (GMAW) the filler wire and parent materials, under the power of the arc, melt and fuse together. The welding gap therefore will have an effect on the amount of energy required to achieve sufficient melting of the parent material to ensure full penetration. The smaller the welding gap the more parent material will need to be melted. Additionally published data states that variation of the torch angle affects the level of penetration within a weld and that welding backhand (with the electrode directed away from the direction of travel) will increase the penetration of the weld (American Welding Society, 1991) possibly allowing a reduction in the heat input of the joint to be made. Accordingly a trial was conducted at Sheffield Hallam University, using 2mm thick, 1.4016 material and followed up using 2mm thick 1.4509, to determine the minimum heat input achievable with different joint gaps and torch angles, whilst still maintaining complete penetration of the joint. The amount of parent material available allowed trials at three different welding gaps, values of 1mm, 1.15mm and 1.25mm were chosen. Torch angles of 15° lead (forehand) and 15° drag (backhand - described within the report as -15°) were used. Based on earlier experience, welds were produced at differing torch traverse speeds of 762, 1016 and 1270 millimetres per minute and the welding power adjusted in an attempt to maintain penetration, whilst minimising the power used to produce the joint.

3.4 Trial to Determine the Consistency of Welds Produce Using CMT Process

As the effect of the CMT variables is not well known a trial was conducted to allow assessment of these and determine the effect on changing variables would have on the consistency of the weld. The shielding gas used for all welds produced in this trial was Argon with 1% O₂ and the filler wire was 1mm diameter 308L Si.

A 2.5m x 1.25m sheet of 2mm thick, 1.4016 was marked out into sections 200mm long X 120mm wide for sectioning and each coupon was identified in terms of orientation and position relative to the uncut sheet. This allowed the sheets to be welded back to the same piece they were originally joined to, prior to sectioning. The reason for this was to eliminate any variations which may occur across the plate in terms of dimensions, microstructure and or composition.

Assessment was made of the effect and consistency of a number of parameters which can be seen in Table 8. These settings were determined for the wire feed speed by the power used to produce similar fully penetrated welds in previous work (Magowan S. , 2010), with the 3.5m/min, wire feed speed, having provided sufficient power to produce a fully penetrating weld. The 4.5m/min, was set as a base as it was found in previous work that this level of power consistently provides fully penetrating welds and the 5.5m/min to allow comparison when providing too much power. At these settings the torch angle was set to drag (-15°), the pulse correction and arc length correction set to zero and the traverse speed set to 1.016m/min, as can be seen in Table 8. For the rest of the trials the variation in parameters had the wire feed speed set to 4.5m/min as this then allowed the effect of changes in each variable to be identified.

Setting	Wire Feed Speed			Arc Length		Pulse		Traverse		Torch
	Slow	Average	Fast	Min	Max	Min	Max	Slow	Fast	Angle
Variable										+15
Wire Feed (m/min)	3.5	4.5	5.5	4.5	4.5	4.5	4.5	4.5	4.5	4.5
Traverse Speed (m/min)	1.016	1.016	1.016	1.016	1.016	1.016	1.016	0.762	1.27	1.016
Arc Length Correction	0	0	0	-30	+30	0	0	0	0	0
Pulse Correction	0	0	0	0	0	-5	+5	0	0	0
Torch Angle °	-15	-15	-15	-15	-15	-15	-15	-15	-15	+15

Table 8. Table showing variation of each of the ten settings used in the CMT consistency trial (Boulding, The Effects of Parameters and Consistency of Cold Metal Transfer Welded Ferritic Stainless Steel Joints, 2012).

For each of the settings six welds were produced, with the exception of the traverse speed setting at 1.27m/min, where only five welds were made and the ALC setting at -30 where seven welds were produced. The reason for the variation in number of welds was to permit data logging equipment to be used whilst welding.

One of each of the welds, for each setting was monitored during the welding, using a fully calibrated Arc Logger Ten (ALX) weld data logger, serial number 0138 manufactured and subsequently calibrated by The Validation Centre, Great Yarmouth.

Calibrations of this type of equipment last only for 6 months. Parameters that are recorded through the use of this equipment include:

- Voltage (V) (via connection to the machine circuitry)
- Current (A) (inductance from the earth return lead)
- Traverse speed (mm/min) (sensor connected to traverse equipment)
- Wirefeed speed (m/min) (sensor connected to filler wire between reel and push rollers)

The welds were then sectioned, with a targeted six samples from each weld, the sampling position can be seen in Figure 45 identified by the red lines.

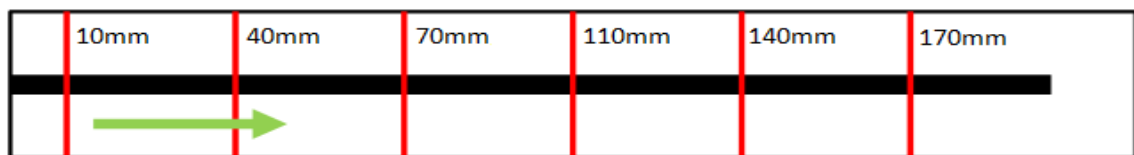


Figure 45. Sectioning of weld plan, sections taken at 10mm, 40mm, 70mm, 110mm, 140mm and 170mm. Green arrow shows welding direction (Boulding, The Effects of Parameters and Consistency of Cold Metal Transfer Welded Ferritic Stainless Steel Joints, 2012).

Each sample was then microstructurally assessed with measurements made of, Heat Affected Zone (HAZ) width, weld cap height and width and grain size in the HAZ. There was also a visual assessment made of the level of penetration at the root of the weld.

3.5 EN1.4003 CMT/MAG Welding Comparison Trial Comparing Microstructure and Mechanical Properties.

A trial was created on the basis of comparing the effects on the parent material of welding with CMT and welding using the MAG technique. CMT welds were optimised at Sheffield Hallam University on the 3.8mm & 5.8mm thick EN1.4003 grade material. The MAG welds for optimisation were created by Outokumpu Tornio, Finland and assessed at Sheffield Hallam University. The comparison MAG welds were then replicated at Sheffield Hallam University, using the optimised parameters identified previously.

The parameters used for all these welds can be seen in Table 9. For the CMT equipment the Pulse correction factor is a unit less parameter, which can be varied from -5 to +5, adjustment from the lower value to higher value increases the peak current of the pulsed current.

Samples	Pulsed	Torch Traverse Speed (mm/s)	Plate gap (mm)	Current (A)	Voltage (V)	Wire Feed Speed (m/min)	Arc Length Correction (%)	Pulse Correction
CMT 3.8mm	Yes	8	1.4	144	19	5	10	+5
CMT 5.8mm	Yes	6	1.9	161	20	5.8	10	+5
MAG 3.8mm	Yes	6.92	1	214	23.5	7.3	-30	+5
MAG 5.8mm	Yes	7.97	1.88	229	24.3	7.8	-30	+5

Table 9. Welding parameters used in the EN1.4003 CMT/MAG comparison trial.

3.6 HAZ Thermal Cycle Simulation Trials

To identify key temperatures and times at temperature, where microstructural changes take place for the EN1.4003 material a series of trials was conducted which involved heating 25mm X 25mm X 5.8mm samples up to particular pre-determined temperatures in an attempt to identify the temperature at which phase change from ferrite to austenite began to occur and also the temperature and time for a given temperature at which grain growth was detected.

Samples were loaded into a muffle furnace at temperatures ranging from 700°C to 1200°C and held from times of 20 mins, to 6 hours followed by a quench. The specific temperatures can be seen in Table 10.

Temperature (°C)	Duration (mins)	Cool
700	20	WQ
700	30	WQ
740	120	WQ
747	20	WQ
750	30	WQ
750	120	WQ
758	20	WQ
760	30	WQ
760	120	WQ
769	20	WQ
770	30	WQ
770	120	WQ
779	20	WQ
780	30	WQ
790	20	WQ
790	30	WQ
800	20	WQ
800	30	WQ
800	120	WQ
800	120	Furnace cool
800	360	30°C/hour
850	30	WQ
900	20	WQ
900	30	WQ
900	360	30°C/hour
910	30	WQ
920	30	WQ
930	30	WQ
940	30	WQ
950	30	WQ
1000	20	WQ
1000	30	WQ
1000	360	30°C/hour
1100	20	WQ

Table 10. Showing heat treatment temperature, durations and method of cooling for samples of 5.8mm thick EN1.4003 (where WQ = Water Quenched).

Once key temperatures were identified, following hardness testing and microstructural evaluation (microstructure and grain size) showed a change to that of the parent, then a number of non-standard Charpy impact specimens (5.8 x 10 x 55mm) were subjected to the same heat treatment cycle and then subsequently tested to identify the effect on impact properties. The samples had to be non-standard as the thickness of the parent material limited one of the dimensions, therefore the standard size of 10 x 10 x 55mm could not be created.

3.7 Process for the Creation of all CMT Welds & MAG Welds created at Sheffield Hallam University using EN1.4003 Grade Stainless Steel Parent Material in 3.8 & 5.8mm Thicknesses

Following the welding consistency trials and the trials to optimise process parameters, the welds created for the research were consistently produced in terms of the procedures and equipment used, this information is described below.

3.7.1 Description of the Welding Test Coupon

The weld coupons used for the welding trials were 120mm wide and either 200mm or 400mm long, with the weld being made in the longer dimension as per Figure 46. The rolling direction was maintained parallel to the 120mm dimension on all welds produced at Sheffield Hallam University.

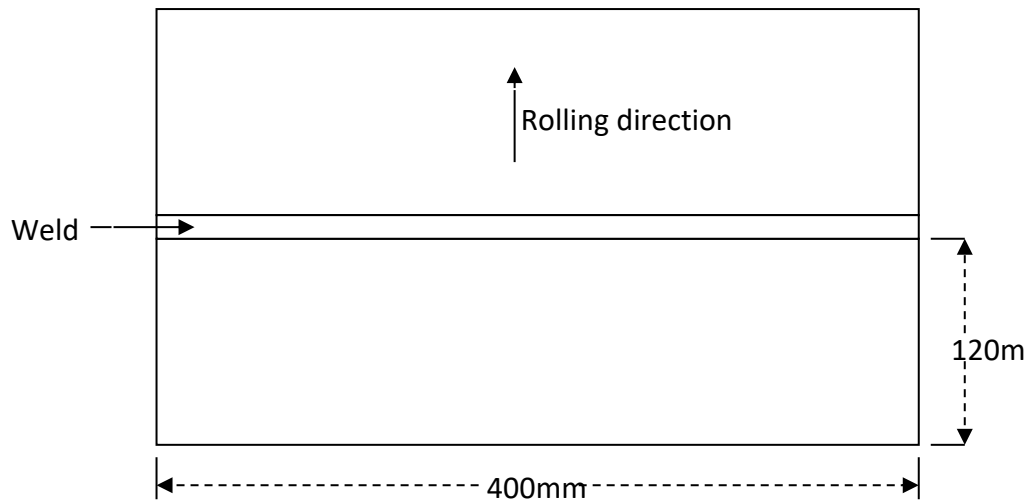


Figure 46. Schematic of parent plate size and setup for all CMT & MAG welded samples the plate length was either 400mm as indicated above, or 200mm.

3.7.2 Equipment Used to Create the Welds and Monitor the Welding

Parameters

The information that follows details the equipment used during the manufacture and monitoring of the welds created during the work. The tractor and track combination was used for the work conducted on the thinner grades of stainless and the robot arm was used for the work conducted on the 3.8 and 5.8mm thick materials.

3.7.2.1 CMT

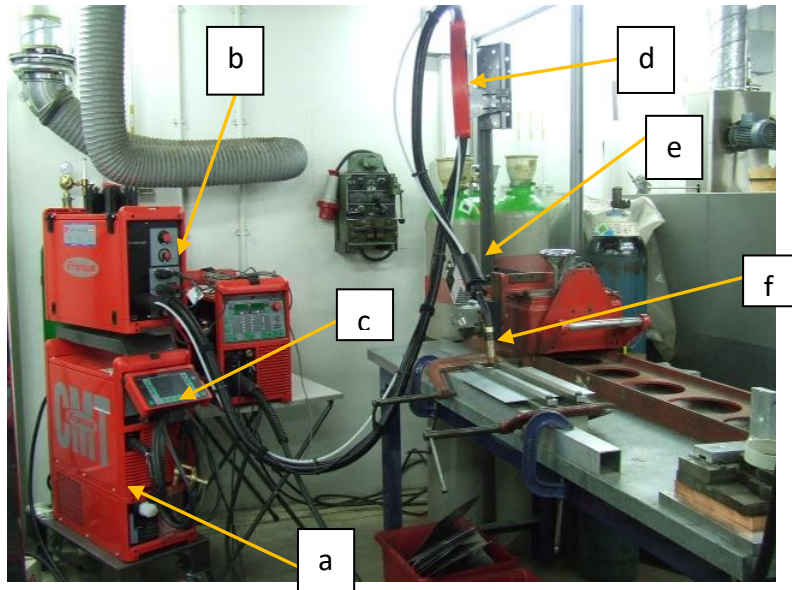


Figure 47. Showing the CMT welding equipment at Sheffield Hallam University.

The Cold Metal Transfer (CMT) welding equipment comprises of a power source as seen in Figure 47 as (a), a wire feed unit (b) the remote pendant that permits the user to alter the parameters and create welding programs (c), the wire buffer which allows excess wire to be accommodated in the hose leading to the torch (d) the torch pack which has the incorporated motor to drive the wire forwards and backwards (e) and the welding nozzle and contact tube (f).

3.7.2.2 Tractor/Track



Figure 48. Image showing tractor and track used to traverse the welding torch.

The welding tractor and track as can be seen in Figure 48 with the welding torch attached, allows the user to set a traverse speed so that upon releasing the clutch, the tractor would move along the track at the predetermined speeds. This facilitates the manufacture of welds at predetermined traverse speeds. The traverse speed range of the equipment was from 0mm/min up to a maximum of 1270mm/min. The angle of the torch was readily adjusted via the clamping mechanism to the tractor and for this element of the research was altered from -15° to $+15^{\circ}$ in the orientation of the weld.

3.7.2.3 Robot Arm



Figure 49. Image showing ABB robotic arm used in some of the CMT and MAG welding trials.

The ABB IRB1600-5/1.45 robot arm seen in Figure 49, links up to the CMT welding equipment so that within the program of the robot it can call up the welding settings when required. The software used for the control of the robot is ABB Robotware version RW5.11_0160. The robot has a 1.45 metre reach and can support a welding torch up to 5kg, with welding speeds upto 1.8m/second, it can maintain an accuracy of +/- 0.05mm (ABB, 2007).

3.7.2.4 ALX - Weld Monitoring

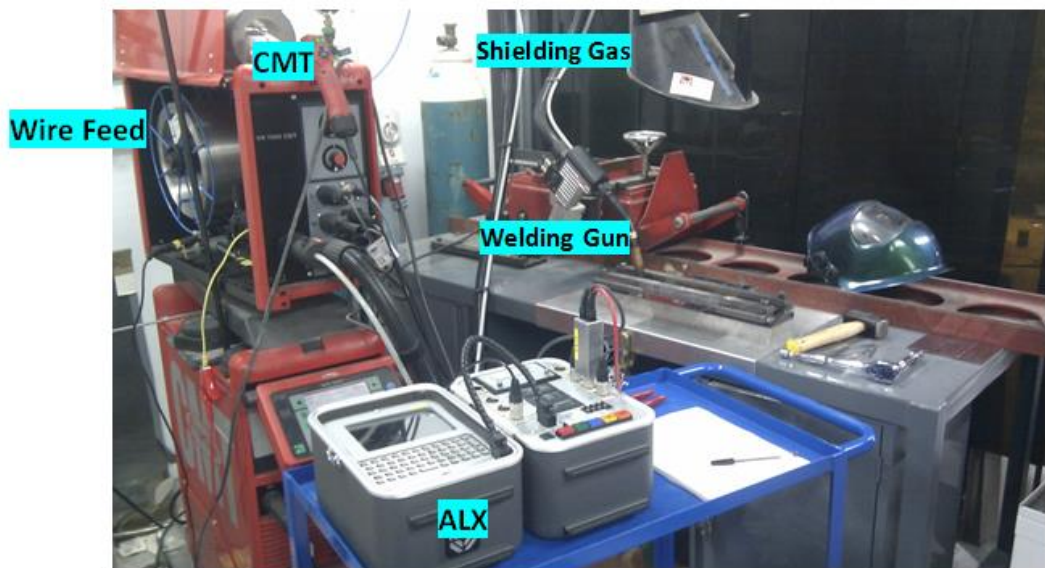


Figure 50. Welding set up showing ALX weld monitoring equipment (Boulding, The Effects of Parameters and Consistency of Cold Metal Transfer Welded Ferritic Stainless Steel Joints, 2012).

The Arc Log Ten (ALX) weld monitoring equipment, by the Validation Centre, as seen in

Figure 50, allows the user to monitor a range of welding parameters throughout the weld duration. The wire feed speed is monitored by an attachment which fits within the wire feed unit of the CMT equipment, a wheel is attached to the tractor which monitors the speed of the torch traverse and voltage and current are monitored via an attachment in the wire feeding unit and around the earth return lead respectively.

This then allows post weld analysis of these parameters including pulsed current information.

Within the welding and consistency trials one of the welds for each of the welding conditions was monitored using the ALX equipment, for each of the parameter settings.

3.7.2.5 Sample Positioning and Securing



Figure 51. Showing clamping arrangement for holding the parent material in place whilst welding.

3.7.3 Heat Input

Calculated values of heat input were made using the following equation:

Equation 2. Equation to calculate arc energy.

$$\text{Arc Energy (J/mm)} = \frac{VI}{v}$$

Where;

V = Voltage used (Volts)

I = Current used (Amperes)

v = Travel of welding torch (mm per second)

From the calculation of arc energy, the heat input is calculated by using the equation below (British Standards Institution, 1998);

Equation 3. Equation to calculate weld heat input.

$$\text{Heat Input (J/mm)} = \eta AE$$

Where;

η = Process efficiency (0.8 for GMAW) (British Standards Institution, 1998)

AE = Arc Energy (J/mm)

3.8 Non Destructive Examination

Radiographic equipment, Xograph Bucky Star with a Canon LANMIX CDXI-50G detector was used to assess CMT welds, in a bid to identify defects within them. This was used on initial CMT welds created using 3.8mm & 5.8mm EN1.4003. The parameters used for these inspections were:

Distance from source: 115cm

for 3.8mm welds: 80kV & 50mAs

for 5.8mm welds: 80kV & 40mAs

From one of the test radiographs a complete assessment was made destructively to assess the suitability of the technique for the identification of defects within these welds.

3.9 Microstructural Evaluation of all Welded Samples

Microstructural evaluations were made on samples throughout the work, the following section describes the procedure for the preparation of the welds to produce these samples.

3.9.1 Sectioning of As-Welded Samples

Sectioning of samples throughout the work varied according to the thickness of the material. Samples required for mechanical tested were water jet cut to eliminate any heat being put into the material during this stage of the preparation. Materials for metallurgical examination at 2mm thick and under were first sectioned using a mechanical shear and then samples for examination were extracted using a Beuhler AbrasiMet precision cutting machine.

Materials thicker than 2mm, had sections milled or water jet cut from the weld and then sections were cut from these more manageable pieces using the Beuhler AbrasiMet precision cutting machine.

The samples taken were cross sections of the weld and were less than 30mm long to enable them to fit into the hot mounting press for mounting in conductive bakelite.

3.9.2 Hot Mounting of Welded Cross Sections

Hot mounting was achieved using a Beuhler SimpliMet 2000 and a conductive Bakelite. The mould size for the hot mounting was 30mm diameter and the cycle time was 4 minutes heating and 4 minutes cooling. Immediately after removing from the hot mounting press, the sample identification was engraved on the reverse of the mounted sample. The temperatures involved in hot mounting are up to 190°C and as

it is below tempering temperatures of the material would not be considered to have any significant detrimental effect on the materials involved in this work.

3.9.3 Grinding/Polishing of Welded Cross Sections

The grinding and polishing was conducted in the laboratories at Sheffield Hallam University on Beuhler Alpha Beta grinder polishing stations. The route adopted included grinding using a P120 silicon carbide paper to ensure the sample was flat, then subsequent operations to gradually reduce the level of deformation in the sample through P400, P600 and finally P1200 silicon carbide papers. All these stations had water projected onto the platen to keep the sample cool and remove the grinding debris.

Polishing was conducted on identical equipment to the grinding, however a pad impregnated with a diamond paste was used with first 6 μ m maximum particle size, then after cleaning with a detergent and water, another pad containing a diamond paste with a maximum particle size of 1 μ m. In both cases the sample was contra-rotated on the pad to eliminate any directionality. Following the final stage the sample was cleaned using water and detergent and then dried with the aid of a solvent (industrial methylated spirits).

3.9.4 Etching of the As-Polished Welded Cross Sections

A number of etchants were tried with these samples, however due to the significant difference in parent material composition and that of the filler material, for a number of the etchants tried (electrolytic 10% Oxalic, 50% Hydrochloric acid, 50% ammonium peroxide immersion) there was over etching in the ferritic material and under etching in the weld. Therefore the main etchant used to reveal the microstructure of the welds and component materials was glyceresia as this was found to give an even etch across the parent and weld materials. The chemical composition for manufacture of this etchant can be seen in Table 11. The mode of etching with this etchant is via swabbing and the etchant must be made fresh and not stored. After a period of use, generally between 30 minutes and one hour, the etchant will begin to discolour and the etchant properties will degrade (see Figure 52) .

Chemical	Quantity (ml)
Glycerol	60
Hydrochloric Acid	40
Nitric Acid	20

Table 11. Showing chemical composition to make 120ml of glyceresia.

The manufacture and use of this etchant should be conducted under an appropriate extraction hood and the chemicals should be measured and mixed with glycerol first, then the hydrochloric acid is added and mixed and then slowly the nitric acid is added whilst mixing to prevent varying concentrations. It is also a requirement when undertaking etching that suitable Personal Protective Equipment (PPE) is worn, which should include safety spectacles, chemical resistant gloves and to that protective clothing is worn that covers all exposed skin.

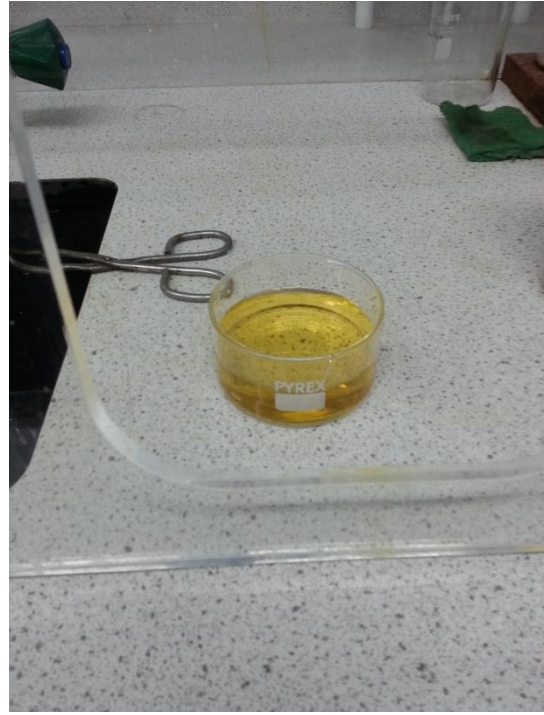
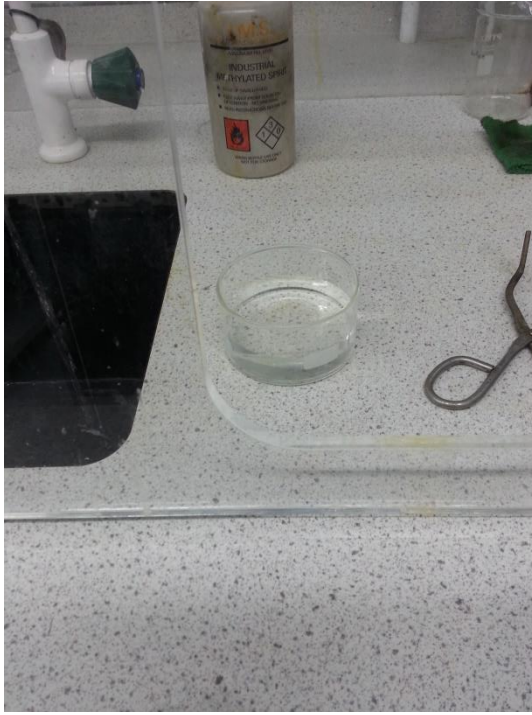


Figure 52. Images showing fresh glyceric acid (left) and glyceric acid following approximately 1 hours use (right) where it requires disposal.

3.9.5 Optical Examination of Welded Cross Sections

Optical assessments were made of the welds, using a Leica DM2500 reflected light microscope, connected to Beuhler Omnimet 9.0 image analysis software (seen in Figure 55) and a number of the features were able to be quantified for analysis. Measurements were made of the HAZ width, the weld height and weld cap width as seen in **Error! Reference source not found.**. Calibration of the measuring system was undertaken using a calibrated slide with a 1mm total line length and graduated marks every 10 μ m as can be seen in Figure 54.

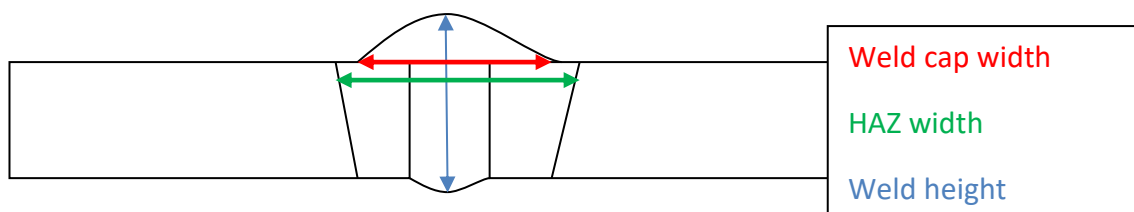


Figure 53. Schematic of weld cross section showing measurements made on optical examination

Grain size assessments, against ASTM E112, were also made in the coarsest region of the HAZ to assess, and allow comparison of, the most severe of this structurally affected area.

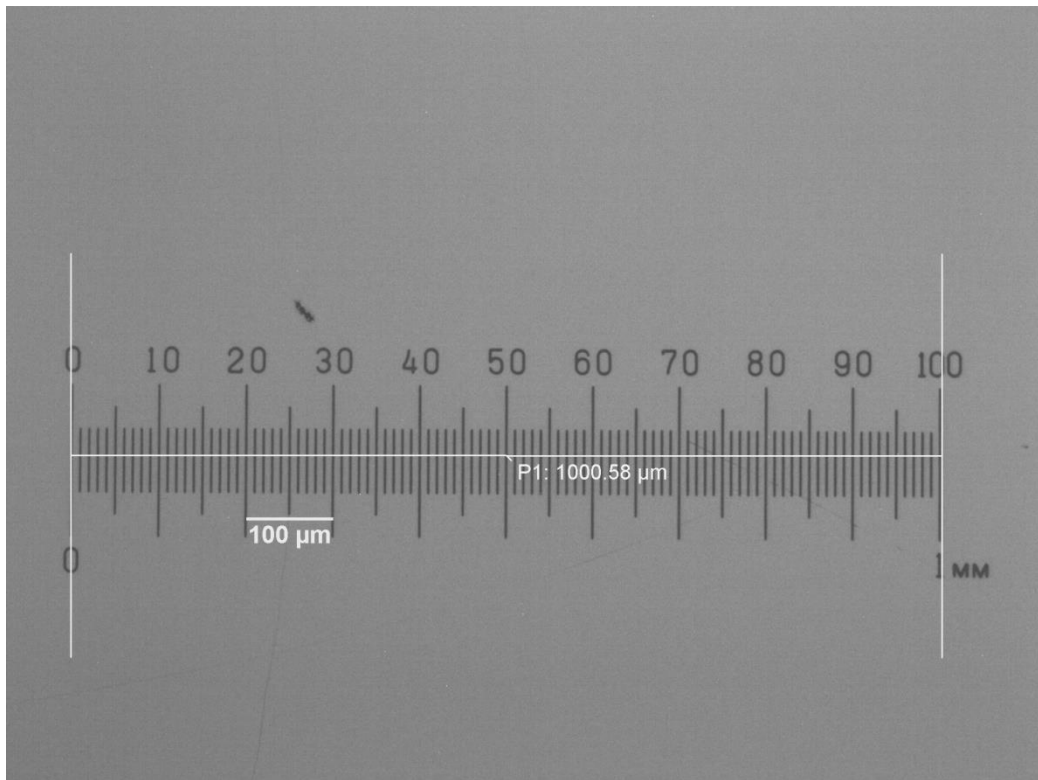


Figure 54. Image showing calibration of measurement capability of DM2500 optical measuring system.



Figure 55. Leica DM2500 optical microscope, connected to Buehler Omnimet 9.0 image analysis software.

3.9.6 Infinite Focus Microscope Examination of Weld Profiles on Untested Fatigue Samples

The Infinite Focus Microscope (IFM), which is a confocal microscope manufactured by the Austrian company, Alicona, was used to give 3D surface profilometry of the weld cap and root prior to fatigue testing, so that information relating to the weld profile could be assessed against fatigue performance. The parameters used for the scans can be seen in Table 12.

Objective Lens	G4 5X
Exposure	24.3ms
Contrast	0.38
Vertical resolution	5.77 μ m
Lateral resolution	14.02 μ m

Table 12. Table showing parameters for scans performed on the IFM

From each scan, of each side of the weld, a number of measurements were made relating to the angle of the change in section from the parent material to the weld cap or weld root.

3.10 Mechanical Evaluation of Welds

A means of quantitatively assessing the welds produced was through assessment of various mechanical properties, these included micro and macro hardness testing, uni axial tensile testing, impact testing and fatigue testing.

3.10.1 Hardness Testing

Hardness testing was conducted using a Wilson Vickers hardness testing machine, with loads that can be varied from 1kg to 30kg and a Buehler microhardness testing machine, which is capable of using loads as low as ten grams up to one thousand

grams (1kg). Unless otherwise specified tests were conducted using a 1kg load for the microhardness testing. Macrohardness testing was conducted using either 10 or 20kg loads.

Microhardness surveys were conducted on the cross section of selected welds with indents taken at 0.5mm intervals 4mm either side of the weld centre line and then 1mm intervals thereafter. This regime was conducted at the top, middle and bottom of the cross section as shown in Figure 56.

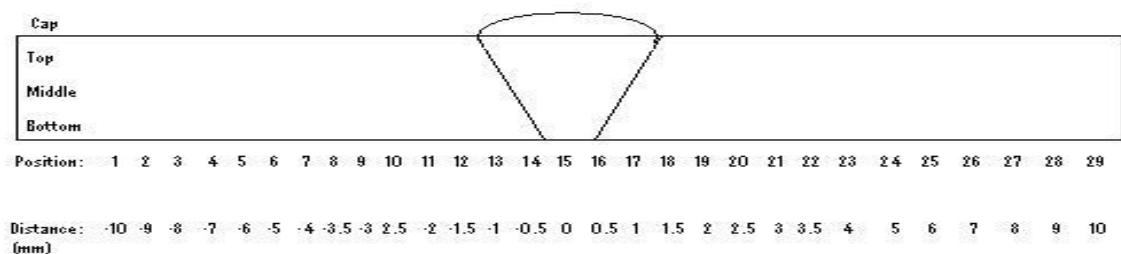


Figure 56. Schematic of hardness testing survey positions.

3.10.2 Tensile Testing of Welded Samples

Tensile testing was conducted in line with BSEN ISO 6892 using an Instron 3369 dual column benchtop 50kN tensile testing machine and controlled via the Instron Bluehill software (Instron). Sixteen tensile tests were conducted from each parent metal thickness for both the CMT and MAG welded plates and values of yield strength, maximum tensile strength and elongation were recorded. The 'dogbone' specimens as seen in Figure 58 were water jet cut with the addition of an abrasive media, to minimise any changes to the microstructure. This process did create a taper on the width of the samples, by upto 1mm and so the largest value measured was used in the calculations. The weld caps were left intact for the tests.

3.10.3 Impact Testing of Welded and Heat Treated Samples

Non-standard size Charpy impact specimens, with the size being the thickness of the plate x 10 x 55mm, manufactured to ASTM E45 were tested for both MAG and CMT welded plates. The root of the notch placed within the coarsest region of the HAZ, to determine the area with the greatest effect from the welding process. Samples were also manufactured from unwelded plate, that were subsequently subjected to a thermal cycle to replicate that experienced in the heat affected zone during the welding cycle. Impact testing was conducted on the fully calibrated Instron Dynatup 9250 drop tower impact test machine as seen in Figure 57.



Figure 57. Instron Dynatup 9250 impact test machine.

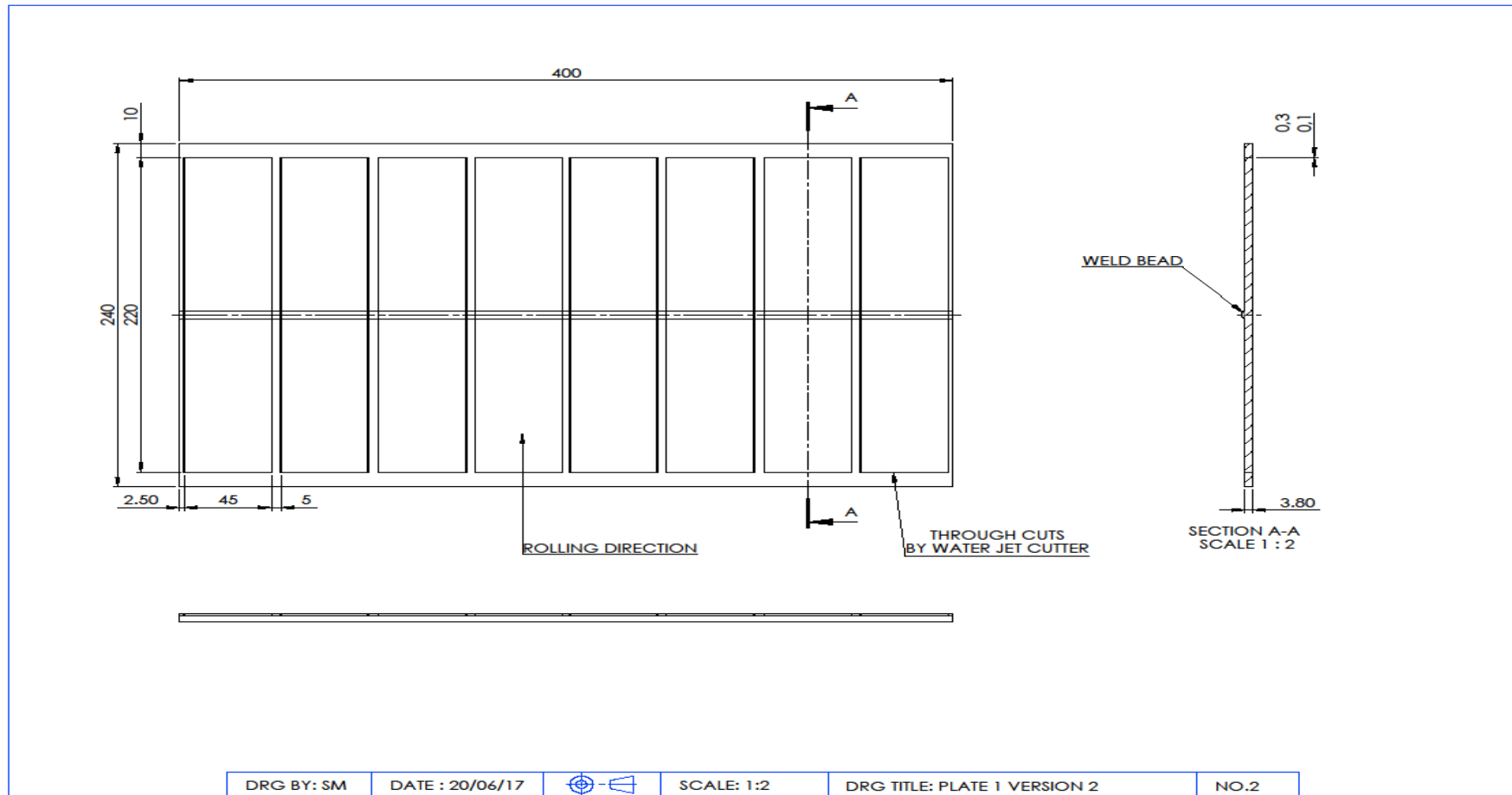


Figure 58. Showing the sampling of impact (left), microstructural (middle) and tensile specimens (right) from the welded sheet.

3.10.4 Fatigue Testing of As-Welded Samples

Fatigue testing was undertaken using an ESH Servo-hydraulic mechanical test machine, as seen in Figure 59, with a Rubicon control interface. The fatigue testing had a pull-pull characteristic and therefore went from zero load to tension and back to zero load and followed the staircase method and the frequency used was 6Hz.

The samples were 45mm wide and 220mm long, the weld cap was not removed for the tests and the weld orientation was 90° to the loading direction. The diagram showing how fatigue samples were removed from the welded sheet can be seen in Figure 60.



Figure 59. ESH Fatigue testing machine.

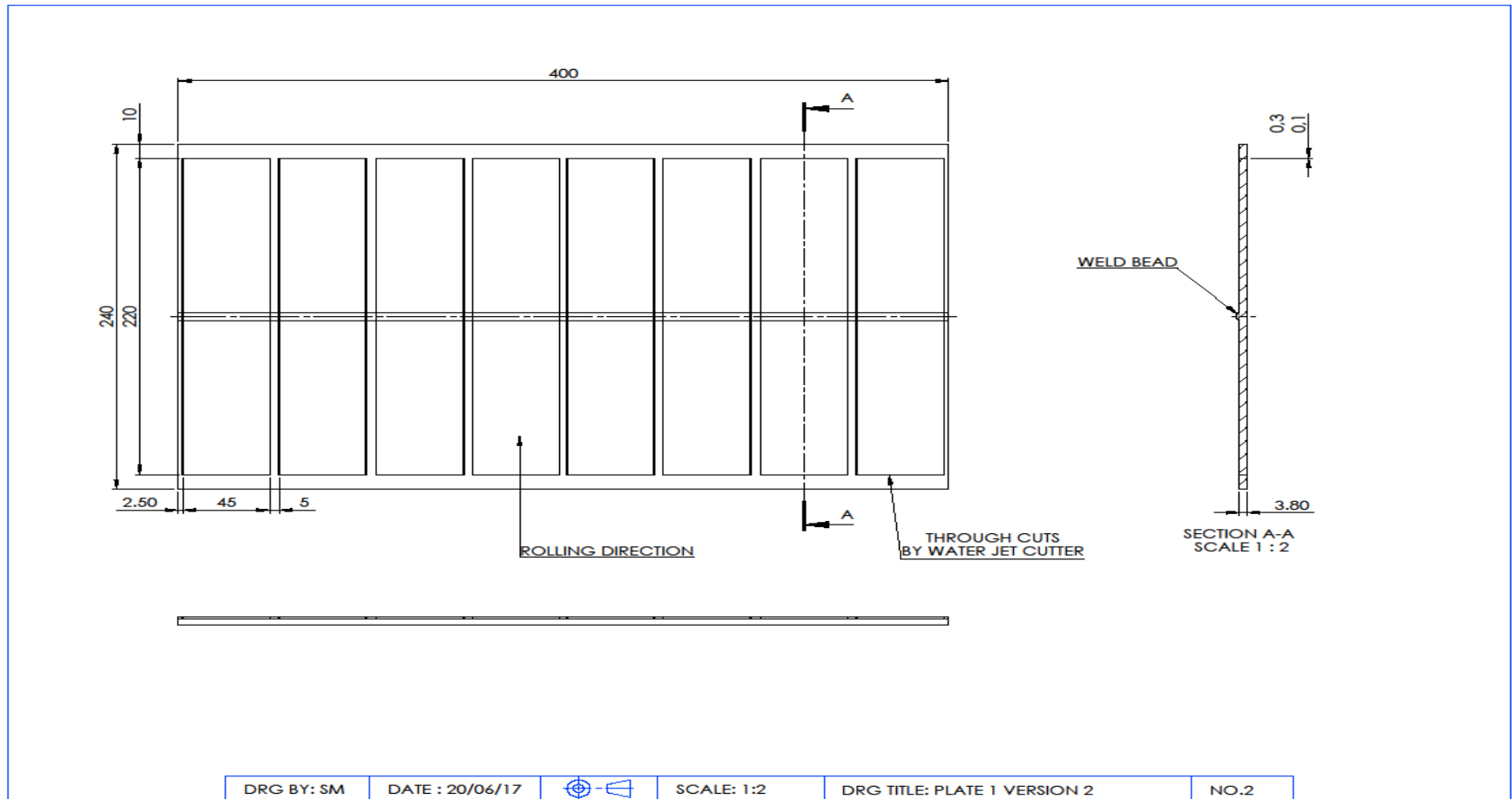


Figure 60. Showing the sampling of fatigue specimens from the as-welded sheet.

3.10.5 Staircase Fatigue Testing Procedure and Equations

The staircase testing regime, as discussed previously was used to provide statistically valid data for the mean load and standard deviation. The procedure begins with an estimation of the fatigue load and a series of sequential tests conducted, if the sample survived the pass criteria of 2 million cycles then the next sample was increased by a specific load, if it failed then it was reduced by the same amount. This continued until an indication of the range of the testing loads was ascertained for each series then the samples in each of the two series were tested (CMT welds & MAG welds).

For the CMT series, the tests were started at 46kN and the step increments were 0.5kN. For the MAG series the tests were started at 35.5kN and the step increments were 3kN.

The results are entered into a table similar to Table 13 which then provides the data to calculate the mean fatigue strength, convergence factor (if the convergence factor falls between 0.3-1.2 then the results are statistically valid), standard deviation and standard error for the mean fatigue load, the calculations for which are determined using Equation 14 to Equation 17.

Load kN	Sample	1	2	3	4	5	6	7	Number of		Using LFE as N	
	Step (i)								Runouts (r)	Failures (f)	iN	i ² N
L ₃	3					X			0	1	3	9
L ₂	2		X		O		X		1	2	4	8
L ₁	1	O		O				O	3	0	0	0
L ₀	0								0	0	0	0
									Σr	Σf	ΣiN	Σi ² N
									4	3	7	17

Table 13. Table used to collect the staircase fatigue testing data also provides information necessary for calculations to determine mean fatigue load.

Calculated Mean Fatigue Load (kN): $\chi = P_d + d \left(\frac{A}{N} \pm \frac{1}{2} \right)$
 When N= failure + $\frac{1}{2}$, when N= runout - $\frac{1}{2}$

Equation 14. Equation to calculate mean fatigue load

Convergence Factor: $= \left(\frac{(N \times B) - A^2}{N^2} \right)$
 >0.3 or <1.2 for statistical validity

Equation 15. Equation to calculate convergence factor

Standard Deviation (kN): $s = 1.620 \times d \left(\frac{(N \times B) - A^2}{N^2} + 0.029 \right)$

Equation 16. Equation to calculate standard deviation

Standard Error for Mean Fatigue Load (kN): $s_x = \frac{s}{\sqrt{N}} \cdot g$

Equation 17. Equation to calculate standard error for mean fatigue load

Where;

χ = Mean fatigue load (kN)

s = Standard deviation (kN)

P_o = Total load for step 0 (kN)

N = Total number of Least frequent Events (LFE) - failure or runout

d = Step divide/load interval (kN)

A = $\sum_i * N_i$

B = $\sum_i^2 * N_i$

i = Step number

g = 1.15 (Nordeberg, 1973)

3.11 Compositional Analysis of Parent Materials Used in the Study

It was important to have the capability to determine the composition of the materials in use throughout the research, this enabled the comparison with analysis supplied or stated on supply of the materials used.

3.11.1 Optical Emission Spectrometry

Compositional data was analysed using a Spectromax optical emission spectrometer, this allowed the complete composition to be determined, including the lighter elements such as carbon and nitrogen.

4 Experimental Results

The following section shows results gained from the research.

4.1 Materials Characterisation of the Parent Materials Used in the Study

Each of the materials utilised in the work were first characterised in the as received condition to allow the comparison with the material after it has been subjected to the thermal input as a result of the welding thermal cycles.

All the parent materials used in the project work would be expected to have a fully ferritic microstructure, when examined, in the as received condition.

4.1.1 EN 1.4003 Grade Stainless Steel

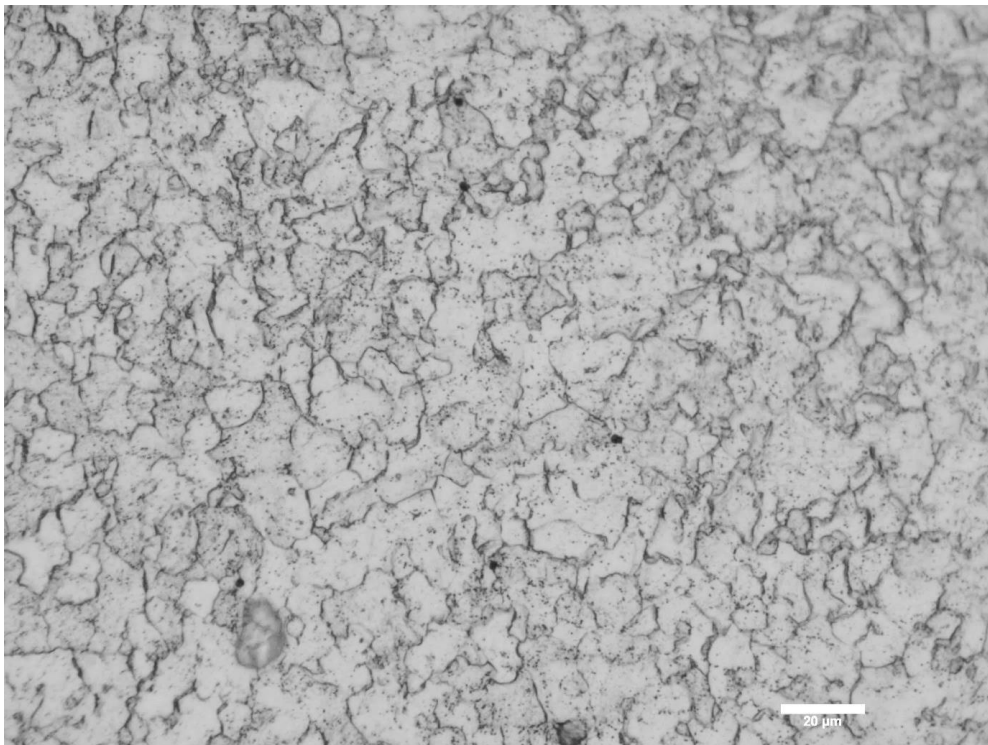


Figure 61. Etched microstructure of 3.8mm thick EN1.4003 used in the study showing an equiaxed fully ferritic structure (Etched in Glyceregia).

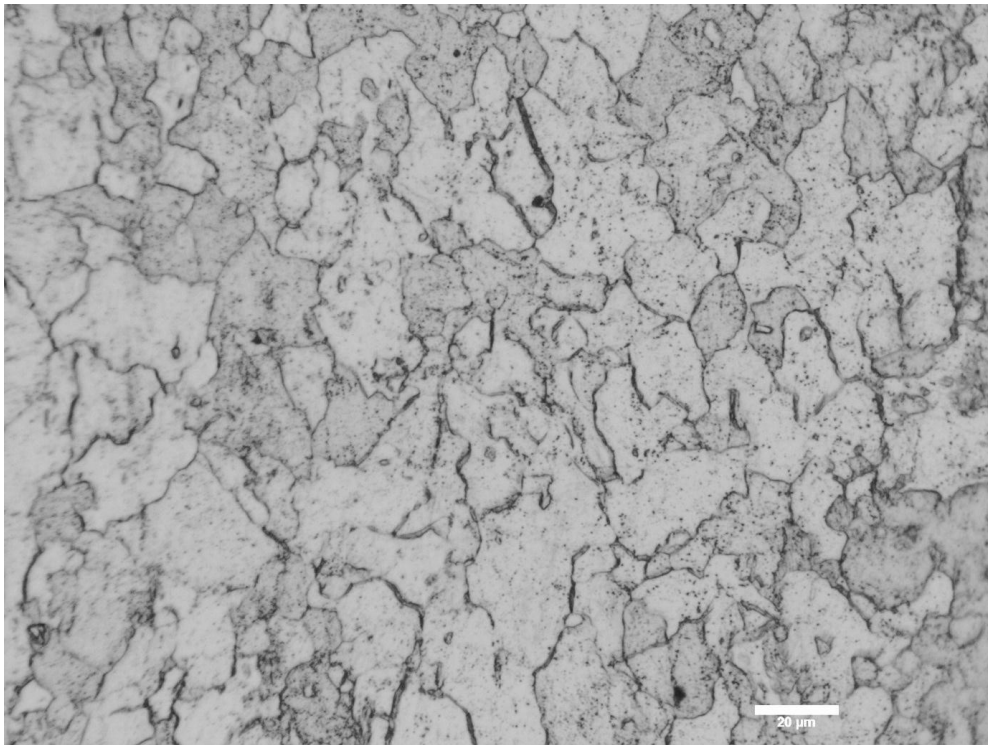


Figure 62. Etched microstructure of 5.8mm thick EN1.4003 used in the study showing an equiaxed fully ferritic structure (Etched in Glyceregia).

EN 1.4016 Grade Stainless Steel

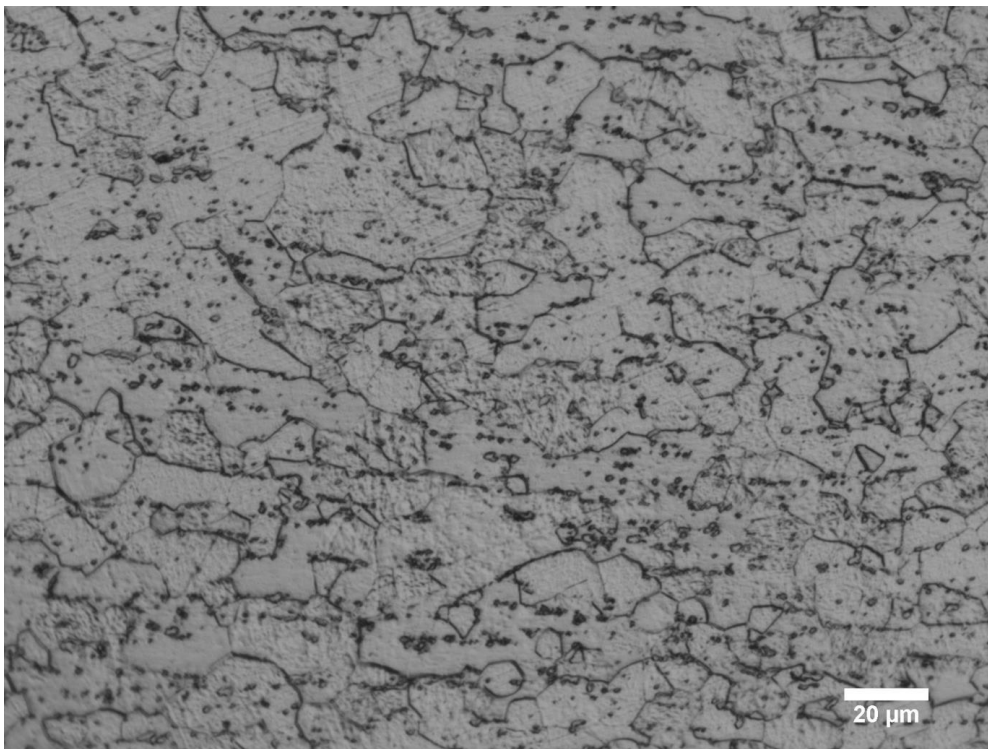


Figure 63. Etched microstructure of the EN1.4016 material used in the study showing an equiaxed fully ferritic structure (Etched in Glyceregia).

4.1.2 EN 1.4509 Grade Stainless Steel

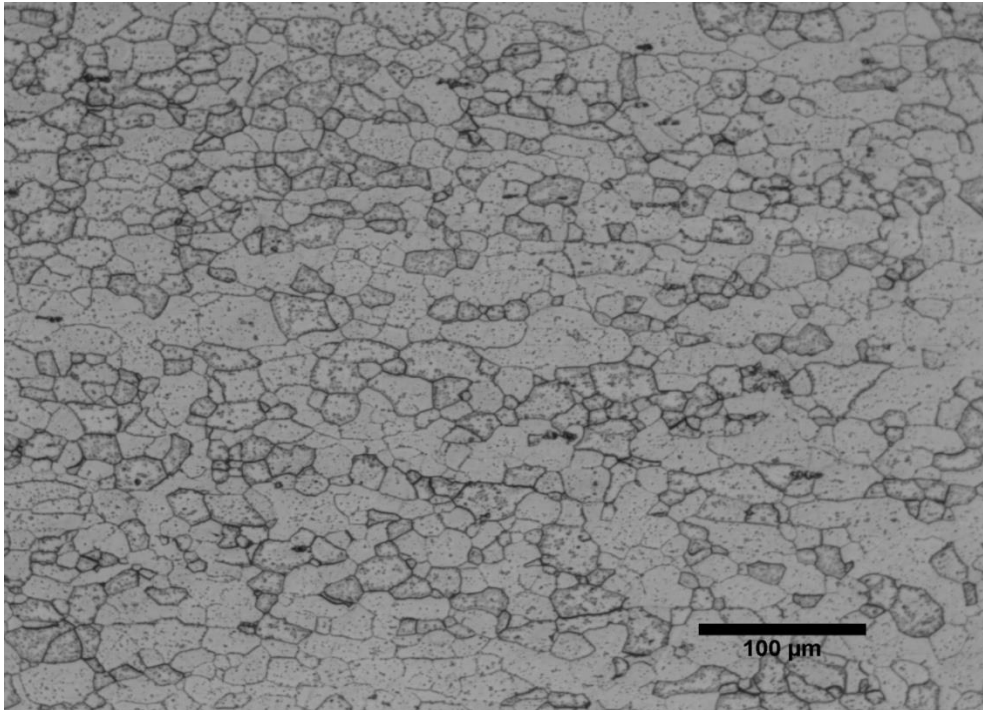


Figure 64. Etched microstructure of the EN 1.4509 material used in the study showing an equiaxed fully ferritic structure (Etched in Glyceregia).

4.1.3 EN 1.4521 Grade Stainless Steel

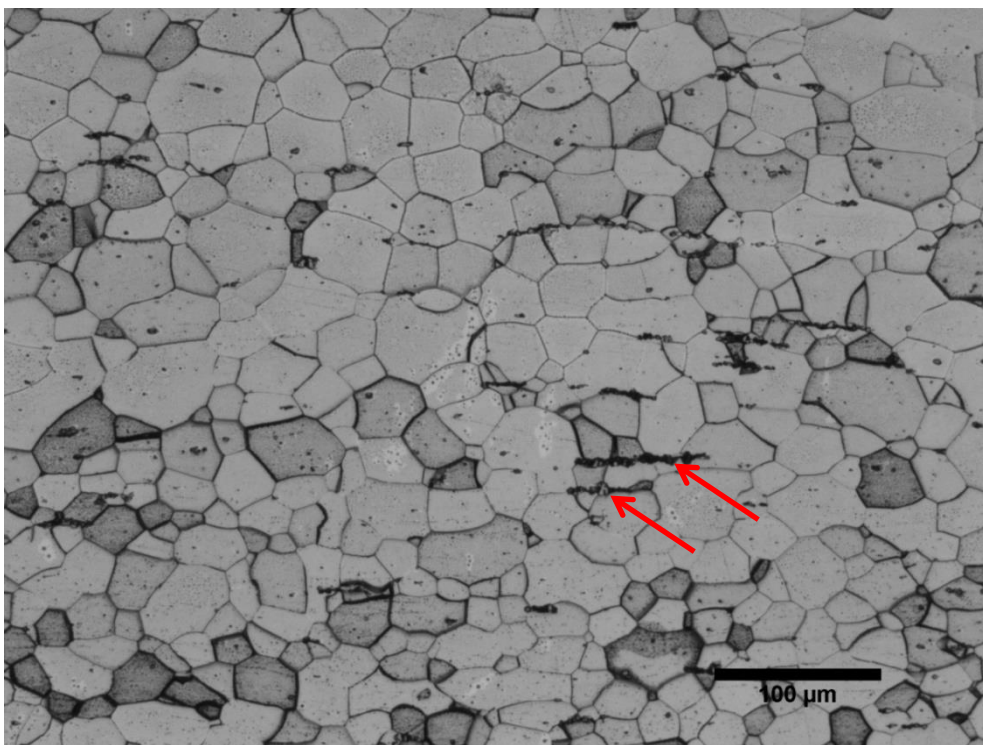


Figure 65. Etched microstructure of the EN 1.4521 material used in the study showing an equiaxed fully ferritic structure with carbides arrowed (Etched in Glyceregia).

4.2 Initial Comparison of Requisite Heat Input for MAG and CMT Welds on EN1.4016, EN1.4509 & EN1.4521 Ferritic Stainless Steel Parent Materials.

Table 14 shows the welding parameters and subsequent heat inputs for welds manufactured using Cold Metal Transfer, with and without pulsed arc and welds produced using conventional Metal Active Gas welding process. All welds were consistent in terms of length and the aim was to produce a fully penetrating weld.

Joint Type	Identification No.	Material	Voltage (V)	Current (A)	Welding Speed (mm/min)	Arc Energy (kJ/mm)	Heat Input (kJ/mm)
CMT	702852	1.4016	19.2	136	1270	0.123	0.099
CMT+P	702852	1.4016	20.3	107	1016	0.128	0.103
MAG	702852 (1)	1.4016	21.01	101.32	1080	0.118	0.094
MAG	702852 (2)	1.4016	21.15	98.81	900	0.139	0.111
CMT	794895	1.4509	19.8	138	1016	0.161	0.129
CMT+P	794895	1.4509	20	107	1016	0.126	0.101
MAG	794895 (4)	1.4509	23.16	116.68	800	0.203	0.162
MAG	794895 (5)	1.4509	22.47	116.80	1080	0.146	0.117
CMT	781436	1.4521	20	137	1270	0.129	0.104
CMT+P	781436	1.4521	21.2	107	1016	0.134	0.107
MAG	781436 (1)	1.4521	21.42	94.92	900	0.136	0.108
MAG	781436 (2)	1.4521	20.83	93.21	1080	0.108	0.086

Table 14. Showing some of the welding parameters and calculated heat inputs.

The graph seen in Figure 66 shows the weld cap width, heat affected zone width and the heat input for the welds made using the CMT process and the MAG welding process.

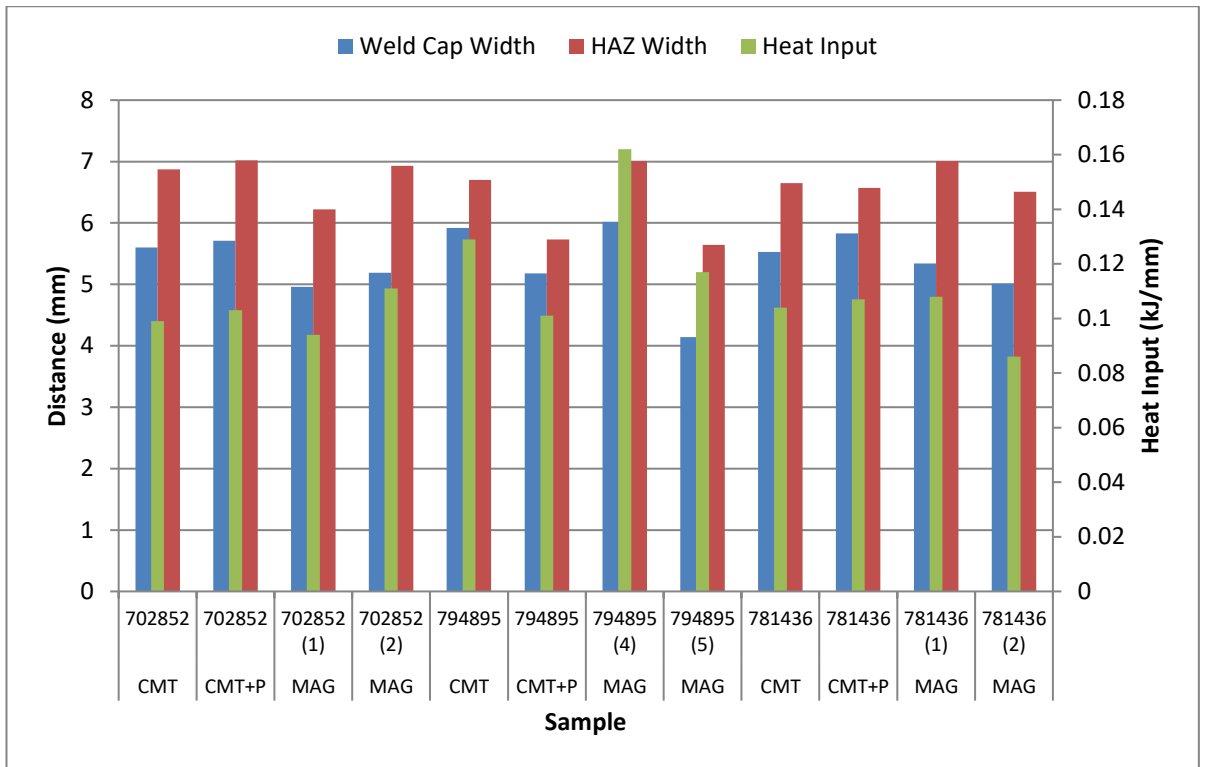


Figure 66. Graph comparing calculated heat input, weld bead and heat affected zone width of MAG and CMT welded joints.

Microstructural evaluations made on the EN1.4016 samples showed a phase change within the HAZ this can be seen in Figure 67 which was made on sample 702852 CMT. The other grades of stainless welded remained fully ferritic in the HAZ.

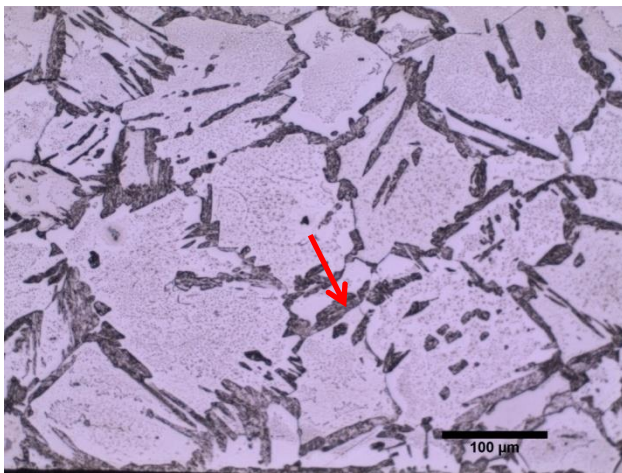


Figure 67. Image taken within the HAZ of the CMT welded EN1.4016 material, showing martensite (red arrow) at the grain boundaries.

The image seen in Figure 67 shows martensite forming at the grain boundaries following the thermal cycle experienced in the heat affected zone of the parent material (EN1.4016). Therefore a partial transformation has been made during the

thermal cycle into an austenitic phase, which under the fast cooling conditions experienced during welding the transformation has changed to martensite and not ferrite.

Figure 68 & Figure 69 shows the hardness profiles across the weld cross section for each of the welds made on the EN1.4016 grade parent material and prepared with approximately 1mm of material removed. The welds made using the conventional MAG welding techniques (Figure 68) have a reduced consistency to those produced using CMT and the maximum hardness levels reach a level 100HV higher.

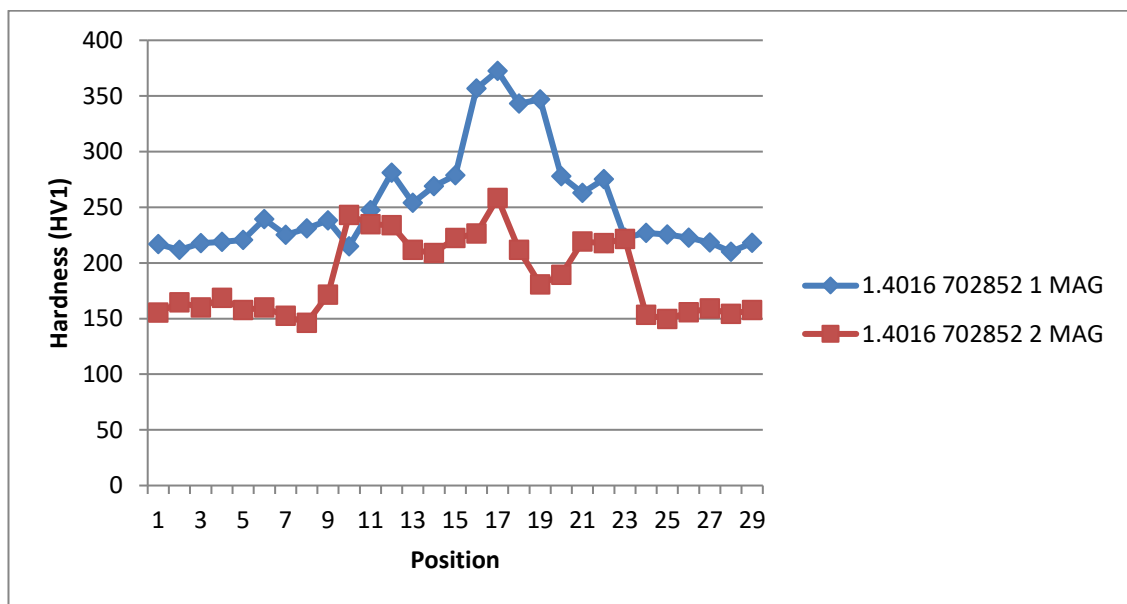


Figure 68. Comparison of the 1.4016 MAG weld/HAZ middle hardness profiles.

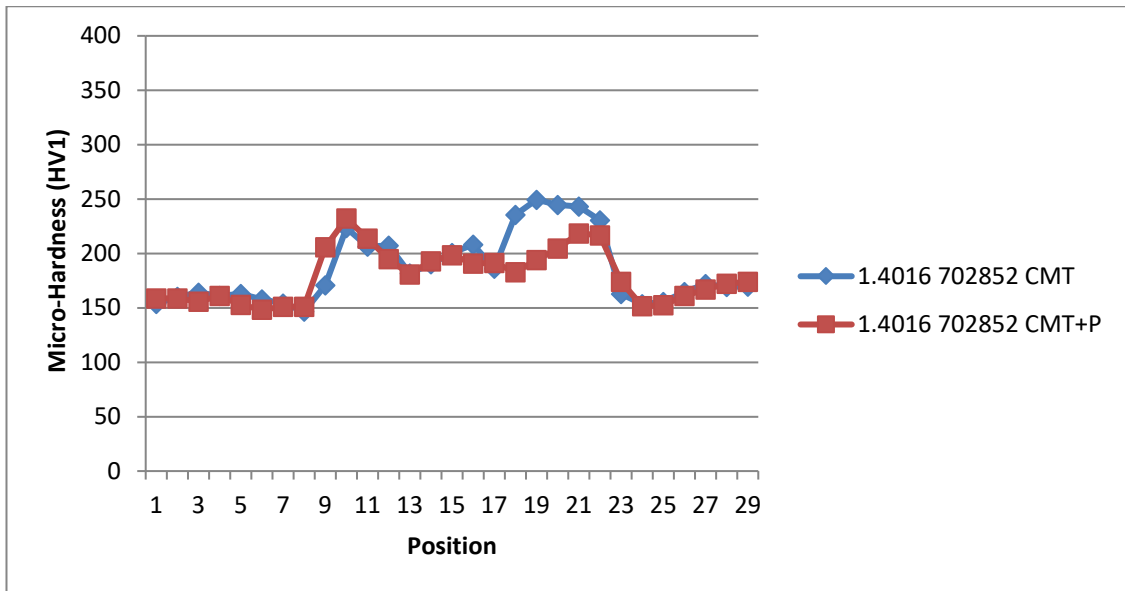


Figure 69. Comparison of the 1.4016 CMT weld/HAZ middle micro hardness profiles.

4.3 The Effect of Heat Input on Weld/HAZ Shape & Size, Penetration Levels and HAZ Grain Size, using CMT

Sample	Average Width of HAZ (μm)	Average Area of Weld Metal (mm ²)	Average Height of Weld Bead (mm)	Average Width of Weld Bead (mm)	Average Angle of Weld Bead (°)	Average Perimeter of Weld Bead (mm)	Average Grain Size in HAZ (ASTM)	Average Grain Size in Parent Metal (ASTM)	Weld Penetration Sufficient
Pure CMT 0.06 KJ/mm	339	4.32	2.39	3.58	124.62	9.21	4.4	6.5	NO
Pure CMT 0.07 KJ/mm	698	5.07	2.58	3.70	125.02	9.27	4.1	7	NO
Pure CMT 0.08 KJ/mm	778	7.00	2.84	5.54	135.09	10.35	3.4	6.4	NO
Pure CMT 0.09 KJ/mm	1002	7.99	3.51	5.09	128.97	10.39	2.6	7.3	YES
Pure CMT 0.10 KJ/mm	1036	10.24	3.95	4.47	124.52	10.55	1.9	7.1	YES
Pure CMT 0.11 KJ/mm	1048	10.35	3.73	5.67	121.57	10.50	1.6	6	YES

Table 15 Summary of weld/HAZ dimensions for pure CMT welded samples with increasing net heat input.

Sample	Average Width of HAZ (μm)	Average Area of Weld Metal (mm ²)	Average Height of Weld Bead (mm)	Average Width of Weld Bead (mm)	Average Angle of Weld Bead (°)	Average Perimeter of Weld Bead (mm)	Average Grain Size in HAZ (ASTM)	Average Grain Size in Parent Metal (ASTM)	Weld Penetration Sufficient
CMT Pulsed Arc 0.06 KJ/mm	532.2	3.92	2.46	3.47	134	9.63	4.9	6.9	NO
CMT Pulsed Arc 0.07 KJ/mm	687.6	4.76	2.57	3.77	125	10.1	4.3	7	NO
CMT Pulsed Arc 0.08 KJ/mm	741.6	5.22	3.18	3.79	141	10.15	3.4	6.6	NO
CMT Pulsed Arc 0.09 KJ/mm	935	5.38	3.16	4.26	134	10.23	3.1	6.4	NO
CMT Pulsed Arc 0.10KJ/mm	1033	6.65	3.50	4.55	141	10.30	2.4	6.5	YES
CMT Pulsed Arc 0.11 KJ/mm	1042	8.14	3.52	5.42	146	10.44	2.3	7.8	YES

Table 16. Summary of weld/HAZ dimensions for CMT with pulsed arc welded samples with increasing net heat input.

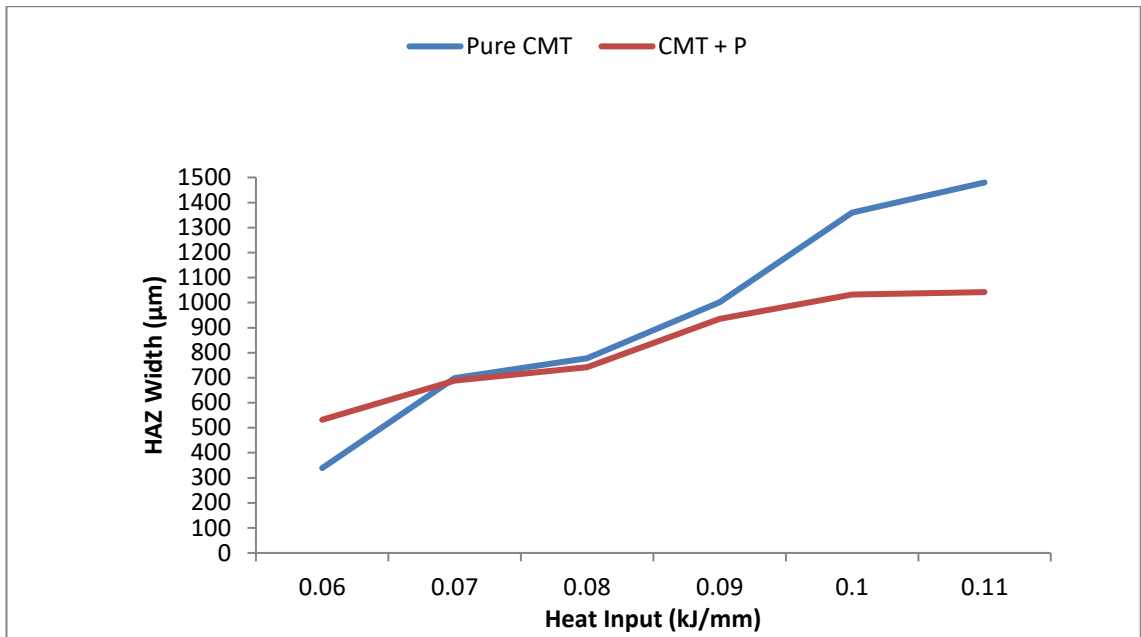


Figure 70. Showing effect of heat input on HAZ width for pure CMT and CMT with Pulsed arc welded samples, EN1.4016 parent material.

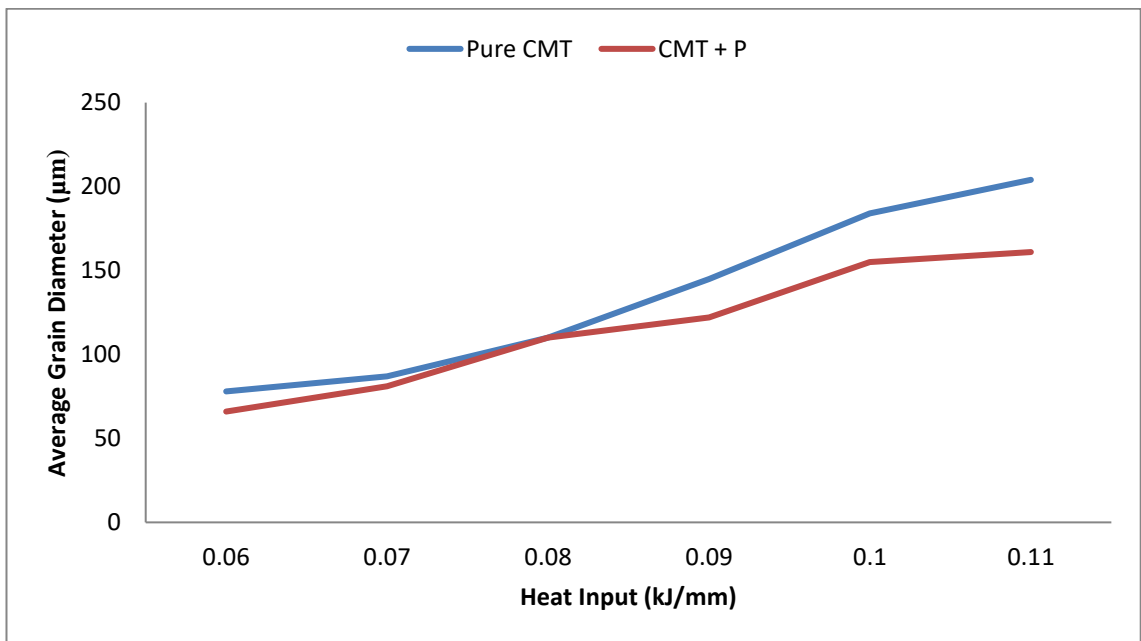


Figure 71. Showing effect of heat input on grain size for pure CMT and CMT with pulsed arc welded samples, EN1.4016 parent material.

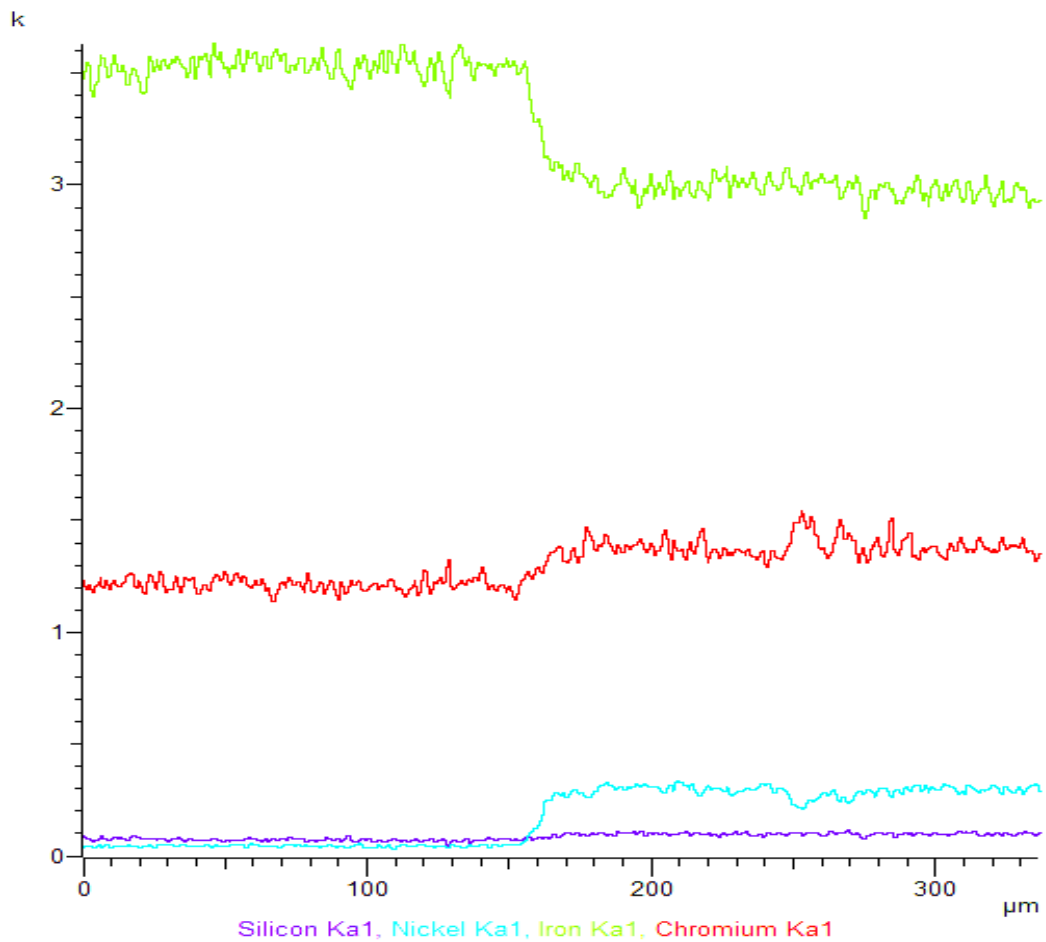
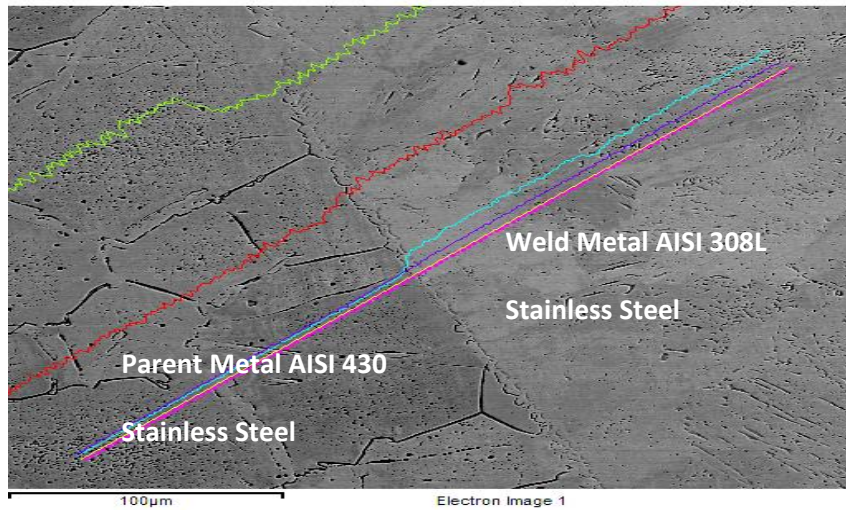


Figure 72. Line scan of interface between AISI 430 parent metal and AISI 308L weld metal.

Table 15 and Table 16 with Figure 70 to Figure 71 show the effect of the welding heat input on the heat affected zone width and the heat affected zone grain size.

Elemental Map of HAZ

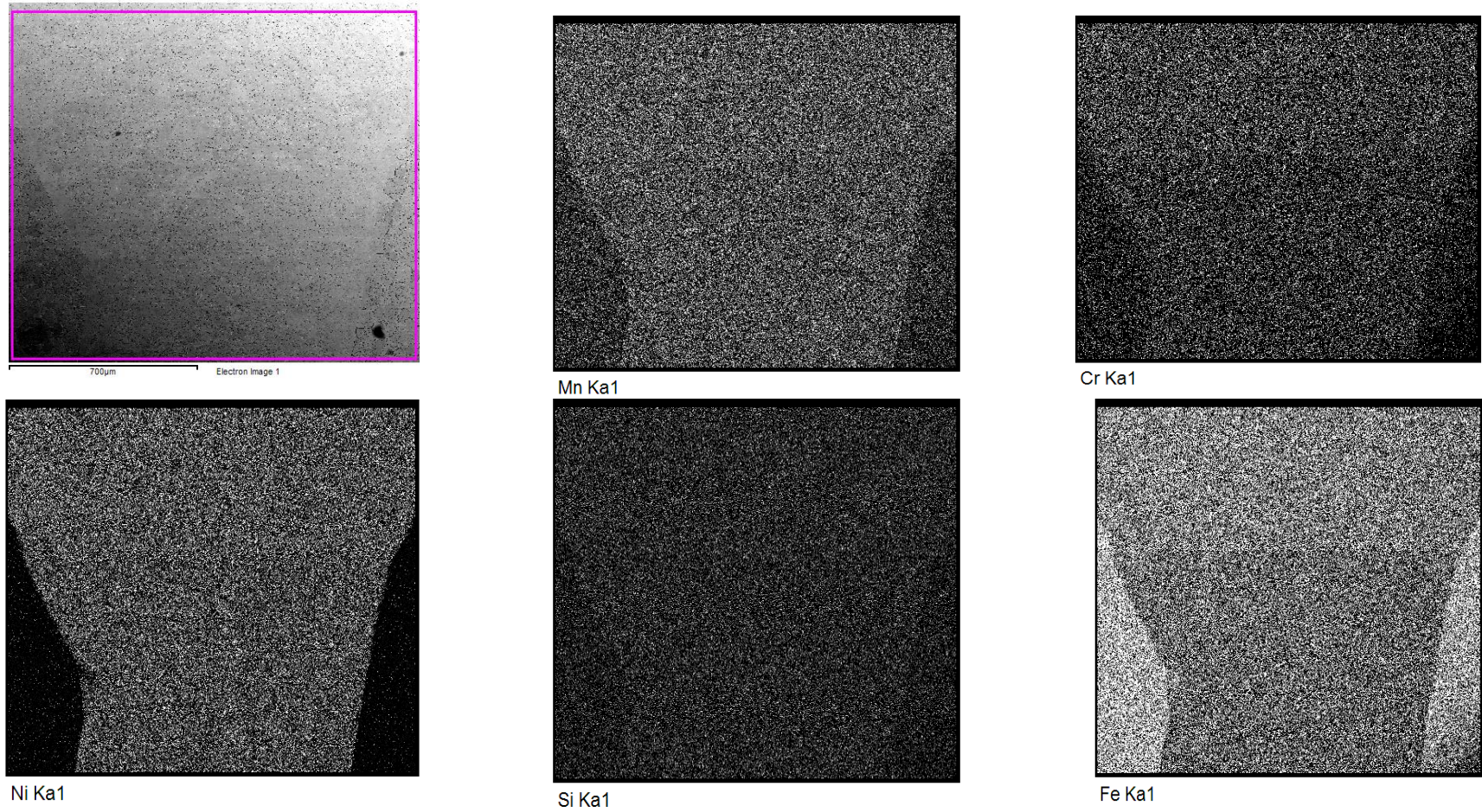


Figure 73. Elemental Map of parent metal and weld metal interface for AISI 430 parent material and 308LSi filler.

4.4 Trial to Examine the Effects of Variation in the Welding Gap, Torch Traverse Speed and Torch Angle using 2mm Thickness EN1.4016 and EN1.4509 Parent Materials.

It can be seen in Figure 74 and Figure 75 the effects on the heat input for a fully penetrating weld through increasing the torch traverse speed and increasing the welding gap (spacing between the parent plates). Figure 76 & Figure 77 show the heat input required to produce a fully penetrating weld varies according to the speed and torch angle. Figure 78 shows the weld cross section with the right hand side of the image showing the weld and HAZ of a high heat input and the left hand side of the image, a weld subjected to a lower heat input, with the subsequent difference in the HAZ grain size and width.

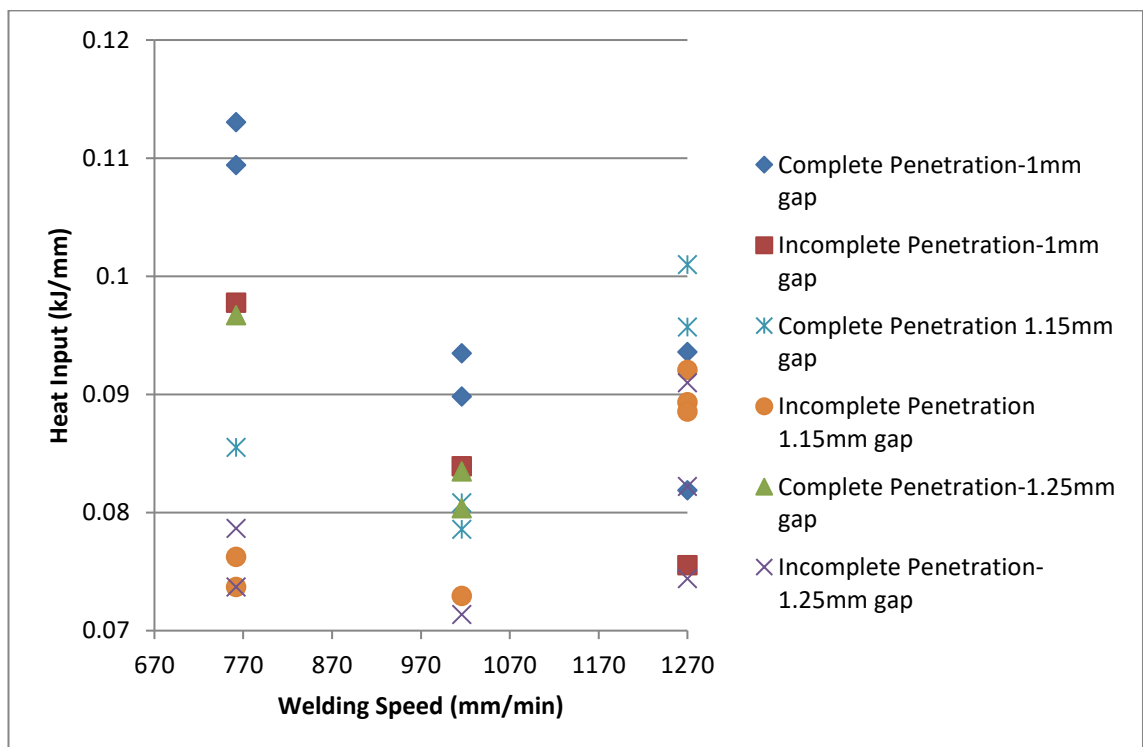


Figure 74. Graph showing forehand (15°) welds produced using 1.4016 material at 1mm, 1.15mm and 1.25mm joint gaps and 762, 1016 & 1270 mm/min welding speeds, categorised according to whether weld penetration was achieved.

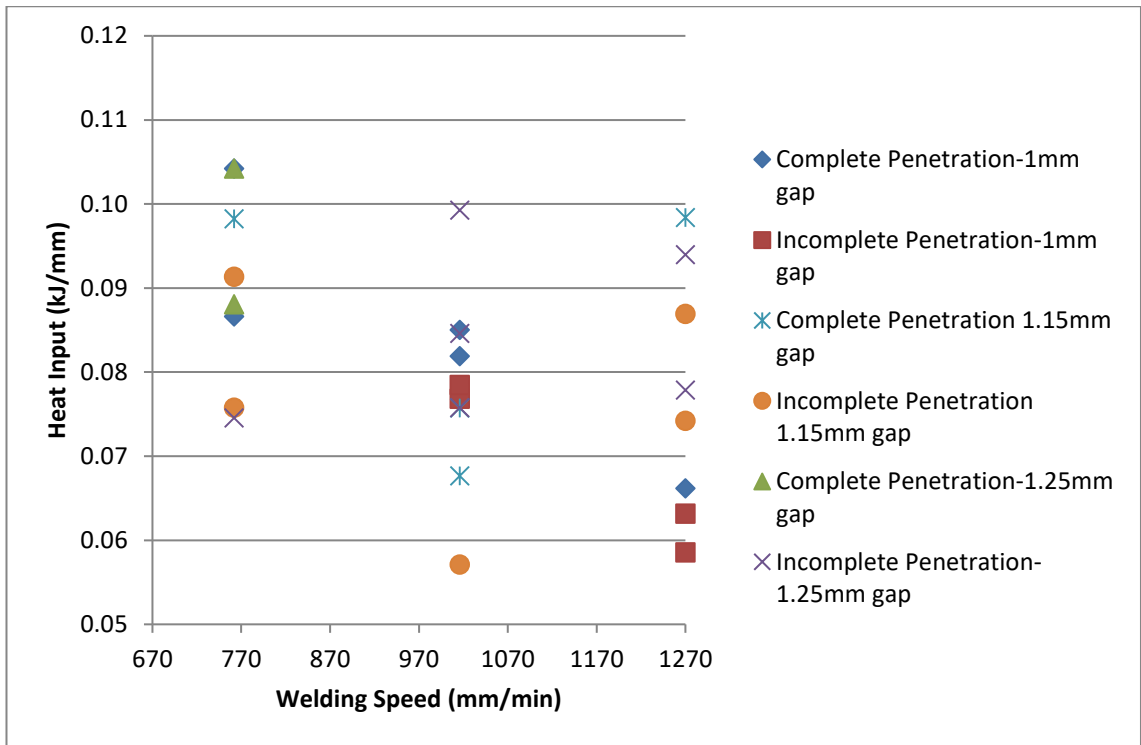


Figure 75. Graph showing forehand (15°) welds produced using 1.4509 material at 1mm, 1.15mm and 1.25mm joint gaps and 762, 1016 & 1270 mm/min welding speeds, categorised according to whether weld penetration was achieved.

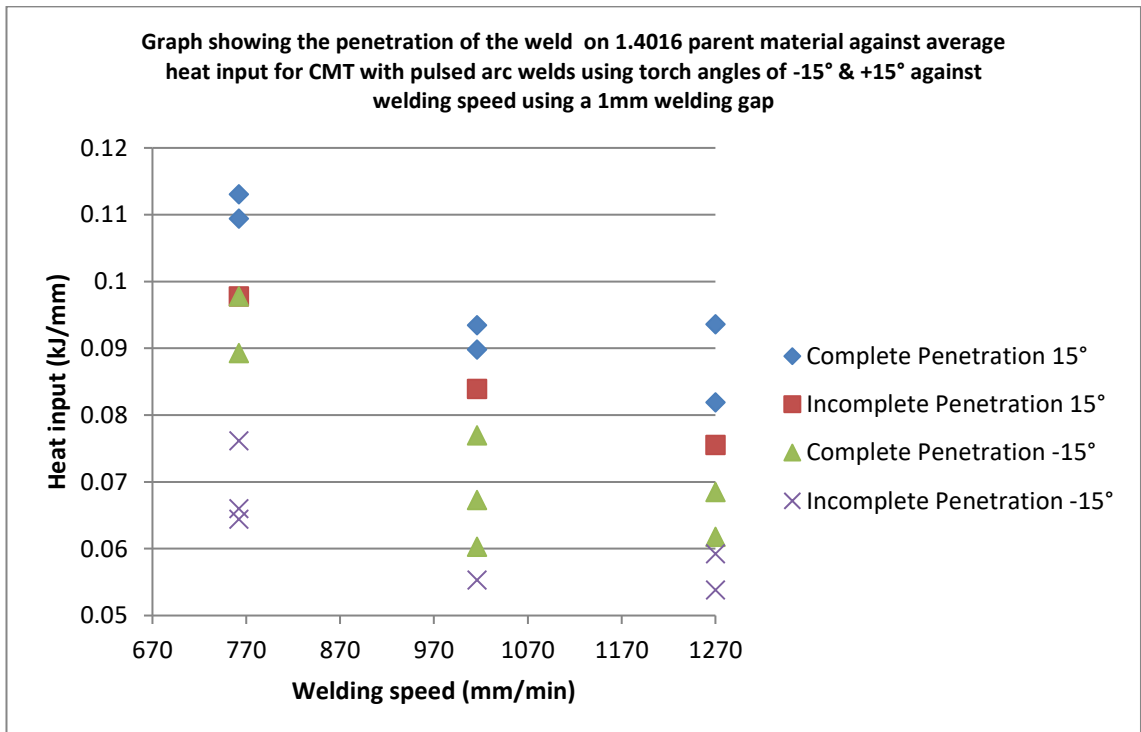


Figure 76. Graph showing the effect of torch angle on achieving penetration of welds produced using grade 1.4016 parent material, using a 1mm joint gap, at different welding speeds.

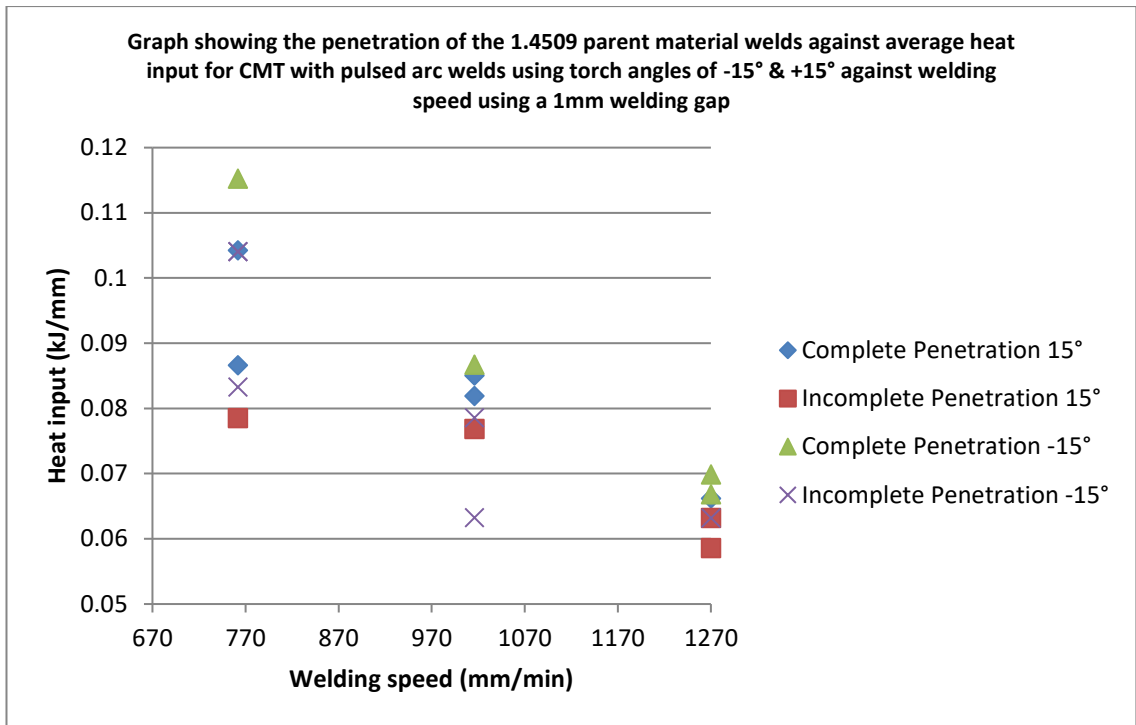


Figure 77. Graph showing the effect of torch angle on achieving penetration of welds produced using grade 1.4509 parent material, using a 1mm joint gap, at different welding speeds.

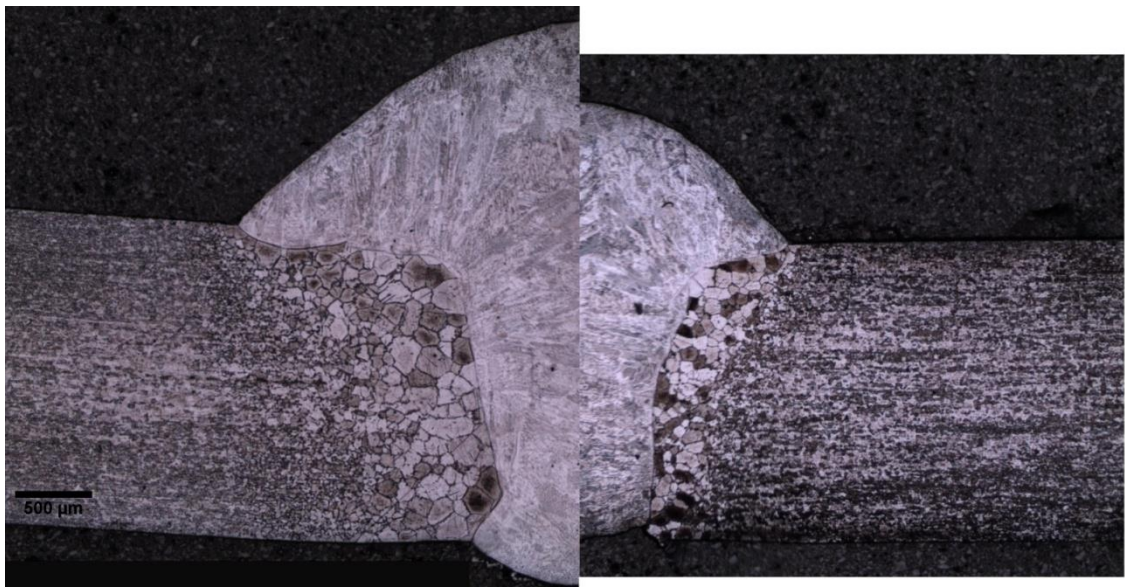


Figure 78. Image showing the effect of heat input on weld and HAZ dimensions. The left hand weld cross section of 2mm thick, CMT+P welded, 1.4016 material with heat input of 0.113 kJ/mm and the right is the same material and welded using the same process but with a net heat input of 0.060 kJ/mm.

4.5 Trial to Determine the Consistency of the Welding Parameters and Subsequent Welds with the CMT Welding Process

Table 18 shows the results from an inspection of the cross section of the welds to identify if the welds had sufficient penetration, for welds produced with a variation in one parameter, therefore in most cases for each variation in parameter, 6 welds were created and from each of these welds six areas along that weld were examined.

Setting	Run Number	Voltage (V)	Current (A)	Velocity (mm/min)	Heat Input (J/mm)
3.5m/min Wire Feed	290	19.7	77	1016	71.67
	291	19.9	77	1016	72.40
	292	20.4	75	1016	72.29
	293	19.5	78	1016	71.87
	294	19.2	79	1016	71.67
	295	19.9	78	1016	73.34
4.5m/min Wire Feed	296	20.5	92	1016	89.11
	297	20.6	94	1016	91.50
	298	21.5	85	1016	86.35
	299	21	89	1016	88.31
	300	21.4	85	1016	85.95
	301	19.6	97	1016	89.83
5.5m/min Wire Feed	302	21.9	99	1016	102.45
	303	21	110	1016	109.15
	304	20.6	112	1016	109.02
	305	20.6	114	1016	110.96
	306	20.8	114	1016	112.04
	307	20.8	114	1016	112.04
ALC -30	308	19.3	98	1016	89.37
	309	19.4	101	1016	92.58
	310	19.5	101	1016	93.06
	311	19.2	99	1016	89.81
	312	19.3	101	1016	92.11
	313	19.3	101	1016	92.11
ALC +30	314	20.1	91	1016	86.43
	315	20.2	91	1016	86.86
	316	20.2	91	1016	86.86
	317	20.3	91	1016	87.29
	318	20.2	90	1016	85.90
	319	20	96	1016	90.72
PC -5	320	19.3	82	1016	74.78
	321	19.4	81	1016	74.25
	322	19.3	81	1016	73.87
	323	19.2	82	1016	74.39
	324	19.2	81	1016	73.48
	325	19.2	88	1016	79.83
PC +5	326	20.8	106	1016	104.18
	327	21.2	102	1016	102.18
	328	21	103	1016	102.20
	329	21.2	102	1016	102.18
	330	21	102	1016	101.21
	331	20.8	106	1016	104.18
Trav 0.762	332	20	94	762	118.42
	333	20.1	95	762	120.28
	334	20	92	762	115.90
	335	20.1	93	762	117.75
	336	20.1	94	762	119.01
	337	19.9	97	762	121.59
Trav 1.27	339	19.9	94	1270	70.68
	340	19.9	92	1270	69.18
	341	19.8	93	1270	69.58
	342	19.8	91	1270	68.08
	343	19.9	97	1270	72.94
Trav 1.016 TA+15	344	19.9	93	16.93	87.45
	345	20.1	94	16.93	89.28
	346	20	94	16.93	88.83
	347	19.9	95	16.93	89.33
	348	19.9	101	16.93	94.97
	349	19.9	97	16.93	91.21

Table 17. Table showing actual readings and calculated heat inputs for each weld produced on the trial.

	Weld Run No.	1	2	3	4	5	6		Weld Run No.	1	2	3	4	5	6
Wire Feed 3.5m/min	290	Red	Red	Red	Red	Yellow	Yellow	Pulse Correction (PC) setting -5	320	Red	Yellow	Yellow	Red	Yellow	
	291	Red	Yellow	Yellow	Yellow	Red	Yellow		321	Red	Red	Yellow	Yellow	Yellow	Yellow
	292	Red	Red	Red	Red	White	White		322	Red	Red	Red	Red	Red	Yellow
	293	Red	Red	Red	Red	Red	Yellow		323	Red	Red	Yellow	Red	Red	Yellow
	294	Red	White	Red	Red	Red	Red		324	Red	Red	Yellow	Red	Red	Yellow
	295	Red	Red	Red	Red	Red	Yellow		325	Red	Red	Red	White	White	White
Wire Feed 4.5m/min	296	Red	Red	Yellow	Yellow	Red	Red	Pulse Correction (PC) setting +5	326	Green	Green	Green	Green	Yellow	Yellow
	297	Yellow	Yellow	Yellow	Yellow	Yellow	Yellow		327	Green	Green	Green	Green	Yellow	Green
	298	Yellow	Yellow	Red	White	White	White		328	Green	Green	Green	Green	Green	Green
	299	Yellow	Yellow	Yellow	Yellow	Yellow	Yellow		329	Green	Green	Yellow	Green	Green	Red
	300	Red	Red	Red	Red	White	White		330	Green	Green	Green	Green	Green	Green
	301	Yellow	Green	Yellow	Yellow	Yellow	Yellow		331	Green	Green	Green	Green	Green	Green
Wire Feed 5.5m/min	302	Green	Green	Green	White	White	White	Trav 0.762 m/min	332	Green	Green	Green	Green	Yellow	Yellow
	303	Green	Green	Green	Green	Green	Green		333	Green	Green	Green	Green	Green	Green
	304	Green	Green	Green	Green	Green	Green		334	Green	Green	Green	Green	Green	Green
	305	Green	Green	Green	Green	Green	Green		335	Green	Green	Green	Green	Green	Green
	306	Green	Green	Green	Green	Green	Green		336	Green	Green	Green	Green	Green	Yellow
	307	Green	Green	Green	Green	Green	White		337	Green	Green	Green	Green	Green	Green
ALC - 30	308	Yellow	Green	Green	Yellow	Yellow	Yellow	Trav 1.27 m/min	339	Red	Red	Yellow	Yellow	Yellow	Yellow
	309	Green	Green	Green	Green	Green	Yellow		340	Yellow	Green	Green	Yellow	Yellow	Yellow
	310	Green	Yellow	Yellow	Green	Green	Green		341	Green	Yellow	Yellow	Yellow	Yellow	Green
	311	Green	Green	Green	Green	Yellow	Green		342	Yellow	Red	Yellow	Red	Yellow	Yellow
	312	Green	Green	Green	Green	Green	Green		343	Yellow	Green	Red	Red	Yellow	Yellow
	313	Green	Green	Green	Green	Green	Yellow								
	338	Yellow	Red	Yellow	Yellow	Yellow	Yellow								
ALC +30	314	Yellow	Green	Green	Yellow	Yellow	Yellow	Trav 1.016 m/min (TA +15)	344	Yellow	Yellow	Yellow	Red	Red	Red
	315	Yellow	Yellow	Yellow	Yellow	Yellow	Yellow		345	Red	Green	Green	Red	Green	Green
	316	Green	Yellow	Green	Green	Yellow	Green		346	Green	Green	Green	Yellow	Green	Green
	317	Yellow	Yellow	Yellow	Green	Yellow	Yellow		347	Green	Red	Red	Red	Red	Green
	318	Yellow	Yellow	Yellow	Yellow	Red	Yellow		348	Yellow	Yellow	Yellow	Red	Green	Green
	319	Yellow	Yellow	Yellow	Yellow	Yellow	Yellow		349	Yellow	Yellow	Yellow	Green	Yellow	Yellow

Table 18. Showing assessments of the extent of penetration of the filler metal for each sample examined (Boulding, The Effects of Parameters and Consistency of Cold Metal Transfer Welded Ferritic Stainless Steel Joints, 2012). For colour coding PTO.

Full Penetration	Example 1 (Figure 79)
Not Fully Penetrated	Example 2 (Figure 80)
Misaligned Parent	Example 3 (Figure 81)

Table 19. Showing key to assessments made on penetration (Boulding, The Effects of Parameters and Consistency of Cold Metal Transfer Welded Ferritic Stainless Steel Joints, 2012).



Figure 79. Example 1, showing a fully penetrated weld (Boulding, The Effects of Parameters and Consistency of Cold Metal Transfer Welded Ferritic Stainless Steel Joints, 2012).



Figure 80. Example 2, showing an incomplete penetrated weld (Boulding, The Effects of Parameters and Consistency of Cold Metal Transfer Welded Ferritic Stainless Steel Joints, 2012).

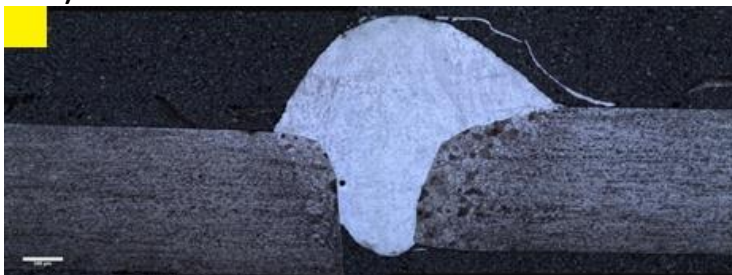


Figure 81. Example 3, showing misaligned parent/penetration to one side (Boulding, The Effects of Parameters and Consistency of Cold Metal Transfer Welded Ferritic Stainless Steel Joints, 2012).

Table 19 and Figure 79 to Figure 81 show the key to the colour coding seen in Table 18. The weld cross sections shown in Figure 79 to Figure 81 are representatives of the different categories highlighted, with the first being a fully penetrating weld, the second showing a weld with a lack of root penetration and the third, where the parent plate is misaligned. In all cases the parent material was a 2 mm thick EN1.4016 grade ferritic stainless steel.

4.5.1 Power Setting

The welds were created in a synergic mode and therefore the wire speed, voltage and current are all linked. Adjustment of power is made through variation of the wire feed speed, an increase in wire feed speed increases the power levels, a decrease in the wire feed speed decreases the power. The following three graphs (Figure 82 to Figure 84) shows the effects of varying the power levels in the welding process on the heat affected zone width, they also show the consistency of the measurements made from weld to weld and at various distances along each of the welds. There appears to be a variation in the measurements from weld to weld and also along the length of the plate. It is also worth noting the increase in HAZ width as a result of increasing the power.

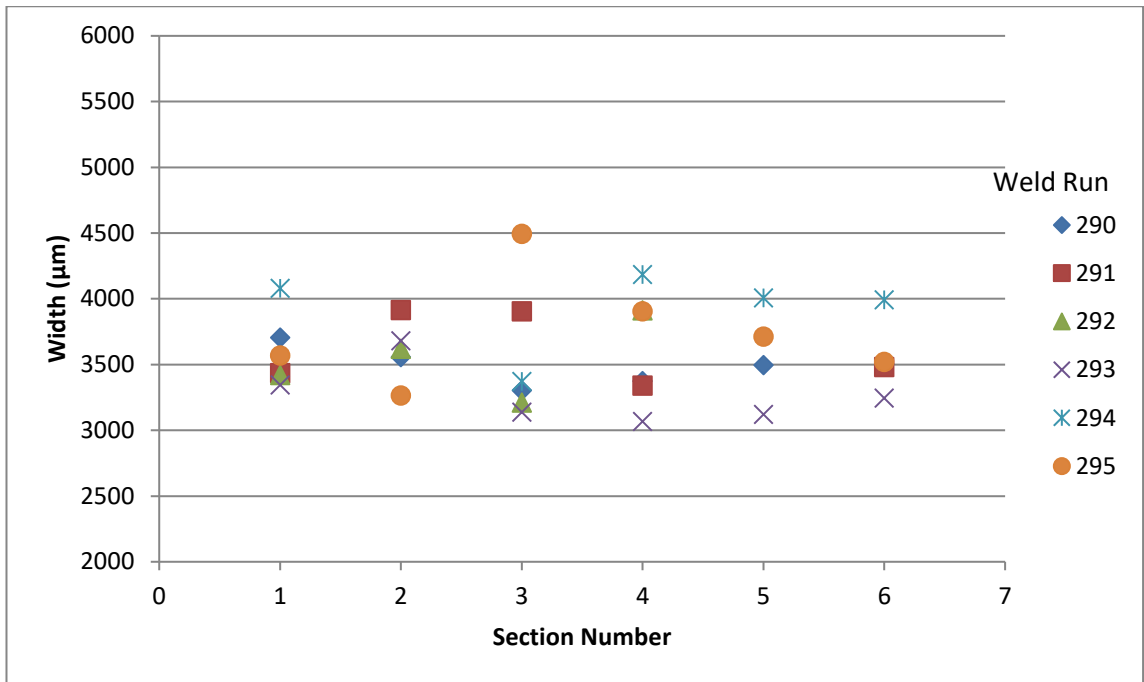


Figure 82. Graph showing the width of the HAZ for each of the CMT welds conducted at 3.5m/min (average net heat input 72.2 J/mm) on EN1.4016 grade parent material.

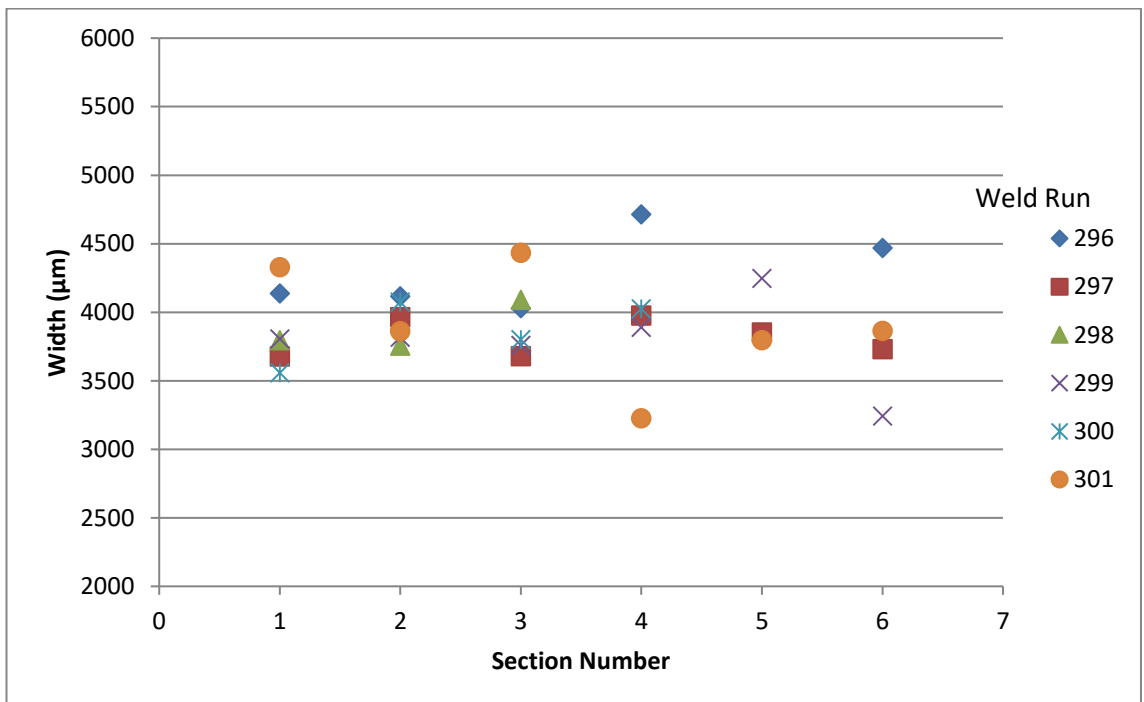


Figure 83. Graph showing the width of the HAZ for each of the CMT welds conducted at 4.5m/min (average net heat input 88.5 J/mm) on EN1.4016 grade parent material.

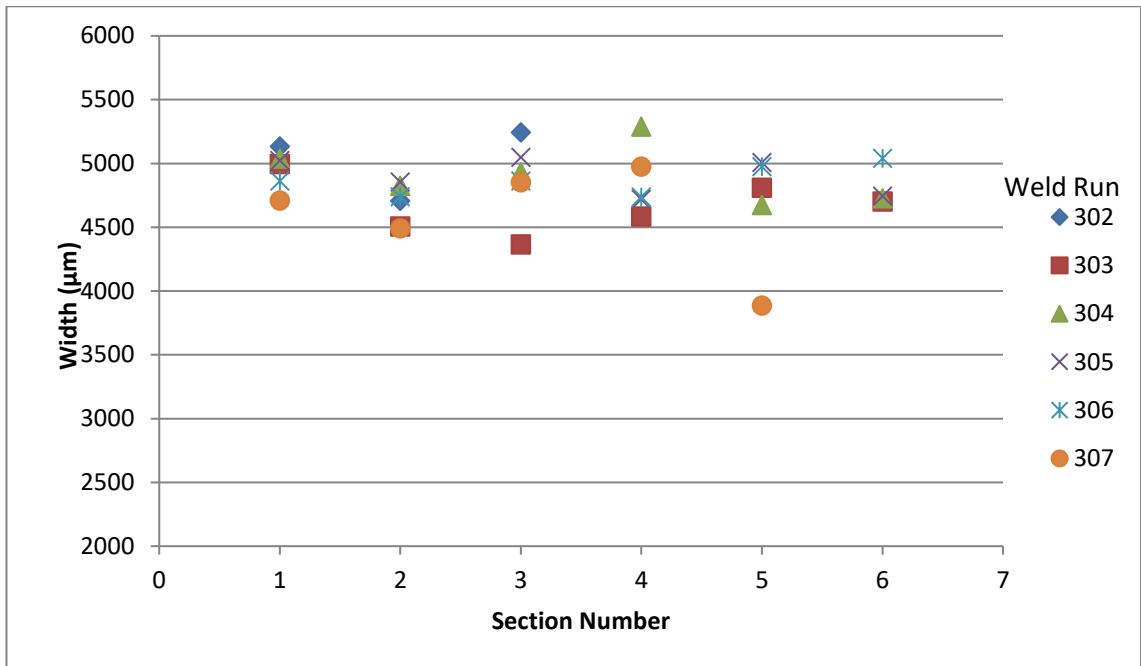


Figure 84. Graph showing the width of the HAZ for each of the CMT welds conducted at 5.5m/min (average net heat input 109.3 J/mm) on EN1.4016 grade parent material.

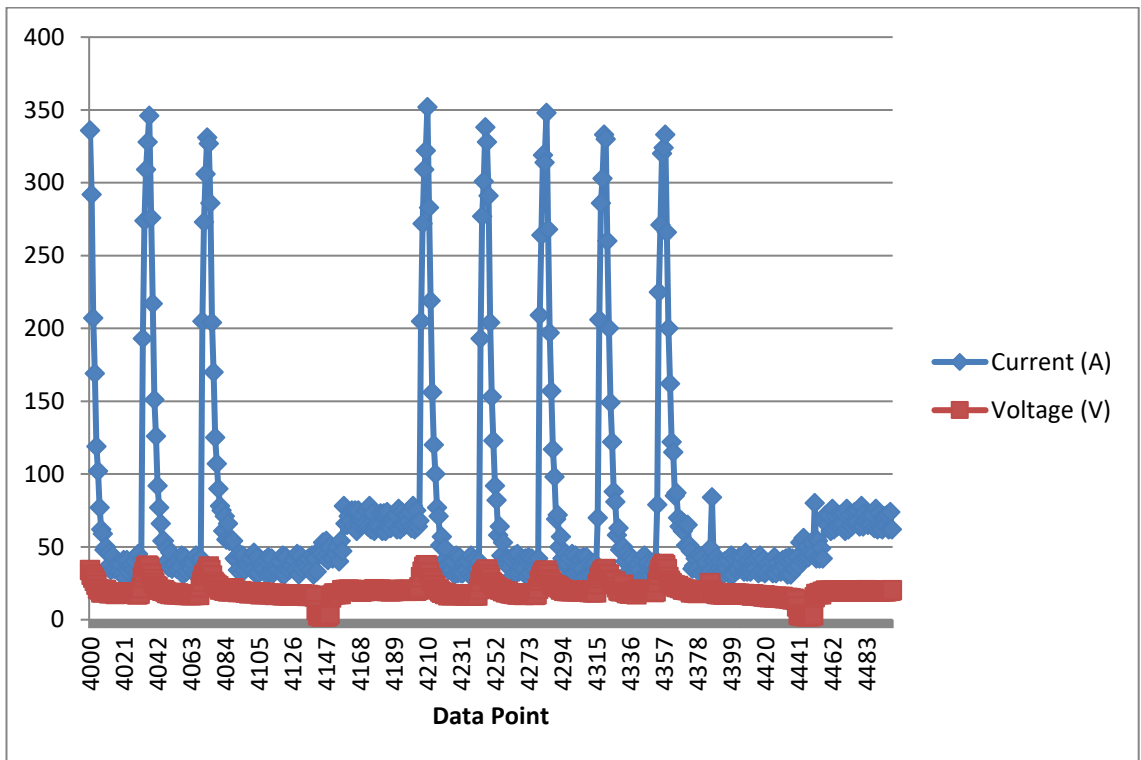


Figure 85. Graph showing the current and voltage trace for the CMT weld conducted at 3.5m/min on EN1.4016 grade parent material.

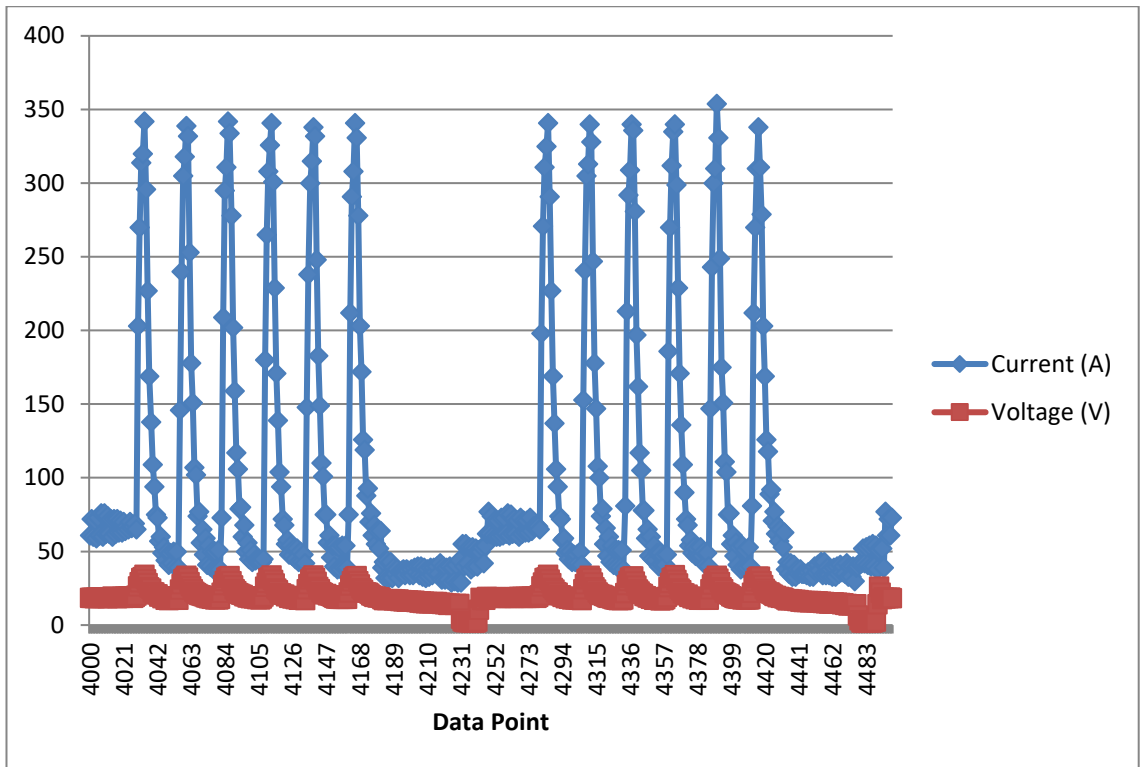


Figure 86. Graph showing the current and voltage trace for the CMT weld conducted at 4.5m/min on EN1.4016 grade parent material.

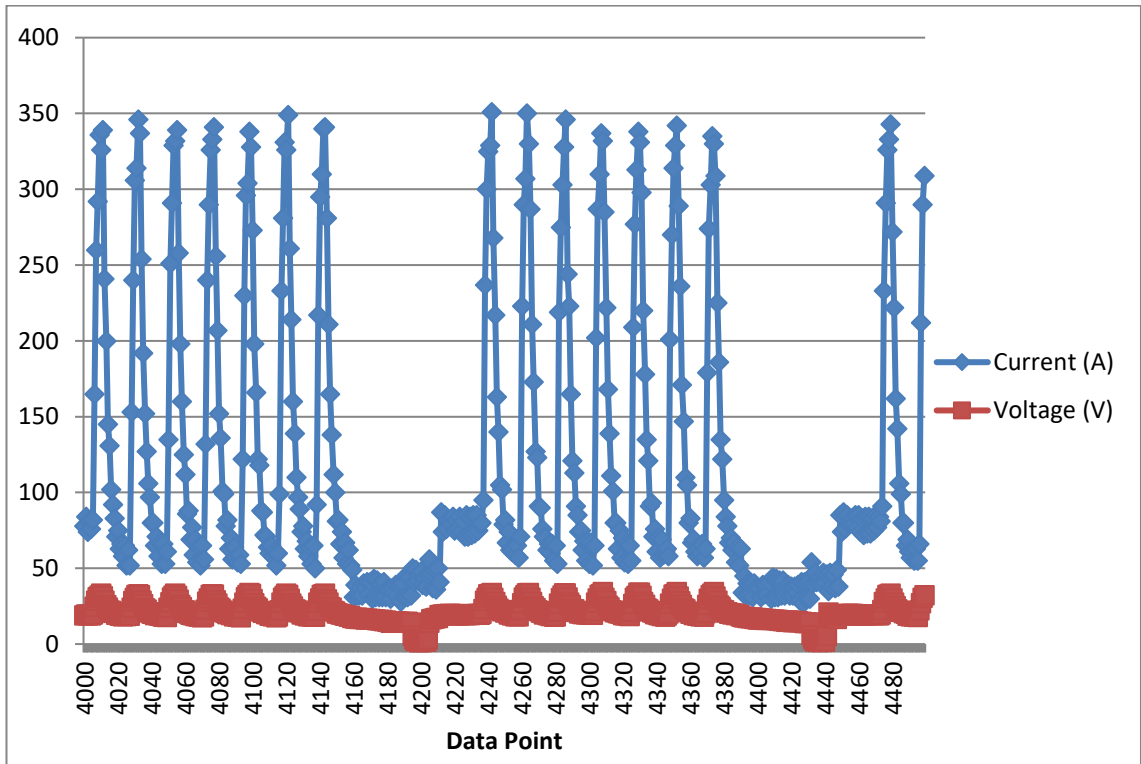


Figure 87. Graph showing the current and voltage trace for the CMT weld conducted at 5.5m/min on EN1.4016 grade parent material.

The ALX data seen in Figure 85 to Figure 87 shows the change in the cycle through variation of the power setting. So at the lower power setting the CMT cycle contains 5 pulses. In the medium power setting used in the work the CMT cycle contains 6 pulse peaks and the higher power setting used in the work had 7 pulse peaks.

4.5.2 Traverse Speed

The following two graphs (Figure 88 & Figure 89) show the variation measured in the HAZ width for each of the sections examined in each of the welds created, with the torch traverse speed at 0.762m/min and 1.27m/min. The faster speed welds showing a reduced HAZ width.

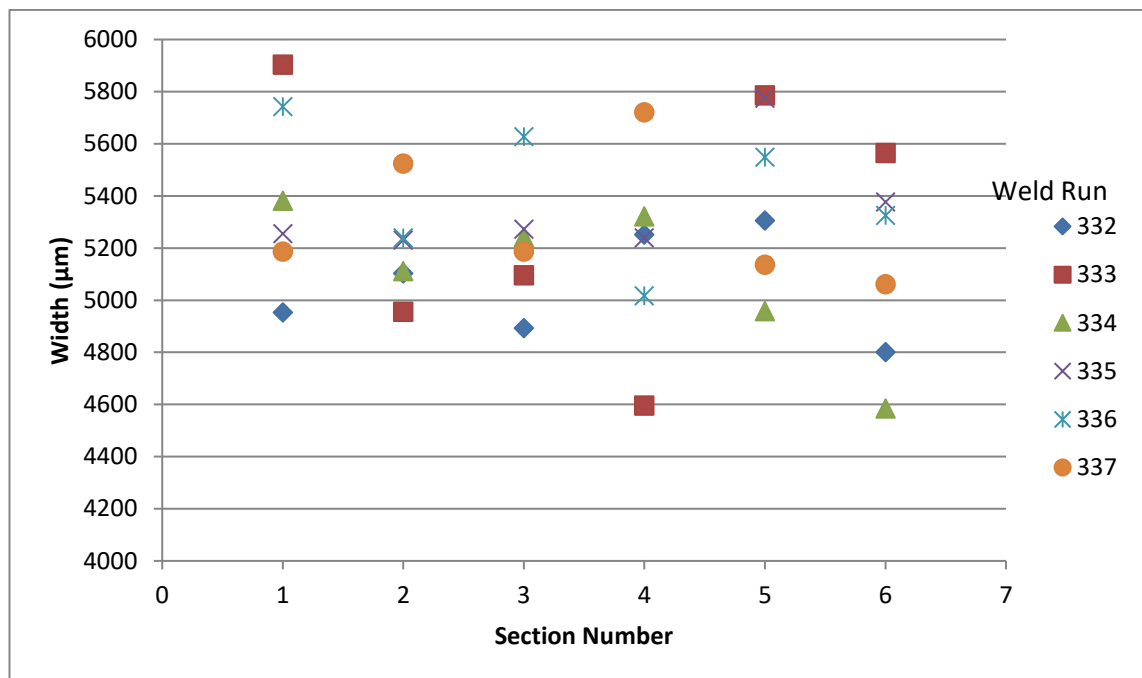


Figure 88. Graph showing the width of the HAZ for each of the CMT welds conducted at a traverse speed of 0.762m/min (average net heat input 118.3 J/mm) on EN1.4016 grade parent material.

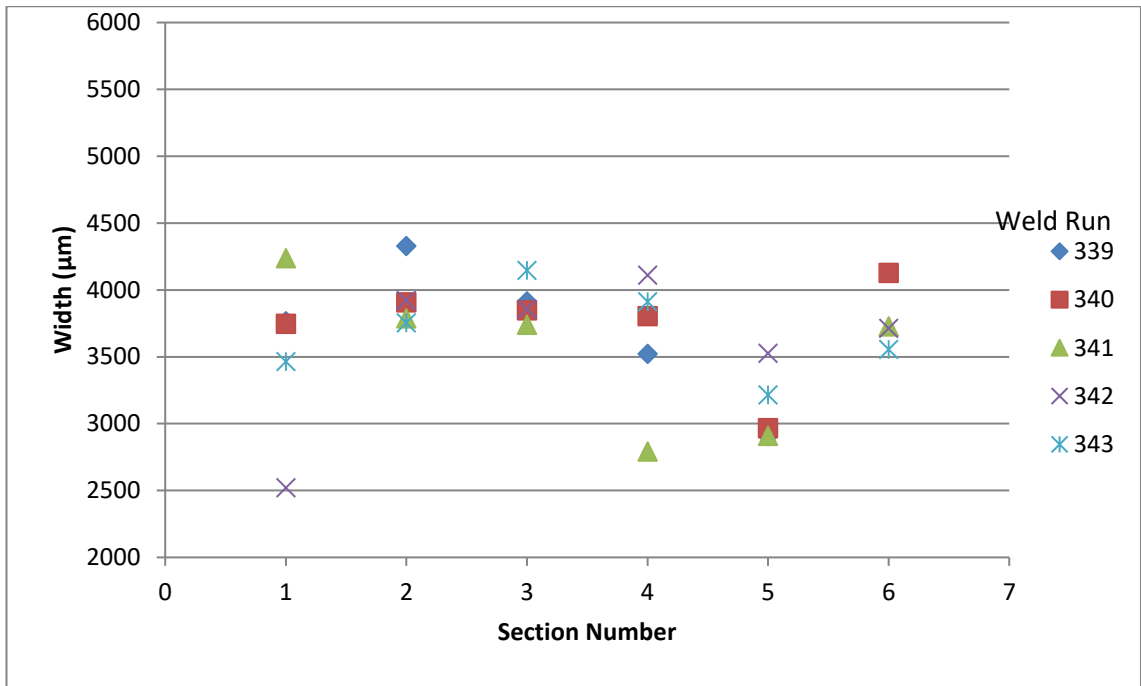


Figure 89. Graph showing the width of the HAZ for each of the CMT welds conducted at a traverse speed of 1.27m/min (average net heat input 69.6 J/mm) on EN1.4016 grade parent material.

4.5.3 Torch Angle

The following two graphs (Figure 90 & Figure 91) show the effect on the HAZ from varying the angle of the welding torch to pointed toward the direction of travel (+15°) to pointing away from the direction of travel (-15°). It can be noted that the HAZ width appear more consistent with a push angle, but with a drag angle there is a reduction in the width of the HAZ.

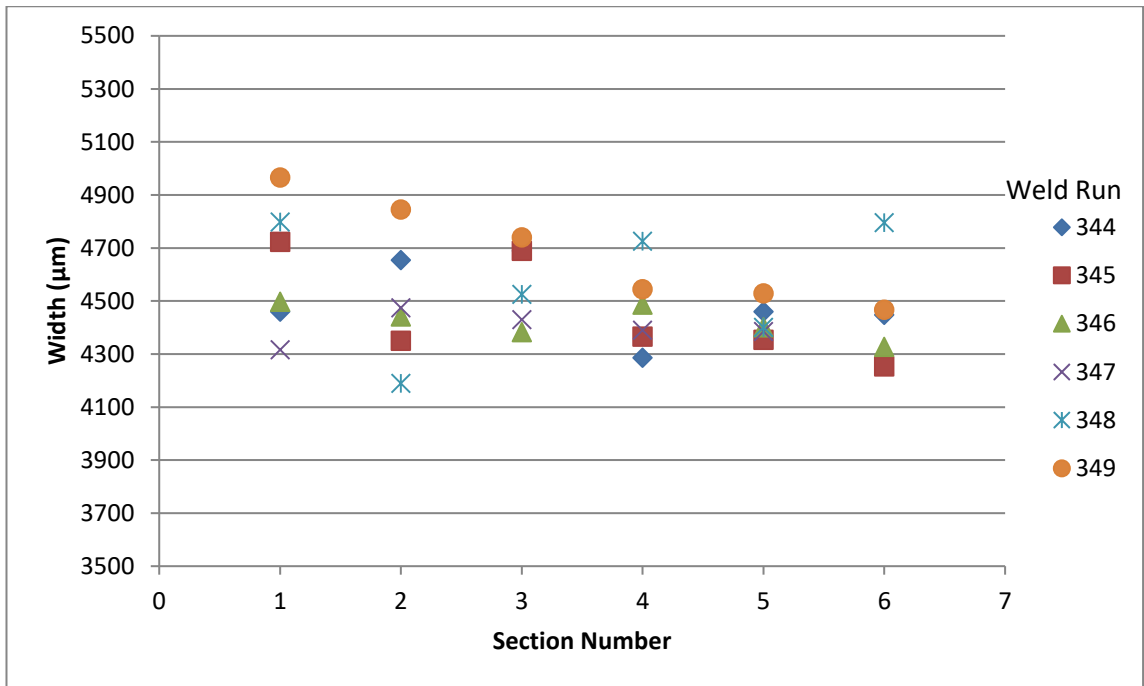


Figure 90. Graph showing the width of the HAZ for each of the CMT welds created using a torch orientation +15° to the direction of traverse on EN1.4016 grade parent material.

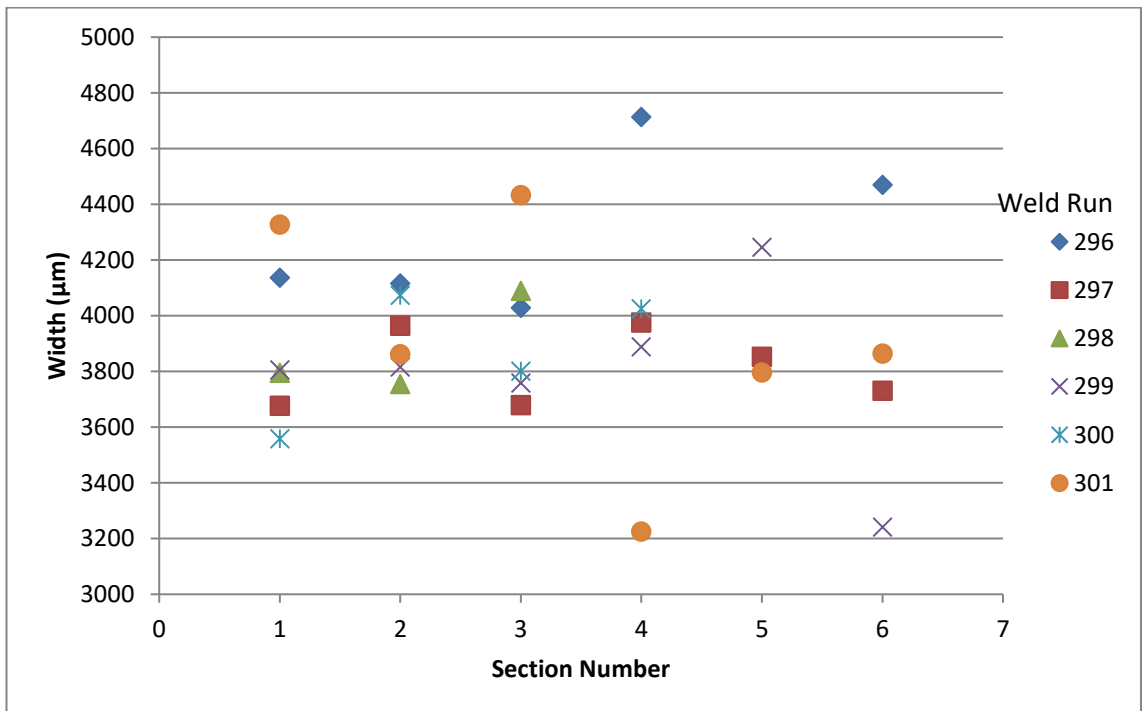


Figure 91. Graph showing the width of the HAZ for each of the CMT welds created using a torch orientation -15° to the direction of traverse on EN1.4016 grade parent material.

4.5.4 Arc Length Correction

Variation in arc length correction as seen in Figure 92 & Figure 93 has an effect on the consistency of the HAZ widths and also changing the ALC from +30 to -30 increases the HAZ width and increases the average net heat input from 87.3J/mm to 91.8 J/mm.

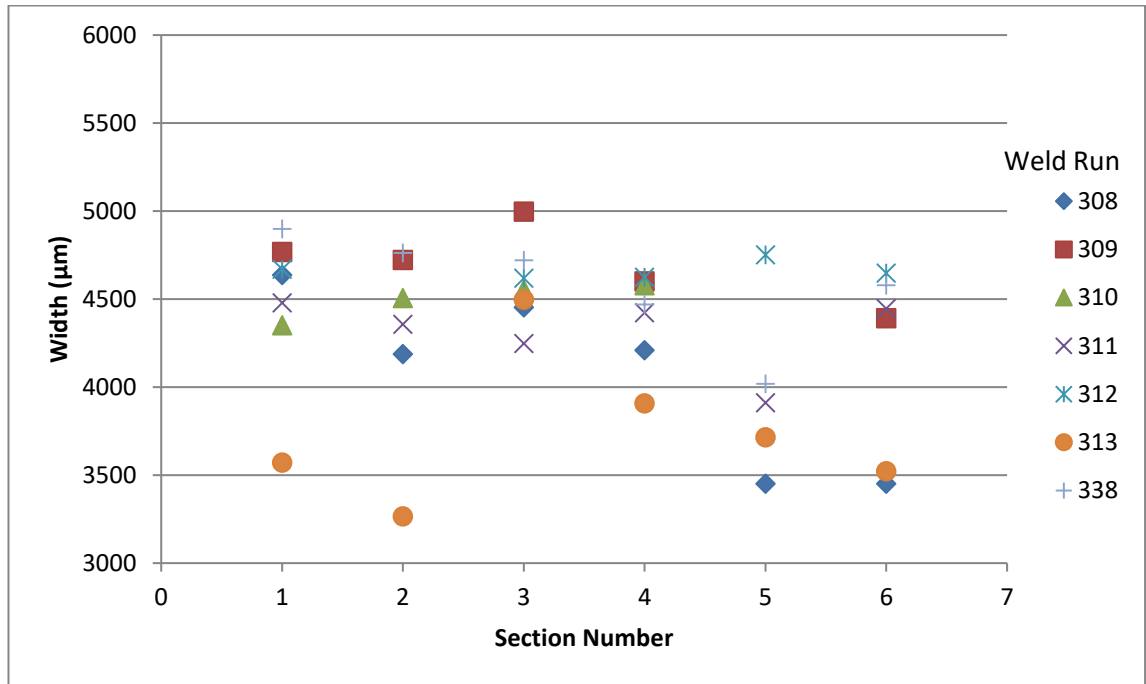


Figure 92. Graph showing the width of the HAZ for each of the CMT welds conducted with an ALC value of -30 on EN1.4016 grade parent material.

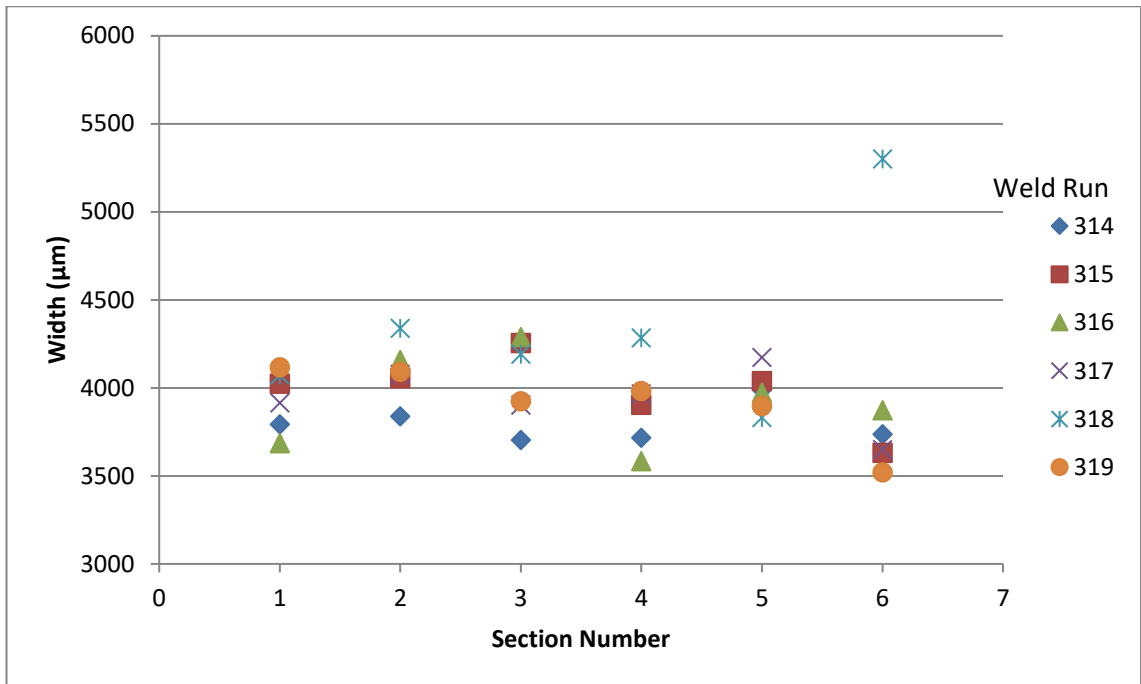


Figure 93. Graph showing the width of the HAZ for each of the CMT welds conducted with an ALC value of +30 on EN1.4016 grade parent material.

The ALX data presented in Figure 94 & Figure 95 shows a change to the short circuit phase duration as a result of the change in the ALC adjustment. Changing the ALC parameter from -30 to +30 decreases the short circuit duration phase.

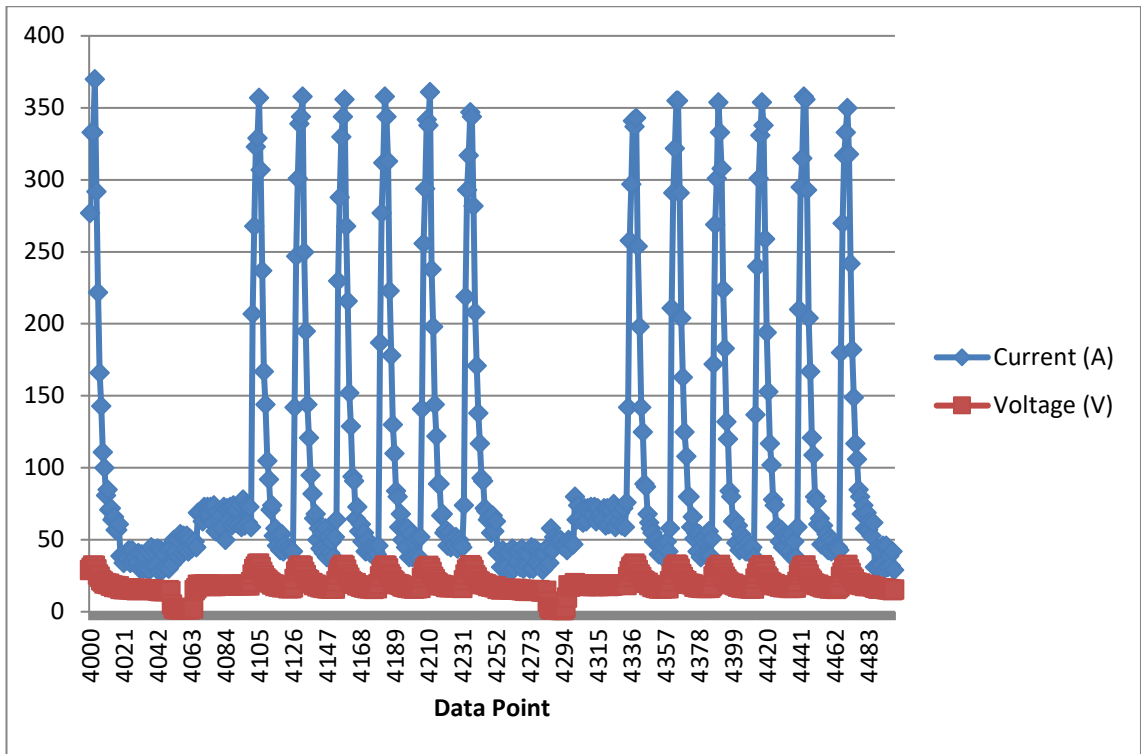


Figure 94. Graph showing voltage and current trace for a CMT weld conducted with an ALC of -30 on EN1.4016 grade parent material.

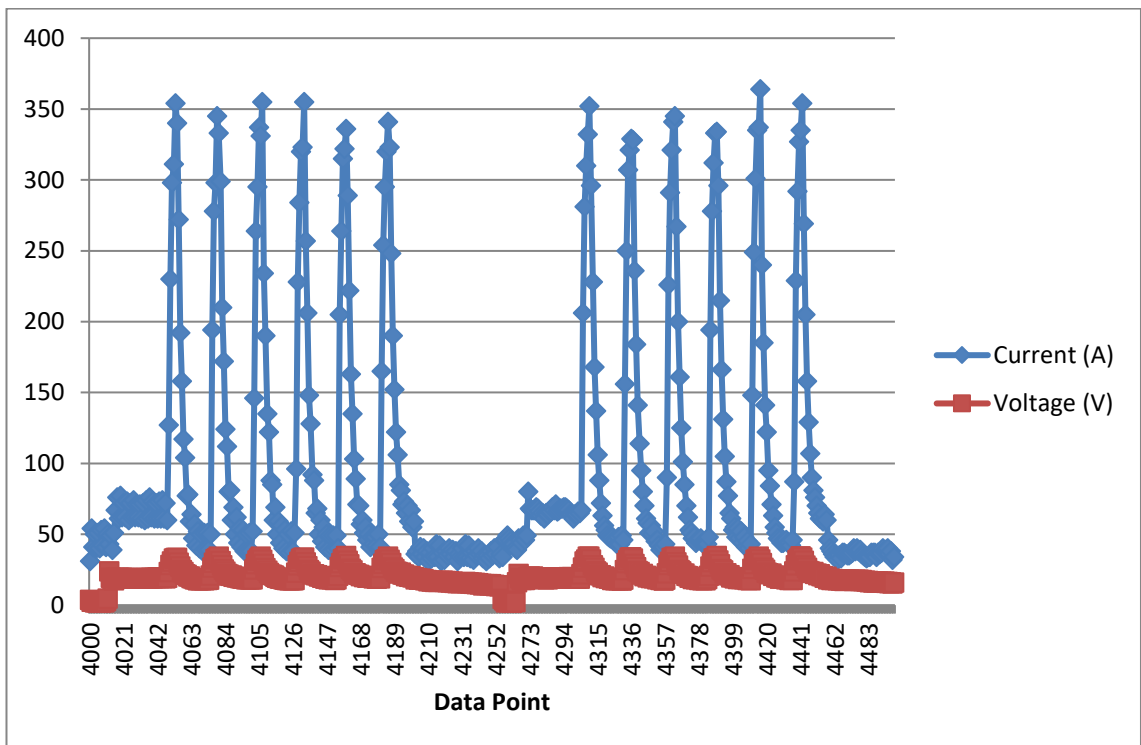


Figure 95. Graph showing voltage and current trace for a CMT weld conducted with an ALC of +30 on EN1.4016 grade parent material.

4.5.5 Pulse Correction

Within the welding programme when welding with a pulsed current is the Pulsed Correction (PC), this variable is unit-less and can be altered from -5 to +5. Variation of the Pulse Correction from -5 to +5 increases the width of the HAZ but doesn't show any change in the consistency of the HAZ widths, this is seen in Figure 96 & Figure 97.

Figure 98 & Figure 99 show the ALX data for the change in PC and as can be seen, there is an increase of over 100 amps in the peak pulse current going from a PC setting of -5 to +5, there is also an effect on the duration of the short circuit phase, with the PC parameter at +5, showing a longer short circuit duration.

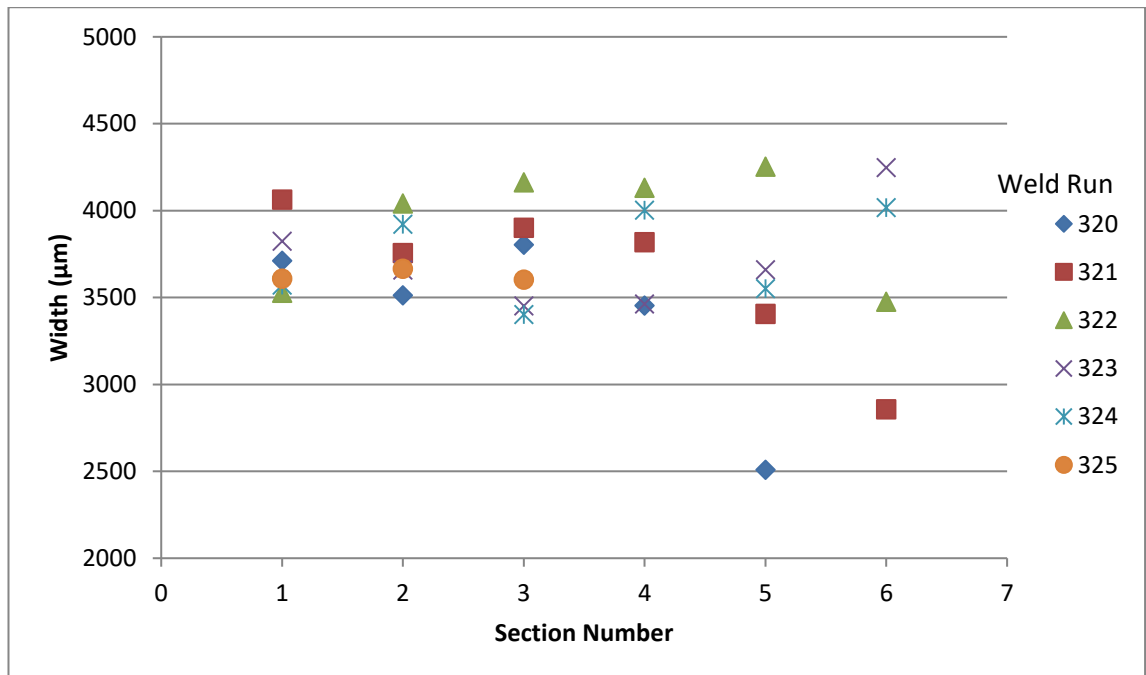


Figure 96. Graph showing the width of the HAZ for each of the CMT welds conducted with a PC of -5 on EN1.4016 grade parent material.

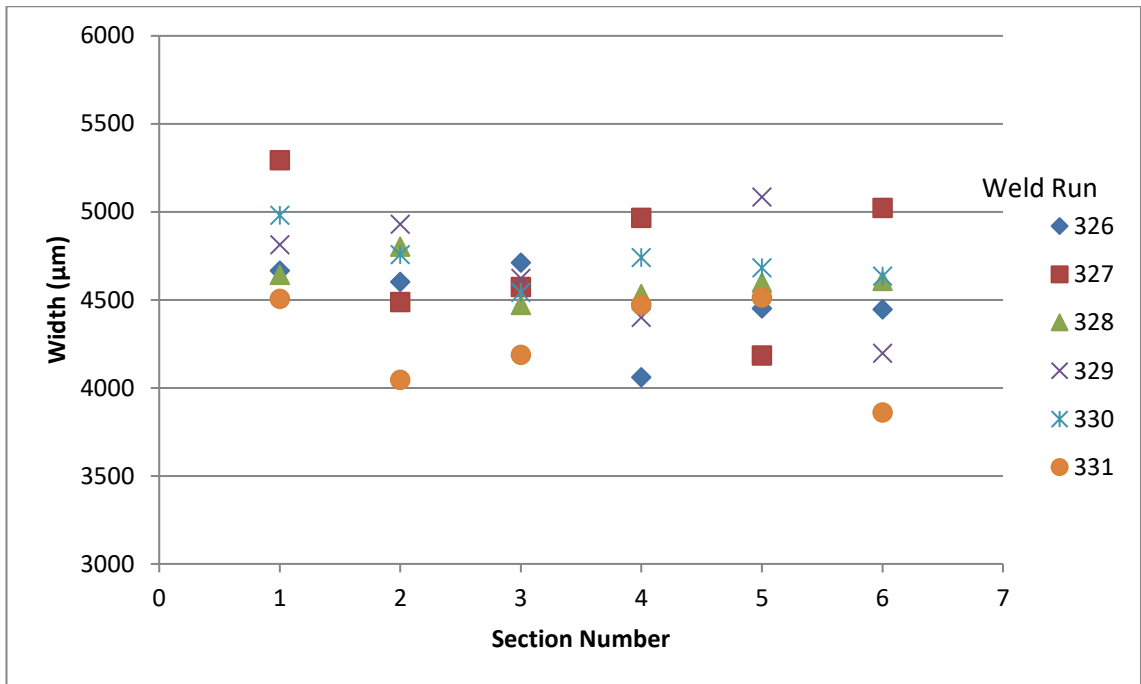


Figure 97. Graph showing the width of the HAZ for each of the CMT welds conducted with a PC of +5 on EN1.4016 grade parent material.

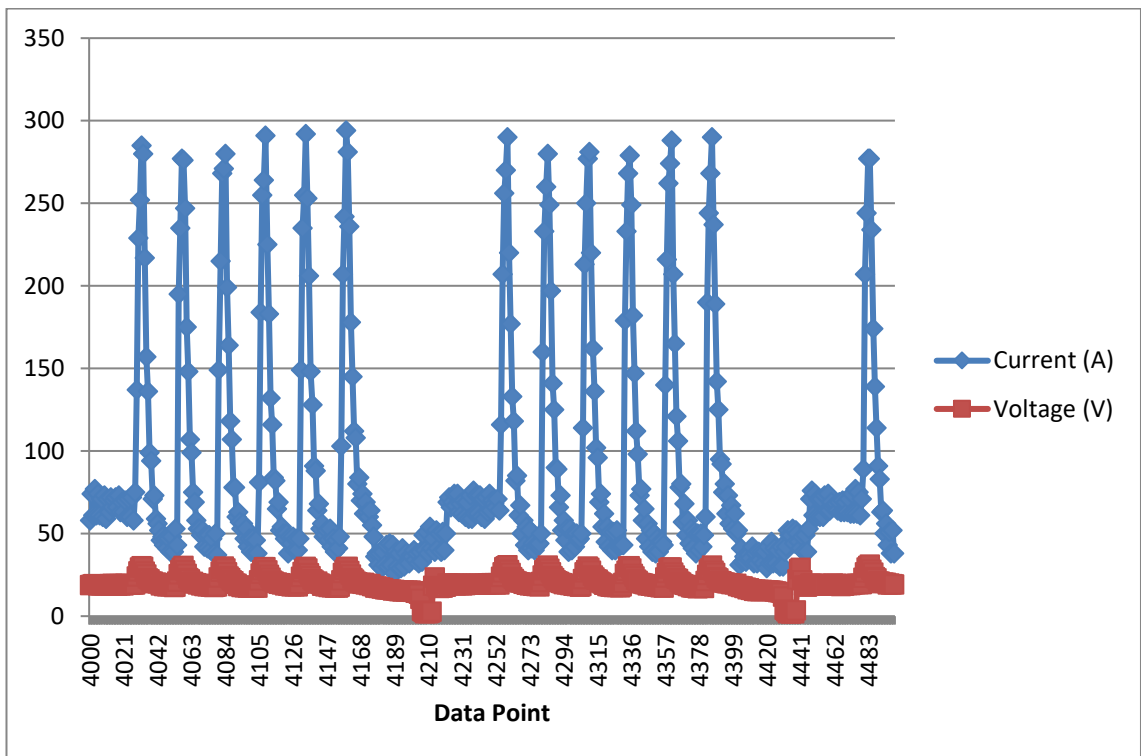


Figure 98. Graph showing the current and voltage trace for a CMT weld conducted with a pulse correction of -5 on EN1.4016 grade parent material.

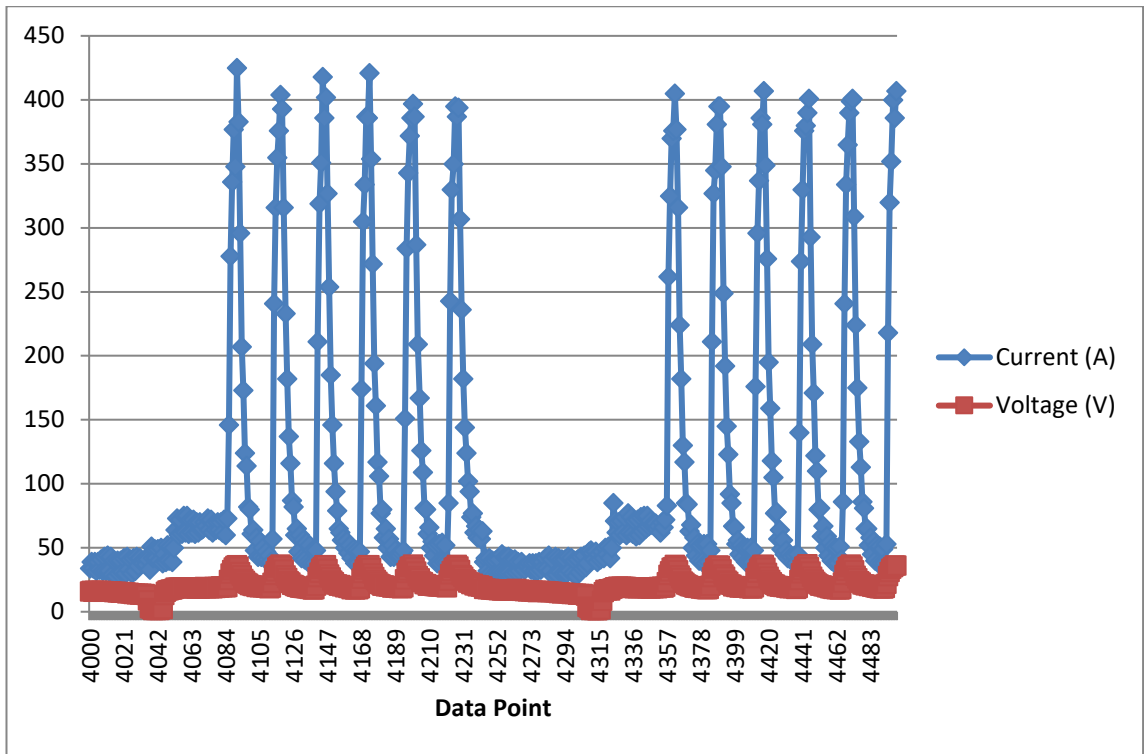


Figure 99. Graph showing the current and voltage trace for a CMT weld conducted using a pulse correction of +5 on EN1.4016 grade parent material.

4.6 Comparison of CMT Welded and MAG Welded EN 1.4003 Parent Material in 3.8mm & 5.8mm Thicknesses

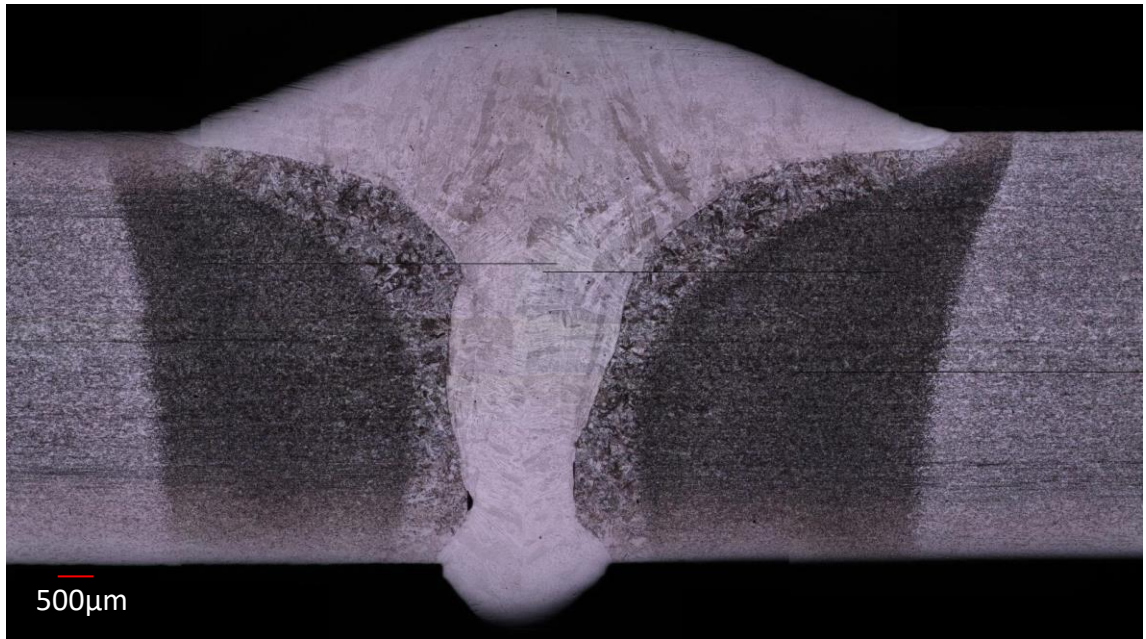


Figure 100. CMT weld cross section of the 5.8mm thick EN1.4003 grade parent material

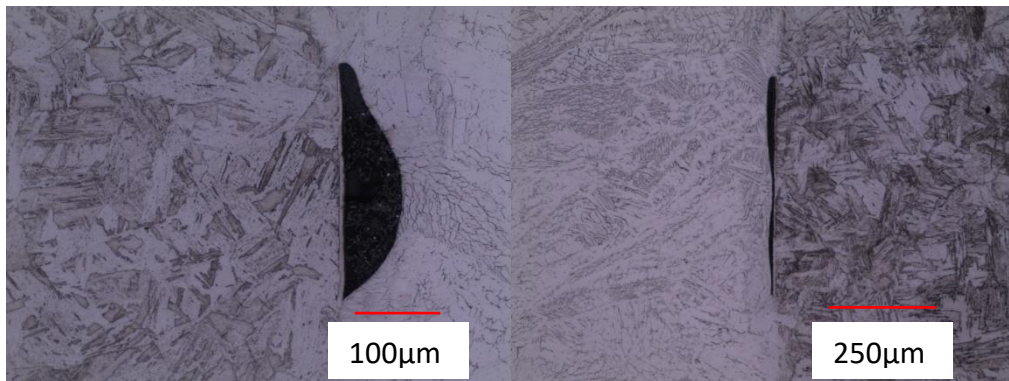


Figure 101. Lack of side wall fusion in CMT weld produced using the 5.8mm thick EN1.4003 grade material.

4.7 CMT/MAG 1.4003 Comparison Trial

The following section reports the results from the trial comparing the CMT and MAG welding processes using EN1.4003 grade ferritic stainless steel. Initial assessments were made of the welds using radiography to try and identify defects in the welds. Subsequently presented are the results from destructive mechanical assessments that were made including tensile, impact, fatigue tests and microstructural examination.

4.7.1 Non Destructive Examination and Destructive Validation

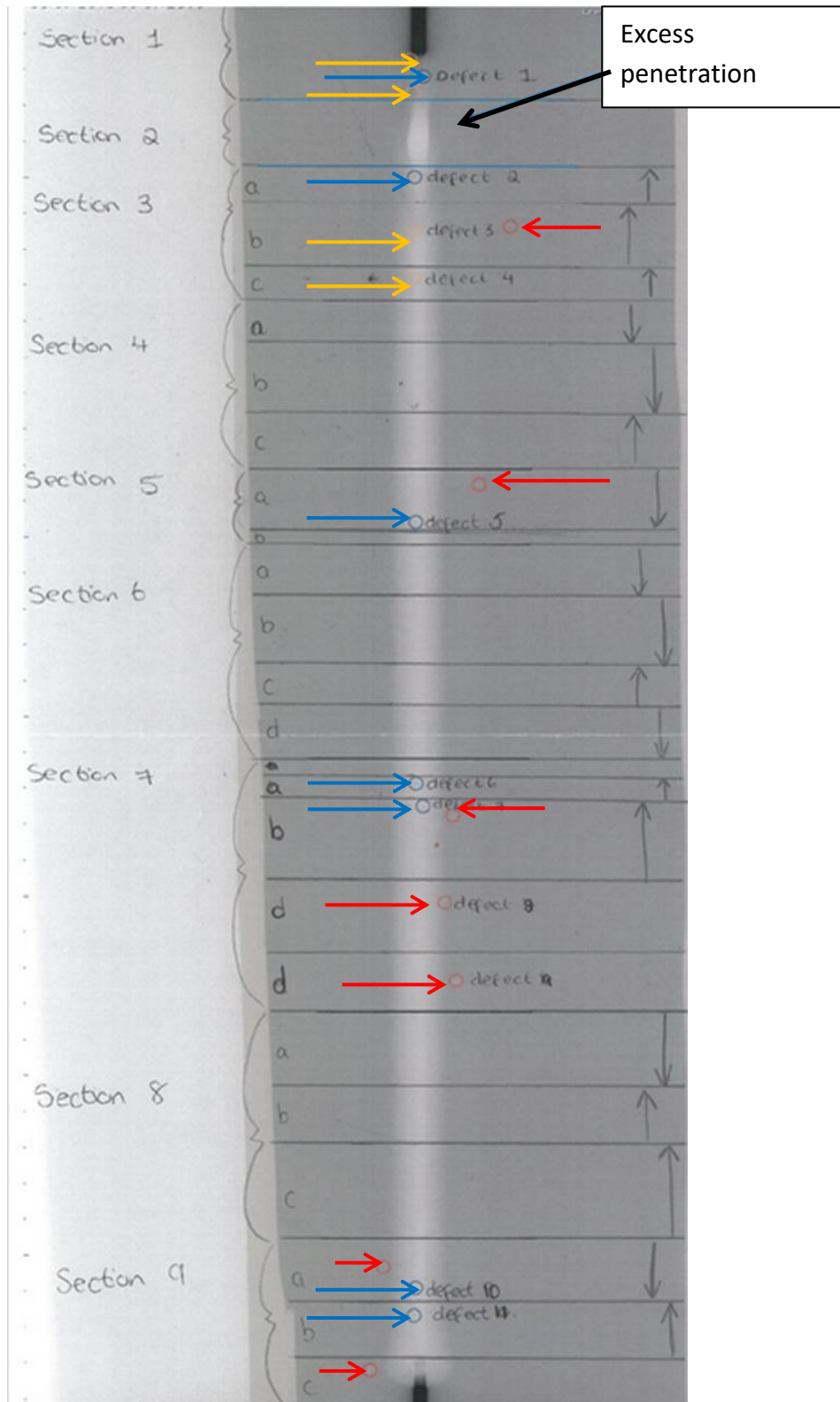


Figure 102. Showing radiograph for test weld that was sectioned to destructively examine, with identification of indications observed through examination of the radiograph and suggested possibility of defect type. Red arrows showing spatter, blue arrows showing gas porosity and yellow arrows showing indications of a lack of side wall fusion.

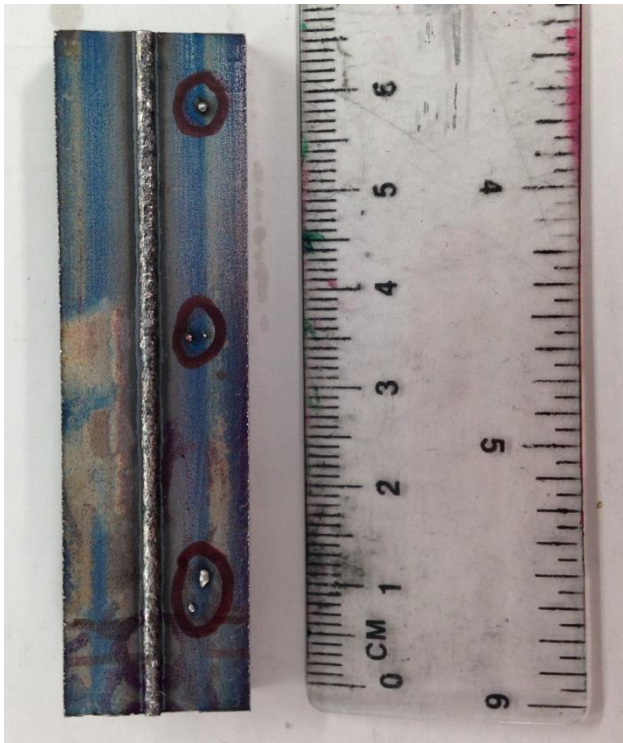


Figure 103. showing section 7 of the weld, the three pieces of spatter circled (Robinson, 2014)

Section	Defect(s) Observed
1	Lack of side wall fusion
2	Excess penetration
3a	Excess penetration
3b	Lack of side wall fusion
3c	Lack of side wall fusion
4a	Gas porosity & Lack of side wall fusion
5a	Gas porosity
6a	Lack of side wall fusion
6b	Lack of side wall fusion
7a	Lack of side wall fusion
7c	Spatter
7d	Spatter
8b	Lack of side wall fusion
8c	Gas porosity & Lack of side wall fusion
9a	Gas porosity & Lack of side wall fusion
9b	Lack of side wall fusion
9c	Gas porosity & incomplete penetration

Table 20. Table showing defects observed through microstructural examination of EN1.4003 5.8mm thick CMT welded plate. The sample identification numbers in the left hand column are based on those presented in Figure 102.

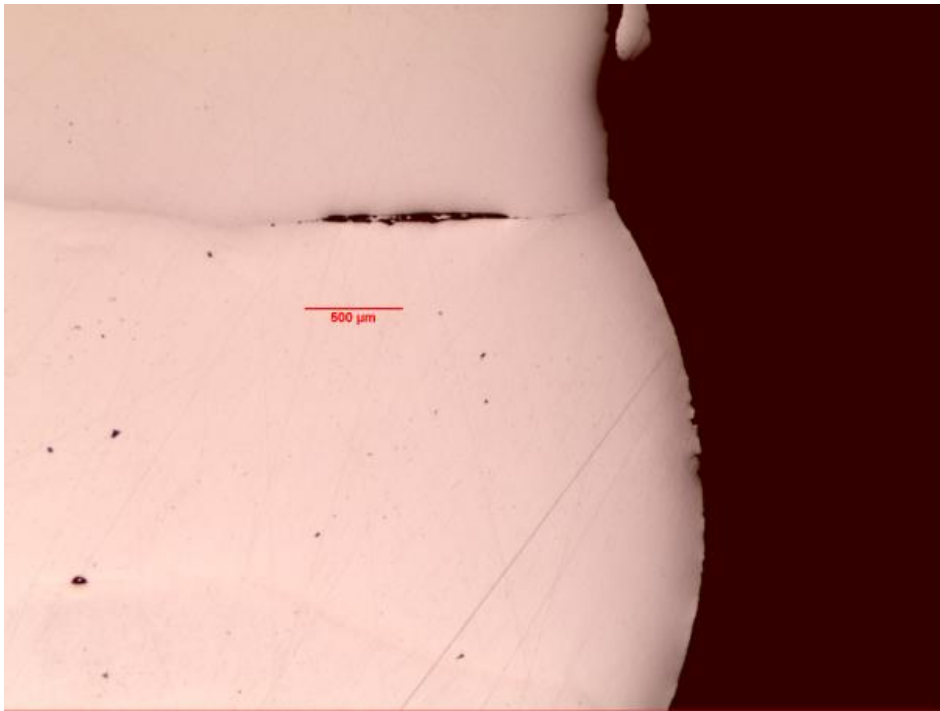


Figure 104. Lack of side wall fusion in root of section 1a of CMT welded 5.8mm thick EN1.4003 (Robinson, 2014).

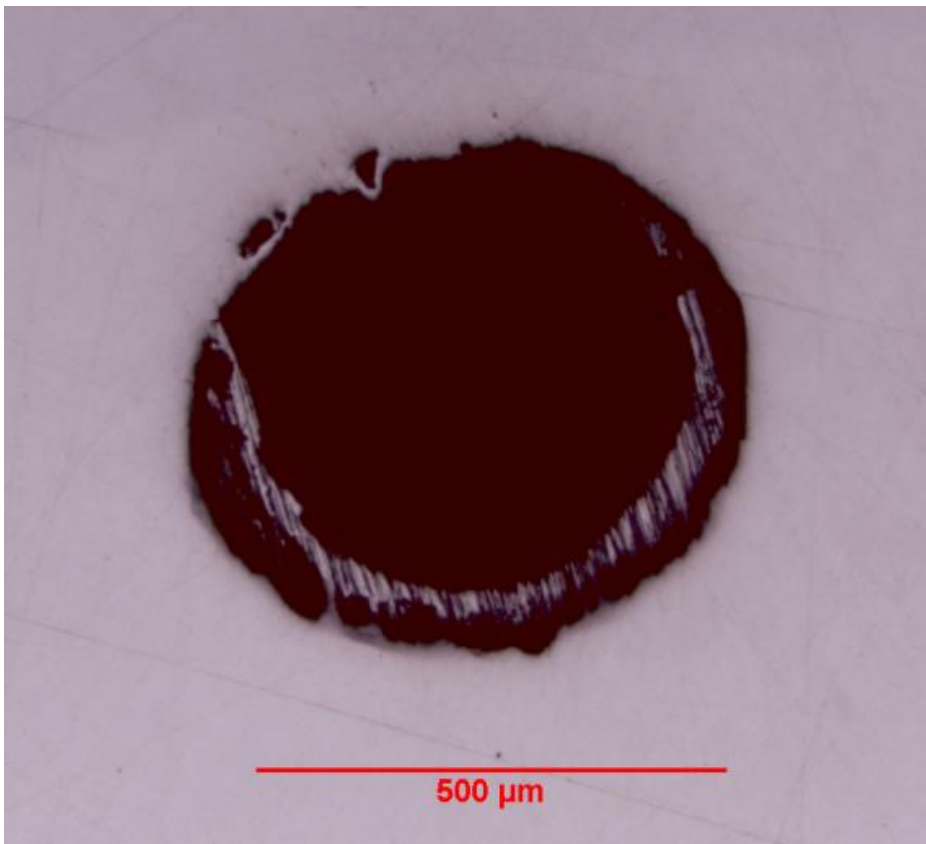


Figure 105. Showing gas porosity in section 5a of CMT welded 5.8mm thick EN1.4003 (Robinson, 2014).

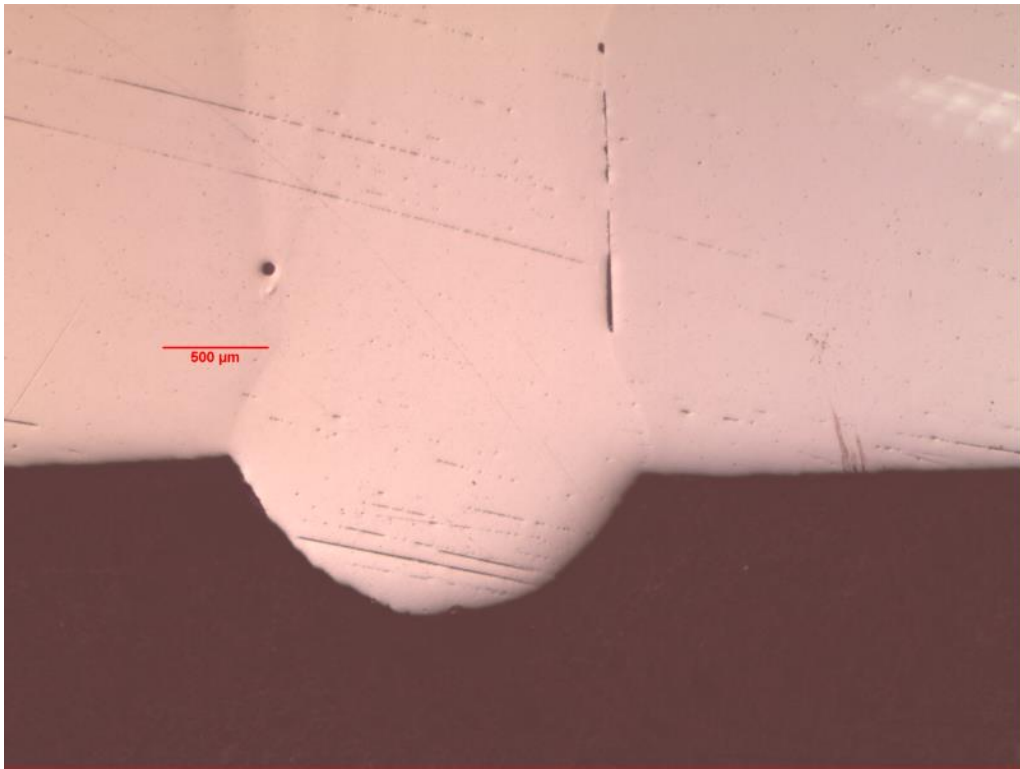


Figure 106. Gas porosity (left) lack of side wall fusion (right) in section 9a of CMT welded 5.8mm thick EN1.4003 (Robinson, 2014).

4.7.2 Comparison of Microstructural Analysis of CMT & MAG Welds in

3.8mm Thick EN1.4003 Parent Material

As has been discussed the low level of chromium within this grade of stainless steel means during welding a portion of the parent material adjacent the weld experiences temperatures sufficient to cause microstructural changes, such as a phase change to martensite and with an increase in temperature grain coarsening also occurs. Therefore within the welded EN1.4003 material, it would be expected to observe an area of the HAZ, next to the fusion zone with a martensitic structure and a coarsened grain size as this area will have been subjected to temperatures up to the melting point of the material. As the distance increases away from the fusion zone, the temperatures experienced will be reducing and therefore there would be a component of the HAZ that has reached temperatures sufficient to change the microstructure but not high enough to cause grain coarsening. Moving further away from the fusion zone, there wouldn't be sufficient heat to cause any change to the parent material and therefore this area is as the parent material supplied and falls outside of the HAZ.

Any change within the parent as a result of the thermal input of welding is the HAZ. The following section examines and quantifies the effects on the microstructure within the HAZ for welds created in the 3.8mm thick EN1.4003 parent materials for welds created using CMT and welds created using the MAG process.

Welding Process	Average Grain Coarsened HAZ Width (μm)	Average Total HAZ Width (μm)	Average Grain Diameter (μm)
CMT	1067	4447	93
MAG	1184	4727	117

Table 21. Showing average measured values for the HAZ in the coarse region and the entire HAZ width and the grain size taken in the coarse region of the HAZ of 3.8mm thick EN1.4003 grade parent material.

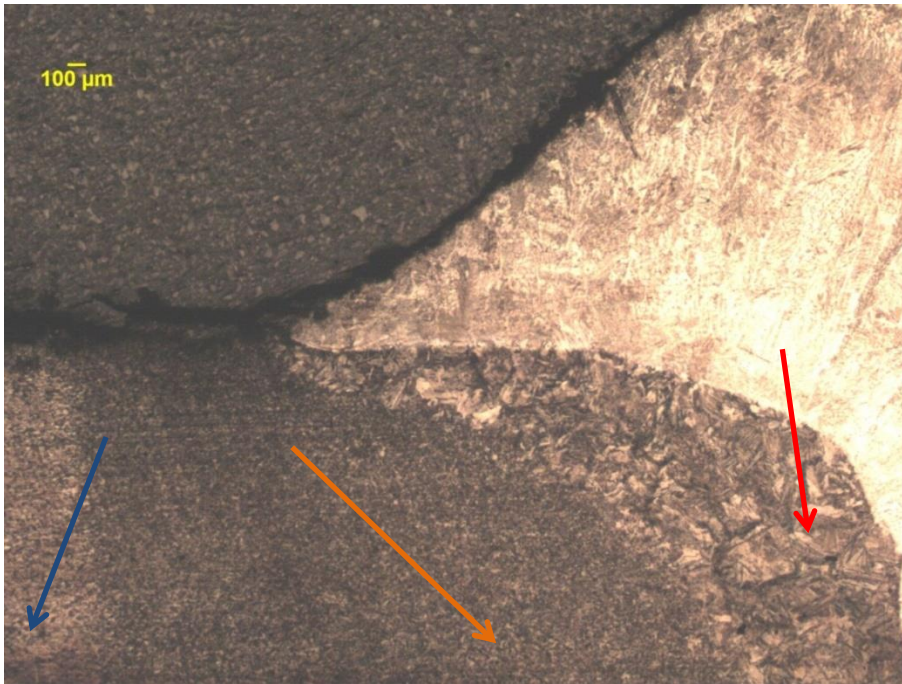


Figure 107. Image showing weld (top right) and HAZ , which has two distinct regions, the first next to the weld (red arrow) has a martensitic structure and grain coarsening, the second region of the HAZ (orange arrow) has a martensitic structure but without any grain coarsening and then the blue arrow indicates unaffected parent material of 3.8mm thick EN1.4003 parent, CMT welded sample 25.10 (etched in glyceresia).



Figure 108. Image showing weld (top right) and grain coarsened with martensite HAZ (mid image) and martensite HAZ (bottom left) of 3.8mm thick EN1.4003 parent, CMT welded sample 25.10 (etched in glyceresia)

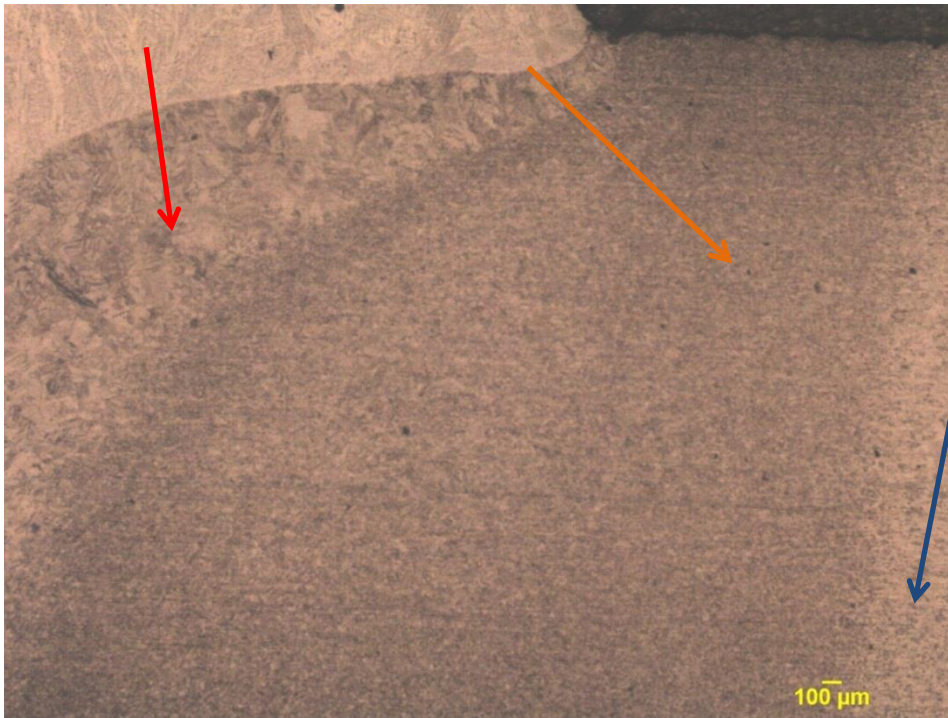


Figure 109. Image showing weld (top left) and HAZ , which has two distinct regions, the first next to the weld has a martensitic structure and grain coarsening (red arrow), the second region of the HAZ (orange arrow) has a martensitic structure but without any grain coarsening and then the blue arrow indicates unaffected parent material of 3.8mm thick EN1.4003 parent, MAG welded sample 30.7 (etched in glycergia).



Figure 110. Image showing weld (top left) and twin region HAZ (mid image & bottom right) of 3.8mm thick EN1.4003 parent, MAG welded sample 30.7 (etched in glycergia).

4.7.3 Tensile Data of CMT and MAG Welded Joints

Sample ID	0.2% Proof Strength (MPa)	Maximum Strength (MPa)	Elongation (%)	Failure Location
25.1	354	488	21	Parent
25.2	354	485	19	Parent
25.3	362	490	21	Parent
25.4	364	489	21	Parent
25.5	358	483	21	Parent
25.6	352	479	21	Parent
25.7	360	485	21	Parent
25.8	362	487	21	Parent
26.1	369	490	21	Parent
26.2	367	492	21	Parent
26.3	364	490	21	Parent
26.4	370	493	21	Parent
26.5	364	490	21	Parent
26.6	369	493	23	Parent
26.7	369	492	21	Parent
26.8	371	493	21	Parent
Average	363.0	488.7	21	
Standard Deviation	6.1	4.0	0.7	
Coefficient of Variation	1.68%	0.82%	3.33%	

Table 22. CMT 3.8mm EN1.4003 Tensile results.

Sample ID	0.2% Proof Strength (MPa)	Maximum Strength (MPa)	Elongation (%)	Failure Location
M28.9*	326	483	9	Spatter
M28.10	345	489	20	Parent
M28.11	349	488	20	Parent
M28.12	350	489	19	Parent
M28.13	349	491	20	Parent
M28.14	353	487	20	Parent
M28.15	349	487	19	Parent
M28.16	348	489	20	Parent
M30.9	361	488	17	Parent
M30.10	361	491	19	Parent
M30.11	364	493	19	Parent
M30.12	364	493	19	Parent
M30.13	361	489	19	Parent
M30.14	364	495	17	Parent
M30.15	363	494	17	Parent
M30.16	355	494	19	Parent
Average	355.7	490.5	18.9	
Standard Deviation	7.0	2.7	1.1	
Coefficient of Variation	1.97%	0.55%	5.82%	

Table 23. MAG 3.8mm EN1.4003 Tensile results. (* sample M28.9 not included in calculations as failed next to spatter).

	0.2% Proof Strength	Maximum Strength	Elongation
T Test - P value	0.004	0.162	9.174E-07

Table 24. Statistical T.Test P values comparing the data for the 3.8mm thick CMT and MAG welded tensile data.

Sample ID	0.2% Proof Strength (MPa)	Maximum Strength (MPa)	Elongation (%)	Failure Location
50.9	312	447	26	Parent
50.10	307	441	13	Weld
50.11	307	441	21	Parent
50.12	308	445	27	Parent
50.13	312	450	26	Parent
50.14	310	446	29	Parent
50.15	315	455	30	Parent
50.16	312	446	30	Parent
52.1	309	447	24	Parent
52.2	314	451	27	Parent
52.3	309	447	30	Parent
52.4	310	448	30	Parent
52.5	314	453	26	Parent
52.6	315	453	30	Parent
52.7	312	450	29	Parent
52.8	313	454	27	Parent
Average	311.2	448.4	26.6	
Standard Deviation	2.7	4.2	4.4	
Coefficient of Variation	0.87%	0.94%	16.54%	

Table 25. CMT 5.8mm EN1.4003 Tensile results.

Sample ID	0.2% Proof Strength (MPa)	Maximum Strength (MPa)	Elongation (%)	Failure Location
M1.1	279	381	7	Weld
M1.2	297	410	9	Weld
M1.3	318	459	23	Parent
M1.4	317	458	23	Parent
M1.5	311	441	10	Weld
M1.6	314	455	21	Parent
M1.7	312	416	7	Weld
M1.8	315	422	7	Weld
M11.1	274	345	4	Weld
M11.2	307	430	7	Weld
M11.3	318	463	23	Parent
M11.4	316	462	24	Parent
M11.5	314	419	7	Weld
M11.6	316	445	9	Weld
M11.7	318	447	9	Weld
M11.8	312	391	6	Weld
Average	308.6	427.8	12.3	
Standard Deviation	13.6	33.5	7.5	
Coefficient of Variation	4.41%	7.83%	60.98%	

Table 26. MAG 5.8mm EN1.4003 Tensile results.

	0.2% Proof Strength	Maximum Strength	Elongation
T Test - P value	0.466	0.021	2.724E-07

Table 27. Statistical T.Test P values comparing the data for the 5.8mm thick CMT and MAG welded tensile data.

4.7.4 Impact Results of CMT and MAG Welded Joints

Sample ID	Impact Strength (kJ/m ²)
25.11	757
25.12	724
25.13	724
25.14	2928
25.15	789
26.11	954
26.12	724
26.13	1086
26.14	789
26.15	757
Average	1023
Standard Deviation	680
Coefficient of variation (%)	66

Table 28. Impact test results for CMT welded 3.8mm thick EN1.4003.

Sample ID	Impact Strength (kJ/m ²)
M28.2	1283
M28.3	329
M28.4	1349
M28.5	1480
M28.6	855
M30.2	2204
M30.3	921
M30.4	954
M30.5	296
M30.6	362
Average	1003
Standard Deviation	602
Coefficient of variation (%)	60

Table 29. Impact test results for MAG welded 3.8mm thick EN1.4003.

T Test - P value	0.945957
------------------	----------

Table 30. Statistical T.Test P values comparing the data for the 3.8mm thick CMT and MAG welded impact data.

Sample ID	Impact Strength (kJ/m ²)
5.1	776
5.2	733
5.3	668
5.4	841
5.5	1078
52.11	603
52.12	884
52.13	625
52.14	754
52.15	517
Average	748
Standard Deviation	161
Coefficient of variation (%)	21

Table 31. Impact test results for CMT welded 5.8mm thick EN1.4003.

Sample ID	Impact Strength (kJ/m ²)
M1.11	797
M1.12	560
M1.13	1272
M1.14	1078
M1.15	625
M11.1	711
M11.2	754
M11.3	474
M11.4	625
M11.5	560
Average	746
Standard Deviation	250
Coefficient of variation (%)	34

Table 32. Impact test results for MAG welded 5.8mm thick EN1.4003.

T Test - P value	0.981952
------------------	----------

Table 33. Statistical T.Test P values comparing the data for the 5.8mm thick CMT and MAG welded impact data.

Step Divide: 0.5kN

Least Frequent Event: Runouts

Calculated Mean: $x = 41.5 + 0.5 \left(\frac{47}{11} - \frac{1}{2} \right)$

$$x = 43.386 \text{ kN}$$

Convergence Factor: $= \left(\frac{(11 \times 321) - 47^2}{11^2} \right)$

$$= 10.926$$

Standard Deviation: $s = 1.620 \times 0.5 \left(\frac{(11 \times 321) - 47^2}{11^2} + 0.029 \right)$

$$s = 8.873 \text{ kN}$$

Standard Error for Mean: $s_x = \frac{8.873}{\sqrt{11}} \cdot 1.15$

$$s_x = 3.076 \text{ kN}$$

Line Load: $= 964.13 \text{ N/mm}$

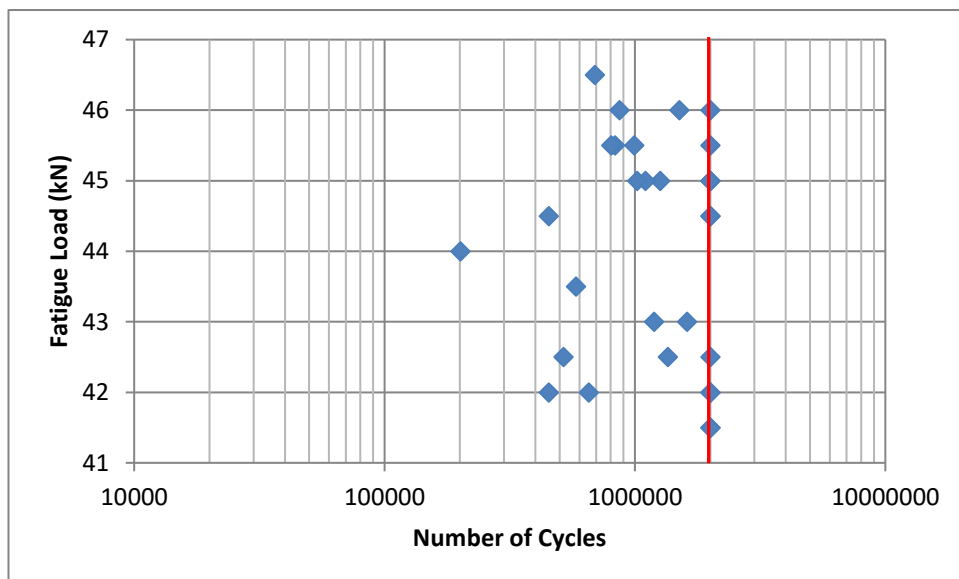


Figure 112. Graph to show fatigue load range for CMT welded 3.8mm thick EN1.4003 (red line indicates the pass criteria of 2 million cycles).

	Sample	1	2	3	4	5	6	7	8	9	10	11	12	13	14	15	16	17	18	19	20	21	22	23	24	25	Number of		Using LFE as N	
Load kN	Step (i)																										Runouts (r)	Failures (f)	iN	i ² N
38.5	3						X						X		X		X										0	4	12	36
35.5	2	X				0		X		X		0		0		0		X				X		X		0	5	6	12	24
32.5	1		X		0				0		0								X		0		0		0		6	2	2	2
29.5	0			0																	0						2	0	0	0
26.5																														
																											Σr	Σf	ΣiN	Σi^2N
																											13	12	26	62

Figure 113. Staircase Fatigue results for the MAG welded samples.

Step Divide: 3.0kN

Least Frequent Event: Failures

Calculated Mean:

$$x = 29.5 + 3 \left(\frac{26}{12} + \frac{1}{2} \right)$$

$$x = 37.5 \text{ kN}$$

Convergence Factor:

$$= \left(\frac{(12 \times 62) - 26^2}{12^2} \right)$$

$$= 0.472$$

Standard Deviation:

$$s = 1.620 \times 3 \left(\frac{(12 \times 62) - 26^2}{12^2} + 0.029 \right)$$

$$s = 2.435 \text{ kN}$$

Standard Error for Mean:

$$s_x = \frac{2.435}{\sqrt{12}} \cdot 1.15$$

$$s_x = 0.808 \text{ kN}$$

Line Load:

$$= 833.33 \text{ N/mm}$$

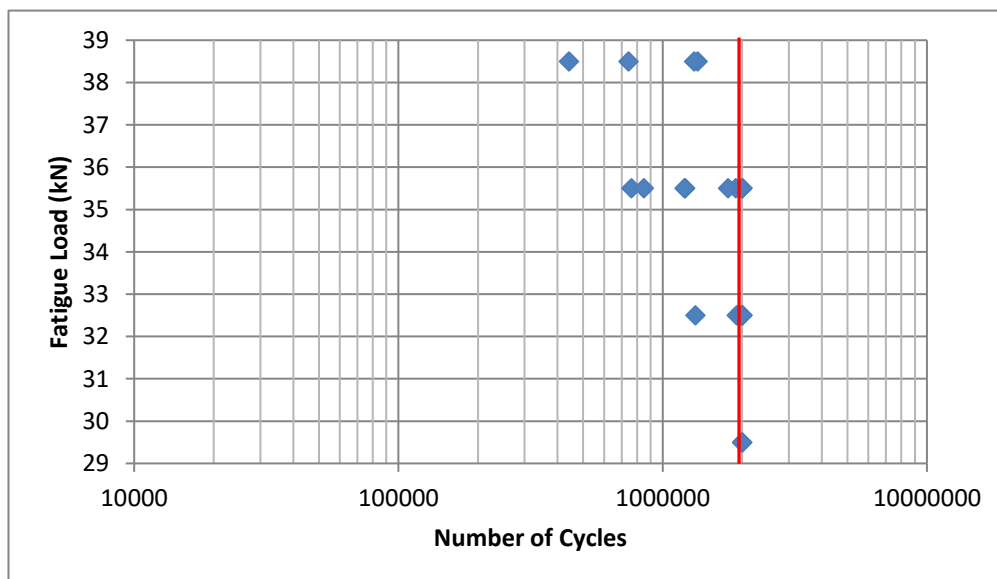


Figure 114. Graph to show fatigue load range for MAG welded 3.8mm thick EN1.4003 (red line indicates the pass criteria of 2 million cycles).

4.7.6 Bulk Effect of Fusion Defects on Fatigue Properties

The following section examines the effects of defects such as porosity, lack of fusion and insufficient penetration on the fatigue properties of the welds. Therefore the fracture surfaces of a number of welds following fatigue testing, were examined, the percentage of defects within the fracture surface were determined and then related back to the fatigue data. The defects were not analysed by type against the fatigue data, but as a collective.

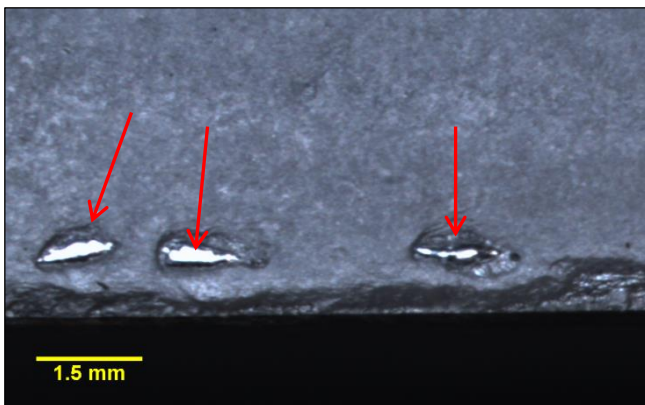


Figure 115. Image showing a lack of side wall fusion (arrowed).

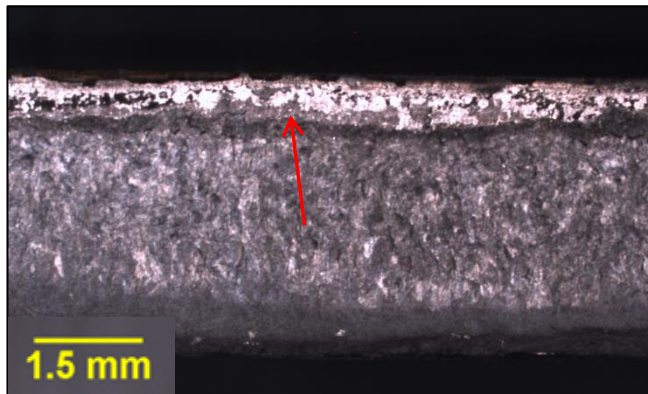


Figure 116. Image showing a lack of root penetration (arrowed)

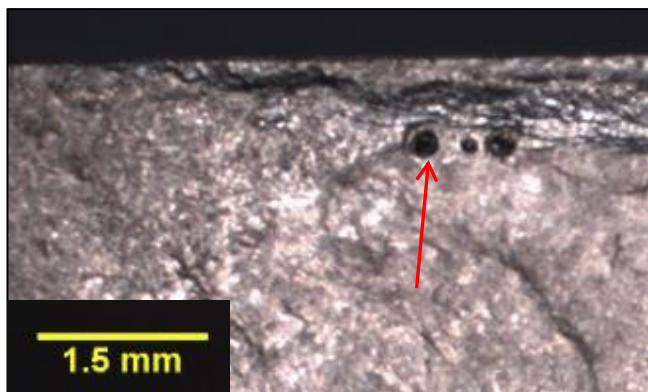


Figure 117. Image showing weld porosity (arrowed).

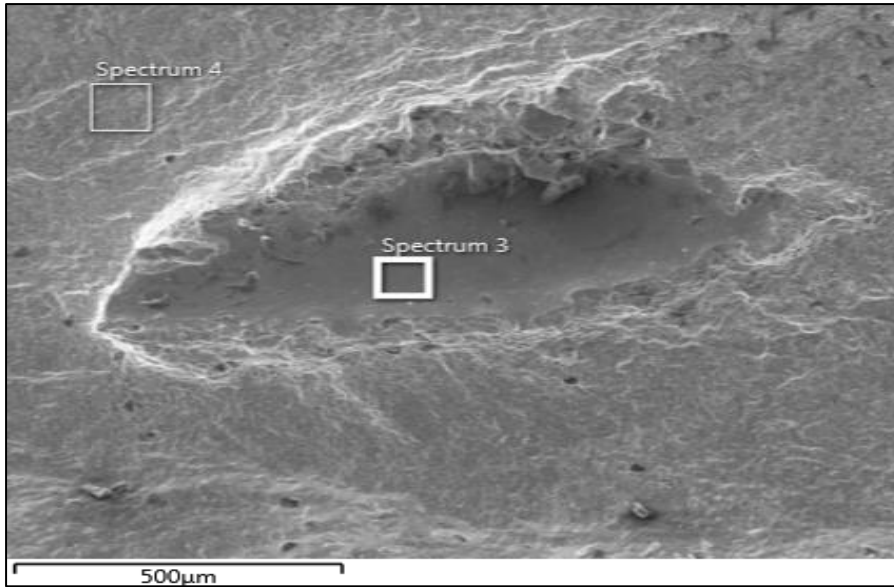


Figure 118. SEM image showing a region with a lack of fusion and the areas where analysis was made.

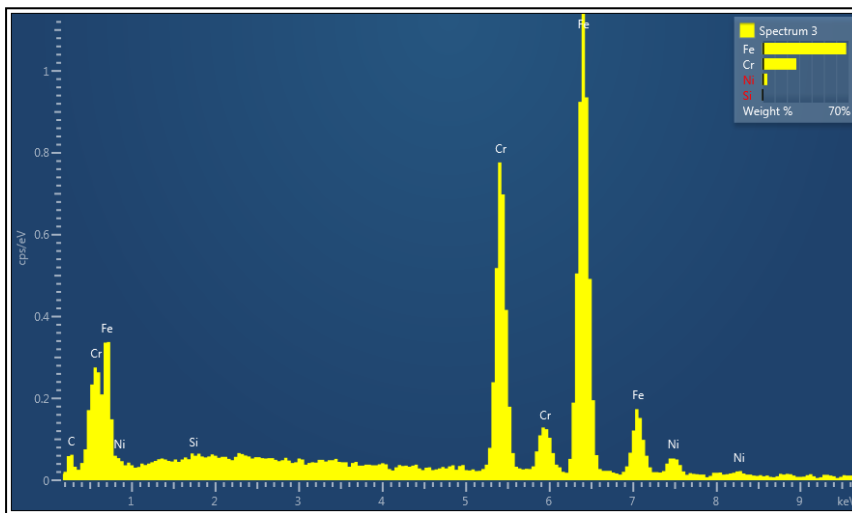


Figure 119. Graph of element analysis spectrum 3

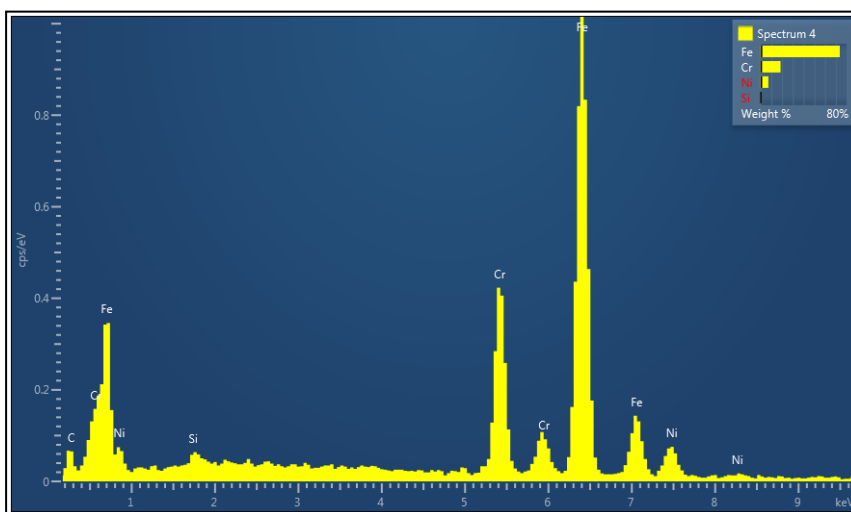


Figure 120. Graph of element analysis spectrum 4.

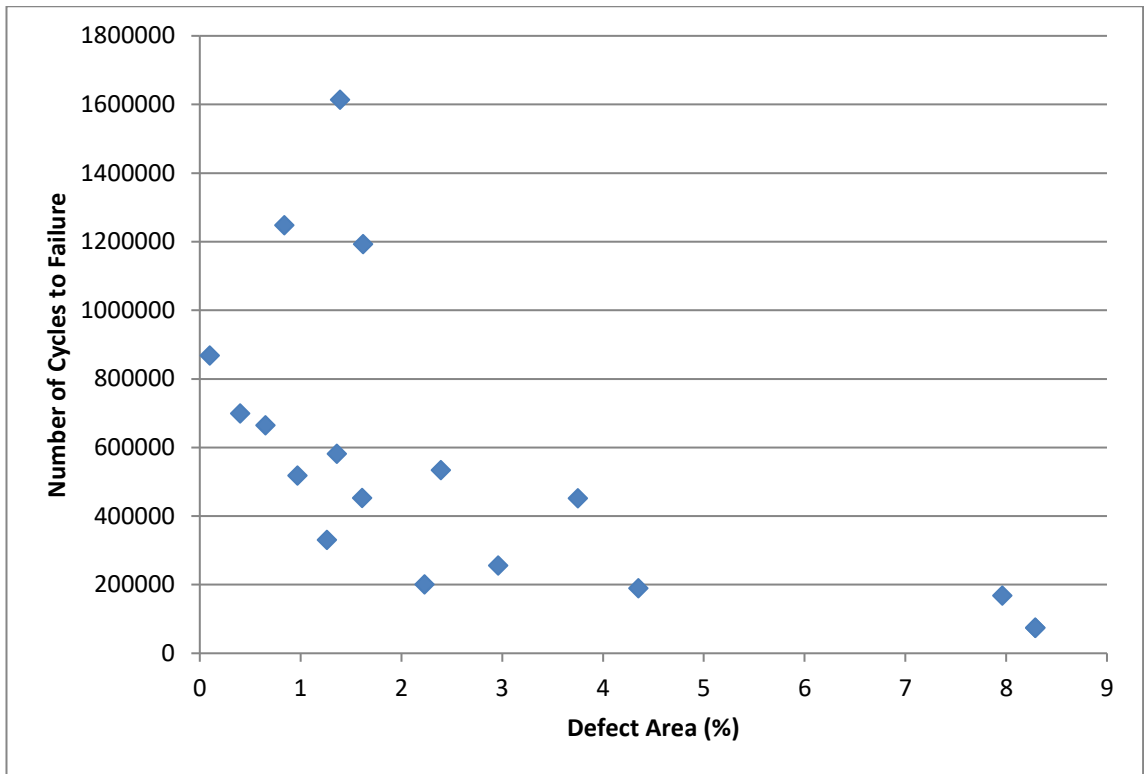


Figure 121. Graph showing the effect of defect area of the fracture face against number of cycles to failure for CMT welded samples.

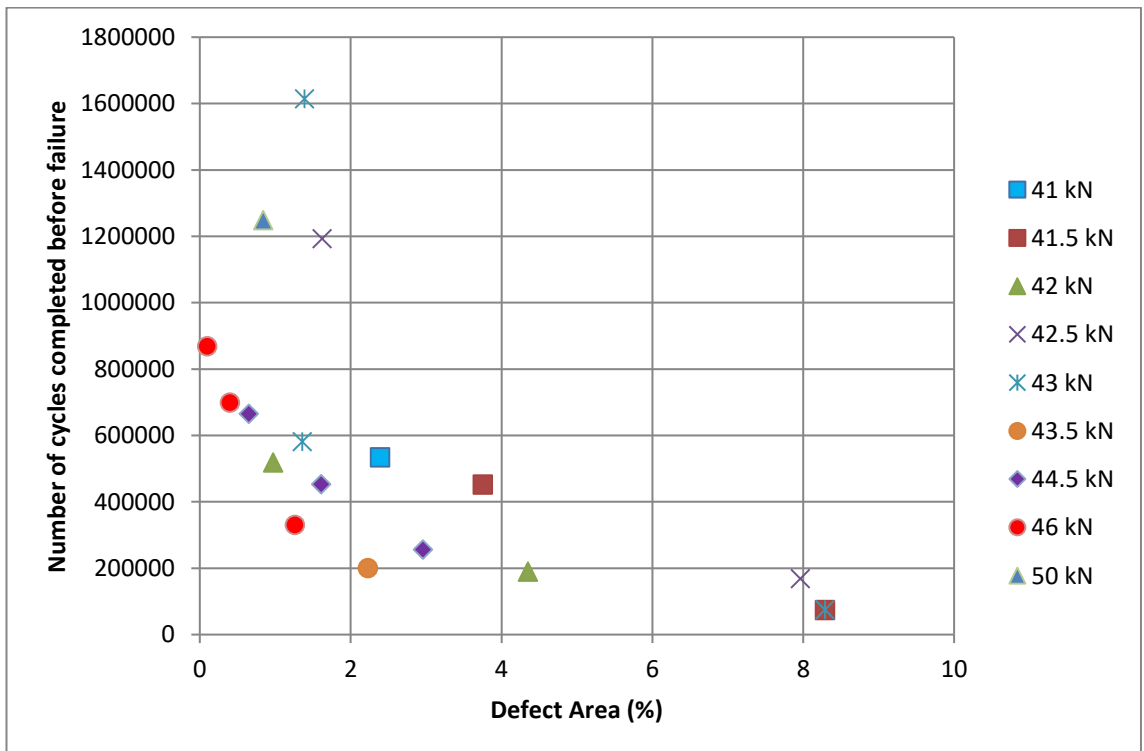


Figure 122. Graph showing the effect of defect area of the fracture face against the number of cycles to failure for each of the tested loads on CMT welded samples.

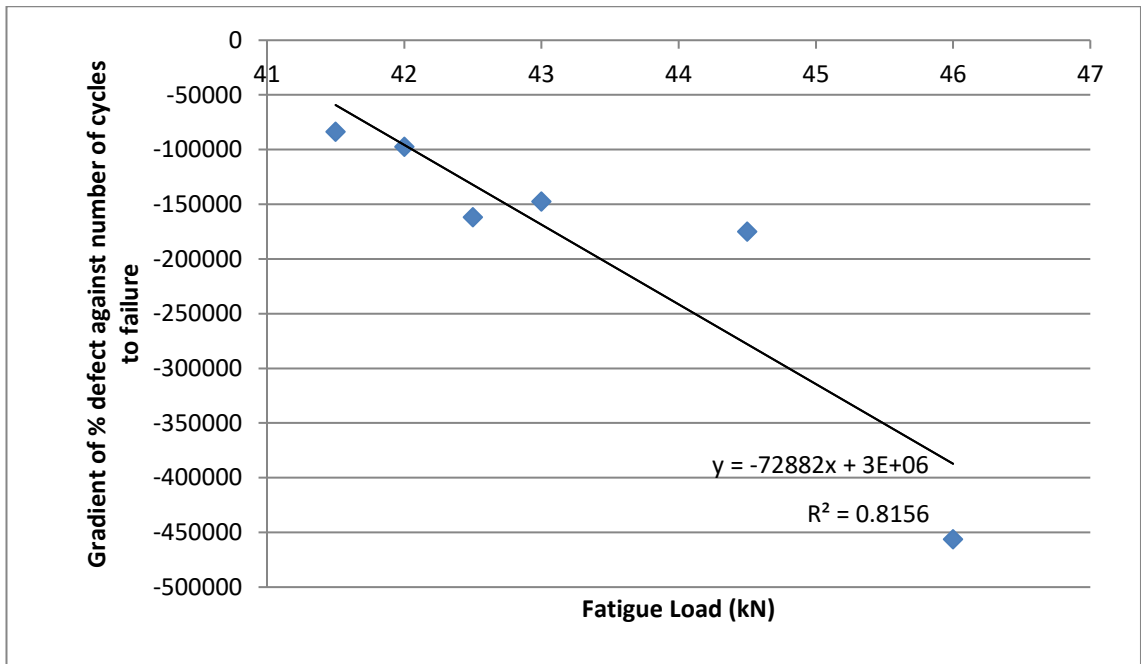


Figure 123. Graph showing the effect on gradient of the % defects within the fracture surface against the number of cycles survived for each load, therefore as the load is increased the gradient also increases on the EN1.4003 parent CMT welded samples.

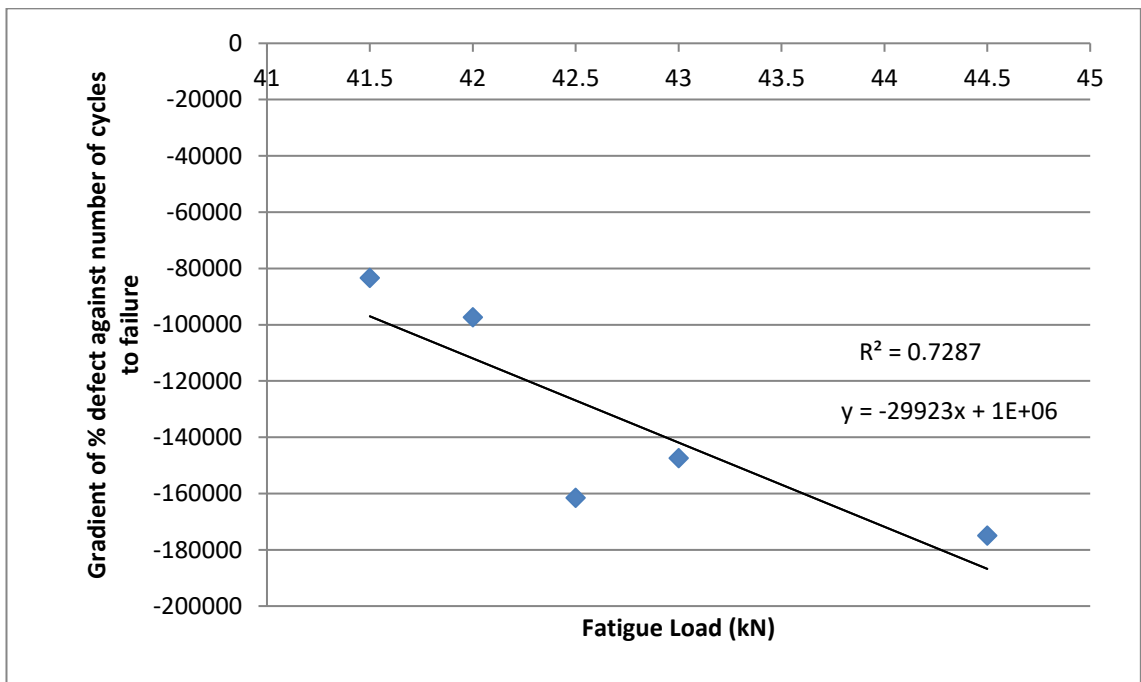


Figure 124. Graph showing the effect on gradient of the % defects within the fracture surface against the number of cycles survived for each load, with the result for 46kN removed, therefore as the load is increased the gradient also increases on the EN1.4003 parent CMT welded samples

4.7.7 Comparison of Weld Angle with Fatigue Results

This aspect of the work reviews possible relationships between the angle between the parent and weld material at the root of the weld against the fatigue results to determine if there is a relationship between the angle and fatigue properties as has been determined in the literature (section 2.4.4, page 78).

Where the data was available for the defects within the fracture surface, this has been annotated onto the graphs as this potentially skews the data, which does appear to show a correlation.

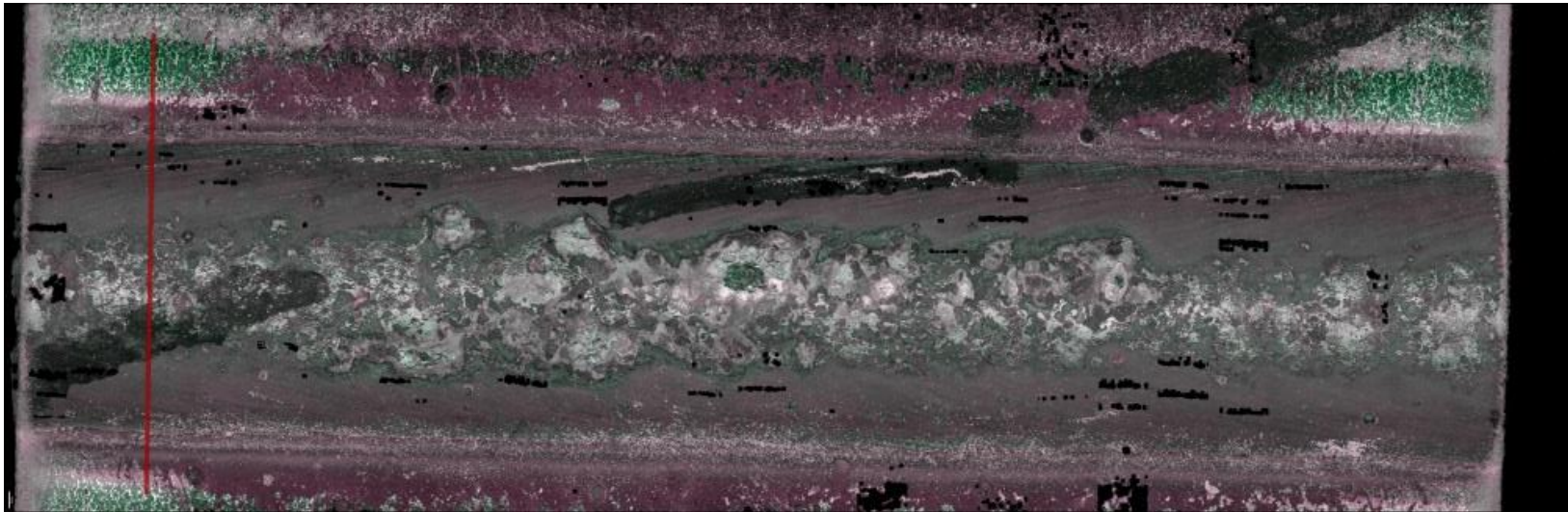


Figure 125. Showing plan of the weld cap of a MAG welded sample, red line showing location for one of profiles taken.

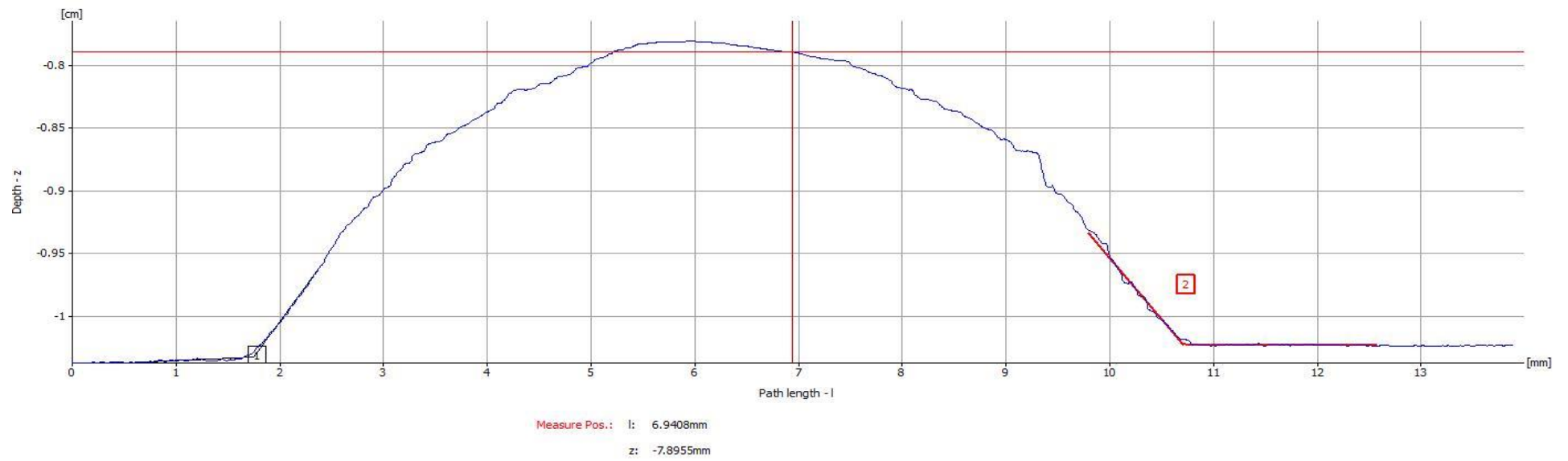


Figure 126. Profile trace for weld cap of MAG welded sample as seen in Figure 125.

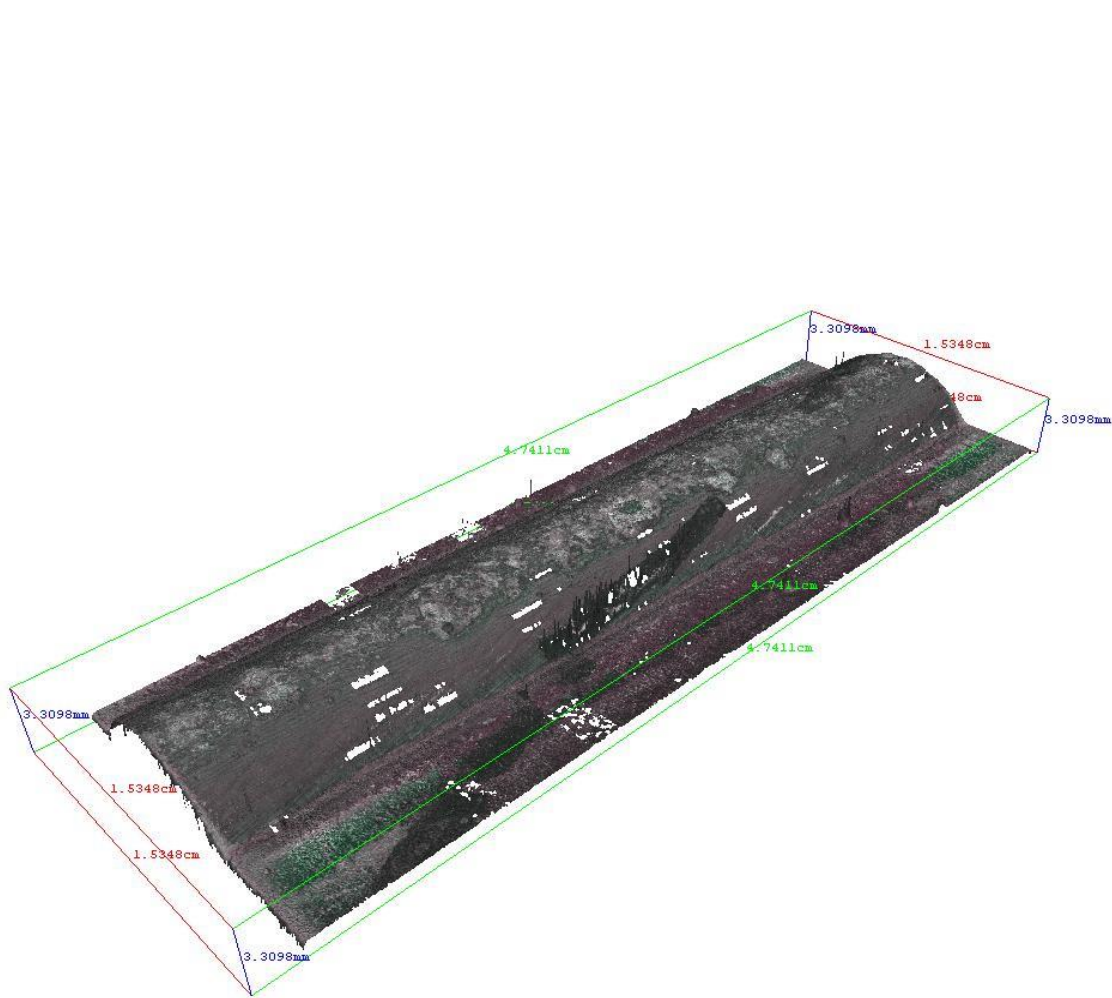


Figure 127. Showing IFM 3D scan of the weld cap of a MAG welded sample.

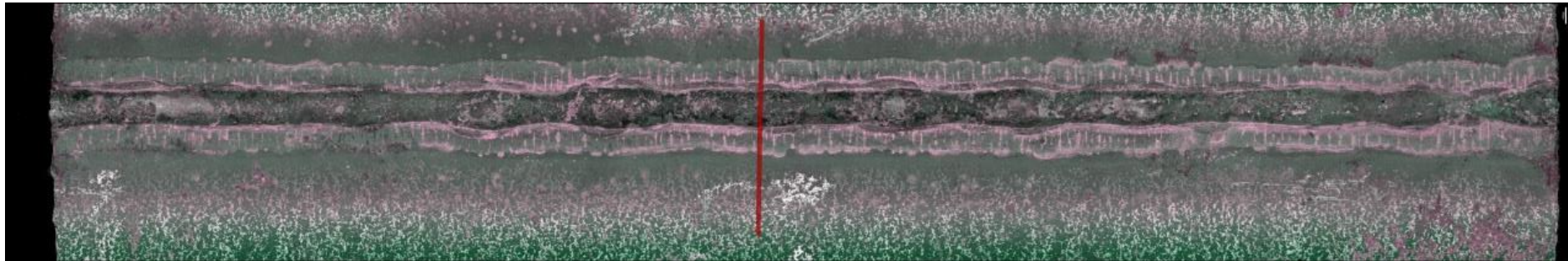


Figure 128. Showing plan of the weld root of a MAG welded sample, red line showing location for one of profiles taken.

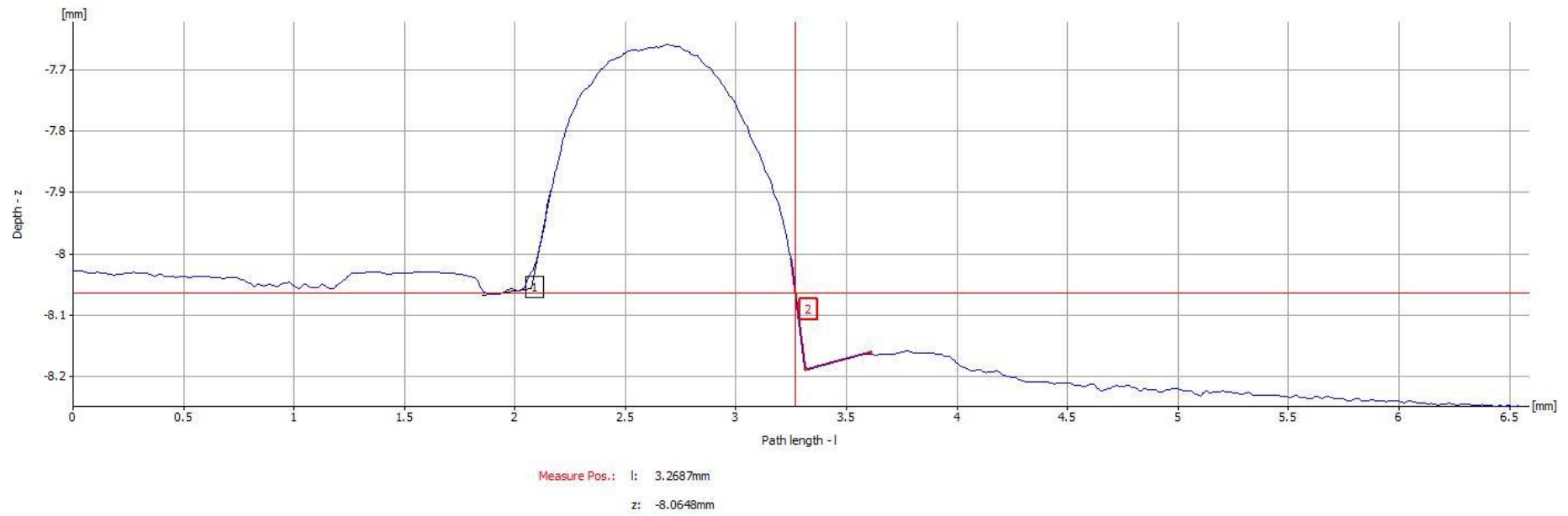


Figure 129. Profile trace for weld root of MAG welded sample as seen in Figure 128.

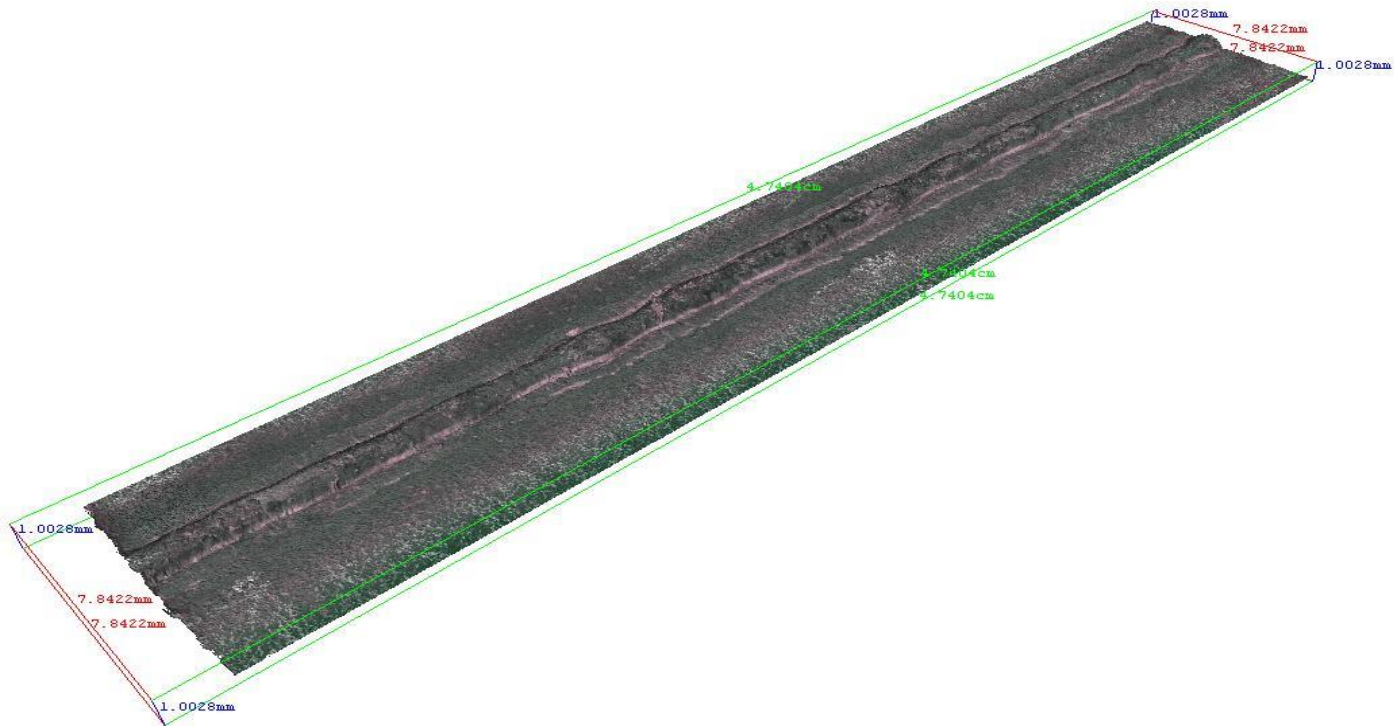


Figure 130. Showing IFM 3D scan of the weld root of a MAG welded sample.

The following graphs depict the number of each cycles survived by the samples that were subjected to the particular load. The graphs do show some correlation between the weld angle and the number of cycles survived for each of the loads, shown by an increase in the number of cycles survived as the root angle increases, which is giving a flatter bead. The pass criteria was 2 million cycles therefore once the sample exceeded this value the test was stopped. Where the information has been determined the percentage of defects within the fracture surface has been identified.

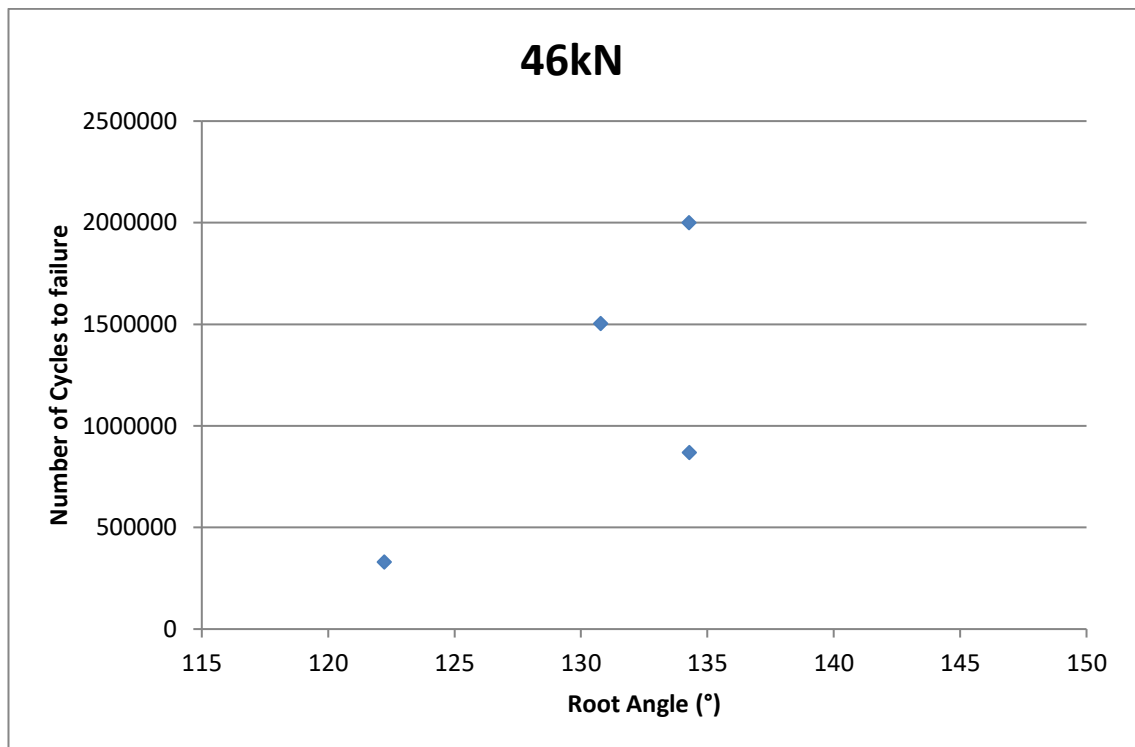


Figure 131. Graph showing weld root angle against the number of cycles before failure for the CMT welded samples fatigue tested at 46 kN

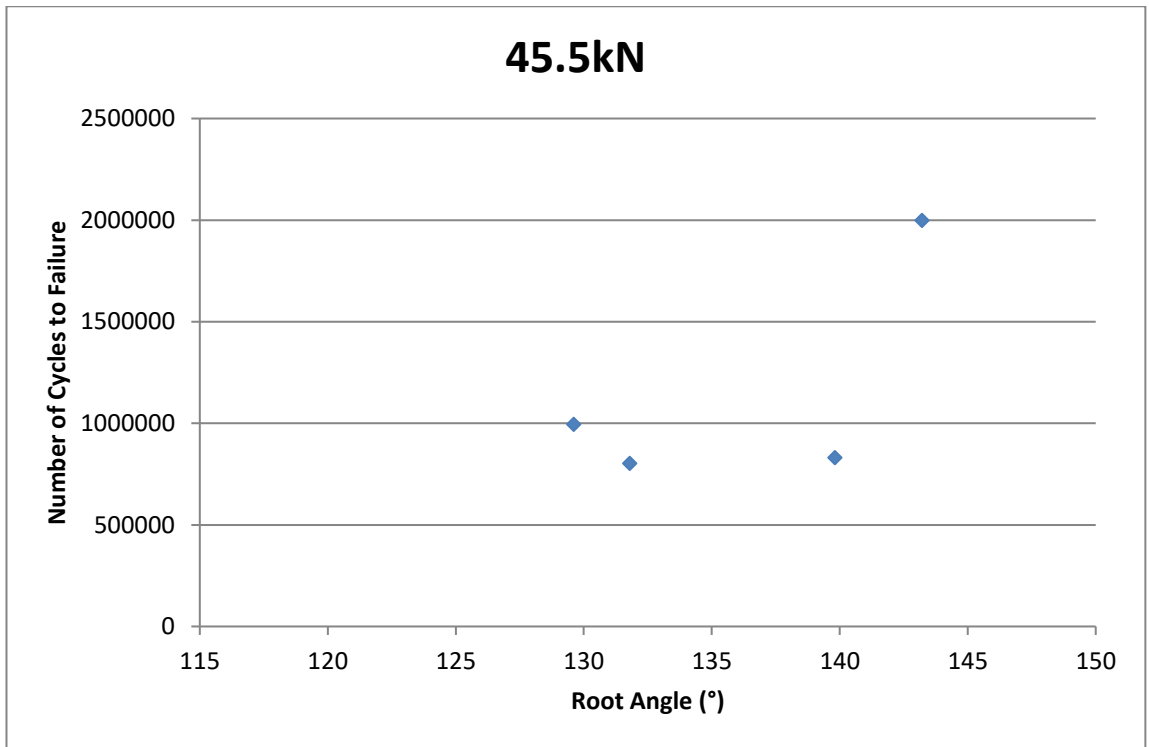


Figure 132. Graph showing weld root angle against the number of cycles before failure for the CMT welded samples fatigue tested at 45.5 kN

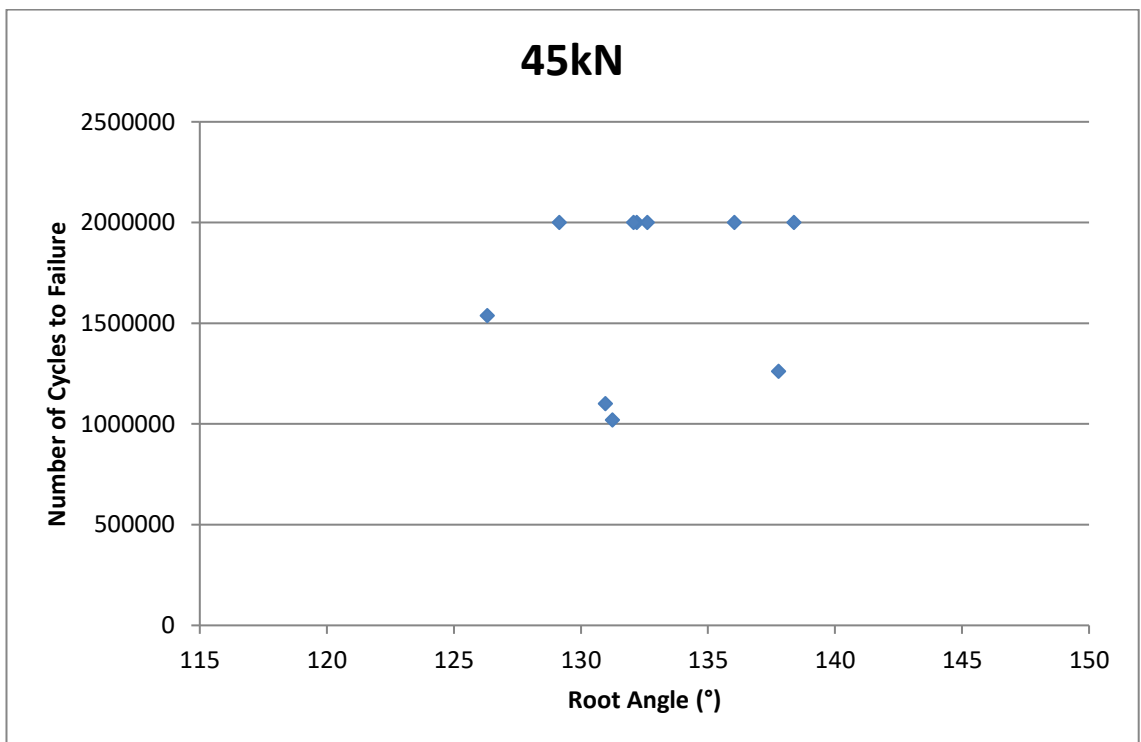


Figure 133. Graph showing weld root angle against the number of cycles before failure for the CMT welded samples fatigue tested at 45 kN

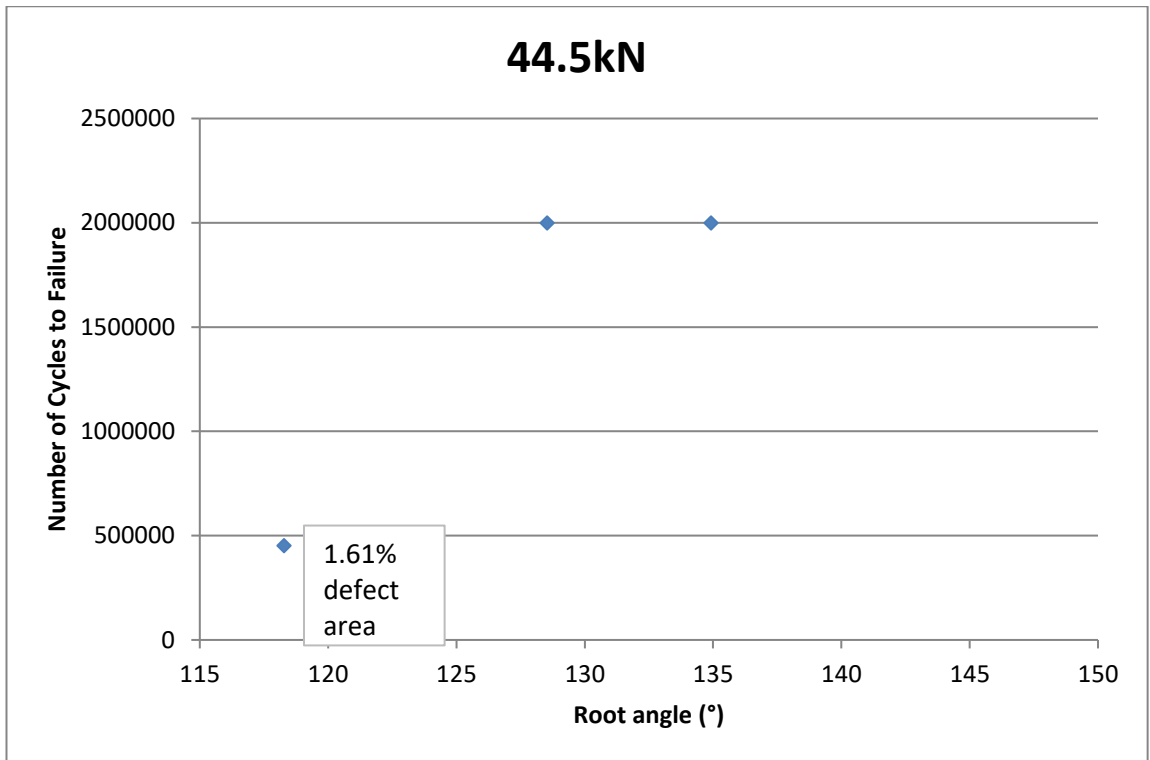


Figure 134. Graph showing weld root angle against the number of cycles before failure for the CMT welded samples fatigue tested at 44.5 kN

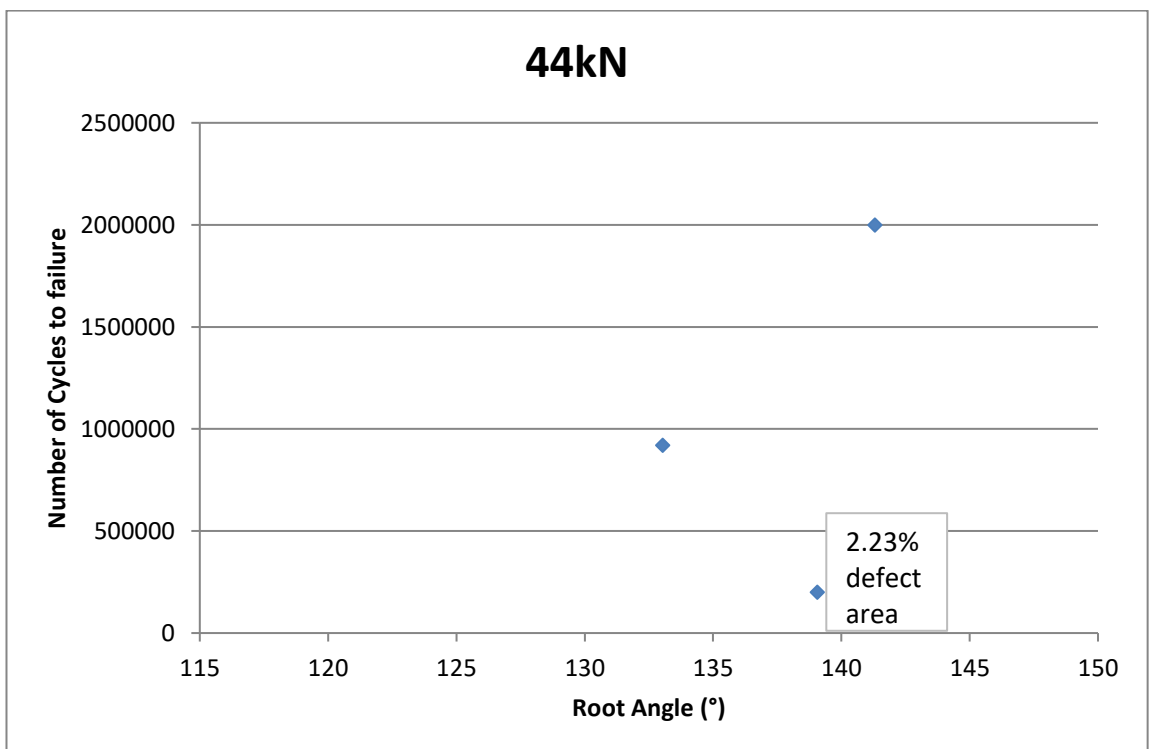


Figure 135. Graph showing weld root angle against the number of cycles before failure for the CMT welded samples fatigue tested at 44 kN

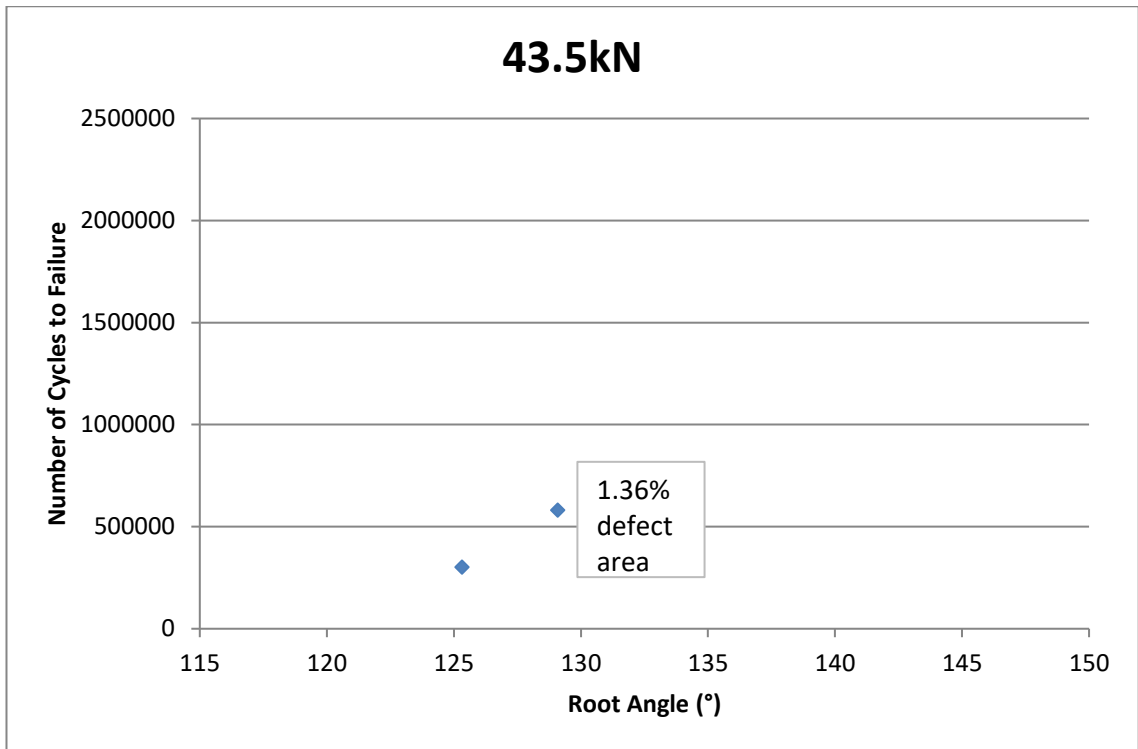


Figure 136. Graph showing weld root angle against the number of cycles before failure for the CMT welded samples fatigue tested at 43.5 kN

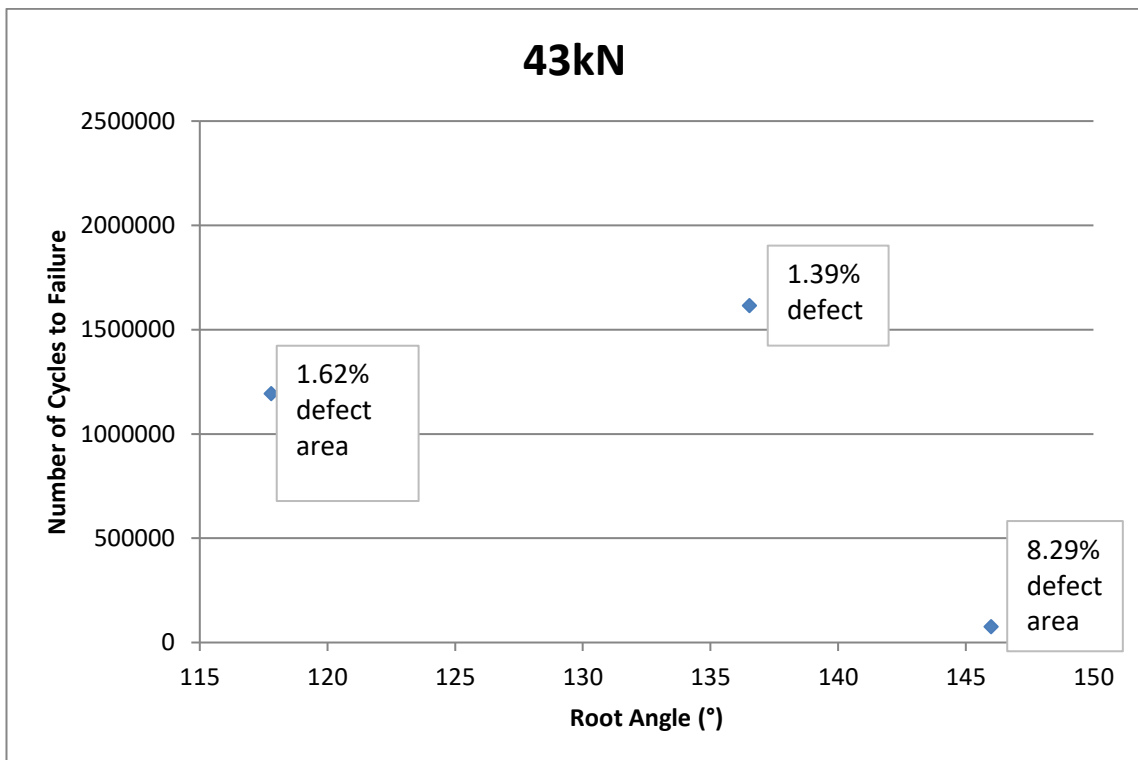


Figure 137. Graph showing weld root angle against the number of cycles before failure for the CMT welded samples fatigue tested at 43 kN

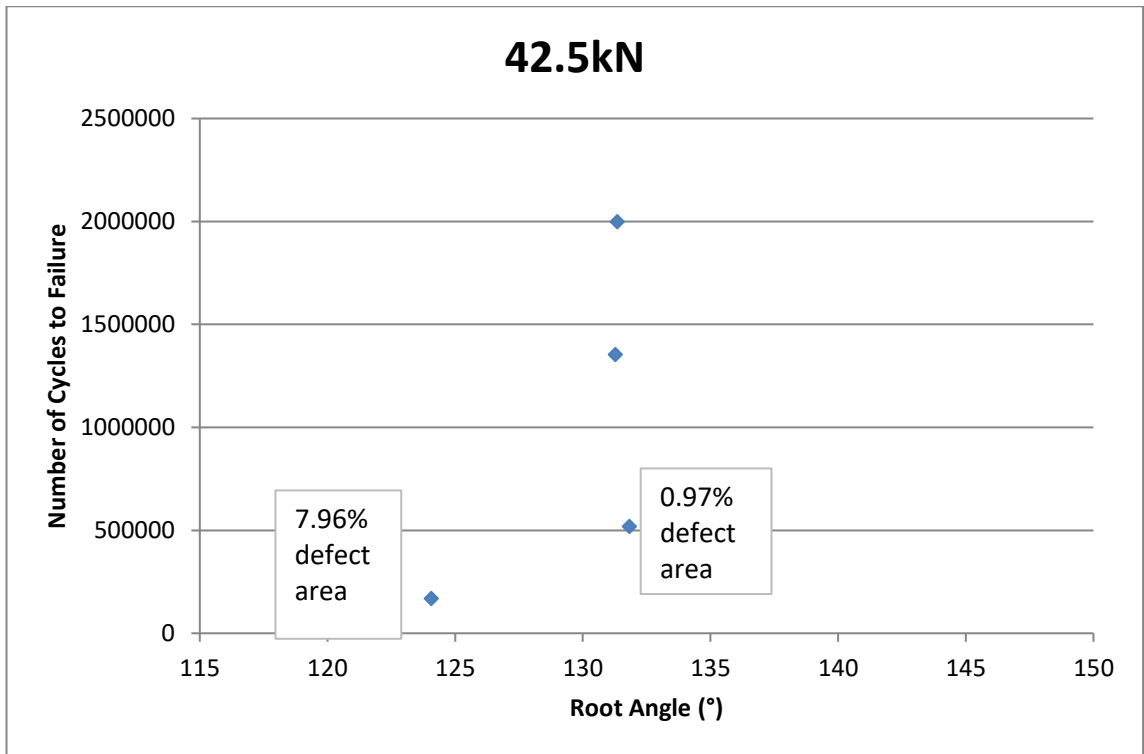


Figure 138. Graph showing weld root angle against the number of cycles before failure for the CMT welded samples fatigue tested at 42.5 kN

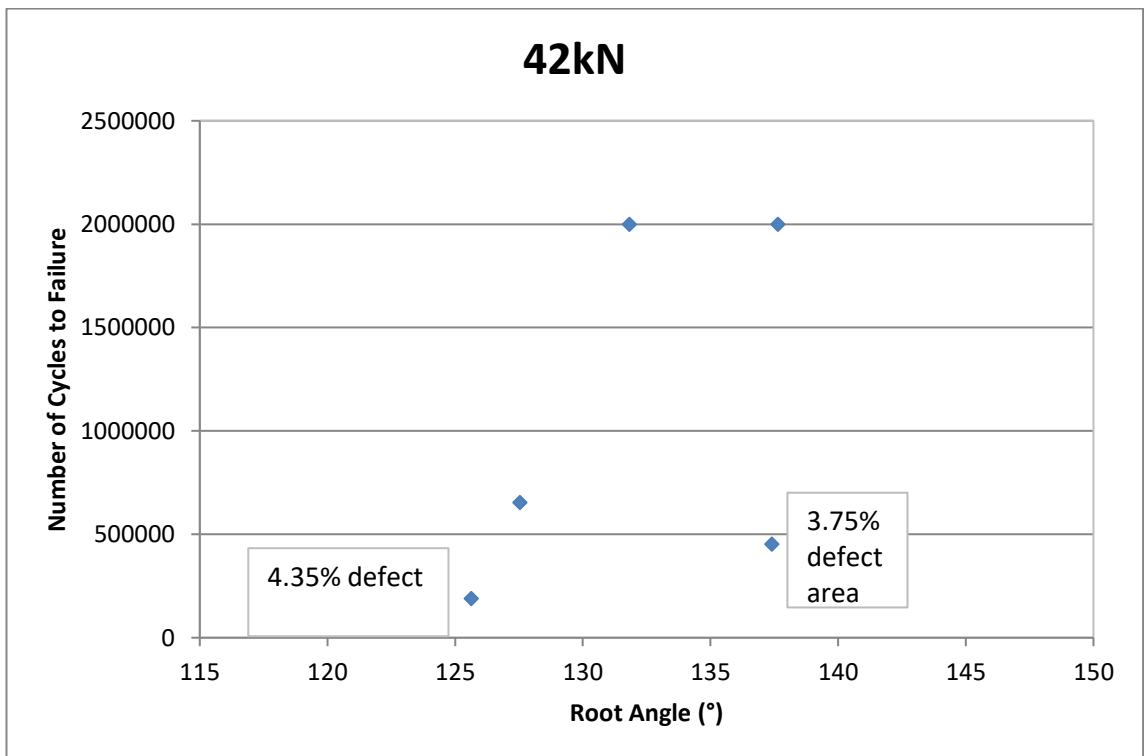


Figure 139. Graph showing weld root angle against the number of cycles before failure for the CMT welded samples fatigue tested at 42 kN

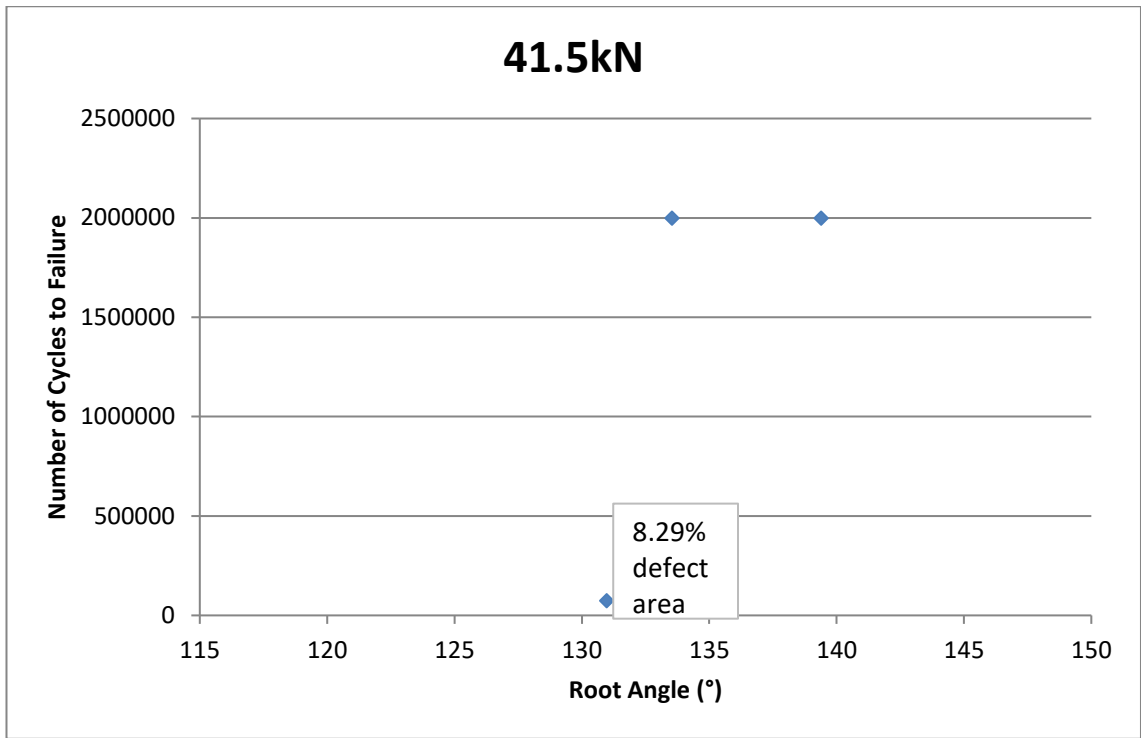


Figure 140. Graph showing weld root angle against the number of cycles before failure for the CMT welded samples fatigue tested at 41.5 kN

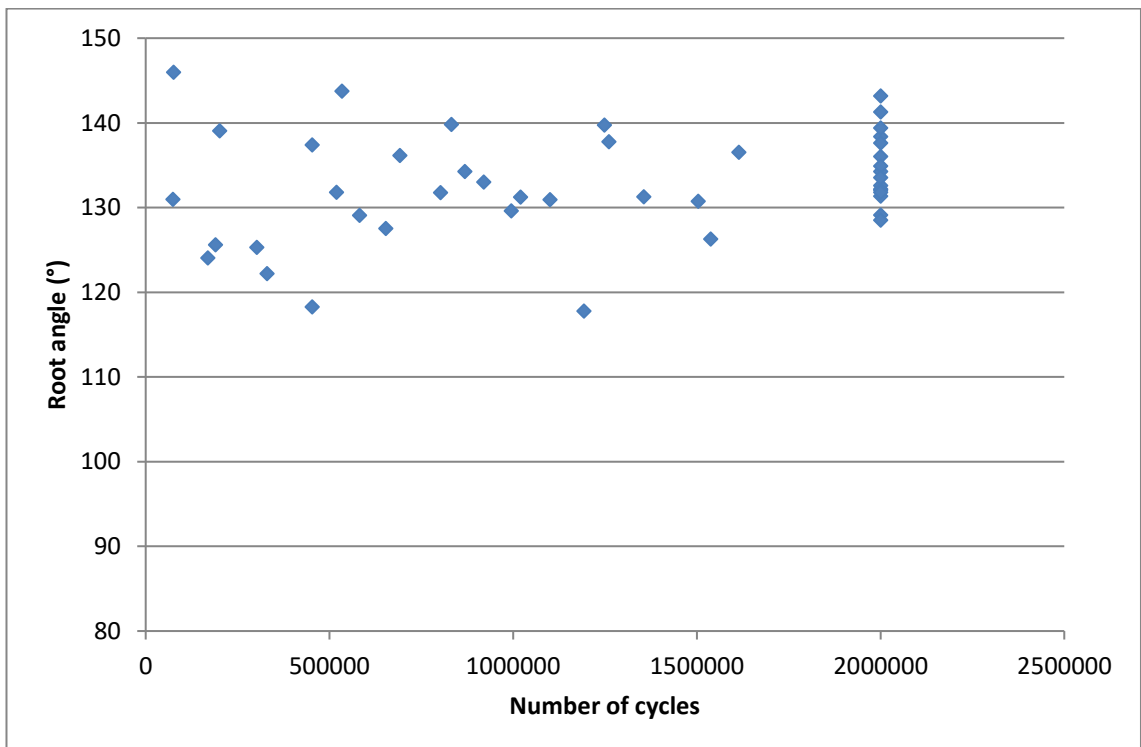


Figure 141. Showing the root angle against number of cycles for the CMT welded samples.

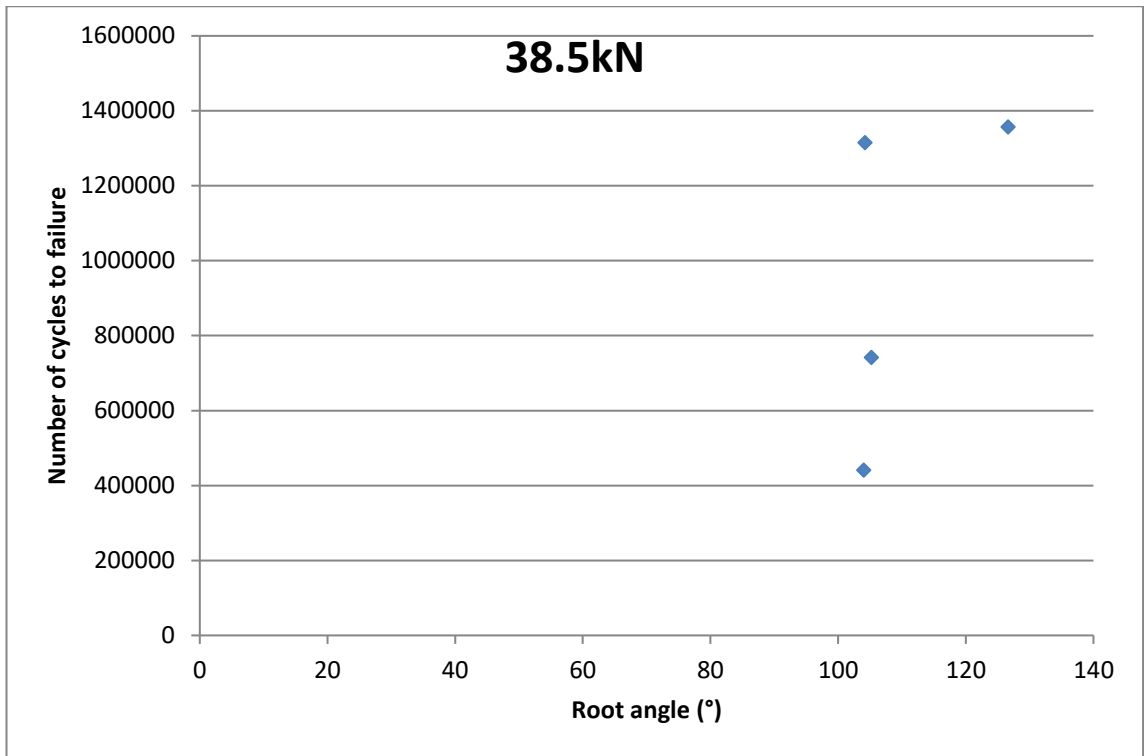


Figure 142. Graph showing weld root angle against the number of cycles before failure for the MAG welded samples fatigue tested at 38.5kN

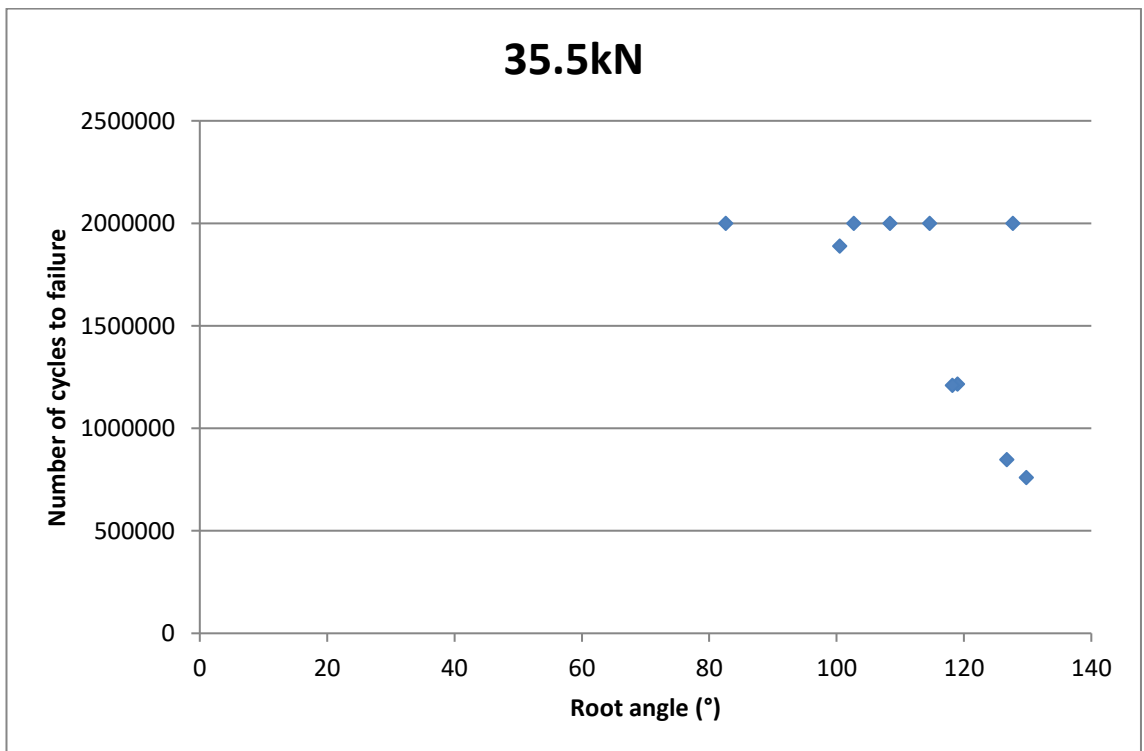


Figure 143. Graph showing weld root angle against the number of cycles before failure for the MAG welded samples fatigue tested at 35.5kN

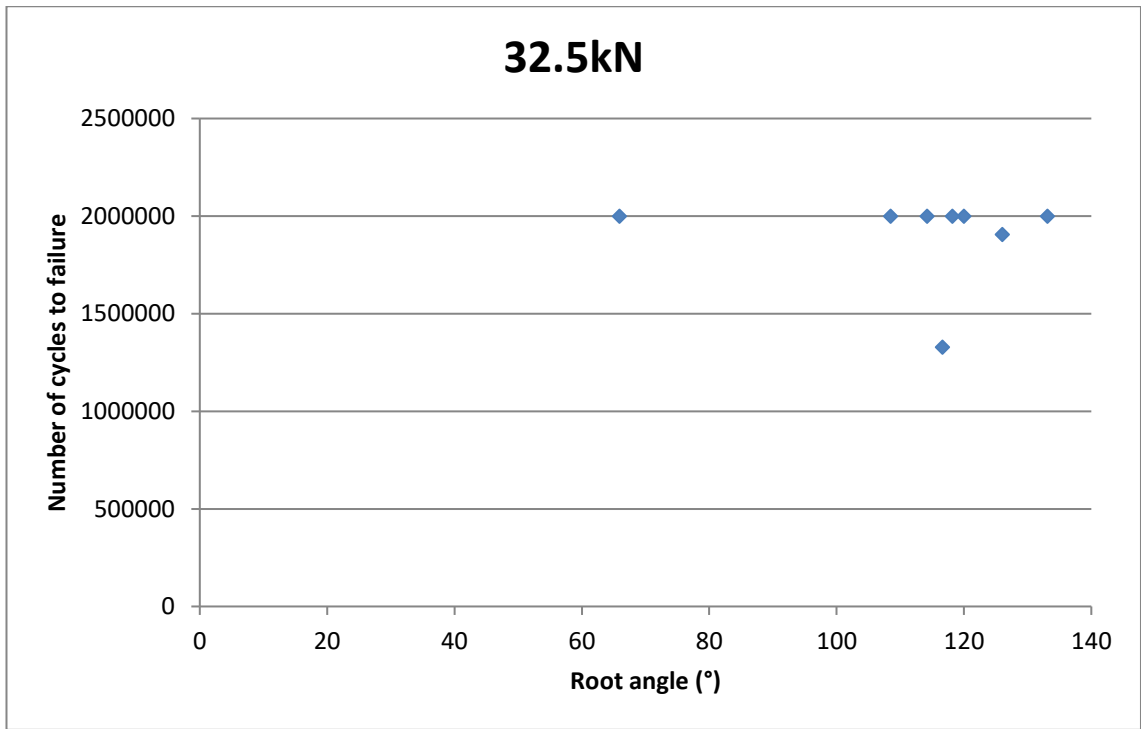


Figure 144. Graph showing weld root angle against the number of cycles before failure for the MAG welded samples fatigue tested at 32.5kN

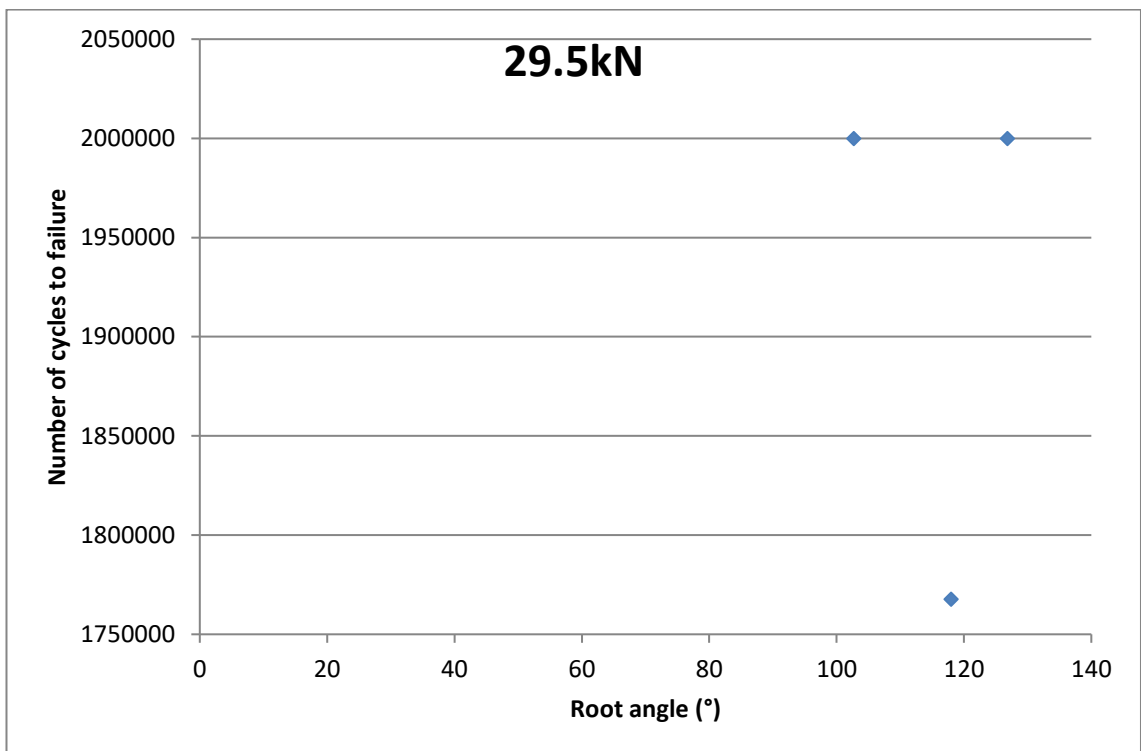


Figure 145. Graph showing weld root angle against the number of cycles before failure for the MAG welded samples fatigue tested at 29.5kN

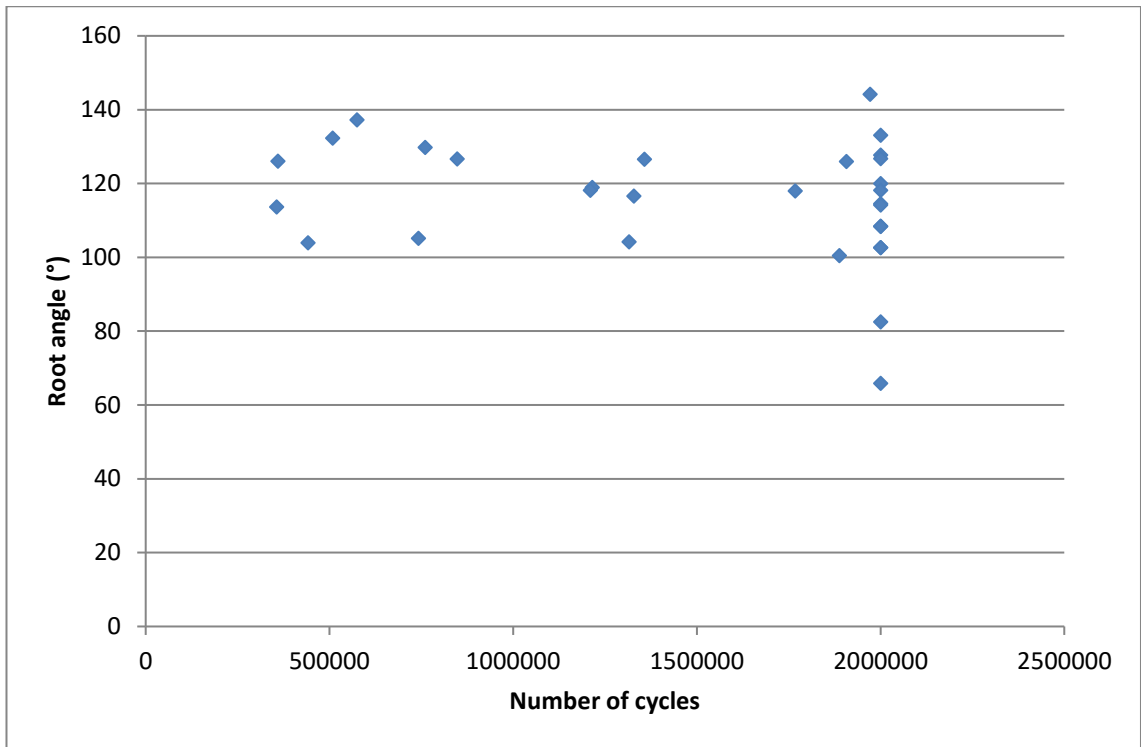


Figure 146. Showing the root angle against number of cycles for the MAG welded samples.

4.8 Heat Treatment Trial To Identify Key Temperatures At Which Microstructural Changes Occur And The Effect of Time On These Changes.

The trial was conducted to ascertain the temperatures at which an accicular phase begins to form and the temperature at which grain coarsening begins to occur within the parent material, therefore replicating the various regions within the HAZ. The second part of this was to then assess the actual effect these microstructural changes had on modification of the mechanical properties of the material through hardness testing and Charpy impact testing.

700°C 20 min soak



Figure 147. Image showing fully ferritic microstructure of sample subjected to 700°C 20 min soak water quench as seen in the as received EN1.4003 material

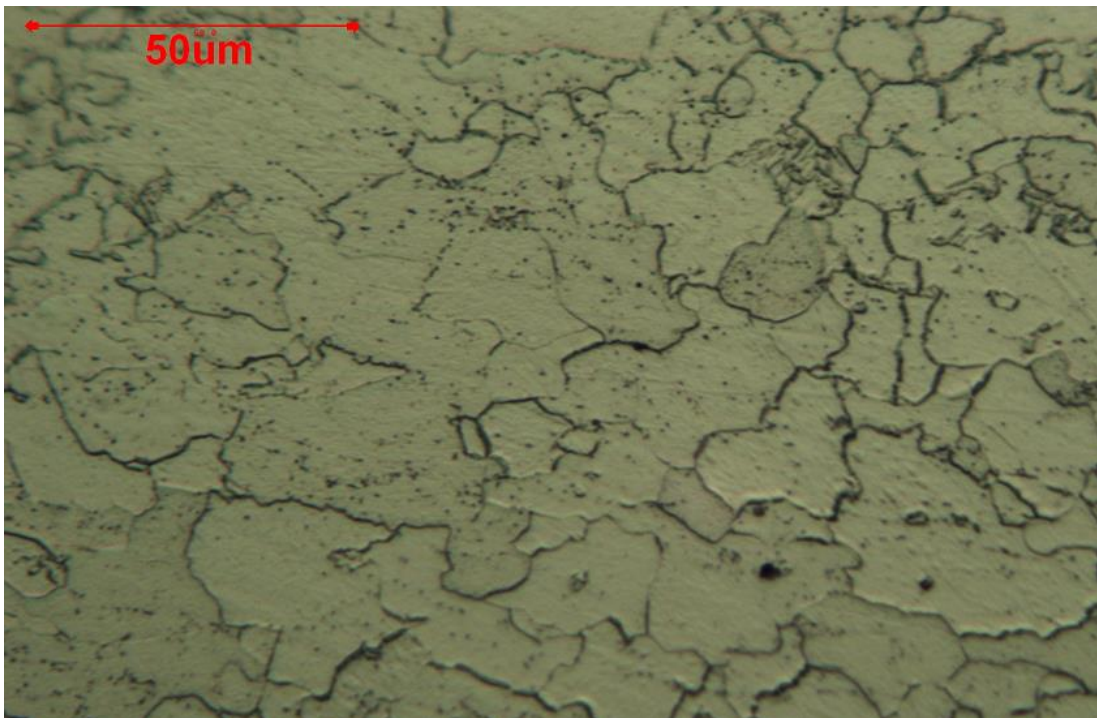


Figure 148. Image Showing fully ferritic microstructure of sample subjected to 700°C 20 min soak water quench as seen in the as received EN1.4003 material.

800°C 20 min soak

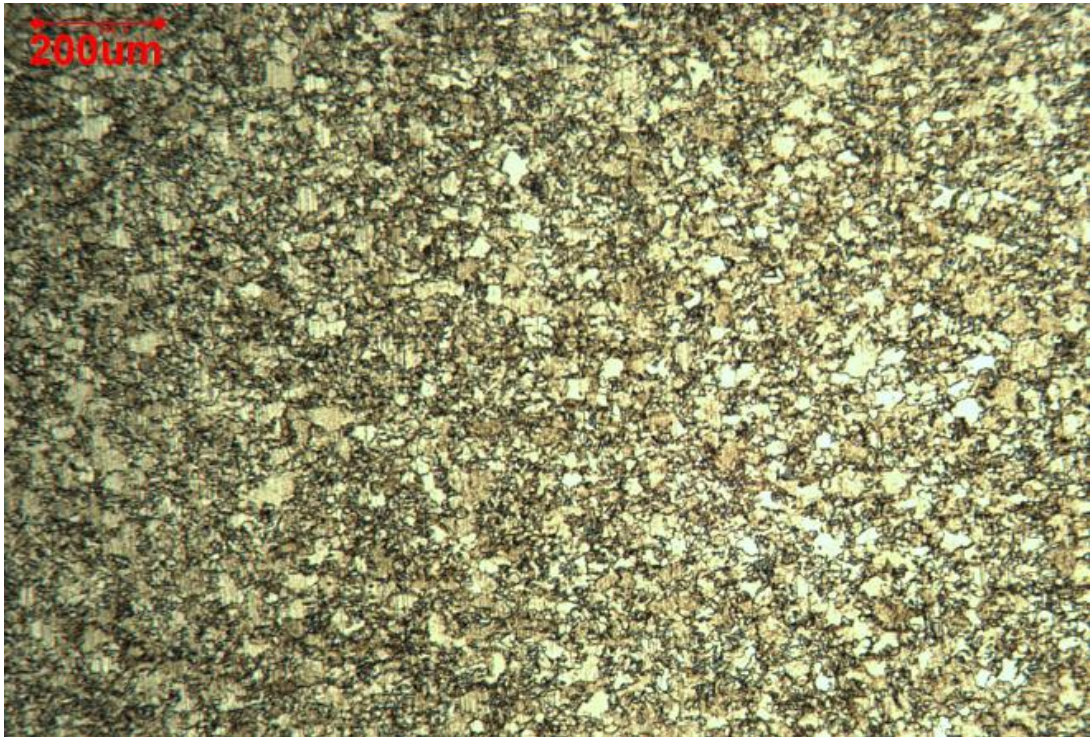


Figure 149. Image showing ferritic (light areas) and martensitic (dark areas) microstructure of sample subjected to 800°C 20 min soak water quench similar to the microstructure in the region of the HAZ furthest from the fusion zone of welds on a EN1.4003 grade material.

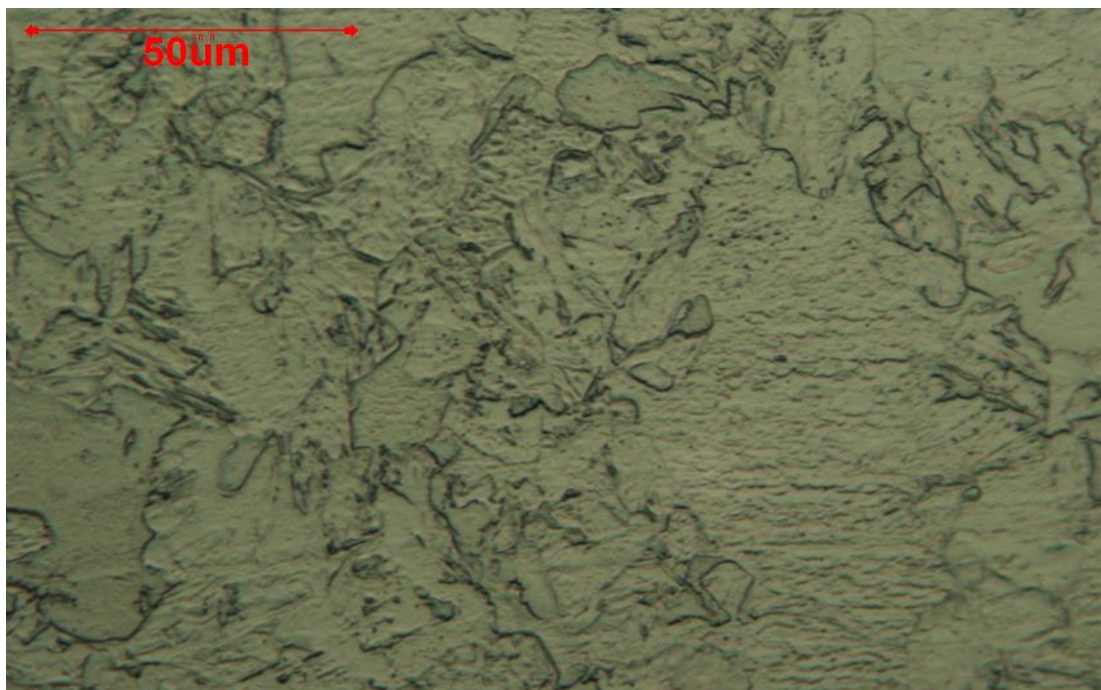


Figure 150. Image showing ferritic and martensitic microstructure (250 HV₁₀) of sample subjected to 800°C 20 min soak water quench similar to the microstructure in the region of the HAZ furthest from the fusion zone of welds on an EN1.4003 grade material.

900°C 20 min soak



Figure 151. Image showing martensitic microstructure of EN1.4003 sample subjected to 900°C 20 min soak water quench.

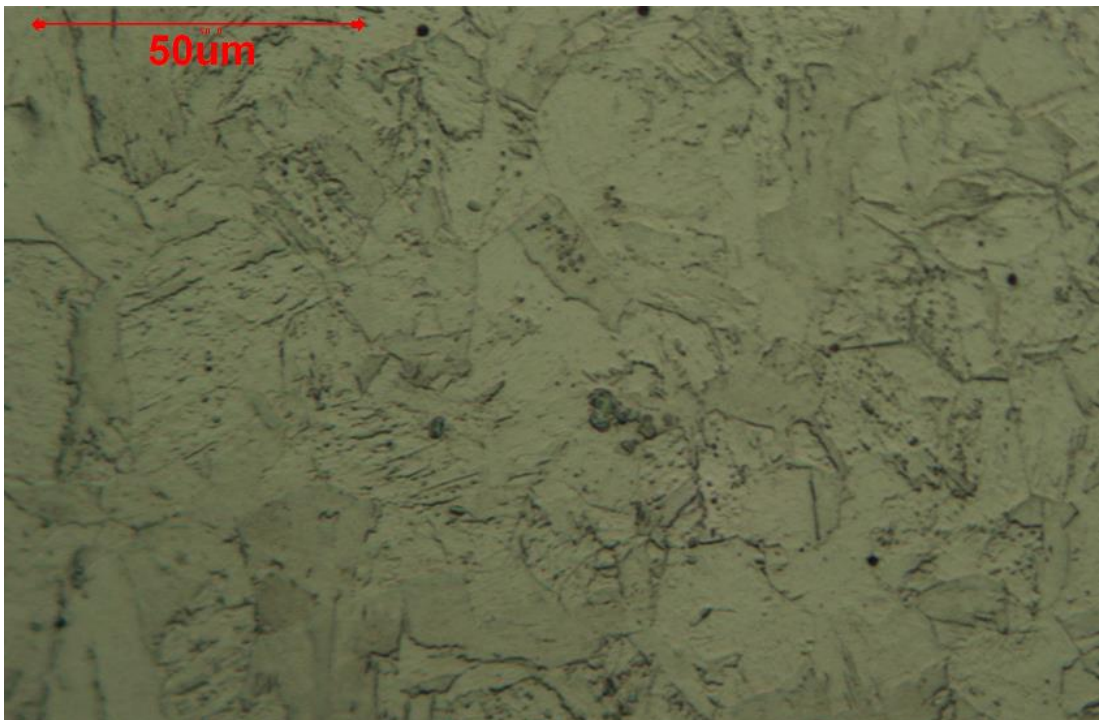


Figure 152. Image showing martensitic microstructure (277 HV₁₀) of EN1.4003 sample subjected to 900°C 20 min soak water quench.

1000°C 20 min soak



Figure 153. Image showing martensitic microstructure with some grain growth of EN1.4003 sample subjected to 1000°C 20 min soak water quench, this is similar to what would be seen in the region of the HAZ closest to the fusion zone.

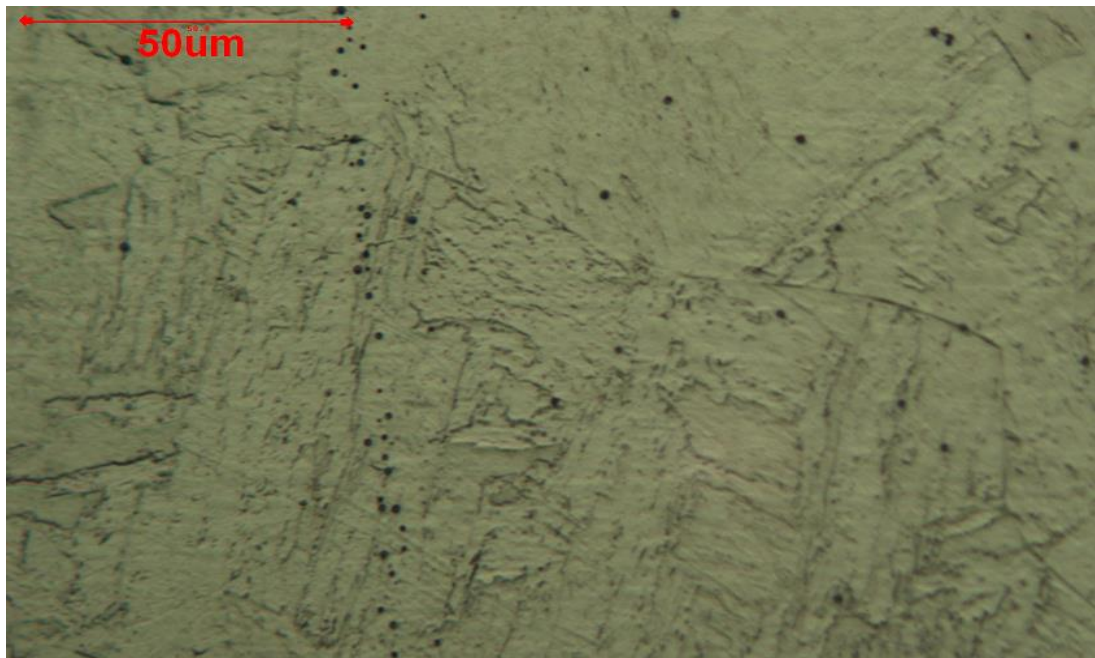


Figure 154. Image showing martensitic microstructure with some grain growth of EN1.4003 sample subjected to 1000°C 20 min soak water quench, this is similar to what would be seen in the region of the HAZ closest to the fusion zone.

1100°C 20 min soak

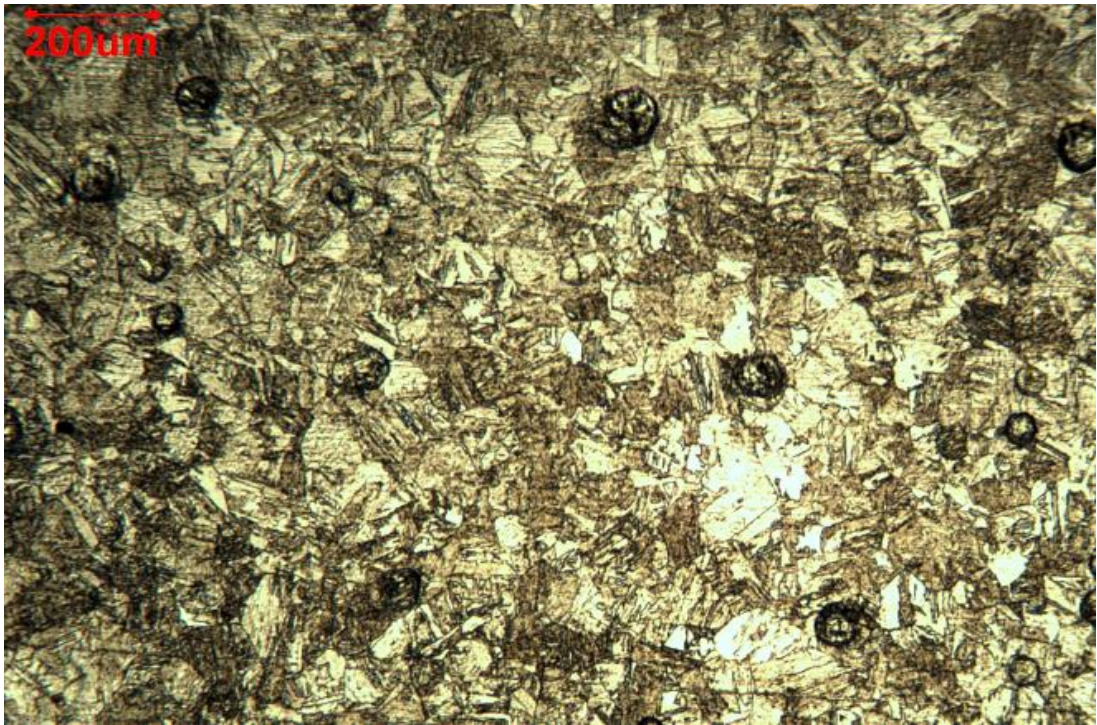


Figure 155. Image showing martensitic microstructure and grain growth of EN1.4003 sample subjected to 1100°C 20 min soak water quench, this is similar to what would be seen in the region of the HAZ closest to the fusion zone.

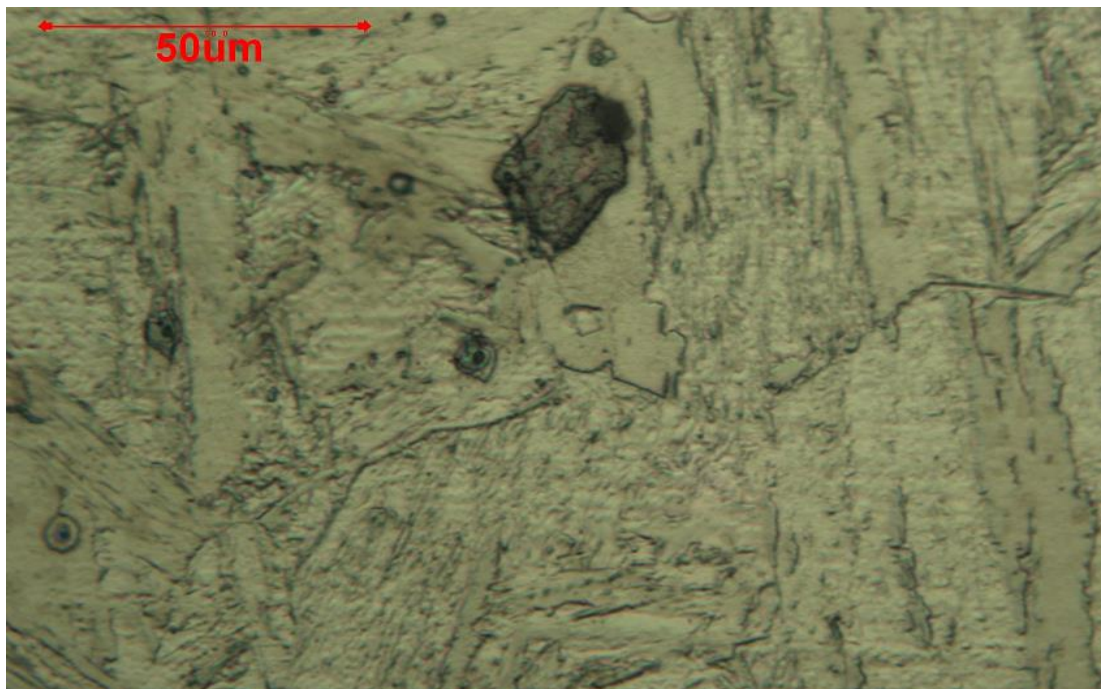


Figure 156. Image showing ferritic and martensitic microstructure and grain growth of EN1.4003 sample subjected to 1100°C 20 min soak water quench, this is similar to what would be seen in the region of the HAZ closest to the fusion zone.

747°C 20 min soak



Figure 157. Image showing ferritic microstructure of EN1.4003 sample subjected to 747°C 20 min soak water quench, as would be seen in the unaffected parent material.

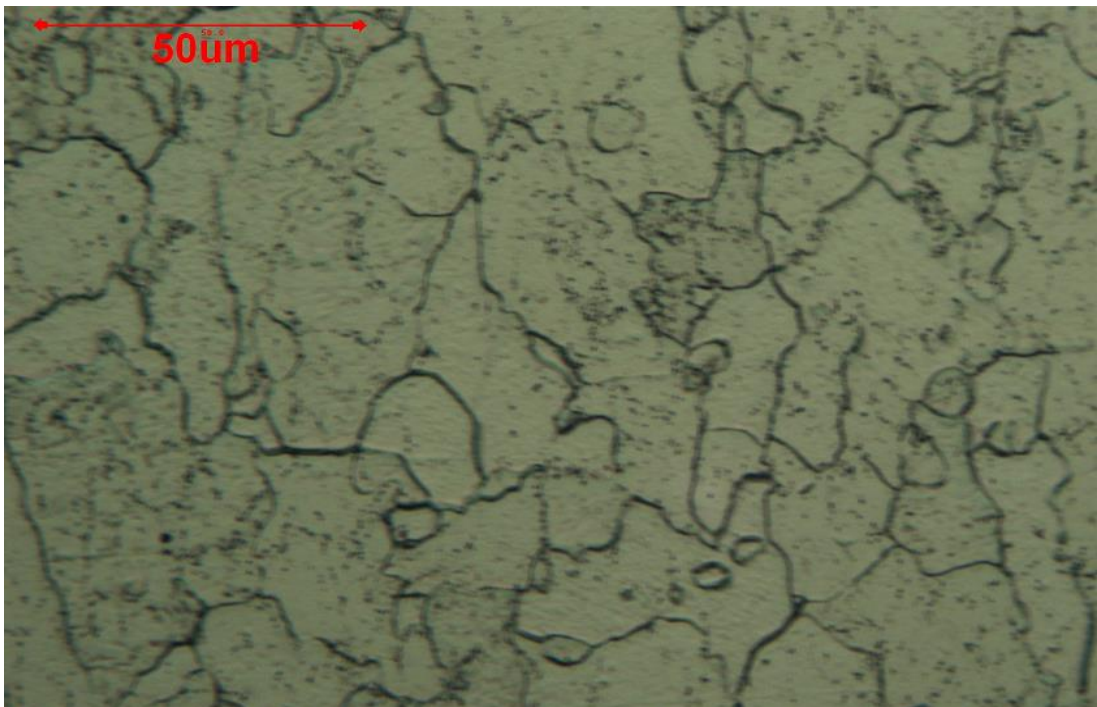


Figure 158. Image showing ferritic microstructure of sample subjected to 747°C 20 min soak water quench, as would be seen in the unaffected parent material.

758°C 20 min soak

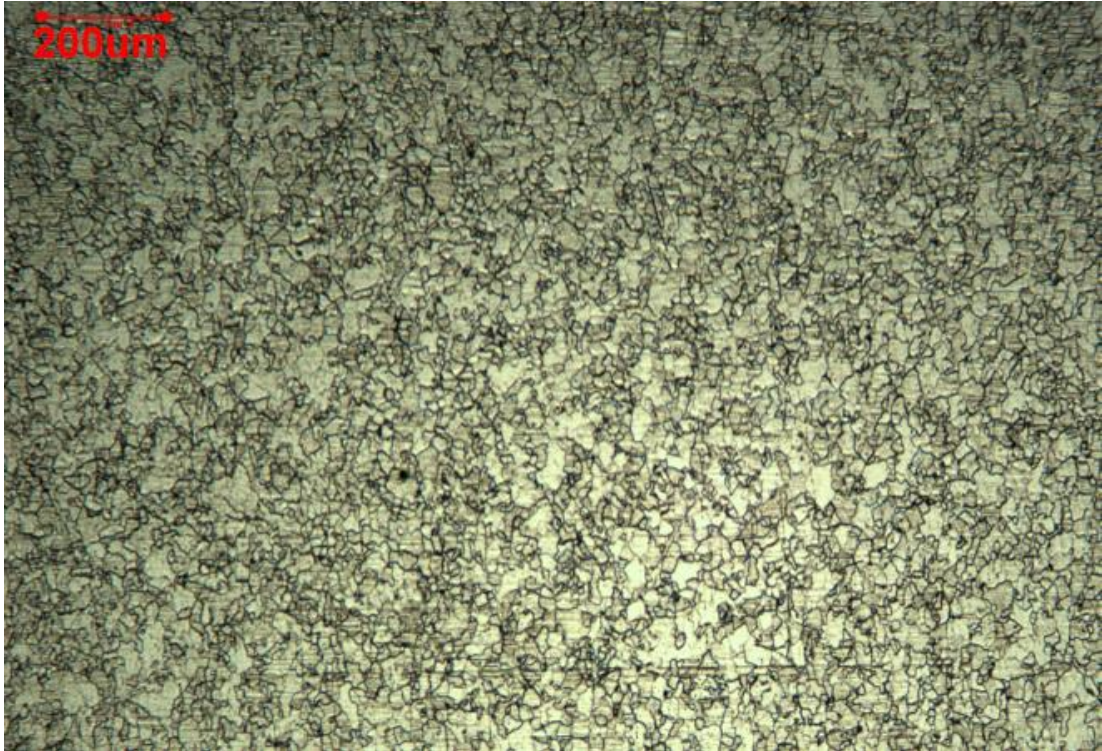


Figure 159. Image showing ferritic microstructure of an EN1.4003 sample subjected to 758°C 20 min soak water quench as would be seen in the unaffected parent material.

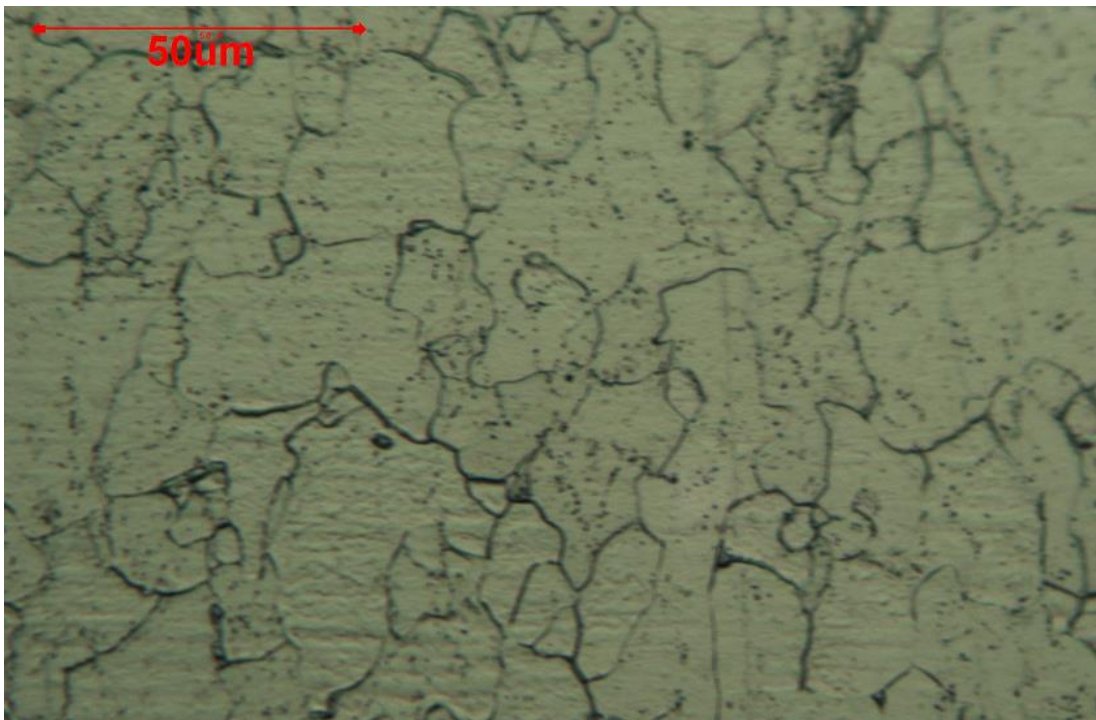


Figure 160. Image showing ferritic microstructure of an EN1.4003 sample subjected to 758°C 20 min soak water quench as would be seen in the unaffected parent material.

769°C 20 min soak



Figure 161. Image showing ferritic microstructure (light areas) with martensite (dark areas) at the grain boundaries of an EN1.4003 sample subjected to 769°C 20 min soak water quench, this would be typical of a microstructure seen in the HAZ at its furthest distance from the fusion zone.

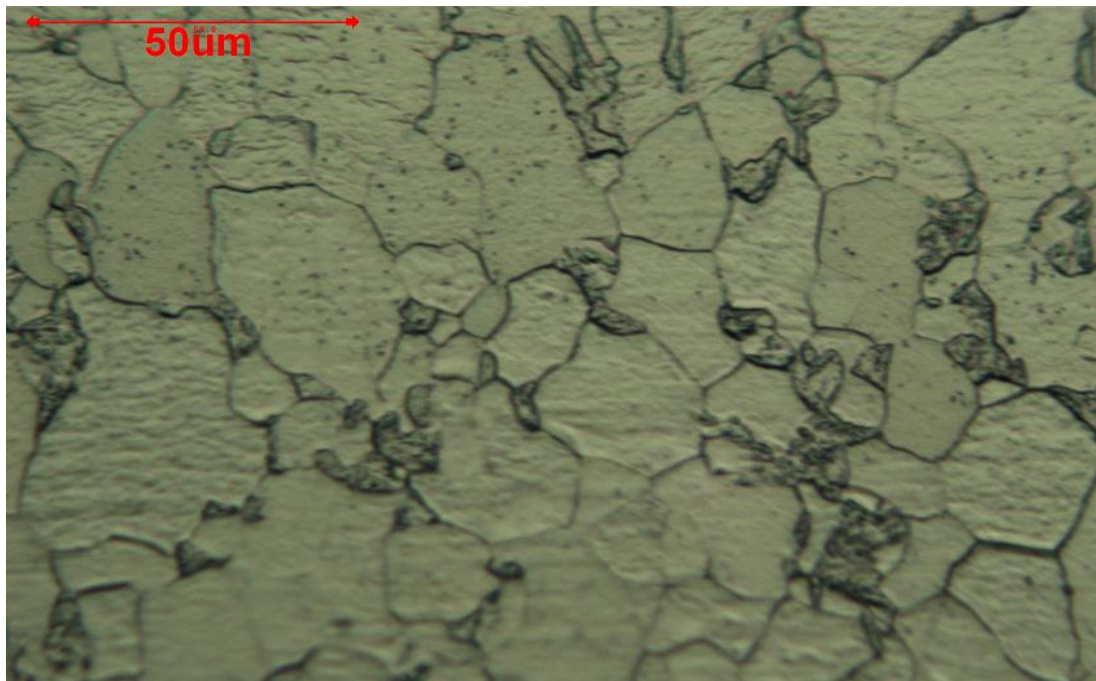


Figure 162. Image showing ferritic microstructure with martensite at the grain boundaries of an EN1.4003 sample subjected to 769°C 20 min soak water quench, this would be typical of a microstructure seen in the HAZ at its furthest distance from the fusion zone.

779°C 20 min soak

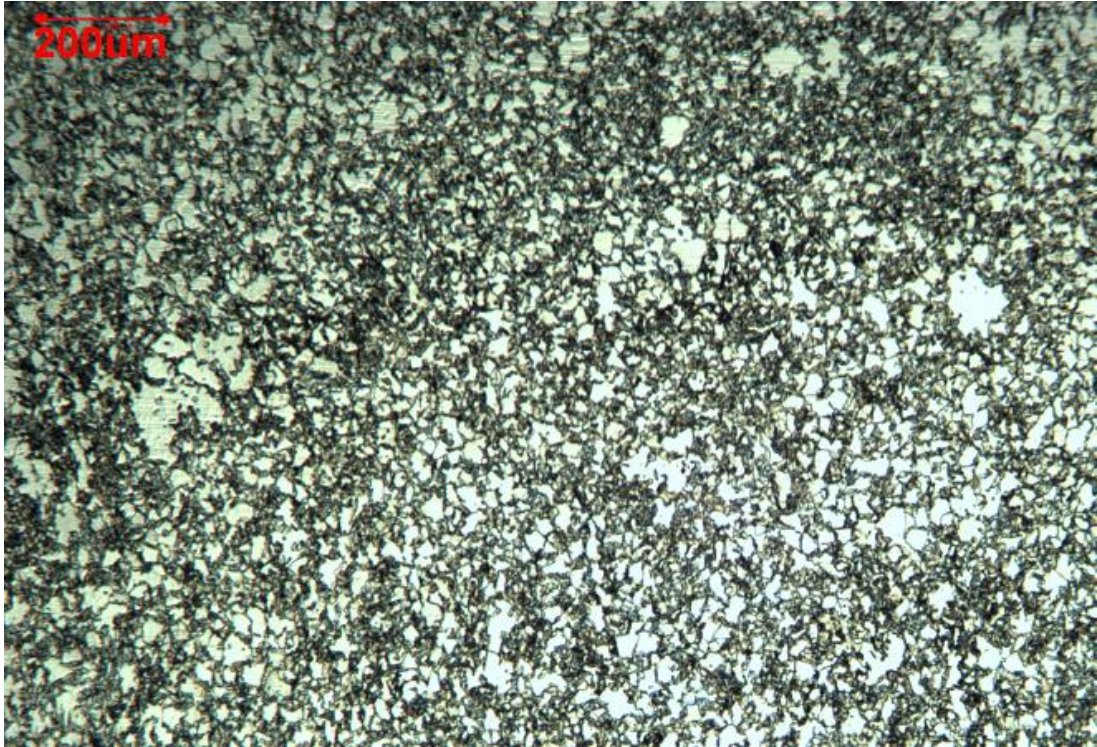


Figure 163. Image showing ferritic (light areas) and martensitic (dark areas) microstructure of an EN1.4003 sample subjected to 779°C 20 min soak water quench.

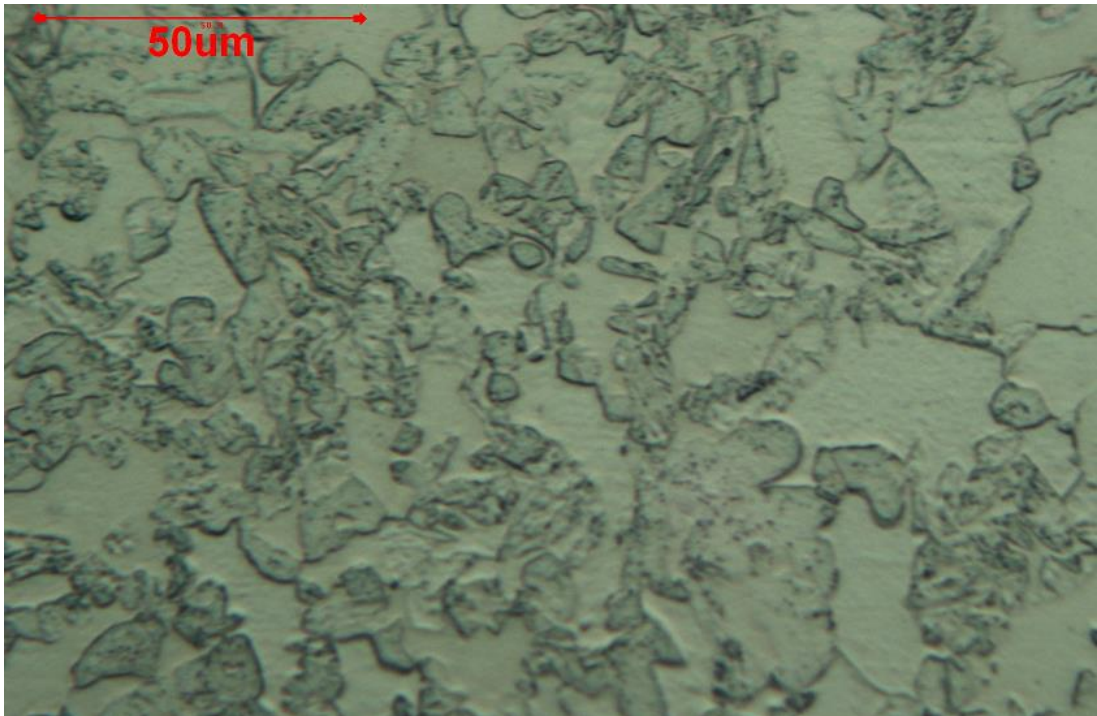


Figure 164. Image showing ferritic (light areas) and martensitic (dark areas) microstructure of an EN1.4003 sample subjected to 779°C 20 min soak water quench.

790°C 20 min soak

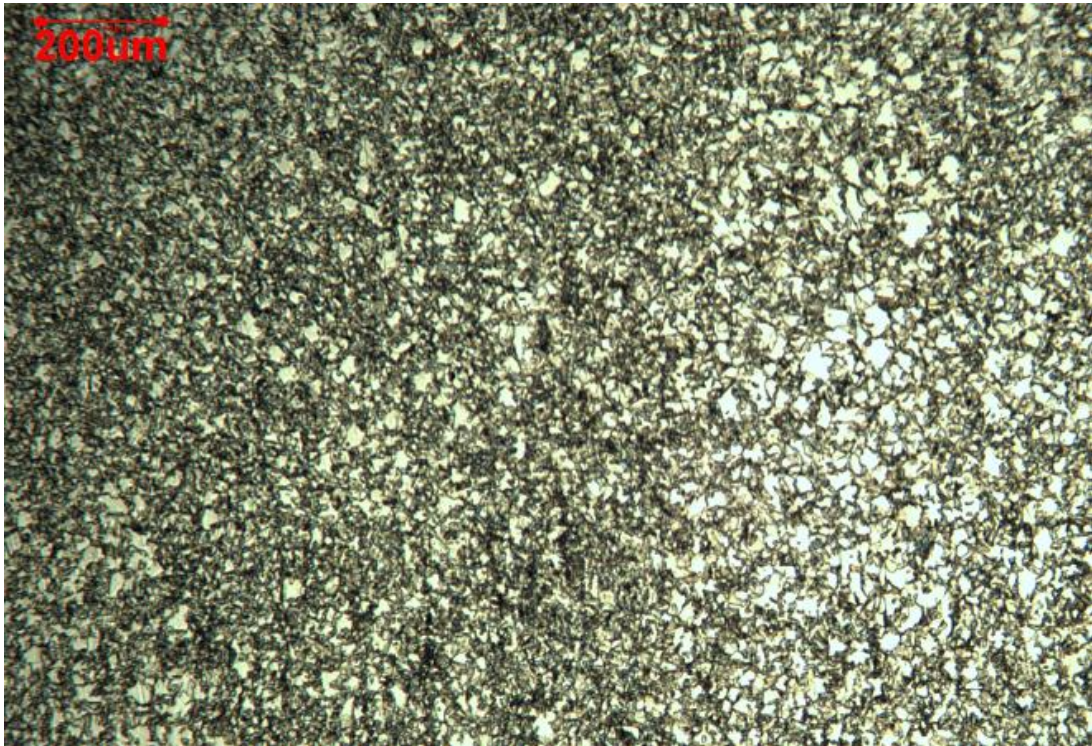


Figure 165. Image showing ferritic (light areas) and martensitic (dark areas) microstructure of an EN1.4003 sample subjected to 790°C 20 min soak water quench.

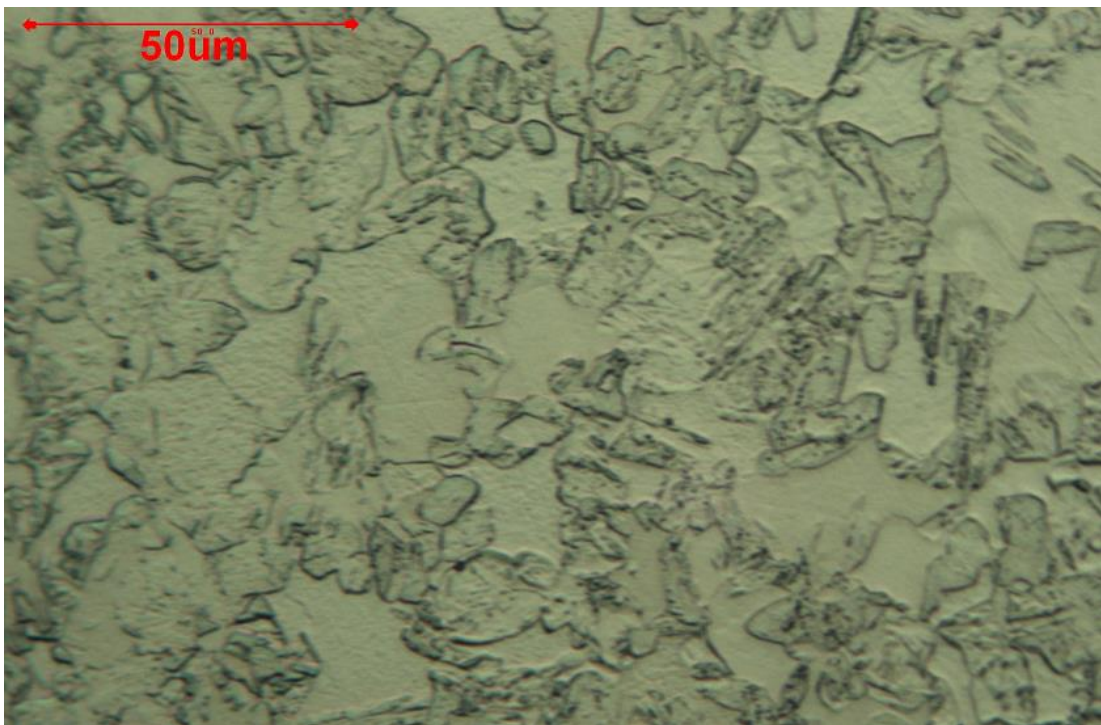


Figure 166. Image showing ferritic (light areas) and martensitic (dark areas) microstructure of an EN1.4003 sample subjected to 790°C 20 min soak water quench.

800°C 2 hour soak Water Quench



Figure 167. Image showing martensitic microstructure of an EN1.4003 sample subjected to 800°C 2 hour soak water quench.

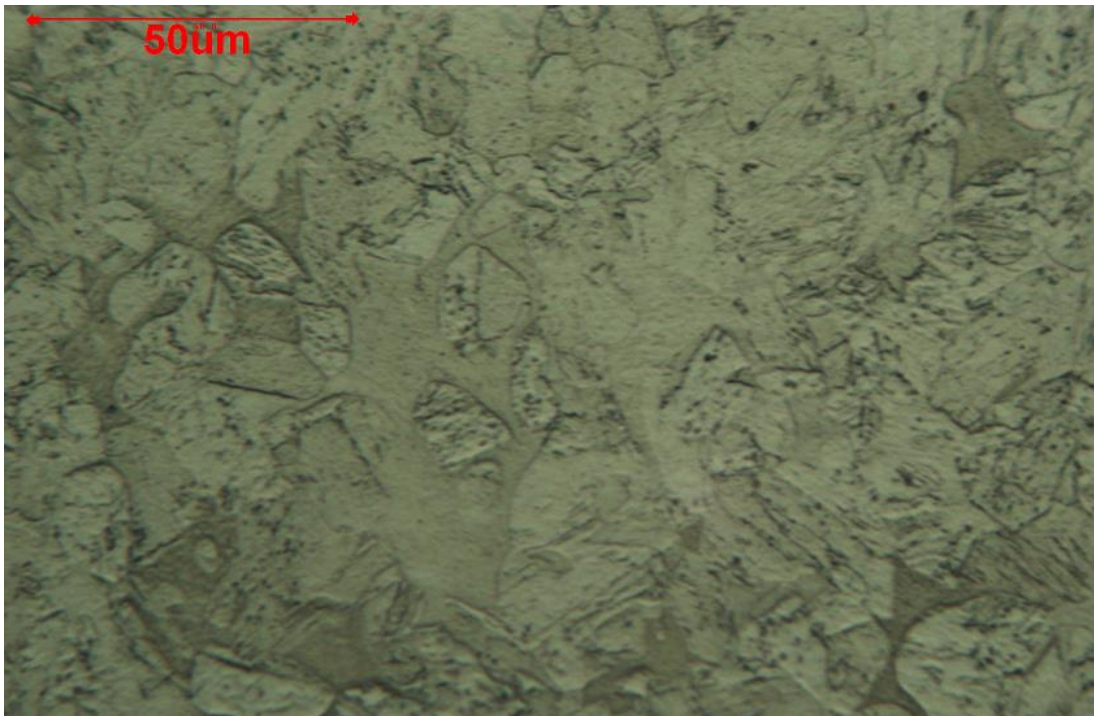


Figure 168. Image showing martensitic microstructure of an EN1.4003 sample subjected to 800°C 2 hour soak water quench.

770°C 2 hour soak Water Quench



Figure 169. Image showing ferritic (light areas) and martensitic (dark areas) microstructure of an EN1.4003 sample subjected to 770°C 2 hour soak water quench.

760°C 2 hour soak water quench

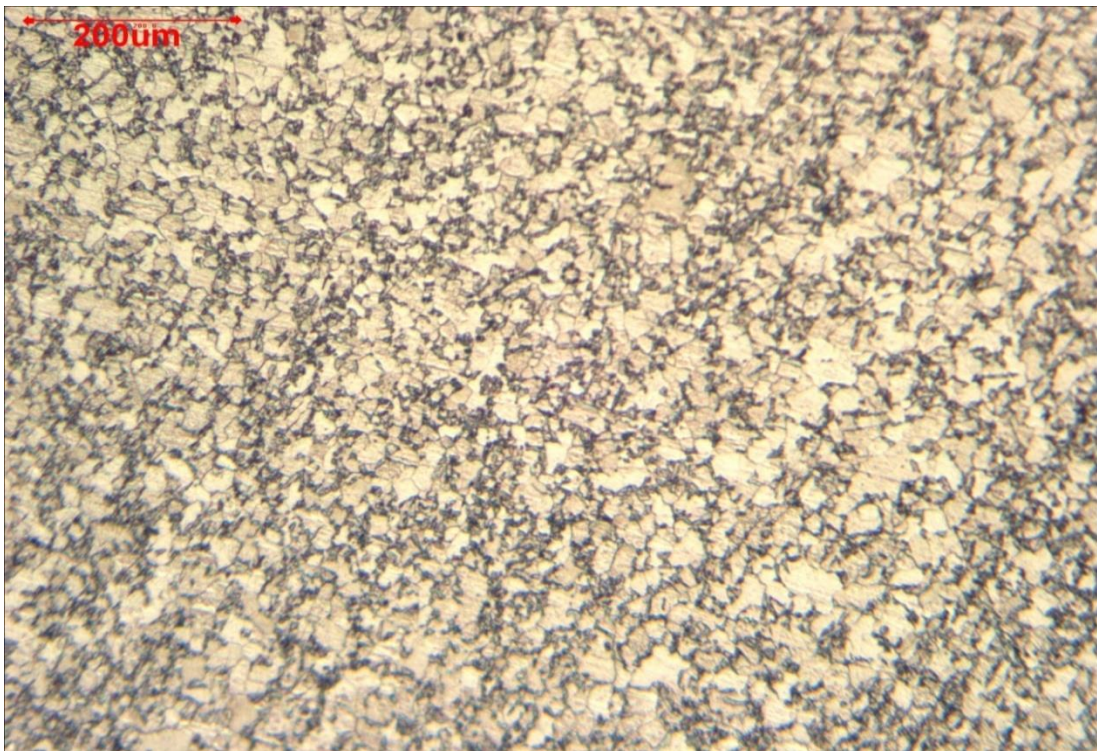


Figure 170. Image showing ferritic (light areas) and martensitic (dark areas) microstructure of an EN1.4003 sample subjected to 760°C 2 hour soak water quench.

750°C 2 hour soak water quench

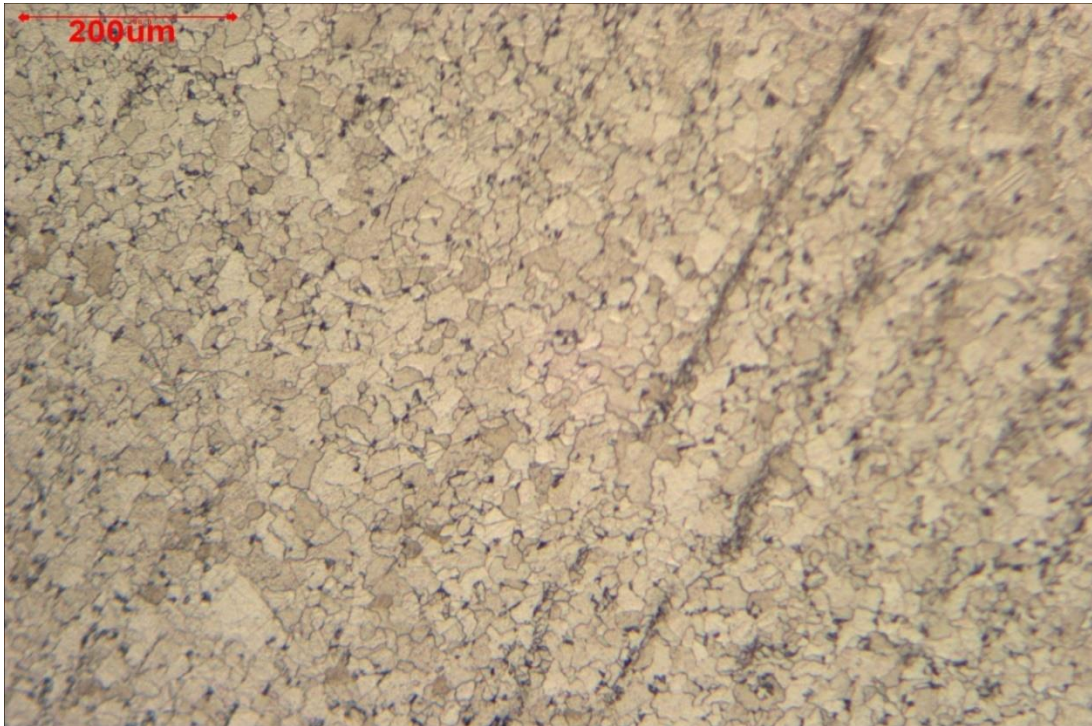


Figure 171. Image showing ferritic (light areas) and martensitic (dark areas) microstructure of EN 1.4003 sample subjected to 750°C 2 hour soak water quench.

740°C 2 hour soak water quench

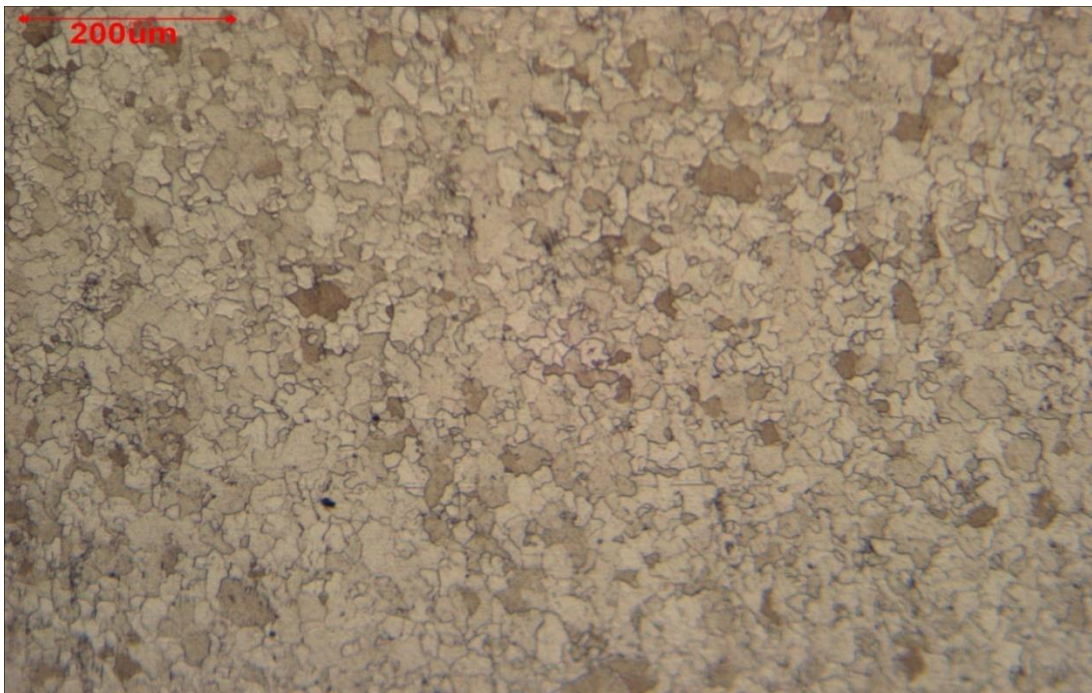


Figure 172. Image showing ferritic microstructure of an EN 1.4003 sample subjected to 740°C 2 hour soak water quench.

800°C 2 hour soak Furnace Cool



Figure 173. Image showing martensitic microstructure of an EN1.4003 sample subjected to 800°C 2 hour soak Furnace cool to determine the effect of time at temperature.

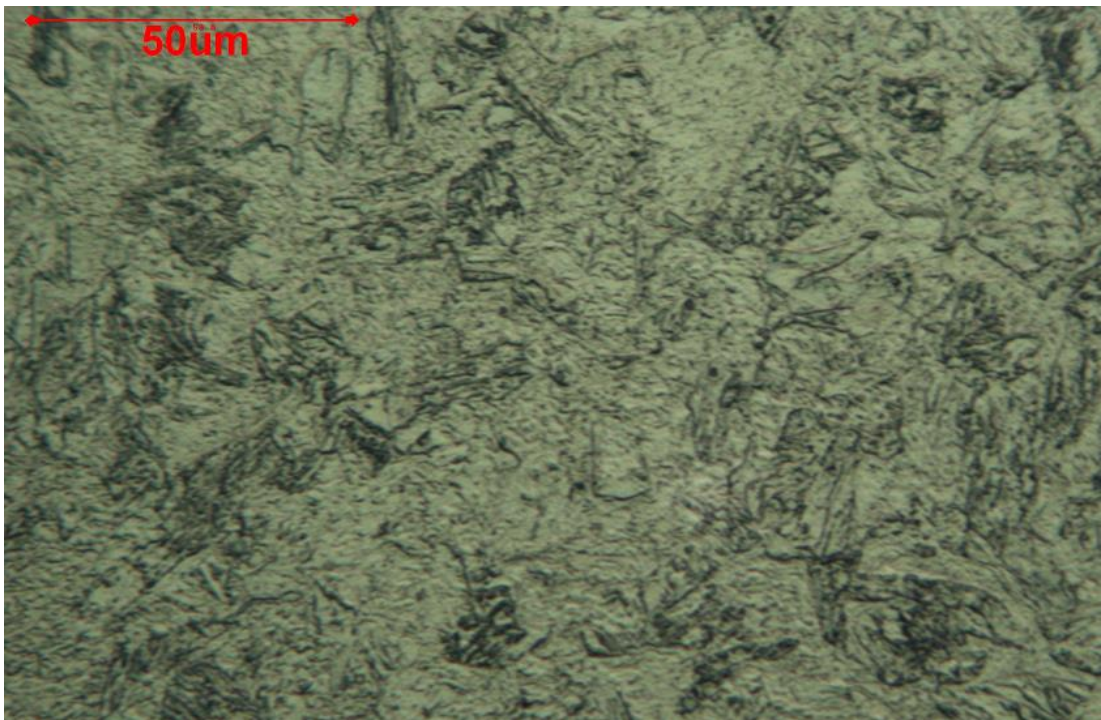


Figure 174. Image showing martensitic microstructure of an EN1.4003 sample subjected to 800°C 2 hour soak Furnace cool to determine the effect of time at temperature.

800°C 6 hour soak 30°C/Hour cool rate



Figure 175. Image showing ferritic (light areas) and martensitic (dark areas) microstructure of an EN1.4003 sample subjected to 800°C 6 hour soak 30°C/hour cool rate.

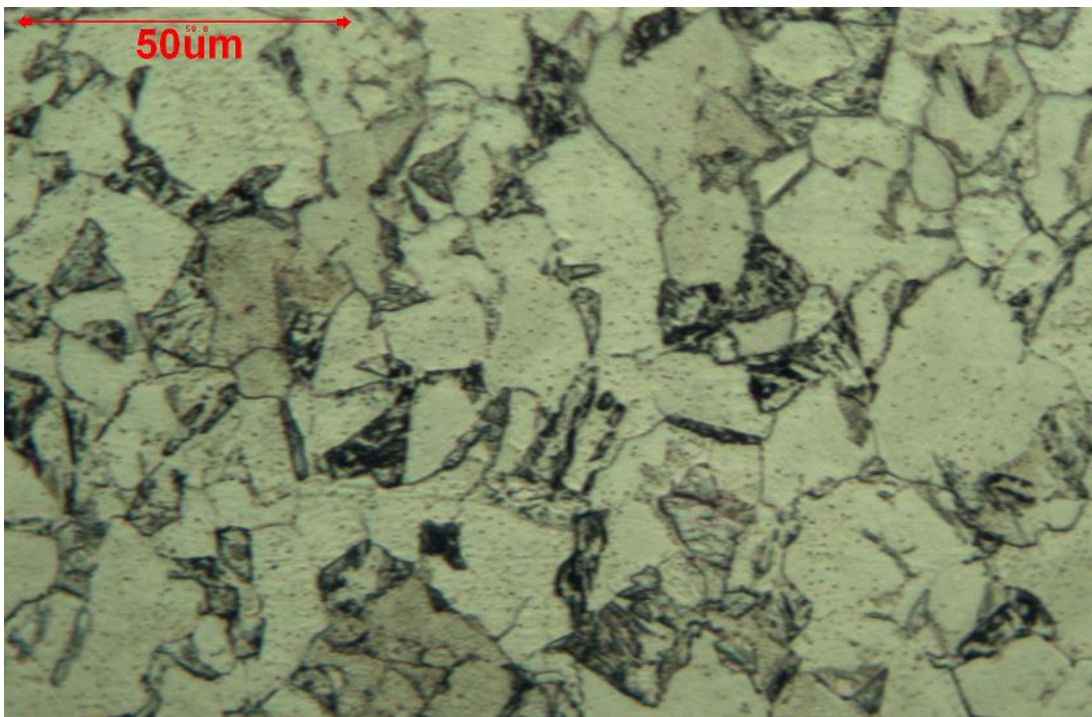


Figure 176. Image showing ferritic (light areas) and martensitic (dark areas) microstructure of an EN1.4003 sample subjected to 800°C 6 hour soak 30°C/hour cool rate.

1000°C 6 hour soak 30°C/Hour cool rate



Figure 177. Image showing martensitic microstructure of an EN1.4003 sample subjected to 1000°C 6 hour soak 30°C/hour cool rate grain coarsening also evident.

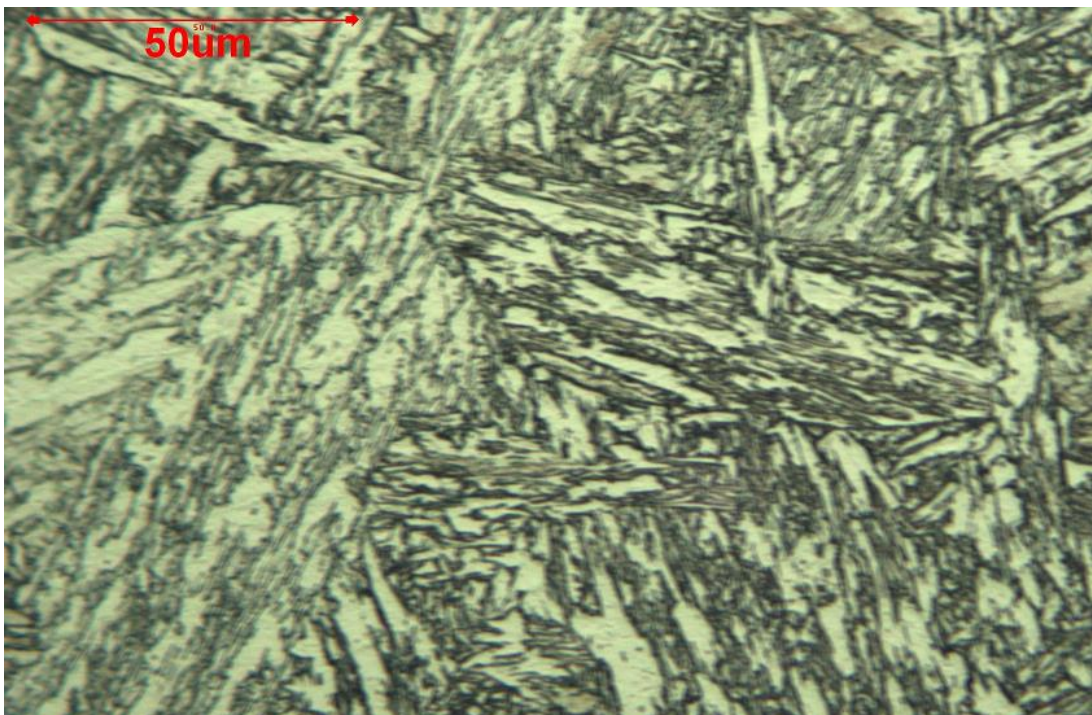


Figure 178. Image showing martensitic microstructure of an EN1.4003 sample subjected to 1000°C 6 hour soak 30°C/hour cool rate, grain coarsening also evident.

900°C 6 hour soak 30°C/Hour cool rate



Figure 179. Image showing martensitic microstructure of an EN1.4003 sample subjected to 900°C 6 hour soak 30°C/hour cool rate, grain coarsening also evident.

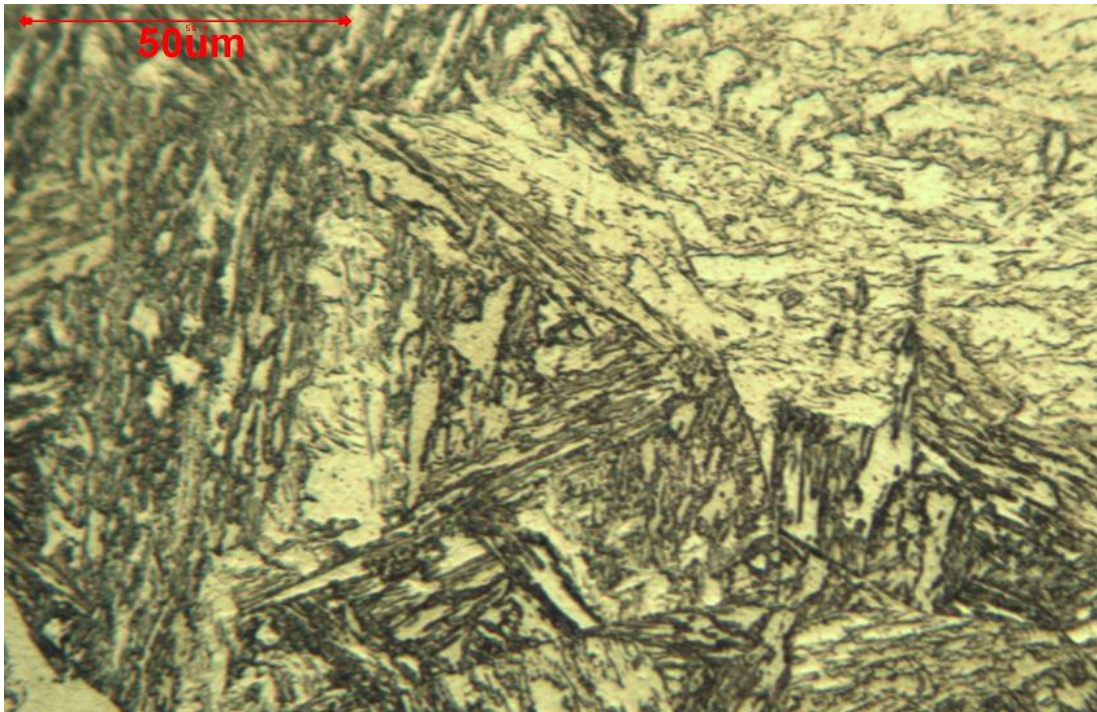


Figure 180. Image showing martensitic microstructure of an EN1.4003 sample subjected to 900°C 6 hour soak 30°C/hour cool rate, grain coarsening also evident.

Holding time (minutes)

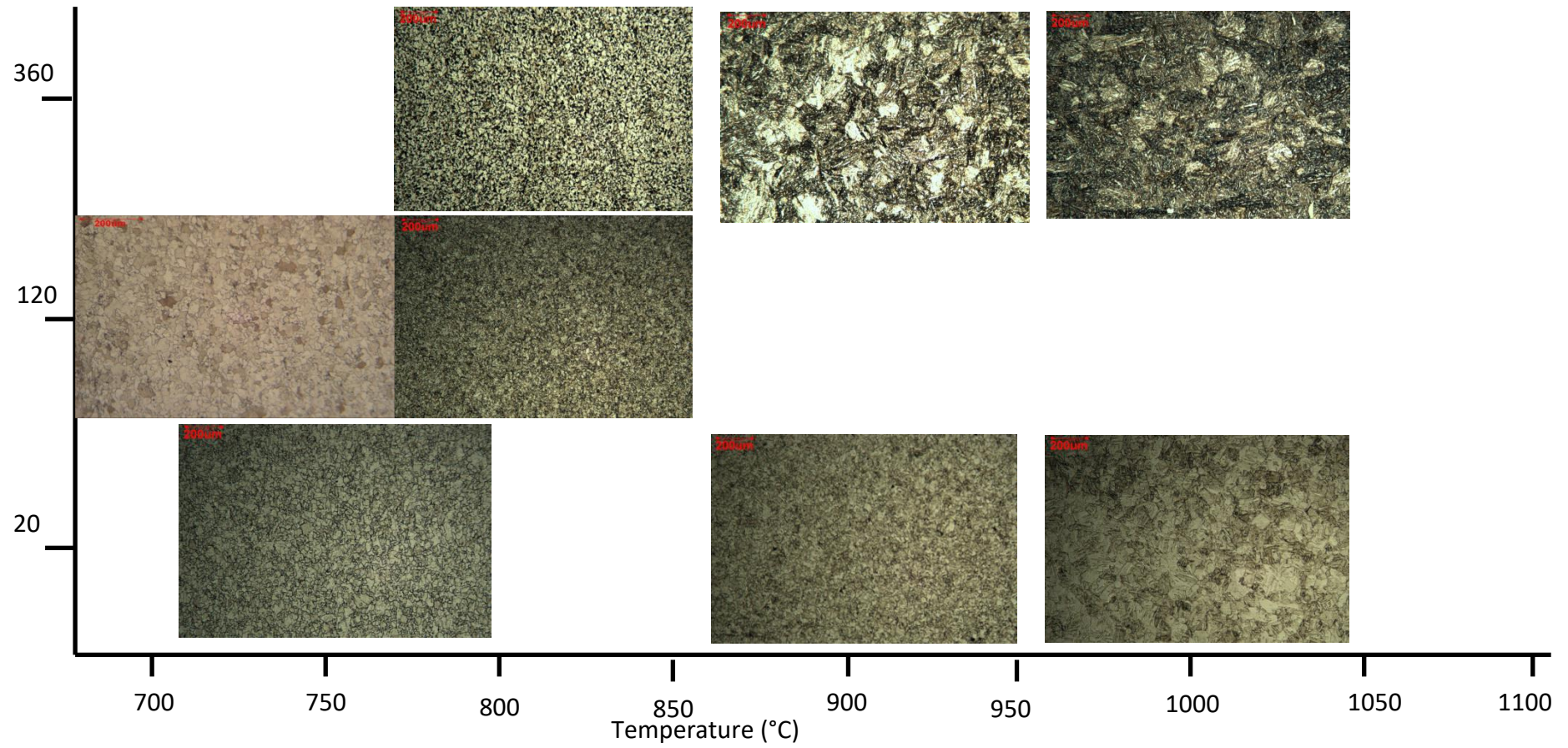


Figure 181. Figure showing microstructures of samples subjected to a hold for a time at a temperature.

4.8.1 Effect of Thermal Cycles on the Mechanical Properties and Grain Size of the EN1.4003 Grade Stainless Steel

The following graphs show the effects on grain size, impact properties and hardness of EN1.4003 being exposed to high temperatures as this provides a greater understanding of the effects of the microstructural changes that drive these properties, have on the HAZ of a weld using this grade of material.

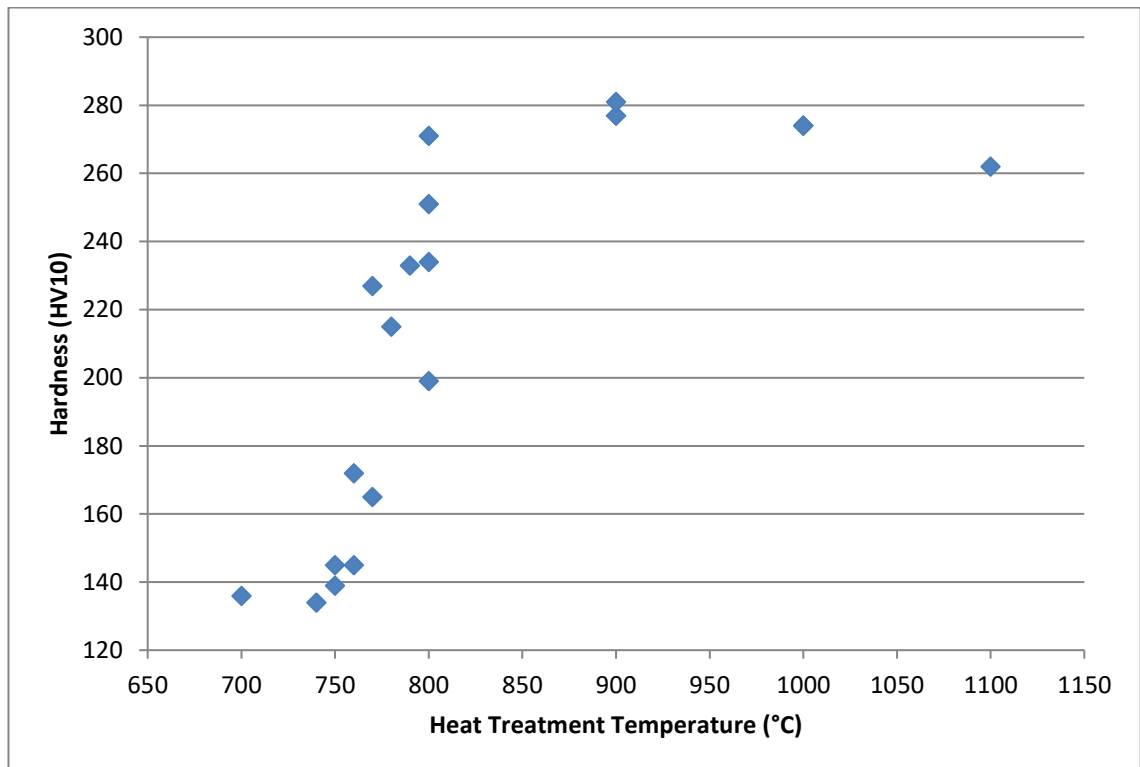


Figure 182. Graph showing effect of peak temperature on hardness (HV₁₀).

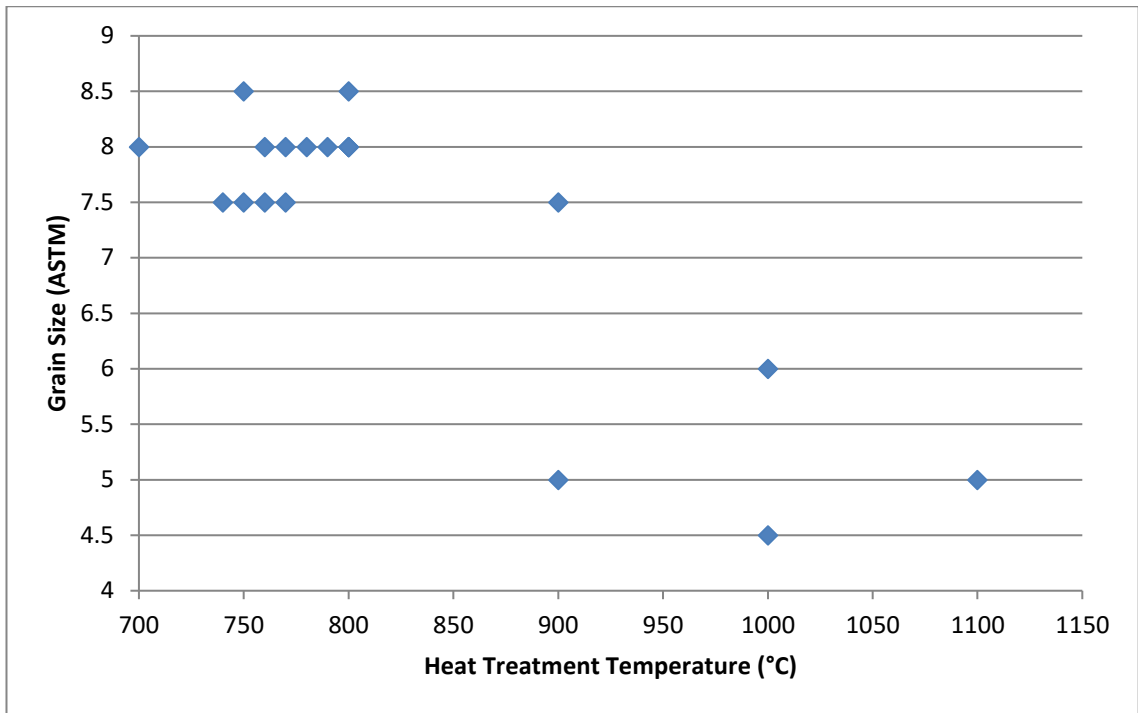


Figure 183. Graph showing effect of peak temperature on grain size.

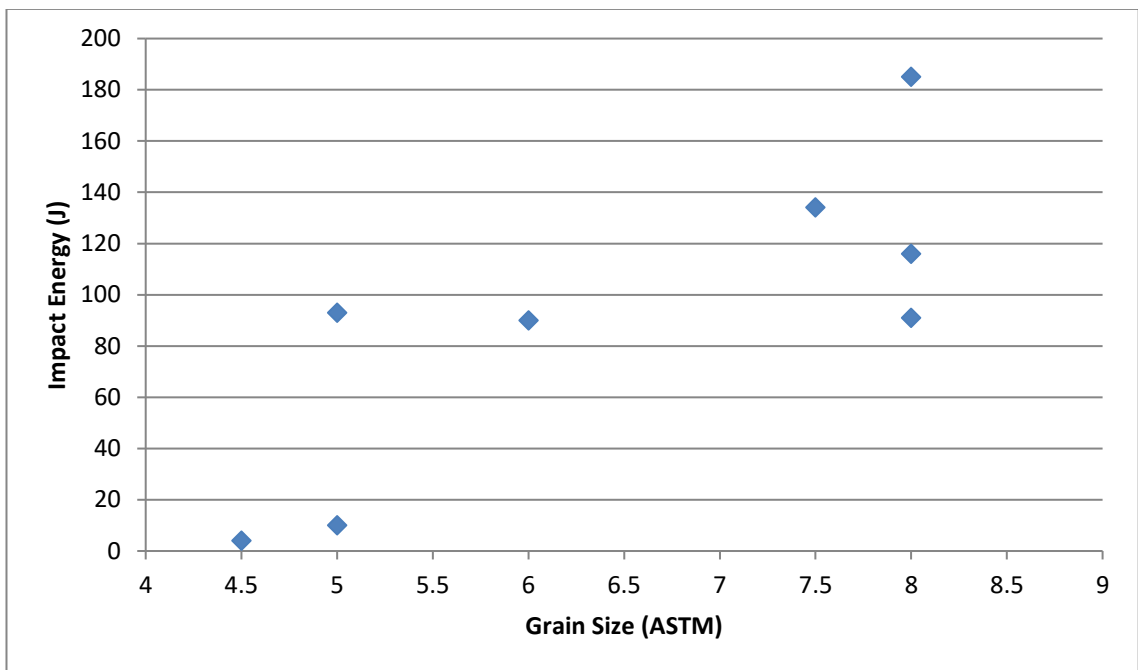


Figure 184. Graph showing effect of grain size on material toughness.

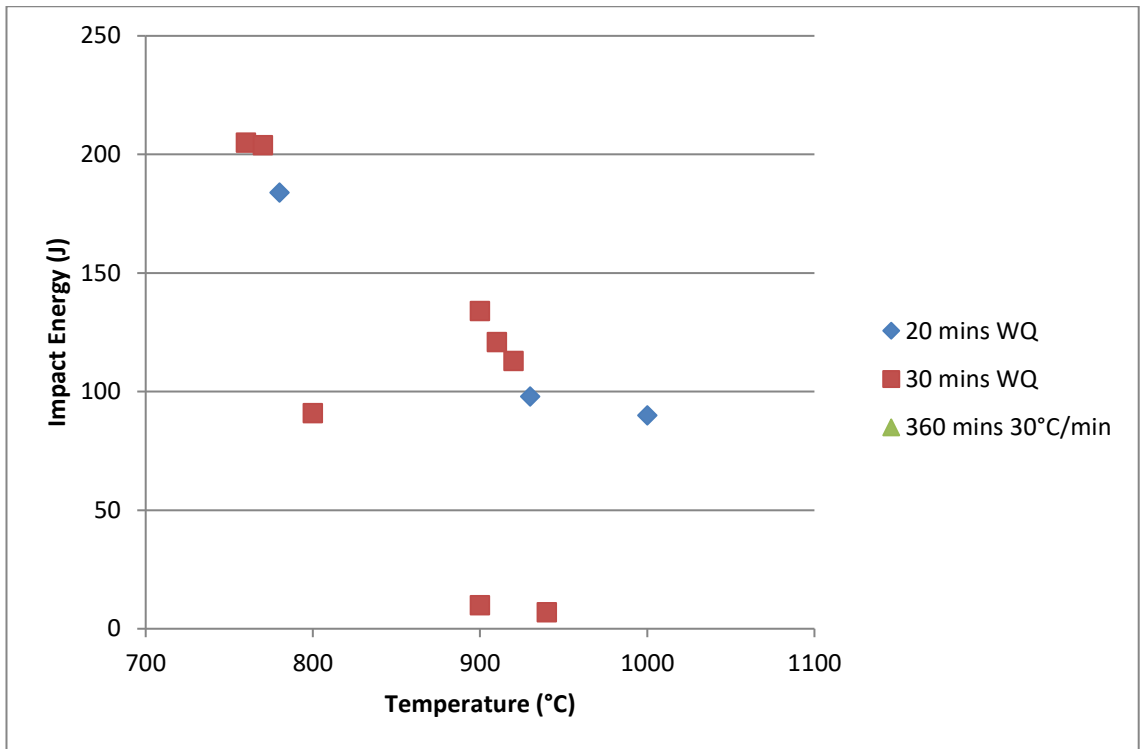


Figure 185. Graph showing effect of different thermal cycles on impact properties.

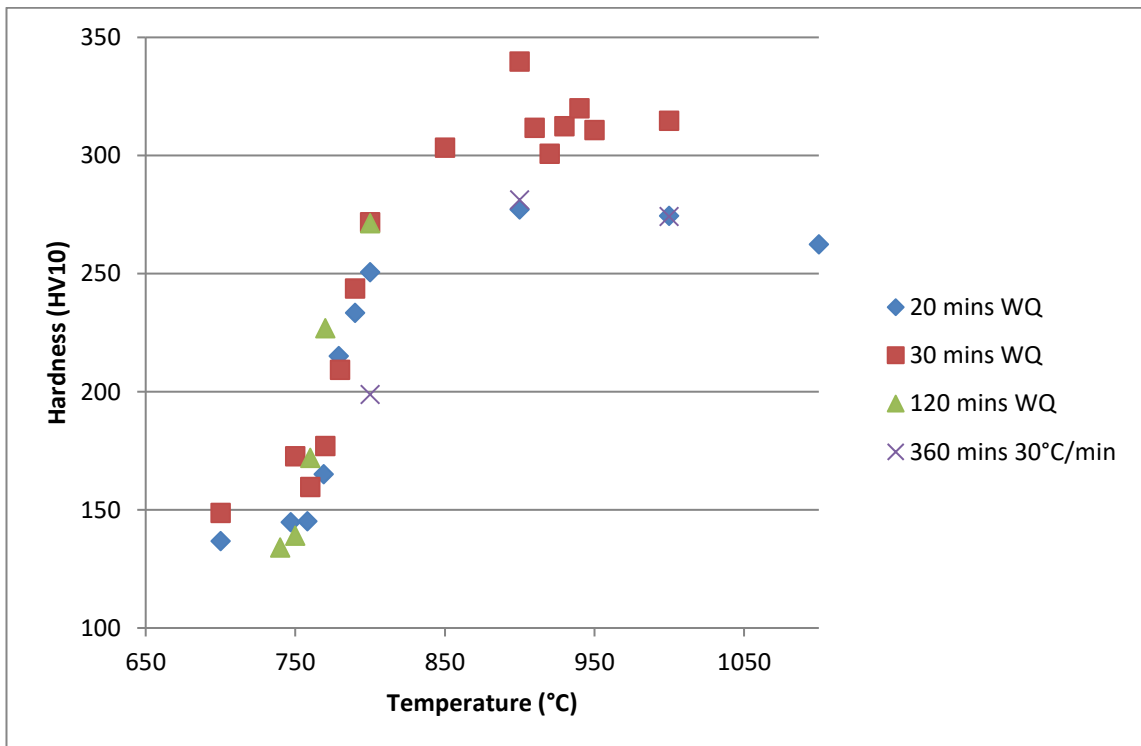


Figure 186. Graph showing effect of various thermal cycles on hardness.

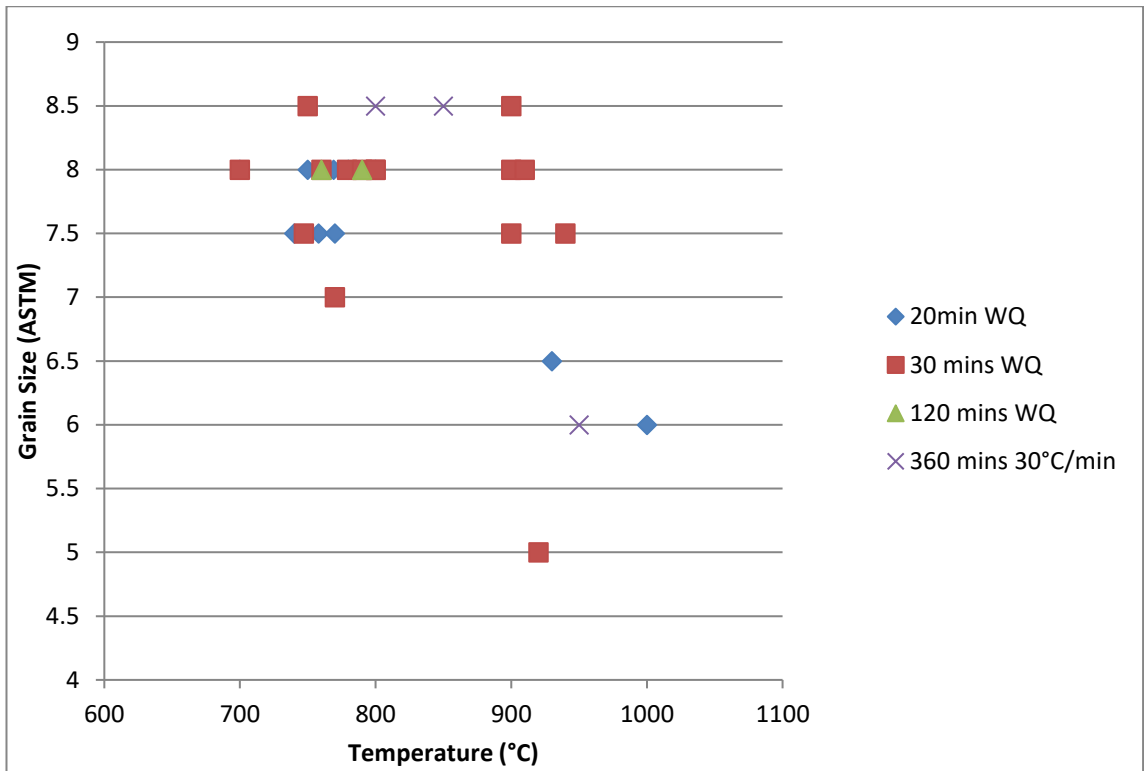


Figure 187. Graph showing effect of various thermal cycles on grain size.

5 Discussion

5.1 Microstructural Materials Characterisation

The microstructural characterisation of the parent materials used in the study showed the structures that would be expected for each of the grades used. Therefore as can be seen in Figure 61 to Figure 65 the parent materials show a fully ferritic microstructure with equi-axed grains. The only evidence of directionality comes from the consistent orientation of the carbides as seen in Figure 65.

5.2 Initial Comparison of Required Heat Input for MAG and CMT On EN1.4016, EN1.4509 & EN1.4521 Ferritic Stainless Steel Parent Materials.

The results obtained were based on a relatively small set of samples under laboratory conditions and it is possible that both the MAG and CMT welding parameters were capable of further optimisation. The trials did identify the importance of the joint fit up.

There was a presumption at the commencement of the work that the CMT+P process would offer the advantage of a reduction in spatter and, more importantly, potential for a reduction in net heat input, which would be relevant to microstructural control in ferritic stainless steel joints.

The results from this element of the work indicated that the cold metal transfer process, with and without pulsed arc, offered no apparent benefit with regards to the net heat input when compared with MAG welding when joining the 1.5mm thick materials and under the conditions of test. This is also indicated by the analysis of the HAZ grain size, where the CMT welded 1.5mm thick 1.4016 & 1.4521 materials had

larger average grain sizes, within the coarsest zones, when compared with the results from the MAG welded joints. However it needs to be taken into account that only limited material was supplied with the MAG welds to allow the production of the comparator CMT welds and so full optimisation was not possible on the welds produced.

The measurements made of the heat affected zone width through optical assessment, on samples in the etched condition, appear to be confirmed, in most cases, by the hardness profiles. The exception to this is the MAG welded 1.4016 (702852 1) as seen in Figure 68 where the hardness in the 20mm span does not return to the base hardness that is apparent on the other joints produced using the same parent material. These measurements were checked to confirm the findings. It is likely that there was some other difference in that area of the plate, possibly compositional difference, which could be difficult to check as techniques such as XRF are unable to determine carbon levels and carbon is one of the key elements that can affect the hardness of a stainless steel, it may also have been as a result of additional cold work. This would have been evident prior to welding if tests had have been conducted before the weld was made. It may have been possible that there was cold work induced in the material due to restraint from the clamping mechanism and the thermal expansion/contraction associated with the welding process, but this is highly unlikely as the clamping was consistent across all the samples welded and therefore this would have been observed in multiple samples and not just the one.

Indications from this work suggest that the CMT process may be of benefit for thicker materials. When the cold metal transfer welds produced using the 1.4509 (2mm thick) material are compared, in coarse grain size, with the MAG controls, the grain size for

the CMT/CMT+P are ASTM 3.5 and 3.6 respectively. The same material/thickness combination joined using the MAG process had measured grain sizes, made in the same locations, of ASTM 3.0 & 3.1, with net heat inputs of 0.129 & 0.101 kJ/mm for the CMT/CMT+P, the MAG welds had heat inputs of 0.162 & 0.117 kJ/mm.

5.3 Effect on Microstructure and Weld Dimensions of Heat Input Using Pulsed Arc with CMT on EN1.4016 2mm Thick Parent

The purpose of this aspect of the work was to assess the effect on weld dimensions and microstructure through variation of the heat input, using CMT welding, with and without a pulsed arc. Therefore welds were produced at predefined parameter settings to give specific heat inputs. As can be seen in Table 15 & Table 16 as the heat input increases, so does the average width of the heat affected zone, this is to be expected as with an increase in energy into the joint would increase the area that is affected by this energy. It has also been observed with these results that in the case of the CMT with the additional pulsed arc, as the heat input increases, the parent to weld cap angle increases, which therefore means that the weld cap is getting flatter. This trend was not observed in the results for the pure CMT welds. The power levels and therefore the heat input was at the same level, as the welds created using the additional pulsed arc, but the pure CMT welds had a consistent angle across all the power settings. This indicates that the weld pool had a reduced wettability, which would indicate the temperature was lower than that with the addition of the pulsed arc.

The grain size measurements made in the parent material give an ASTM grain size of approximately 7. The results show that in the HAZ there is a significant change in this

grain size and that as the heat input is increased the coarser the grain size in the HAZ becomes. Additionally between the process with and without pulsed arc, it was found that without pulsed arc the grain coarsening effect is greater, indicating that the HAZ had experienced higher temperatures for longer. Although it was noted that with pure CMT there was acceptable levels of root penetration at a lower heat input than with the additional pulsed arc at 0.09 kJ/mm (Table 15 & Table 16). Therefore from this it can be determined that although the amount of energy that is put into the joint has a pronounced effect on the penetration and HAZ, it is not just about the heat input, but the way the heat is applied that also has influence on the microstructure in the HAZ and therefore subsequent properties of the joint. This is because with the addition of a pulsed arc, the levels of high energy are cycled therefore the material has sufficient time to cool between cycles and so the thermal energy is reduced and therefore the material either side of the weld was not at sufficient temperatures high enough or long enough to cause the same growth of the grains.

It can also be observed from the line scans (Figure 72) that there is no obvious segregation of elements and that the difference across the interface is just down to the difference in the composition of the filler material compared with the parent. The austenitic filler material is used as it doesn't have the same detrimental effects associated with reduction in toughness and manifest of an acicular phase as the austenitic material is a single phase from room temperature to melting point and also the material has an FCC crystal structure so isn't susceptible to the reduction in toughness in the same way that a ferritic stainless steel is during welding. Therefore is a good filler material to use to determine the effects on the parent materials.

5.4 Trial to Examine the Effects of Variation in the Welding Gap, Torch Traverse Speed and Torch Angle on the Heat Input Required to Give a Fully Penetrating Weld using 2mm Thickness EN1.4016 and EN1.4509 Parent Materials.

The first part of the trial made attempt to examine the relationship between weld gap and weld speed and the ability to produce fully penetrating welds, with identification of the heat input associated with the welds for both a EN1.4016 and EN1.4509 grade material. Weld penetration was assessed through a visual inspection of the completed weld. It can be seen through examination of Figure 74 & Figure 75 that three welding gaps were tested, 1mm, 1.15mm and 1.25mm and these were welded at three different welding speeds, 762, 1016 & 1270mm/min. It can be seen that for both materials there is advantage to increasing the welding gap size, this relates back to Pepe et al (2011) who identified that it may be more efficient when welding in a gap. Also increasing the torch traverse speed to reducing the required heat input to complete a fully penetrating weld. Also subsequently variation of the torch angle from 15° to -15° has a significant effect on the ability to produce a fully penetrating weld at lower heat inputs in the EN1.4016 material as can be seen in Figure 76, but this was not as clear when looking at the results for the welding tests conducted on the EN1.4509 grade material (Figure 77) although the effect of increasing the traverse speed can be observed.

The use of gap and welding speed variations produced welds in 2mm 1.4016 & 1.4509 with calculated heat inputs significantly lower than those achieved by comparable MAG welds in 1.4509 in the main comparison programme (Table 14). From this work images have been taken which show the effect on heat affected zone microstructure of a reduced heat input (Figure 78). For the welds calculated to have a lower heat

input, the extent of grain coarsening and width of the affected region is seen to be significantly lower than the samples with a higher measured heat input.

The results from the welding gap/speed trial indicate that increasing the torch traverse speed results in the expected reduction in the heat input into the joint, Figure 74. This trend can also be observed for all joint gaps, (with the exception of the 1.4016 grade using the 1.25mm joint gap at 1270 mm per minute welding speed where it was not possible with the limited material to achieve a joint with complete penetration). This is consistent with difficulties in bridging the weld gap at 1.25mm so clearly this problem is exacerbated at higher traverse speeds. Further work undertaken on the effect of traverse speed indicated that speeds up to the maximum available at the time at Sheffield Hallam University, were towards the upper end of the spectrum for providing the ability to decrease the heat input, whilst still maintaining a fully penetrating weld. Welds were produced at speeds of 2200mm/min with complete penetration at TPS weldtech, Bilston; however they could not consistently be replicated.

The results obtained from trials conducted with variation on the torch position for the 1.4016 grade material indicates that for this material there is a distinct benefit to using a drag angle i.e. the direction of the torch is opposing the direction of travel. As can be seen in Figure 76, by altering the torch to weld backhand (drag), allowed fully penetrating welds to be completed with a reduced calculated heat input, than those produced using a 15° lead angle ("lead" is when the torch angle is in the same direction as the direction of travel). Which is as would be expected from the literature (American Welding Society, 1991), which identifies that welding backhand gives a narrower more penetrating weld than back hand, which is considered to give a wider,

but shallow weld profile. This behaviour was not observed in the trials conducted on the 1.4509 grade material.

Grade EN 1.4016, may be more sensitive to the effect of heat in-put and therefore more useful for examining the impact of changes in heat in-put on the microstructural profile. The chemical composition of this material makes it likely that, during welding thermal cycles, it will form small quantities of austenite, which are then transformed to martensite instead of ferrite because of the fast cooling rates.

The trials conducted, varying welding gap, welding speed and torch angle suggested that there was scope for further optimisation of the welding conditions. For example, further variation in torch position (i.e. altering the lead or drag angle) may allow a reduction or increase in the net heat in-put in its own right but may also influence the optimum size of the gap and the welding speed.

5.5 Trial to Determine the Consistency of the Welding Parameters and Subsequent Welds with the CMT Welding Process

The consistency trials conducted on the EN 1.4016 grade 2mm thick ferritic stainless shows that measured (grain size, HAZ width etc) and recorded (welding information) data does not give the same values each time that measurement were undertaken or recorded. This variation could be down to human error in measurements. With some of the measurements, in particular the heat affected zone width, there is no definitive point to measure to. The changes in this region can be quite gradual and therefore deciding on the exact location of the end of this transition is difficult to assess. For this reason the edge of the HAZ was deemed to be at a point where the microstructure returned to the as received condition. The grain size measurements are conducted in

such a way as to capture the coarsest grains within the heat affected zone. This is determined by the operator making the assessments and so subject to errors, but this was considered the best way of capturing this information as it allowed quantitative assessment of the grains most likely to reduce the properties of the joint overall. That said the coarsest grains contained within the heat affected zone, as a rule, tend to be located close to the weld fusion zone, which is due to this area reaching higher temperatures than those experienced further away from the fusion zone (Lakshminarayanan, Shanmugam, & Balasubramanian, 2009) and are generally under the weld cap. The fact that they are under the weld cap potentially provides two benefits, the first is that the cross section in this area is increased to greater than that of the parent material owing to the reinforcement on the weld cap. The second, is that the filler material used was austenitic, therefore the enhanced grain size in the HAZ can reduce the toughness of the steel, through reducing the number of barriers (grain boundaries) to the movement of dislocations, but the filler could compensate for this reduction in properties, due to the austenitic filler having a Face Centred Cubic (FCC) crystal structure (Ashby & Jones, 2001) that allows the mechanism of ductility, dislocation motion, across a greater number of slip systems, than the Body Centred Cubic (BCC) ferritic stainless steel parent material. Consistency with these measurements was maintained through the same operator making them.

5.5.1 CMT Power Setting

The variation in power setting was done via the wire feed adjustment as all welds were conducted using a synergic programme. This automatically adjusts the power settings when the filler material and thickness and shielding gas are inputted into the equipment. Therefore, it was found that increasing the power has a profound effect

on the heat input of the weld, and increasing the power level, increased the heat input, with an associated decrease with a reduction in power level. The consistency of the average values from run to run at the same settings varied. Variations in both the measured average value for current and voltage changing by up to 15 amps and 1.9 volts respectively which is as a result of the CMT control software means that if there is a variation in the energy going in to the material there is bound to be a related variation to the structure and mechanical properties caused through the input of this heat.

The increase in power had the associated increase on the measurements made of the weld cap width, HAZ width and weld cap height. It was found that the weld cap width increased approximately 700 μ m for every 1m/min increase in the wire feed speed. There was a similar increase also seen for the HAZ width and weld cap height. The weld cap height is unsurprising since there was an increase in the amount of wire that was being fed towards the joint it is expected that the weld cap would be either taller, wider or both.

The consistency of the measured data from the microstructural measurements made varied from run to run, as a rule the pattern was similar for each of the HAZ width measurements made on each run. Furthermore there would be the expectation that toward the end of the run the HAZ width would increase, due to the heat build-up, but there was no clear evidence of this occurring.

The investigation also revealed that an increase or decrease of the wire feed setting, affected the number of pulses per CMT cycle. With the 3.5m/min having 5 pulses per CMT cycle, the 4.5m/min setting having 6 pulses per CMT cycle and the 5.5m/min having 7 pulses per CMT cycle. So not only is there an increase in the base power, but

also there is an increase in the number of short bursts of high power inputted into the joint, which will have the associated effects on the microstructure of potentially an extended HAZ and enlarged grain size.

5.5.2 Arc Length Correction

The variation permitted in the arc length correction function ranges from a value of -30 to +30 and was found to have an effect on the HAZ width. The consistency of the HAZ width, reduced by changing the ALC to -30 as when the ALC is set to +30 the results are relatively consistent as can be seen in Figure 92 & Figure 93. The heat input was found to alter slightly through the extremes of this parameter, with a value of -30 showing a higher value than that with an arc length correction of zero. This again was slightly higher than that with an arc length correction of +30, however the total difference was calculated to be approximately 6 J/mm between the two extremities of variation for this parameter.

When examining Table 18, it can be seen a greater number of welds are produced with complete penetration when the arc length correction is set at -30, which may be due to the extended period in the short circuit phase of the cycle as discussed by Pickin et al (2011). There may also be a benefit from the slight additional heat that this setting affords the joint. However it may be as a result of the difference in arc length that this parameter potentially affords. The welds created at the increased levels of arc length correction have a high concentration of welds with penetration bias to one side. This may again be as a direct result of the change in arc length and the ability of deviation of the arc that is facilitating this bias in the weld. This may be due to slight changes in magnetic field as the parent material is magnetic, the filler isn't and therefore slight variations in dilution could affect the orientation of the arc relative to the torch and

work piece. The longer the arc, the greater effect the deviation will have which potentially explains why this is not seen at ALC of -30, where the length of the arc is shorter.

The measurements made under the optical microscope also provide similar results. When the arc length correction factor is set at -30 there is a slight increase in the measured heat affected zone width and weld cap width and height. At both the other settings for this parameter (0 and +30) there was not a distinct difference between the measured heat affected zone or weld cap dimensions, between the two. This suggests that for this material grade, thickness combination the parameter needs to be adjusted to below 0 to produce a fully penetrating weld.

One of the interesting things to note from this parameter setting is that measurements made along each of the weld runs are fairly consistent giving a relatively flat line when the +30 arc length correction is used. With the -30 setting the welds were found to be less consistent than the +30 not just weld to weld but also across the weld.

5.5.3 Pulse Correction

The pulse correction parameter on the CMT equipment has adjustability from -5 to +5, this is a unit less parameter. When the correction was set at -5, the heat input was calculated to be approximately 74 J/mm. When set to zero the calculated heat input was determined to be approximately 88 J/mm and when at +5 the heat input was found to be approximately 102 J/mm. Therefore there appears to be a linear increase in the heat input when altering this setting. It was found through this study that the reason for this is because the variation of this parameter varies the power of each of the pulses. Increasing the pulse correction increases the voltage and current of each

of the pulses within the CMT cycle and therefore gives the increase/decrease in the heat input.

Examination of Table 18 shows that a pulse correction factor of -5 does not produce one part of the weld examined, on any of the welds produced with this setting, with complete penetration and is therefore a product of insufficient heat into the weld.

When the setting is at 0, there are a number of places in the weld where the penetration is insufficient but the majority of the welds show penetration to one side. However this is consistent across most of the weld sections examined therefore from the 31 sections, only one had suitable penetration (9 were identified as not having suitable penetration) and so it is unlikely that achieving a consistently fully penetrating weld is possible with these settings even if the penetration was not bias to one side.

There is a significant increase in the measured values of the width of the heat affected zone for the welds with a pulse correction of +5, with values increasing as much as 1.5mm from those measured from welds created with a -5 pulse correction setting. It is likely however that these results are as a result of the low heat input and therefore lack of penetration of the welds created at -5 pulse correction.

As there is such a dramatic effect from variation of this parameter it would be interesting to repeat this trial but with variation at increased wire feed settings as they would have an increased number of pulses per CMT cycle and therefore the variation of the pulse correction should have notable variation across the whole range from -5 to +5.

5.5.4 Traverse Speed

The heat input formula as seen in Equation 3, as seen on page 47, which is essentially the power divided by the traverse speed means that there is expected to be a significant difference in the heat input by variation of the traverse speed. Variations conducted in a separate trial within this study have shown that there is the possibility of reducing the heat input into a weld through increasing the speed of traverse. The variation in heat input through the change in traverse speed from 0.762 to 1.27m/min, results in a change of up to 50 J/mm from approximately 120 J/mm for the slower traverse speed to 70 J/mm for the faster traverse speed.

The welds created utilising a slower traverse speed produced a significant proportion of fully penetrated welds as compared to the faster speeds which only yielded portions of a weld run with complete penetration, as seen in Table 18.

The heat affected zone as would be expected is significantly larger for the slower traverse speed that with the faster traverse speed (Figure 88 & Figure 89), with a difference between the two of approximately 0.5 to 1mm. It was observed that the reduction in speed also provides a more consistent weld along the length of the run and also reasonable consistency from weld to weld.

The limitation of traverse speed was in the case of these trials of no apparent benefit as at the upper range assessed the welds were incomplete in terms of penetration.

5.5.5 Torch Angle

The variation in torch angle was made from a push angle of approximately +15° to a drag angle of approximately -15°. The calculated heat input showed that changing between the two resulted in a difference, with a marginal increase through using a

push angle. The reason for this is, at this time, unknown and may simply be as a result of the limited number of readings as the range between the two overlap. It could be that as with a push angle there is a flatter bead and therefore an increased time duration to contact with the weld pool and therefore an increase in the open circuit part of the CMT cycle.

There are also a higher number of incompletely penetrated welds with push angle and at the same time a higher number of completely penetrated welds than those welds conducted utilising a -15° torch angle. This goes against the concept of a certain requirement of heat input to provide a fully penetrating weld for certain materials/thickness combination, or alludes that other factors need to be taken into account when calculating the net heat input of a weld as variation of the torch angle does not in itself add any energy, but directs it either at the newly made weld (pull) or away from the weld (push), but has a significant effect on the penetration and geometry of the weld and therefore may influence the efficiency of the process.

The measurements made on the optical microscope show that with a torch angle of $+15^\circ$ (push angle), the heat affected zone is approximately 0.5mm larger, than the results from the examinations taken from the welds produced using a -15° torch angle. This then confirms work done previously in this study where drag angles produce a thin and deep weld profile, whereas a push angle yields a wide and shallow weld profile. This shallow profile produces a wider weld reinforcement and a wider HAZ.

5.5.6 ALX Data

The arc logging equipment provided the ability to monitor the weld as it was being produced, with readings taken of current, voltage, traverse speed and wire feed speed at a rate of 3000 data capture points per second, throughout the duration of the

monitored weld. This enabled the identification of the number of pulses per CMT cycle as identified earlier in this discussion and was easy to determine through examination of the trace of voltage and current against data point as seen in Figure 85 to Figure 87, where the peaks of each pulse can easily be determined. It is also been observed from these graphs that the effect of the pulse correction is to increase the current of the pulse. Therefore when the pulse correction is set to -5, the current for each of the pulses is approximately 280 amps, with the pulse correction set at 0 and +5 the currents are 340 amperes and 400 amperes, respectively. There also appears to be an increased duration between the last pulse within a CMT cycle and the first pulse of the next, as the pulse correction value is increased. The reason for this could be that with an increased pulse correction, there is the determined increase in pulsing current, which in turn would be increasing the amount of material that is melted and projected to the joint and therefore increases the arc length and so the time required for the electrode tip to make contact with the weld pool.

This theory is substantiated when the traces for the arc length correction parameters were altered, as similar differences can be observed with these results. When variation of the arc length correction parameter is made a similar effect can be seen on the graph where the time duration between the last pulse of the CMT cycle and the voltage drop through detection of short circuit. This effect is probably that which provides the slightly higher calculated heat input when the arc length correction is set to -30, than at +30.

5.6 Comparison of Microstructure and Mechanical Properties for CMT

Welded and MAG Welded EN 1.4003 Parent Material in 3.8mm & 5.8mm Thicknesses

Initial CMT welds created using the EN1.4003 parent material in the 3.8mm and 5.8mm thicknesses revealed a number of problems in the welding of these thicker materials, in comparison to the work conducted on the thinner materials, less than 2mm.

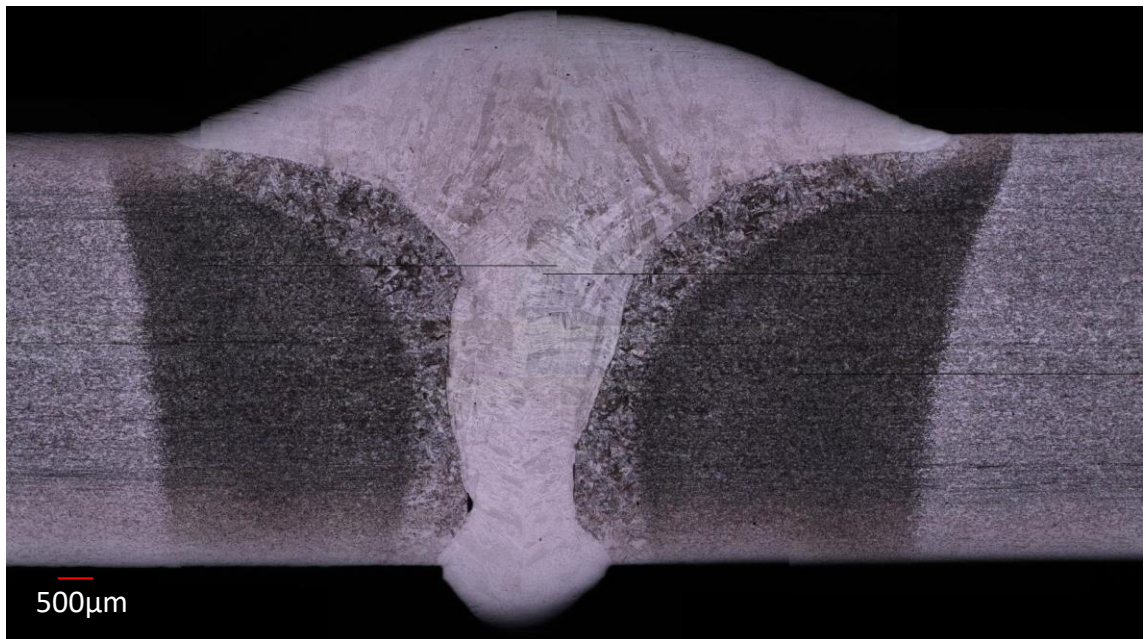


Figure 188. CMT weld cross section of the 5.8mm thick EN1.4003 grade parent material

Figure 188 shows a microstructural cross section of one of these welds and as can be seen in the image, there are four distinct regions associated with the weld. There is the fusion zone in the middle where the filler and a portion of the parent materials have mixed together and then subsequently fused during the welding process to create the joint. Either side of this is the first part of the HAZ, the lighter zone adjacent the fusion zone. In this area there are two notable effects associated with exposure to

the welding thermal cycle. Firstly there is a significant grain coarsening effect evident in this area as discussed by Lakshminarayanan et al (2009) and secondly there has been a phase transformation, so that the ferrite has transformed to austenite upon heating and then as the material cools, the austenite doesn't have sufficient time to transform back to ferrite as the cooling rate was too high, therefore there is the transformation to martensite, which will increase the hardness and strength of this region in contrast to grain coarsening which will have the opposite effect. Both of these changes will have a detrimental effect on the impact properties of the joint.

The next region moving away from the fusion zone is the second part of the HAZ, which doesn't have any grain coarsening but does show the transformation to martensite and therefore the associated effects of this phase in terms of the increase in hardness and strength, with a reduction in the impact properties of the material. Beyond this zone the microstructure is that of the parent material, therefore there are no notable changes as a result of the welding thermal cycle. Work previously undertaken by Zheng et al (2010) described the Ferrite Factor (Equation 4) being important in determining the likely microstructure of low carbon, 12% chromium stainless steels, with indication that a ferrite factor above 9.0 would yield virtually 0% martensite in the structure and a ferrite factor of 7.62 would give 90% martensite in the structure, the EN1.4003 grade material utilised within this research has a ferrite factor of 7.78, therefore the heat affected zone is predicted to have a high proportion of martensite within it, which has been observed.

The images seen in Figure 101 show another potentially detrimental feature identified within the weld that only became evident following sectioning and examination of the weld cross section. This was the lack of side wall fusion, which is apparent towards the

root of the weld. This is where the weld material hasn't had sufficient energy to melt and fuse with the parent material and although in this particular instance is relatively small, it can create a stress concentrator and therefore reduce the fatigue properties of the joint.

5.6.1 Non Destructive Examination - Radiography

To try and identify defects within the welds prior to subsequent processing, a number of the welds were analysed using radiography. Another technique that would have been a potential option for this type of testing would have been Ultrasonic Inspection (UI), however at 5.8mm thick was on the lower limit for the UI equipment available to be able to inspect. An attempt was made to use the UI equipment to inspect the 5.8mm thick welds but was unsuccessful in identifying any defects.

Through a basic visual examination of the welds certain features could be identified without the use of radiography, such as spatter, undercut, a lack of root penetration and excessive penetration. However it was the internal unseen defects that were of interest for these inspections. Therefore one plate that had been used for the optimisation of the radiographic inspection parameters, was then subject to a destructive examination.

As can be seen in Figure 102 the radiograph with the identified known defects and suspected defects were identified and then sections were taken at the specific locations as identified in the figure, for the microstructural examination.

It can be seen through the course of this examination that the weld contained a number of unseen defects that weren't identified on the radiograph as well as those that were. A key issue identified whilst undertaking the examination was that there

were a number of sections where a lack of side wall fusion was identified upon the destructive examination, as seen in Figure 104. Due to the small size and orientation of these defects they were unable to be detected with the equipment used for the radiographic inspections, therefore it was decided that radiography was not an appropriate technique for the examination of the welded sheets as it didn't enable differentiation between good and bad welds.

5.6.2 Microstructural Comparison for Welds Created Using the CMT Welding Process and MAG Welding Process Using 3.8mm Thick EN1.4003

Microstructural evaluation was made on the welds created using the 3.8mm thick EN1.4003 parent material, images of the welds can be seen in Figure 189 & Figure 190.

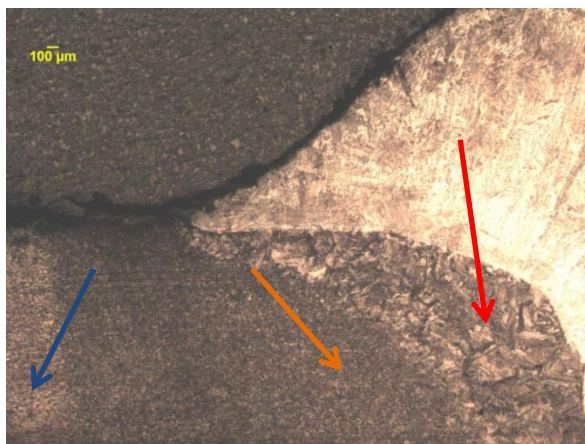


Figure 189. . Image showing weld (top right) and HAZ , which has two distinct regions, the first next to the weld (red arrow) has a martensitic structure and grain coarsening, the second region of the HAZ (orange arrow) has a martensitic structure but without any grain coarsening and then the blue arrow indicates unaffected parent material of 3.8mm thick EN1.4003 parent, CMT welded sample 25.10 (etched in glyceresia).



Figure 190. . Image showing weld (top left) and HAZ , which has two distinct regions, the first next to the weld has a martensitic structure and grain coarsening (red arrow), the second region of the HAZ (orange arrow) has a martensitic structure but without any grain coarsening and then the blue arrow indicates unaffected parent material of 3.8mm thick EN1.4003 parent, MAG welded sample 30.7 (etched in glyceresia).

In both images the fusion zone can be seen followed by the area of the HAZ with the grain coarsening and martensitic microstructure, then next to this is the HAZ with martensite at the grain boundaries, but no change to the grain size from that of the parent material, and then there is the transition point where the heat from the weld didn't reach sufficient temperatures to alter the microstructure and so it reverts back to the structure of the parent material. The first observation is with the difference in the net heat inputs of these welds. The CMT net heat input is calculated to be 273.6J/mm and the MAG net heat input calculated to be 581.4 J/mm. Therefore with such a significant difference in the heat input there would be an anticipated difference in the affect this has on the HAZ, in terms of the extent of grain coarsening and the width of the HAZ as discussed by Lakshminarayanan et al (2009) where they identified that the greater temperatures or extended time at temperature would increase the grain coarsening effects.

With examination of Table 21, it can be seen that there is a difference between the welds created for each process, with an increase in the width of the MAG weld, HAZ that contains grain coarsening by an average of approximately 120µm, and the MAG HAZ width overall is increased by approximately 280µm, this reduction in HAZ size was also noted by Benoit et al (2011) in their research on welding Inconel 718 using the CMT process. The grain size, within the HAZ of the MAG weld over the CMT, going from ASTM 3.9 for the CMT weld, to ASTM 3.2 for the MAG weld.

Therefore the increase in the width of the HAZ of the MAG welds and the increase in grain size, compared to the CMT welds should yield a detrimental effect on the toughness of the joints as the increased grain size reduces the resistance to crack propagation through reducing the number of grain boundaries that hinder the movement of dislocations. The increase in HAZ width also means that the martensitic phase that manifests on the grain boundaries, will also have a damaging effect on the impact properties. This will be discussed in 5.7.

5.6.3 Comparison of Tensile Data for Welds Created Using the CMT Welding Process and MAG Welding Process Using 3.8mm & 5.8mm Thick EN1.4003

The following section, discusses the results gained from tensile testing welds created using the CMT welding process and welds that have been created using the conventional MAG welding process. This evaluation has been made on two different thicknesses of parent material, 3.8mm thick and 5.8mm thick EN1.4003.

5.6.3.1 Comparison of Tensile Data for CMT Welds and MAG Welds in 3.8mm EN1.4003

As can be seen in Table 5, the tensile properties for this material is expected to be a minimum yield point of 320 MPa, tensile strength of 450 MPa with a minimum elongation value of 20% (Outokumpu, 2011). The results achieved for the 3.8mm thickness, CMT welded samples (Table 22) were for the most part in excess of these values, with one exception and that was for sample 25.2, which only had an elongation value of 18.6%. There was no apparent difference noted in the sample to explain this result in comparison with the other samples and the yield and tensile strength were within the range of the results achieved for the other specimens that were testing. All of the specimens tested for the CMT welded 3.8mm thick samples, failed within the parent material. Some of these failures were close to the HAZ region, but the majority were well into the parent material and not close to the HAZ, which was something noted in the work conducted by Madhavan et al (2016) in their research looking at joining aluminium and steel using the CMT welding process. It would be expected that the strength in the outer area of the HAZ (furthest from the weld) would be enhanced due to the formation of the acicular phase present in that area as seen in Figure 107, which would explain why there were no failures in the HAZ region, the areas where coarsening of the grain size had occurred were protected by the increased cross section of the weld cap, which they lay underneath.

The tensile results for the 3.8mm EN1.4003 parent material welding using the conventional MAG process as seen in Table 23 doesn't have such consistency in the results. Sample M28.9 achieved a reduced yield strength in comparison to the rest of the tests conducted for this process at the 3.8mm thickness, but more significantly the elongation was approximately half the value of the lowest of the rest of these samples,

at 8.6%. It was noted for this sample that the failure initiated in the parent material next to a piece of spatter. The remainder of the samples all failed in the parent material, although were noted to have all failed close to the HAZ. These tensile tests also demonstrated a similar yield point to those created using the CMT process, but there was a greater variation and an overall reduction in the average elongation values from 21% for the CMT welds to 18% for the MAG welds and a slight associated increase in the tensile strength to that of the CMT welds.

5.6.3.2 Comparison of Tensile Data for CMT Welds and MAG Welds in 5.8mm EN1.4003

For the tensile tests conducted on the 5.8mm thick material welded using the CMT process, the elongation values (Table 25) are above the specification identified in Table 5 with the exception of sample 50.10, where the value was 12.9%. On this sample the tensile test failed within the weld region and the fracture surface revealed regions that lacked fusion through the welding process, the interesting point to note was that it didn't affect the yield strength or tensile strength values for this sample. Two other samples were also noted to have cracking in the weld region following testing, even though failure was in the parent material away from the weld in both instances (samples 50.11 & 52.1) and both of these demonstrated a slightly reduced elongation value. A high proportion of these tests didn't meet the specification for the material in terms of tensile strength and all of them failed to meet the requirements for yield strength.

The tensile samples testing the properties of the MAG welded 5.8mm thick material (Table 26) had a greater amount of variability to the data, with again none of these samples meeting the minimum criteria for yield strength. A number of the samples

met the minimum tensile strength requirements however only five of the samples failed in the parent material (M1.3, M1.4, M1.6, M11.3, M11.4), with the remainder failing in the weld and a number of instances of evidence showing a lack of fusion observed in these which indicated that the welds were not optimised and therefore the likelihood is that they would need an increase in the power to ensure the fusion in the root of the weld is achieved. This increase in the heat input into the weld would have a more pronounced effect on the detrimental effects associated with welding this material

There was also no removal of the weld cap or any excess penetration in the root, therefore the weld itself and any of the HAZ between the cap and root will have had an increase in cross sectional area, which isn't accounted for in the strength measurements as just the parent cross sectional areas were used for these calculations. Therefore with the additional cross section in the weld area, reduced the likelihood of failure in this region, with a sound weld. Although this test was useful in comparing the two welding processes, failures within the weld themselves have only manifested due to welding defects, rather than providing the ability to differentiate between microstructural differences that are created as a result of the different welding processes. For the welds created using both processes in both thicknesses there appears to be some advantage to the results seen for the CMT welds as at the 3.8mm thickness the difference is marginal, with slightly better results for the CMT welds. With the thicker parent material joints it is evident that the joints in all cases aren't complete and this is having a significant effect on the properties, in particular, the elongation values.

5.6.4 Impact Results From 3.8mm & 5.8mm Thick EN1.4003 MAG/CMT

Comparison

The manufacture of the impact specimens was made to establish the effects of microstructural change in the most severely affected part of the HAZ, closest to the weld, therefore during manufacture the root of the notch was put in this area. The samples made from the 3.8mm material, using the CMT welding process, showed a relatively consistent energy absorption values as can be seen in Table 28 , whereas the samples in the same thickness created using the MAG welding process has a lot more variation in the results (Table 29) with energy absorption as low as 9 Joules (sample M30.5), which is likely as a result of the increased heat input in the creation of the MAG welds over those using the CMT process. This would then increase the detrimental effects of grain coarsening in the HAZ area and therefore reduce the toughness of the weld.

The impact specimens tested that were made by both the MAG and CMT processes (Table 31 & Table 32), didn't show any discernible differences, the averages for the results from the two different processes were the same and the range of results was similar. When this is taken into account that the parent material energy absorption value was tested to be approximately 180 Joules in the 5.8mm thickness, then it can be seen that the effects associated with the acicular phase and grain coarsening , that restricts the use of these grades of stainless steel is quite severe on the impact properties of the material at an average of 34.7J for the samples that were CMT welded and 34.7J for samples that were MAG welded in the 5.8mm thick EN1.4003 parent material.

5.6.5 Fatigue Results From 3.8mm Thick EN1.4003 MAG/CMT Comparison

The staircase fatigue testing undertaken on the CMT welded sample and the MAG welded samples in EN1.4003, 3.8mm thick parent material displays some differences in the fatigue properties of the joints created using the two different processes. The CMT welded samples tested had a higher mean fatigue load at 43kN, but the convergence factor at over 10 means that the results are not statistically valid and carry a high standard deviation. This testing regime would have likely been enhanced and statistically more accurate had the step divide been more appropriate. The 0.5kN step used was too small and although on the initial tests conducted and at the start of the staircase it appeared to be appropriate, the results suggest it wasn't.

The staircase fatigue tests conducted on the MAG welded 3.8mm thick EN1.4003 material gave results that were statistically valid with a convergence factor of 0.472 and therefore between 0.3-1.2, the step divide used for these was at a more appropriate level. However to compare the welds created by the two processes through fatigue, none of the MAG welded samples tested above 35.5kN reached the pass criteria of 2 million cycles whereas all the tests conducted in the CMT staircase that exceeded 2 million cycles were tested above 41.5kN, essentially 2 steps up on the MAG staircase where samples met the pass criteria.

The difference in line load for samples produced using CMT and those produced using MAG welding are also significantly different, CMT welded samples have a line load of 964N/mm and MAG welded samples 833N/mm. Therefore comparing the results from the two processes, there is a significant difference between the fatigue properties of the CMT welds and the MAG welds, with the CMT process producing joints with enhanced fatigue properties. This may be as a result of the slight difference in the

grain size within the coarse region of the HAZ as identified in section 5.6.2 or there may have been some influence from an increased level of defects within the MAG welds.

5.6.6 Effect of Weld Defects on the Fatigue Properties of 3.8mm Thick

EN1.4003 Parent Material

The work looking at the effect of defects on the fatigue properties of the materials, on initial macroscopic evaluation of the fracture surfaces displayed the same defects that were seen in the non-destructive and subsequent destructive evaluation as discussed in section 5.6.1. Work was then conducted to assess the extent of the defects apparent on the fracture surface of a number of samples that had undergone fatigue testing and failed prior to the pass criteria of 2 million cycles.

Therefore the three prominent defects that were seen on the fracture surfaces included, a lack of side wall fusion (Figure 115) with SEM analysis made in Figure 118 to Figure 120, a lack of root penetration (Figure 116) and gas porosity (Figure 117). For the purposes of this element of the work, differentiation wasn't made of the type of defects as a proportion of the overall defective aspect of the fracture surface, however there is the consideration that due to the shape of some of the defects there may be a greater effect on the fatigue properties of the material. Gas porosity, due to its form within the material of being spherical, is likely to have a reduced impact on the fatigue properties than a defect with a high aspect ratio perpendicular to the fatigue load axis, such as with a lack of root penetration.

Examination of Figure 121 shows exponential decay in the results for the plot of percentage area of defects on the fracture surface against the number of cycles to failure. With all of the samples tested with a defect area, on the fracture surface

above 2%, none of the samples survived above 600,000 cycles, just over a quarter of that required against the 2 million cycle pass criteria. These findings relate to the work of Tijani et al (2013) who also found relationships between the percentage of defects in a material and the number of cycles to failure under fatigue loading conditions.

In Figure 121 there is no account taken for the actual load which the samples were subjected to therefore in Figure 122, there is the information relating to the load which the sample was tested under. From this data it can be seen that some of the samples that have relatively low defects observable on the fracture surface and yet have still failed at a low number of cycles, have in fact been tested at a higher load level and therefore would be expected to have a reduced life under fatigue testing conditions. An interesting observation from this figure, is that, where there are multiple results at the same loading criteria, there appears to be a correlation between the number of cycles to failure and the percentage of defects measured on the fracture surface, for each of the testing loads. When the gradient for the number of cycles to failure against percentage area of defects on the fatigue for each is plotted against the load, there is a correlation which can be seen in Figure 123. This, confirming the work that Ottersbock et al (2016) undertook, shows that as the fatigue load is increased and or the area of defects containing within the weld are increased there is a reduction in the number of cycles the weld can be subjected to before failure. But as the load is increased the presence of defects has a more significant impact on the fatigue life of the component.

5.6.7 Effect on Fatigue Properties of the Parent Metal to Reinforcement

Weld Angle

There appears to be a correlation, as seen by Ashcroft (2008) between the root angle and the number of cycles to failure from looking at the results altogether (see Figure 141), for all the samples that passed two million cycles, the angle of the root was as a minimum 128 degrees. There was a great deal of variation within this data and some of this was likely as a result of defects within the joints as discussed in section 5.6.6.

One of the key parameters in the prediction of fatigue life is the load and when examining the graphs for the angles/cycles at each load (Figure 131 to Figure 140) , there would be the expectation from work conducted by Harris and Syers (1979) that as the load is increased the sensitivity to the angle would increase, however the results do not indicate this to be the case and it would be recommended for future work to assess the content of defects evident on the fracture surfaces for all the samples.

5.7 Heat Treatment Trial To Identify Key Temperatures At Which Microstructural Changes Occur And The Effect of Time On These Changes.

The thermal cycle experienced during the welding process has extremely rapid heating and cooling rates associated with it as a result of very high arc temperatures and a high thermal conductivity common to metals. In an attempt to try and simulate the thermal cycle the trial was devised to identify the point at which temperatures are sufficient to create microstructural change, such as that seen in the heat affected zone

and then identify the effects of the change on the impact properties and hardness of the material.

It is well established in the literature (Lippold & Kotecki, 2005) that the microstructural response to a thermal cycle is not just dependant on temperature, but also time and therefore whilst the trial conducted wasn't an exact replication of the thermal cycle that was experienced during the manufacture of a weld, it allows some comparisons to be drawn between observable microstructural features within a heat affected zone, the likelihood of the temperature reached in this area and then the effect of this on the mechanical properties.

It can be seen when comparing the image for the sample that had been subjected to 700°C for 20 minutes (Figure 147) to the image of the material in the un-heat treated state (Figure 62) that there is no observable difference between them in terms of microstructure. This is the same for all the heat treated samples, held for 20 mins at temperature, right up until the temperature gets to approximately 770°C (Figure 161) where the microstructure changes from a fully ferritic structure to one that contains ferrite and martensite. Associated with this, as can be seen in Figure 182 there is an increase in the hardness from below 150HV₁₀ to 165HV₁₀ as a result of the presence of the harder martensite.

When the samples are held for longer (2 hours), the martensitic phase can be seen appearing in the structure on samples exposed to temperatures of 750°C followed by a water quench, as seen in Figure 171, with the same cycle applied at 740°C (Figure 172) the structure remains ferritic which means at this time/temperature combination the transformation to austenite does not take place.

As the temperature is increased, then as is the quantity of martensite within the microstructure and subsequently the hardness which increases from the parent material value of 150 HV₁₀, increasing up to approximately 281 HV₁₀ at 900°C and then as can be seen in Figure 186, the hardness reaches its maximum level of 340 HV₁₀ which varies according to how long the sample has been left at temperature, for the samples left for 20 minutes, the hardness is not as high as for those samples that were left for 30 minutes, this could be that 20 minutes at temperature, may not give sufficient time for elements, particularly carbon, to go into a solid solution, therefore reducing the hardening effect associated with a fast cool. When looking at the results for the samples that have been left for 360 minutes there is a slightly softer material and this will be because holding at the elevated temperatures longer, will permit a greater amount of grain coarsening and also the slower cool afforded to these samples, will reduce the amount of carbon that is trapped in solution and therefore the strain on the structure that gives the increase in hardness associated with martensite. This reduction on the hardness properties may be as a result of the high temperature embrittlement that affects these materials when subjected to temperatures in excess of 900°C, with the additional time allowing the diffusion of carbon to form the detrimental carbides and carbo-nitrides as discussed in section 2.3.

The other observable trend with the results is that the grain size of ASTM 8, remains constant up to 900°C where the sample that was held for an extended period of 360 minutes, showed a significant increase in the grain size, going from the ASTM 8, to ASTM 5 (Figure 187), this is not in agreement with work conducted by Lakshminarayanan et al (2009) who reported that temperatures above 955°C needed to be achieved for grain coarsening. For the samples held at shorter durations (20

and 30 mins) the samples needed to be at higher temperatures, 940°C - 1000°C to have a noticeable effect on the grain size, which then when comparing to the welding process, which experiences temperatures up to the melting point of the material, would suggest that for the grain coarsening observed in the heat affected zone, may occur as a result of the higher temperatures experienced during welding (up to the melting point of the material) rather than the specific temperatures identified in this study. It also must be noted that with the simulations made in this element of the work, it was not possible to replicate the heating rates and superheating which will have effect on the weld and HAZ.

A number of nonstandard impact specimens (5.8 x 10 x 55mm) were created and heat treated to the same parameters identified through the microstructural work and then tested to determine the effect on the impact properties of the various microstructural changes identified. As can be seen in Figure 185 the impact properties of the material that have undergone no microstructural change is at around 200J. When there is the introduction of martensite within the structure this reduced the toughness of the samples down by approximately 30%. When there was not only the martensite within the structure but also grain growth associated with the higher temperatures, then the energy absorbed by the specimens dropped to less than 10 J in some instances. The effect associated with the martensitic structure, is likely as martensite is a brittle phase and therefore doesn't absorb much energy when a crack is propagating through it. The grain coarsening reduces the number of grain boundaries that hinder the motion of dislocations and therefore reduce the toughness of the material.

6 Conclusions

The research has examined and compared the CMT welding process against the conventional GMAW process using ferritic stainless steel and after a review of the literature and analysis of the results from the work conducted within this research the following conclusions can be made;

6.1 Research on thin grades (<2mm) of ferritic stainless steel welded using CMT & MAG techniques

- Increasing the heat input increases the width of the HAZ
- When CMT welding the addition of a pulsed arc, which gives an increase in the heat input, resulting in a flatter weld reinforcement
- With the use of just CMT, without a pulsed arc, it was found to yield a larger grain size within the HAZ
- Pure CMT was found to produce fully penetrating welds at a lower heat input than welds produced with the additional pulsed arc
- The overall heat input has a significant effect on the penetration and HAZ characteristics and it was found that it wasn't just the energy that is put into the weld that controls the weld characteristics, but how that energy is applied e.g. torch angle, pulsed current, torch traverse speed, weld gap as there may be a variation in the efficiency of the arc energy.
- Greater welding gaps create bridgeability issues at higher torch traverse speeds
- Drag torch angle produces fully penetrating welds at lower heat inputs than leading angles possibly due to the filler being directly toward previously heated materials.

- Grade EN1.4016 is more sensitive to the thermal cycle associated with welding than EN1.4009
- The measured power levels of the welds monitored varied by up to 15 amps and 1.9 volts for the same set level using the CMT process
- The variation in ALC between -30% and +30% was calculated to give a difference of approximately 6J/mm to the net heat input
- An ALC setting of -30 gave a greater amount of penetration than when the setting was at +30
- The pulse correction function increases the energy levels of the pulses within the welding cycle to allow incorporation of short bursts of higher energy.

6.2 Grade EN1.4003 3.8mm and 5.8mm thick material welded using CMT and MAG techniques

- The HAZ of a weld using EN1.4003 grade parent material has 2 distinct regions, the first closest the fusion zone has a martensite content and grain coarsening and further away from the fusion zone, martensite alone
- NDT techniques utilised within the research were insufficient to detect the lack of side wall fusion evident in the samples following destructive examination
- Tensile tests conducted on the 3.8mm thickness, welding using CMT, demonstrated 100% joint efficiency
- Tensile tests conducted on the 5.8mm thickness materials produced using each of the welding techniques did not produce welds that consistently demonstrated 100% joint efficiency

- Average values for the impact tests conducted on samples welded using each of the techniques were comparable and therefore no discernible difference could be noted between the effect on toughness
- Fatigue results for CMT shows enhanced properties over the MAG welded samples for 3.8mm thick EN1.4003 grade material likely due to a reduced effect on the heat affected zone and a reduced number of defects within the weld.
- Under fatigue testing, no sample that had the fracture surface examined survived 2 million cycles with a defect area greater than 2% of the fracture surface
- There was found to be a relationship between the number of cycles to failure at a particular load and the percentage of the defect area measured on the fracture surface, which shows the greater the fatigue load the more sensitive the material becomes to the defect content
- The weld root angle was $>128^\circ$ for all fatigue tested samples that exceeded 2 million cycles
- At temperatures in excess of 750°C microstructural change is observed from ferrite to ferrite and martensite for simulated heat treated samples
- The hardness levels associated with martensite in the microstructure of the simulated heat treated samples increase up to 900°C
- Grain coarsening was observed in the heat treated samples at 900°C after being held at this temperature for 360 minutes. An increase in temperature above 900°C was required to observe any grain growth for reduced holding times.
- The reduction in impact properties as a result of martensite in the structure was measured to be approximately 30% for simulated heat treated samples

- Impact tests made on simulated heat treatment samples with grain coarsening and a martensite content were found to reduce the toughness by approximately 95%

7 Further Work

Following a review of the work undertaken, suggestions for further work are highlighted below:

- Explore the modification of other welding parameters, such as shielding gas, the use of a backing gas, welding wire or edge preparation on the production of welds to eliminate the lack of side wall fusion, seen in a number of welds produced in this study.
- As part of this work, two thicknesses (3.8mm & 5.8mm) of EN1.4003 grade stainless steel were subject to assessment, testing of the 5.8mm thick material requires completing as time limitations prevented this occurring within this project.
- The results from the CMT 3.8mm thick EN1.4003 parent material, under fatigue testing didn't produce statistically valid results, therefore for an enhanced comparison, it is suggested that these tests be repeated using a different step divide.
- Increase the analysis on defects within the failed fatigue samples to provide a greater data set and allow comparison between CMT and MAG welded joints.
- Explore options of NDT techniques for the identification of small defects within welds or optimise radiographic parameters to this end.
- Compare CMT with other 'low heat input' GMAW processes that have been brought to market.
- Continue work on heat treatment to explore the temperatures at which the acicular phase first manifests, perhaps using EBSD for phase identification.

- Explore the effect of CMT, compared to conventional GMAW on grades of ferritic stainless more sensitive to embrittlement phenomena.

8 Works Cited

- ABB. (2007, November). *Arc Welding*. Retrieved July 3, 2017, from Complete robot automation packages for industrial applications:
<https://library.e.abb.com/public/91c69c27716683e9c125739b002f8787/Arc%20welding%20folder%20WEB.pdf>
- AIR LIQUIDE. (2009). *Gas Encyclopaedia - Helium*. Retrieved April 26, 2011, from Air Liquide: <http://encyclopedia.airliquide.com/Encyclopedia.asp?GasID=32>
- AIR LIQUIDE. (2009). *Gas Encyclopedia - Air*. Retrieved April 26, 2011, from Air Liquide: <http://encyclopedia.airliquide.com/Encyclopedia.asp?LanguageID=11&CountryID=19&Formula=&GasID=73&UNNumber=&EquivGasID=32&VolLiquideBox=&MasseLiquideBox=&VolGasBox=&MasseGasBox=&RD20=29&RD9=8&RD6=64&RD4=2&RD3=22&RD8=27&RD2=20&RD18=41&RD7=18&RD13=71&RD16=35>
- Air Products. (2017). *Welding Gas Selector*. Retrieved June 27, 2017, from Air Products: http://www.airproducts.co.uk/microsite/uk/welding_selector/aluminium.htm#res2
- Albertson, T. P., Stephens, R. R., & Bayha, T. D. (1997). Fatigue Crack Growth of Two Advanced Titanium Alloys at Room and Elevated Temperature. In R. S. Piascik, R. P. Gangloff, & A. Saxena (Eds.), *Elevated Temperature Effects on Fatigue and Fracture* (pp. 140-161). ASTM.
- American Welding Society. (1991). *Welding Handbook - Welding Processes* (8th Edition ed., Vol. 2). (R. L. O'Brien, Ed.) Miami: American Welding Society.
- AMG Vanadium Inc. (2009). *Manganese*. Retrieved May 26th, 2012, from Metallurgvanadium:
<http://www.metallurgvanadium.com/manganesepage.html>
- Amunda, M. O., & Mridha, S. (2011, April 27th). An Overview of Sensitization Dynamics in Ferritic Stainless Steel Welds. (F. J. Perez, Ed.) *International Journal of Corrosion*, 2011, 1-9.
- ArcelorMittal. (n.d.). *What is Stainless Steel? Manufacturing Process*. Retrieved May 19th, 2012, from ArcelorMittal Stainless Europe:
<http://www.arcelormittal.com/stainlesseurope/manufacturing-process.html>
- Armao, F., Byall, L., Kotecki, D., & Miller, D. (2014). *Gas Metal Arc Welding Guidelines*. Retrieved September 10, 2016, from

http://www.lincolnelectric.com/assets/global/products/consumable_miggmaw/wires-superarc-superarcl-56/c4200.pdf

Ashby, M. F., & Jones, D. R. (2001). *Engineering Materials 2* (2nd ed.). Oxford, UK: Butterworth-Heinemann.

Ashcroft, E. (2008). *Mechanical and Metallurgical Properties of Dissimilar Metal Joints Using Novel Joining Techniques*. Sheffield: Sheffield Hallam University.

ASM Handbook Committee. (1988). *Metals Handbook- Metallography and Microstructures* (9th ed., Vol. 9). (K. Mills, J. R. Davies, J. D. Destefani, D. A. Dieterich, G. M. Crankovic, H. J. Frissell, et al., Eds.) Ohio, USA: American Society For Metals.

ASM International. (2008). *Fatigue*. Retrieved August 5, 2016, from ASM International: http://www.asminternational.org/documents/10192/1849770/05224G_Chapter14.pdf

Avesta Welding. (2006). *Avesta 308LSi Welding Wire*. Retrieved August 28, 2012, from Avesta.com: <http://www.avestawelding.com/3273.epibrw>

Bailey, N. (1994). *Weldability of Ferritic Steels*. Cambridge, UK: Abington Publishing.

Battelle-Columbus, B. L. (1996). Effect of Surface Conditions and Processing on Fatigue Performance. In *Fatigue and Fracture* (Vol. 19, pp. 785-794). ASM International.

Bax, M., Short, D., & Bayliss, M. (1988). *Underwater Inspections* (3rd ed.). Taylor and Francis Ltd.

Bayoumi, M. R., & Abdellatif, A. K. (1995). Effect of Surface Finish on Fatigue Strength. *Engineering Fracture Mechanics*, 51(5), 861-870.

Bayraktar, E., Kaplan, D., & Grumbach, M. (2004). Application of Impact Tensile Testing to Spot Welded Sheets. *Journal of Materials Processing Technology*(153-154), 80-86.

Beddoes, J., & Parr, G. J. (1999). *Introduction to Stainless Steel* (3rd ed.). ASM International.

Benoit, A., Jobez, S., Paillard, P., Klosek, V., & Baudin, T. (2011). Study of Inconel 718 weldability using MIG CMT process. *Science and Technology of Welding and Joining*, 16(6), 477-482.

BOC. (2007). *Welding Processes*. Retrieved September 10, 2016, from <http://www.bocworldofwelding.com.au/media/pdf/file/library/WOWLibrary-GMAW-FCAW-MCAW%20Welding.pdf>

- BOC UK. (2010). *Pureshield Argon - BOC UK*. Retrieved March 12th, 2011, from BOC online:
http://www.boconline.co.uk/products/products_by_type/industrial_gases/inert_gases/pureshield_argon.asp
- Boulding, J. (2012). *The Effects of Parameters and Consistency of Cold Metal Transfer Welded Ferritic Stainless Steel Joints*. Undergraduate Final Year Project, Sheffield Hallam University, Department of Engineering, Sheffield.
- Boulding, J. (2012). *The Effects of Parameters and Consistency of Cold Metal Transfer Welded Ferritic Stainless Steel Joints*. Final Year Project, Sheffield Hallam University, Department of Engineering, Sheffield.
- Breareley, H. (1991). *Harry Breareley Stainless Pioneer - autobiographical notes*. Sheffield: British Steel Stainless in conjunction with The Kelham Island Industrial Museum.
- British Stainless Steel Association. (n.d.). *The Discovery of Stainless Steel*. Retrieved May 26th, 2012, from British Stainless Steel Association:
http://www.bssa.org.uk/about_stainless_steel.php?id=31
- British Standards Institution. (1998). *Welding - Recommendations for Welding of Metallic Materials - Part 1 General guidance for arc welding*. BSI.
- Brownlee, K. A., Hodges, J. L., & Rosenblatt, M. (1953). The up and down method with small samples. *Journal of the American Statistical Association*, 48(262), 262-277.
- Burgin, F. K. (2008). *Liquid Metal Embrittlement in the Arc Brazing of Stainless Steels*. Retrieved July 23, 2011, from Sheffield Hallam University:
http://www.shu.ac.uk/_assets/pdf/ouo-LME%20Poster%20Pres%2004.pdf
- Cary, H. B. (1998). *The History of Welding*. Retrieved June 6, 2010, from Miller:
<http://www.millerwelds.com/resources/articles/index?page=articles14.html>
- Cary, H. B., & Helzer, C. S. (2005). *Modern Welding Technology*. (E. Francis, Ed.) New Jersey, Ohio, USA: Pearson Prentice Hall.
- Chakrabarty, J. (1987). *Theory of Plasticity*. McGraw-Hill.
- Choulet, R. J. (1997). *Stainless Steel Refining. AISE Seminar*. Detroit: Praxair Technology Inc.
- Cobb, H. M. (2010). *The History of Stainless Steel*. USA: ASM International.
- Colombier, L., & Hochmann, J. (1967). *Stainless and Heat Resisting Steels* (1st (English) ed.). St. Etienne, France: Edward Arnold Ltd.

- Computational Thermodynamics Inc. (2011). *Phase Diagrams - Iron Chromium*. Retrieved June 11, 2011, from Computational Thermodynamics: <http://www.calphad.com/iron-chromium.html>
- Cortie, M. B. (1993, July). History and Development of Ferritic Stainless Steels. *Journal of The South African Institute of Mining and Metallurgy*, 93(7), 165-176.
- Cunat, P.-J. (2004). *Alloying Elements*. Retrieved May 26th, 2012, from Euro-Inox: www.euro-inox.org/pdf/map/AlloyingElements_EN.pdf
- Deddoes, J., Parr, G. J., & Hanson, A. (1999). *Introduction to Stainless Steels* (3rd ed.). (J. Beddoes, Ed.) ASM International.
- Demo, J. J. (1982). Structure, Constitution and General Characteristics of Wrought Ferritic Stainless Steels. In R. A. Lula, & R. A. Lula (Ed.), *Source Book On The Ferritic Stainless Steels* (pp. 1-65). American Society For Metals.
- Dixon, W. J., & Mood, A. M. (1948). A Method for Obtaining and Analyzing Sensitivity Data. *Journal of the American Statistical Association*, 43(241), 109-126.
- DuPont, J. N. (1999, July). Microstructural Development and Solidification Cracking Susceptibility of a Stabilised Stainless Steel. *Welding Research Supplement*, 253-263.
- DuPont, J. N., & Marder, A. R. (1995, December). Thermal Efficiency of Arc Welding Processes. *Welding Research Supplement*, pp. 406-416.
- Easterling, K. (1992). *Introduction to the Physical Metallurgy of Welding* (2nd Edition ed.). Butterworth Heineman.
- eFUNDA. (2016). *High Cycle Fatigue*. Retrieved September 17, 2016, from http://www.efunda.com/formulae/solid_mechanics/fatigue/fatigue_highcycle.cfm
- Elrefaey, A. (2015). Effectiveness of cold metal transfer process for welding 7075 aluminium alloys. *Science and Technology of Welding and Joining*, 20(4), 280-285.
- Engineers Edge. (2016). *Fatigue Crack Growth Analysis Review - Strength of Materials*. Retrieved August 5, 2016, from http://www.engineersedge.com/material_science/fatigue_crack_growth_analysis_review_10071.htm
- ESAB. (2002). *Gas Properties*. Retrieved May 21, 2011, from ESAB: http://www.esabna.com/euweb/mig_handbook/592mig4_6.htm
- ESAB. (n.d.). *Short Circuit (Short Arc) Welding*. Retrieved January 27, 2017, from http://www.esabna.com/euweb/mig_handbook/592mig1_4.htm

- EWI. (2016). *Resistance Seam Welding*. Retrieved January 3, 2017, from <https://ewi.org/resistance-seam-welding/>
- Feng, J., Zhang, H., & He, P. (2009). The CMT short-circuiting metal transfer process and its use in thin aluminium sheets welding. *Materials and Design*, 1850-1852.
- Filho, D. F., Ferraresi, V. A., & Scotti, A. (2010). Shielding Gas Influence on the Ferritic Stainless Steel Weldability. *Journal of Engineering Manufacture*, 224(Part B), 951-961.
- Fronius International GmbH. (2005, September). *Weld + Vision Archives*. Retrieved June 5, 2010, from Fronius International: http://www.fronius.com/cps/rde/xchg/SID-35E91591-8A995FC0/fronius_international/hs.xsl/79_11392_ENG_HTML.htm
- Fronius International GmbH. (2004, January). *CMT Process - A Revolution in Materials-Joining Technology*. Retrieved June 5th, 2010, from Guangxi Technological college of Machinery and Electricity: http://www.gxcme.edu.cn/jpkc1/hj060522/weld12.6/lesson/lesson5/5_1_6.pdf
- Fronius International GmbH. (2004, December 17). *The New Revolution in GMA Welding*. Retrieved June 5th, 2010, from Fronius International: http://www.fronius.com/cps/rde/xchg/SID-B6C98EF1-D9C2FB8C/fronius_international/hs.xsl/79_1997_ENG_HTML.htm
- Fronius International GmbH. (2007, July 10). *CMT:Cold Metal Transfer - MIG/MAG Dip Arc Transfer Process*. Retrieved June 5, 2010, from Welding Solutions: <http://www.digitalweldingsolutions.com/CMT.pdf>
- Fronius International GmbH. (2009, September). *Weld + Vision - Even more possibilities, with CMT Advanced*. Retrieved April 26, 2011, from Fronius: http://www.fronius.com/cps/rde/xchg/SID-2A4EB063-79E5B103/fronius_international/hs.xsl/79_17482_ENG_HTML.htm
- Fronius UK. (2015, December 15). *CMT Advanced technology from Fronius is suitable for welding thin sheets of metal*. Retrieved June 27, 2017, from The Engineer: <https://www.theengineer.co.uk/supplier-network/product/cmt-advanced-technology-from-fronius-is-suitable-for-welding-thin-sheets-of-metal/>
- Frost, N. E., Marsh, K. J., & Pook, L. P. (1974). *Metal Fatigue*. Oxford: Oxford University Press.
- Galenko, P., & Zhuravlev, V. (1995). *Physics of Dendrites : Computational Experiments*. World Scientific.

- GKN Aerospace. (2016). *Electron Beam Welding*. Retrieved September 10, 2016, from <http://www.gkn.com/aerospace/products-and-capabilities/capabilities/metallics/electron-beam-welding/Pages/default.aspx>
- Gross, T. S., & Lampman, S. (1996). Micromechanisms of Monotonic and Cyclic Crack Growth. In A. International, *Fatigue and Fracture* (Vol. 19, pp. 124-133). ASM.
- Grove, D., & Campean, F. (2007, December 14). A Comparison of Two Methods of Analysing Staircase Fatigue Test Data. *Quality and Reliability Engineering International*, 24, 485-497.
- Hackl, H. (n.d.). *Digitally Controlled GMA Power Sources*. Austria: Fronius International GmbH.
- Harris, W. J., & Syers, G. (1979). *Fatigue Alleviation*. Oxford University Press.
- Higgins, R. A. (2001). *Properties of Engineering Materials* (2nd ed.). Wednesbury, UK: Butterworth-Heinemann.
- Himmelbauer, K. (2004, 12 17). *The CMT Process - A revolution in welding technology*. Retrieved 6 5, 2010, from Fronius International GmbH Web Site: http://www.fronius.com/internet/eng/doc/ST/22_cmt_the_new_revolution_in_digital_gma_welding_gb.pdf
- Hobart Institute of Welding Technology. (1998). *The History of Welding*. Retrieved September 4, 2016, from <https://www.millerwelds.com/resources/article-library/the-history-of-welding>
- Instron. (n.d.). *Bluehill 3*. Retrieved June 27, 2017, from Instron Testing Software: <http://www.instron.co.uk/en-gb/products/materials-testing-software/bluehill-software>
- International Council on Combustion Engines. (2009). *Guidance for evaluation of Fatigue Tests*.
- Iordachescu, D., & Quintino, L. (2008). Steps Towards a New Classification of Metal Transfer in Gas Metal Arc Welding. *Journal of Materials Processing Technology*(202), 391-397.
- Izutani, S., Shimizu, H., Suzuki, K., & Koshiishi, F. (2007). *Observation and Classification of Droplet Transfer in Gas Metal Arc Welding*.
- Kaul, R., Ganesh, P., Tripathi, P., Nandedkar, R. V., & Nath, A. K. (2003). Comparison of Laser and Gas Tungsten Arc Weldments of Stabilized 17 wt% Cr Ferritic Stainless Steel. *Materials and Manufacturing Processes*, 18(4), 563-580.

- Key to Metals AG. (2005, October). *Structural features of fatigue*. Retrieved August 5, 2016, from totalmateria:
<http://www.totalmateria.com/page.aspx?ID=CheckArticle&site=kts&NM=162>
- Kjellberg, O. (2004). Autobiography - March 1918. (B. Altemuhl, Ed.) *Svetsaren - The ESAB Welding and Cutting Journal*, 59(1), pp. 5-7.
- Koninklijke Philips Electronics N.V. . (2004). *Automotive Headlamp*. Retrieved May 19th, 2012, from Philips.co.uk: <http://www.philips.co.uk/c/car-lamps/longlife-h4-12-v-55-w-12342llecob1/prd/>
- KTH. (2003). *Coffin-Mason Relation*. Retrieved August 3, 2016, from http://www.energy.kth.se/compedu/webcompedu/S5_Aeroelasticity/B1_Introduction_to_Aeroelasticity/C7_Introduction_to_High_Cycle_Fatigue/ID122_files/Coffin-Manson_relation.htm
- Kujanpaa, V., Suutala, N., Takalo, T., & Moisio, T. (1979). Correlation Between Solidification Cracking and Microstructure in Austenitic and Austenitic-Ferritic Stainless Steel Welds.
- Lakshminarayanan, A. K., Shanmugam, K., & Balasubramanian, V. (2009). Effect of Welding Processes on Tensile, Impact, Hardness and Microstructure of Joints Made Of AISI 409M FSS Base Metal and AISI 308L ASS Filler Metals. *Ironmaking and Steelmaking*, 36(1), 75-80.
- Lancaster, J. F. (1984). The Physics of Welding. *Physics in Technology*, 15.
- Lawrence, F. V., Dimitrakis, S. D., & Munse, W. H. (1996). Factors Influencing Weldment Fatigue. In A. International, *ASM Handbook - Fatigue & Fracture* (Vol. 19).
- Lieurade, H.-P. (2008). Fatigue Strength of Welded Joints. In R. Blondeau (Ed.), *Metallurgy and Mechanics of Welding* (pp. 207-237). John Wiley & Sons, Inc.
- Lim, B. S., Jeong, C. S., & Keum, Y. T. (2003, December). Effect of Temperature on Fatigue Crack Growth in P92 Steel. *Metals And Materials International*, 9(6), 543-547.
- Linde AG. (2012). *Gases For All Types of Stainless Steel*. Retrieved September 11, 2016, from http://www.linde-gas.com/internet.global.lindegas.global/en/images/Shielding_gases_for_stainless_steel_60785_1217_82204.pdf?v=2.0
- Linde AG. (2016). *Shielding Gases the right gas working for you*. Retrieved September 10, 2016, from http://www.linde-gas.com/internet.global.lindegas.global/en/images/Overview_of_shielding_gases_60734_1217_82202.pdf?v=3.0

- Lippold, J. C., & Kotecki, D. J. (2005). *Welding Metallurgy and Weldability of Stainless Steels*. Hoboken, New Jersey, USA: John Wiley & Sons, Inc.
- Lucas, W., Iordachescu, D., & Ponomarev, V. (2005). *Classification of Metal Transfer Modes in GMAW*. IIW.
- Lukas, P. (1996). Factors That Influence Crack Nucleation. In *Fatigue and Fracture* (Vol. 19, pp. 261-263). ASM International.
- Lula, R. A. (1989). *Stainless Steel*. Natrona Heights, USA: American Society For Metals.
- Madhavan, S., Kamaraj, M., & Vijayaraghavan, L. (2016). Microstructure and mechanical properties of cold metal transfer welding aluminium/dual phase steel. *Science and Technology of Welding and Joining*, 21(3), 194-200.
- Magowan, S. (2006). *Impact Properties of Arc Brazed Joints*. Undergraduate Final Year Project, Sheffield.
- Magowan, S. (2010). *Initial Investigation of Ferritic Stainless Steel to Ferritic Stainless Steel Joints produced using MAG, CMT & CMT + P Processes*. Research Progress Report, Sheffield.
- Magowan, S. J., & Smith, A. J. (2010). The Effects of Cold Metal Transfer (CMT) Welding on the Properties of Ferritic Stainless Steel. *Junior EuroMat*.
- Marble, W. H. (1921, May 11th). Stainless Steel: To the Editor of The New York Times. *The New York Times*.
- Mathers, G. (2016). *Precipitation hardening stainless steel : Job knowledge 102*. Retrieved September 3, 2016, from The Welding Institute: <http://www.twi-global.com/technical-knowledge/job-knowledge/precipitation-hardening-stainless-steels-102/>
- Mathers, G. (2016). *Welding of Austenitic Stainless Steel: Job Knowledge 103*. Retrieved September 17, 2016, from <http://www.twi-global.com/technical-knowledge/job-knowledge/welding-of-austenitic-stainless-steel-103/>
- Mathison, J. (2008). *Understanding Transfer Modes for GMAW*. Retrieved September 11, 2016, from <http://www.thefabricator.com/article/consumables/understanding-transfer-modes-for-gmaw>
- McEvily, A. J. (1996). Fatigue Crack Thresholds. In *Fatigue and Fracture* (Vol. 19, pp. 351-353). ASM International.
- Mechanical Engineering. (2016). *Gas Tungsten Arc Welding*. Retrieved September 10, 2016, from <http://mechanicalinventions.blogspot.co.uk/2012/12/gas-tungsten-arc-welding-gtaw-or.html>

- Miller. (2013). *Guidelines for Gas Tungsten Arc Welding (GTAW)*. Retrieved September 10, 2016, from <https://www.google.co.uk/url?url=https://www.millerwelds.com/~media/miller%2520electric/files/pdf/resources/bookspamphlets/gtawbook.pdf&rct=j&frm=1&q=&esrc=s&sa=U&ved=0ahUKEwjrs66MoYXPAhXTSxoKHS7aCGAQFgggMAI&usg=AFQjCNGKKY19wVhO5llmt2jN1D4YJnO-HQ>
- Mirzazadeh , M. M., & Plumtree, A. (2012, August). High Cycle Fatigue Behavior of Shot Peened Steels. *Metallurgical and Materials Transactions*, 43(8), 2777-2784.
- NDT Resource Centre. (2016). *Fatigue Properties*. Retrieved August 3, 2016, from <https://www.nde-ed.org/EducationResources/CommunityCollege/Materials/Mechanical/Fatigue.htm>
- Nordeberg, H. (1973). *On Evaluation Methods for Fatigue*. Stockholm: Institute of Metals Research.
- Ono, Y., & Kaito, H. (1986). *Manufacturing Process and Properties of Stainless Steels*. Kawasaki Steel. Kawasaki Steel Corporation.
- Ottersbock, M., Leitner, M., Stoschka, M., & Maurer, W. (2016). Effect of weld defects on the fatigue strength. *Procedia Engineering*, 160, 214-222.
- Outokumpu. (2010, September 23rd). *Stainless Steel Grades*. Retrieved May 26th, 2012, from Outokumpu: <http://www.outokumpu.com/en/Products/Grades/Pages/default.aspx>
- Outokumpu. (2011, September). *Ferritic Stainless Grades Brochure*. Retrieved August 28, 2012, from Outokumpu: http://www.outokumpu.com/SiteCollectionDocuments/Ferritic_Stainless_Grades_Brochure.pdf
- Outokumpu. (2012). *Duplex Stainless Steels*. Retrieved August 28, 2012, from <http://www.outokumpu.com/en/Products/Grades/duplex-stainless-steel-grades/Pages/default.aspx>
- Pal, K., & Pal, S. K. (2011, August). Effect of Pulse Parameters on Weld Quality in Pulsed Gas Metal Arc Welding: A Review. *Journal of Materials Engineering and Performance*, 20(6), 918-931.
- Pepe, N., Egerland, S., Colegrove, P. A., Yapp, D., Leonhartsberger, A., & Scotti, A. (2011). Measuring the Process Efficiency of Controlled Gas Metal Arc Welding Processes. *Science and Technology of Welding and Joining*, 16(5), 412-417.

- Pickin, C. G., Williams, S. W., & Lunt, M. (2011). Characterisation of the Cold Metal Transfer (CMT) Process and its Application for Low Dilution Cladding. *Journal of Materials Processing Technology*, 211, 496-502.
- Pires, I., Quintino, L., & Miranda, R. M. (2007). Analysis of the Influence of Shielding Gas Mixtures on the Gas Metal Arc Welding Metal Transfer Modes and Fume Formation Rate. *Materials and Design*, 28, 1623-1631.
- Pires, J. N., Louriero, A., & Bolmsjo, G. (2006). *Welding Robots-Technology, System Issues and Applications*. Springer.
- Pook, L. (2007). *Metal Fatigue What It Is, Why It Matters* (Vol. 145). (G. M. Gladwell, Ed.) Springer.
- Praveen, P., Kang, M. J., & Yarlagadda, K. D. (2006, January - February). Characterization of Dynamic Behaviour of Short Circuit in Pulsed Gas Metal Arc Welding of Aluminium. *Journal of Achievements in Materials and Manufacturing Engineering*, 14(1-2), 75-82.
- Praxair. (1995, November). *The Basics of Gas Metal Arc Welding - Examining metal transfer modes, electrodes and shielding gases*. Retrieved May 21st, 2011, from Praxair:
[http://www.praxair.com/praxair.nsf/0/c56dbfa8e80d0dbd85256ab300140b28/\\$FILE/P-8126.pdf](http://www.praxair.com/praxair.nsf/0/c56dbfa8e80d0dbd85256ab300140b28/$FILE/P-8126.pdf)
- Praxair. (2005, October 31). *Shielding Gas Selection Manual*. Retrieved August 28, 2012, from
http://www.awssection.org/uploads/longisland/files/Praxair_Shielding_Gas_Manual.pdf
- Rajput, R. K. (2007). *A Text Book of Manufacturing Technology: Manufacturing Processes*. Laxmi Publications.
- Rao, P. (1999). *Manufacturing Technology: Foundry, Forming and Welding* (2nd ed.). McGraw Hill Education.
- Robinson, S. (2014). *Qualification of Radiography Through Destructive Examination*. BEng Final Year Dissertion, Sheffield Hallam University, Department of Engineering and Maths.
- Rosado, T., Almeida, P., Pires, I., Miranda, R., & Quintino, L. (2008). Innovations In Arc Welding.
- Shankar, V., Gill, T. P., Mannan, S. L., & Sundaresan, S. (2003, June/August). Solidification Cracking in Austenitic Stainless Steel Welds. *Sadhana*, 28(3 & 4), 359-382.

- Smith, B. (2014). *Welding Practice*. Routledge.
- Stodart, J., & Faraday, M. (1822, March 21). On the Alloys of Steel. *Philosophical Transactions of The Royal Society of London*, 112, 253-270.
- Streicher, M. A. (1977). Stainless Steels: Past, Present and Future. In R. Q. Barr (Ed.), *Stainless Steel '77*, (pp. 1-34).
- The Specialty Steel Industry of North America. (2016). *Corrosion: Chloride Stress Corrosion Cracking*. Retrieved September 3, 2016, from <http://www.ssina.com/corrosion/stress-corrosion-cracking.html>
- The Welding Institute. (2010). *Job Knowledge for Welders 4: MIG Welding*. Retrieved June 6, 2010, from TWI: <http://www.twi.co.uk/content/jk4.html>
- The Welding Institute Limited. (1995, February). *Job Knowledge 5: Submerged Arc Welding Process*. Retrieved May 19th, 2012, from The Welding Institute: <http://www.twi.co.uk/services/technical-information/job-knowledge/job-knowledge-5-submerged-arc-welding-process/>
- The Welding Institute Ltd. (n.d.). *Peace of Mind Assured Using On-site Metallography*. Retrieved July 23, 2011, from TWI: http://www.twi.co.uk/content/case_495.html
- Tijani, Y., Heinreitz, A., Stets, W., & Voigt, P. (2013). Detection and Influence of Shrinkage Pores and Non Metallic Inclusions on Fatigue Life of Cast Aluminium Alloys. *Metallurgical and Materials Transactions A*, 44A, 5408-5415.
- TWI. (2016). *FAQ: What is Pulsed MIG/MAG welding and what are its advantages over conventional MIG/MAG processes?*. Retrieved September 10, 2016, from <http://www.twi-global.com/technical-knowledge/faqs/process-faqs/faq-what-is-pulsed-mig-mag-welding-and-what-are-its-advantages-over-conventional-mig-mag-processes/>
- TWI Ltd. (2009). *Job Knowledge for Welders 44: Defects - Solidification Cracking*. Retrieved June 11, 2011, from TWI web site: <http://www.twi.co.uk/content/jk44.html>
- University of Ljubljana. (2000). *Lecture 2.6: Weldability of Structural*. Retrieved June 11, 2011, from <http://www.fgg.uni-lj.si/kmk/esdep/master/wg02/l0600.htm>
- Vandervoort, G. F. (2003). *Examination of Microstructures*. Retrieved June 12, 2011, from ASM Handbooks Online: <http://products.asminternational.org.lcproxy.shu.ac.uk/hbk/index.jsp>

- Vandervoort, G. F. (2004). *Colour Metallography - Film Formation and Interference Techniques*. Retrieved June 12, 2011, from ASM Handbooks Online: <http://products.asminternational.org.lcproxy.shu.ac.uk/hbk/index.jsp>
- Wang, J., Feng, J. C., & Wang, Y. X. (2008). Microstructure of Al-Mg dissimilar weld made by cold metal transfer MIG welding. *Materials Science and Technology*, 24(7), 827-831.
- Warmelo, M., Nolan, D., & Norrish, J. (2007). Mitigation of Senitisation effects in unstabilised 12%Cr ferritic stainless steel welds. *Materials Science and Engineering*, 157-169.
- Wermac. (2016). *Shielded Metal Arc Welding*. Retrieved September 10, 2016, from http://www.wermac.org/others/welding_electrode_manual-metal-arc-welding-process_smaw.html
- Westgate, S. (2009). *Resistance Welding of Sheet Metals - A Guide to Best Practice*. (TWI Limited) Retrieved June 6, 2010, from The Welding Institute Limited: <http://www.twi.co.uk/content/bprwsms01.html>
- Williams, R. O., & Paxton, H. W. (1982). *Source Book on The Ferritic Stainless Steels*. (R. A. Lula, Ed.) Natrona Heights, USA: American Society for Metals.
- Wilson, M. (2014). *Simulation of heat affected zones when CMT welding Ferritic Stainless Steel*. Undergraduate Final Year Project, Sheffield Hallam University, Engineering & Maths, Sheffield.
- Wirsching, P. H. (1983). *Statistical Summaries of fatigue Data for Design Purposes*. Iniversity of Arizona. NASA.
- WWS Group. (2005). *An Introduction to MIG Welding*. Retrieved September 11, 2016, from http://www.weldability-sif.com/media/docs/Intro_MIG_Welding.pdf
- Zheng, H., Ye, X., Jiang, L., Wang, B., Liu, Z., & Wang, G. (2010). Study on microstructure of low carbon 12% chromium stainless steel in high temperature heat affected zone. *Materials & Design*, 4836-4841.
- Zielinska, S., Valensi, F., Pellerin, N., Pellerin, S., Musiol, K., de Izarra, C., et al. (2009). Microstructural Analysis of the Anode in Gas Metal Arc Welding (GMAW). *Journal of Materials Processing Technology*, 209, 3581-3591.

9 List of Equipment

ABB IRB 1600-5/1.45 Robot Arm

ABB

Daresbury Park

Warrington

Cheshire

WA4 4BT

<http://new.abb.com/uk>

Arc Logger Ten (ALX)

The Validation Centre Limited

Unit 9 Sinclair Court,

Faraday Road

Great Yarmouth

Norfolk

NR31 0NH

www.tvcalx.co.uk

Cold Metal Transfer (CMT) welding equipment

(Fronius TransPulsSynergic 4000 CMT unit, controlled using a Fronius RCU 500i control unit)

Fronius U.K. Limited

Maidstone Road

Kingston

Milton Keynes

MK10 0BD

United Kingdom

<http://www.fronius.co.uk>

Infinite Focus Microscope (IFM)

Alicona Imaging GmbH

Dr.-Auner-Strasse 21a

8074 Raaba/Graz, Austria

<http://www.alicon.com>

Radiography Equipment

(Xograph Bucky Star with a Canon LANMIX CDXI-50G detector)

Xograph Healthcare

Xograph House

Ebley Road

Stonehouse

Gloucestershire

GL10 2LU

UK

<http://www.xograph.com>

Sample Preparation Equipment for metallographic inspection & Hardness Test equipment

(AbrasiMet precision cutting machine, SimpliMet 2000 hot mounting press, Alpha Beta grinder/polishing stations, Wilson Vickers Hardness Testing machine and Beuhler microhardness test machine)

Beuhler

Warwick Manufacturing Group

IMC Building

University of Warwick

Coventry

CV4 7AL

United Kingdom

www.buehler.co.uk

Tensile Testing and Impact Testing Equipment

(Instron 3369 dual column 50kN tensile machine & Dynatup 9250 drop tower impact machine)

Instron

Coronation Road,

High Wycombe,

Buckinghamshire,

HP12 3SY

United Kingdom

<http://www.instron.co.uk>

Fatigue Equipment/controller

Denison Mayes Group

Unit 14 Enterprise Park Ind Estate,

Beeston,

Leeds

LS11 8HA

<http://www.denisonmayesgroup.com>